

# Close Proximity Spacecraft Maneuvers Near Irregularly Shaped Small-bodies: Hovering, Translation, and Descent

by

Stephen B. Broschart

A dissertation submitted in partial fulfillment  
of the requirements for the degree of  
Doctor of Philosophy  
(Aerospace Engineering)  
in The University of Michigan  
2006

Doctoral Committee:

Associate Professor Daniel J. Scheeres, Chair

Professor Tamas I. Gombosi

Professor Pierre T. Kabamba

Professor N. Harris McClamroch

Laureano A. Cangahuala, Jet Propulsion Laboratory

© Stephen B. Broschart 2006  
All Rights Reserved

## ACKNOWLEDGEMENTS

I would like to acknowledge all the people who have made this work possible. First, I thank my advisor Dan Scheeres for lending his encouragement, patience, and expertise throughout my graduate studies. I am also very grateful for the numerous opportunities he created for my personal and professional growth over the years. I would also like to thank my parents for their steadfast support of my personal and academic pursuits over the years and for (literally) making all of this possible. I will always be grateful to all the teachers at Saint Louis School and the University of Michigan who helped me to get where I am today. I also thank the members of my committee for taking time from their busy schedules to work with me on this dissertation. Last but not least, this could not have been done without all the friends and distractions that have made nine plus years of the scholarly life a whole lot of fun =)

I also graciously acknowledge the financial support provided during this research by the Michigan Space Grant Consortium, the National Aeronautics and Space Administration's Graduate Student Researcher Program, the Jet Propulsion Laboratory at the California Institute of Technology (through an Interplanetary Network Technology Program grant to the University of Michigan, summer employment, and contract work), and the Lockheed Martin Corporation.

# TABLE OF CONTENTS

ACKNOWLEDGEMENTS . . . . .	ii
LIST OF TABLES . . . . .	vi
LIST OF FIGURES . . . . .	vii
LIST OF APPENDICES . . . . .	xii
LIST OF ABBREVIATIONS . . . . .	xiii
NOMENCLATURE . . . . .	xiv
ABSTRACT . . . . .	xx
CHAPTER	
<b>I. Introduction</b> . . . . .	1
1.1 State of Knowledge Previous to this Research . . . . .	5
1.2 Chapter Preview . . . . .	7
1.3 Outline of Original Contributions . . . . .	10
<b>II. Model Definitions</b> . . . . .	14
2.1 Small-body Shape Modeling . . . . .	14
2.2 Small-body Gravity Modeling . . . . .	17
2.3 Equations of Motion . . . . .	20
2.3.1 Two-body Problem in the Small-body Fixed Frame	20
2.3.2 Circular Restricted Three-body Problem . . . . .	22
2.3.3 Hill Three-body Problem . . . . .	23
2.3.4 Generalized Elliptic Restricted Three-body Problem	24
2.3.5 Limitations of the Equations of Motion . . . . .	26
2.4 Measurement Models . . . . .	28
2.4.1 Altimetry Measurements . . . . .	29
2.4.2 Time-of-flight Velocimeter Measurements . . . . .	32
2.4.3 Optical Navigation Measurements . . . . .	33
2.5 Small-body Characterization Tool . . . . .	34

<b>III. Numerical Validation of Hovering</b> . . . . .	35
3.1 Review of the Results of Sawai <i>et al.</i> . . . . .	35
3.2 HoverSim Simulation Tool . . . . .	38
3.2.1 Thrust Control Options . . . . .	39
3.2.2 HoverSim Output . . . . .	40
3.2.3 Simulation Verification . . . . .	40
3.3 Numerical Investigation of the Sawai <i>et al.</i> Results . . . . .	41
3.3.1 Hovering with GDTS w/OL Control . . . . .	42
3.3.2 Analysis of GDTS w/OL Controller Results . . . . .	45
3.4 Other Dead-band Hovering Approaches . . . . .	52
3.4.1 Body-fixed Hovering with IATNS Control . . . . .	52
3.4.2 Inertial Hovering . . . . .	55
3.5 Hovering above Asteroid 25143 Itokawa . . . . .	64
3.5.1 Body-fixed Hovering . . . . .	65
3.5.2 Inertial-Frame Hovering . . . . .	68
3.6 Discussion . . . . .	72
<b>IV. Zero-velocity Surfaces and Hovering</b> . . . . .	76
4.1 Zero-velocity Surface Result for Conservative Systems . . . . .	76
4.2 Zero-velocity Surfaces and Dead-band Hovering Control . . . . .	80
4.2.1 Conservation of the Jacobi Constant under Dead-band Thrust Control . . . . .	82
4.2.2 Dead-band Hovering Controller Design in Conservative Systems . . . . .	84
4.3 Effects of Uncertainty on Zero-Velocity Surfaces . . . . .	85
4.3.1 Local Result . . . . .	85
4.3.2 Formal Local Boundary Definition . . . . .	88
4.3.3 Formal Global Boundary Definition . . . . .	90
4.3.4 Maximum Allowable Perturbations in Initial State . . . . .	91
4.4 Particular Case Studies Applicable to Small-Bodies . . . . .	95
4.4.1 Hovering in the Body-Fixed Frame (Two-body Problem) . . . . .	95
4.4.2 Hovering in the Circular Restricted Three-body Problem . . . . .	98
4.4.3 Hovering in the Hill Three-body Problem . . . . .	100
4.5 Hovering in Non-conservative Systems . . . . .	102
4.5.1 Circular Orbit with Arbitrary Small-body Rotation . . . . .	104
4.5.2 Hovering in the Generalized Elliptic-restricted Three-body Problem . . . . .	106
4.6 Discussion . . . . .	107

<b>V. Hovering Implementation Issues and Simulations</b>	<b>110</b>
5.1 Generalized Hovering Zero-Velocity Surface Result	110
5.2 Using a Reduced Measurement Set for Control	112
5.2.1 Altimetry Measurements	112
5.2.2 Optical Navigation Measurements	125
5.3 Control Application	130
5.3.1 Ideal Fuel Cost of Hovering	131
5.3.2 Fuel Usage Under Dead-band Control	133
5.3.3 Dead-band Control Application Frequency	136
5.4 Simulations	137
5.4.1 Hovering with Small Errors in Initial State and Realistic Thrusters	138
5.4.2 Hovering with Measurement Errors and Finite Sampling Frequencies	140
5.5 Discussion	148
<b>VI. Translation and Descent</b>	<b>150</b>
6.1 Problem Formulation	151
6.2 Free-drop Solution	152
6.3 Constant Thrust Solution	152
6.3.1 Estimate of Linear Error	153
6.3.2 Accuracy of Translation Controller	155
6.4 Sensitivity to Parameter Uncertainty	156
6.4.1 Qualitative Sensitivity Results	159
6.4.2 Covariance Simulations	164
6.5 Detailed Descent Scenario	170
6.6 Sliding Dead-band Descent	172
6.6.1 Derivation of Necessary Control Thrust	174
6.6.2 Effect of Thrust on Surface Material	175
6.6.3 Results of Sliding Dead-band Descent Simulations	177
6.7 Discussion	178
<b>VII. Conclusions</b>	<b>182</b>
7.1 Summary of the Research Results	182
7.1.1 Summary of Hovering Strategies Discussed	185
7.2 Topics for Future Study	187
7.3 Application of this Research	189
<b>APPENDICES</b>	<b>192</b>
<b>BIBLIOGRAPHY</b>	<b>209</b>

## LIST OF TABLES

### Table

3.1	Asteroid (25143)Itokawa and Hayabusa Mission Parameters[1][2] . . .	73
4.1	Shape of the Nominal Local Zero-Velocity Surface for Hovering[3] . . .	78
4.2	Shape of the Perturbed Zero-velocity Surface[3] . . . . .	86
5.1	Daily Fuel Cost Coefficient for Several Small-bodies . . . . .	133
6.1	One-sigma Parameter Uncertainties for Descent Simulations . . . . .	164
6.2	Results of Covariance Analysis of Descents Above Itokawa . . . . .	165
6.3	Results of Covariance Analysis of Descents above Eros . . . . .	168
6.4	Results of Covariance Analysis of Descents above a 289 x 280 x 220 <i>km</i> Ellipsoid . . . . .	170

## LIST OF FIGURES

### Figure

2.1	Polyhedral Model of the Martian Moon, Deimos[4] . . . . .	15
2.2	Polyhedral Model of Asteroid 216 Kleopatra[5] . . . . .	15
2.3	Polyhedral Model of Asteroid 6489 Golevka[6] . . . . .	16
2.4	Altitude Measurement Geometry . . . . .	30
3.1	Angular Deviation for GDTS w/OL Body-fixed Hovering Controller, 20000 s ( $X - Z$ plane) . . . . .	45
3.2	Angular Deviation for GDTS w/OL Body-fixed Hovering Controller, 50000 s ( $X - Z$ plane) . . . . .	46
3.3	Angular Deviation for GDTS w/OL Body-fixed Hovering Controller, 20000 s ( $X - Y$ plane) . . . . .	47
3.4	Angular Deviation for GDTS w/OL Body-fixed Hovering Controller, 50000 s ( $X - Y$ plane) . . . . .	48
3.5	Dead-band Orientation Diagram . . . . .	49
3.6	Dead-band Dynamics Above an Ellipsoid under GDTS w/OL Con- trol, (a)Leading and (b)Trailing Edges . . . . .	50
3.7	Angular Deviation for IATNS Body-fixed Hovering Controller, 20000s ( $X - Y$ plane) . . . . .	55
3.8	Angular Deviation for IATNS Body-fixed Hovering Controller, 50000s ( $X - Y$ plane) . . . . .	56
3.9	Angular Deviation for IATNS Body-fixed Hovering Controller, 20000s ( $X - Z$ plane) . . . . .	57

3.10	Angular Deviation for IATNS Body-fixed Hovering Controller, 50000s ( $X - Z$ plane) . . . . .	58
3.11	Regions of Instability for Inertial Hovering above a 15x7x6 Ellipsoid for Various Rotation Rates, $T_{Eros} = 5.27$ hrs . . . . .	60
3.12	Magnitude of Floquet Multipliers for Inertial Hovering above a 15x7x6 Ellipsoid for Various Rotation Rates, Latitude = $0^\circ$ . . . . .	62
3.13	Deviation from Nominal for Inertial Hovering above a 15x7x6 Ellip- soid, Latitude = $0^\circ$ . . . . .	64
3.14	Angular Deviation of Body-Fixed Hovering above Asteroid (25143)Itokawa as a Function of Radius, GDTS w/OL Controller ( $5^\circ$ latitude, $45^\circ$ longitude) . . . . .	67
3.15	Angular Deviation of Body-Fixed Hovering above Asteroid (25143)Itokawa as a Function of Radius, GDTS w/OL Controller ( $30^\circ$ latitude, $45^\circ$ longitude) . . . . .	68
3.16	Angular Deviation of Body-Fixed Hovering above Asteroid (25143)Itokawa as a Function of Radius, GDTS w/OL Controller ( $0^\circ$ latitude, $-30^\circ$ longitude) . . . . .	69
3.17	Angular Deviation of Body-Fixed Hovering above Asteroid (25143)Itokawa as a Function of Radius, IATNS Controller ( $5^\circ$ latitude, $45^\circ$ longitude)	70
3.18	Angular Deviation of Body-Fixed Hovering above Asteroid (25143)Itokawa as a Function of Radius, IATNS Controller ( $30^\circ$ latitude, $45^\circ$ longitude)	71
3.19	Angular Deviation of Body-Fixed Hovering above Asteroid (25143)Itokawa as a Function of Radius, IATNS Controller ( $0^\circ$ latitude, $-30^\circ$ longi- tude) . . . . .	72
3.20	Magnitude of Floquet Multipliers for Inertial Hovering above Aster- oid (25143)Itokawa, $15^\circ$ Latitude . . . . .	74
4.1	Quadratic Zero-velocity Boundaries . . . . .	79
4.2	Allowable Regions of Motion for Different Eigenvalue Sets (shaded regions), Each Contour Represents Allowable Positions for some Non-negative Velocity Magnitude . . . . .	80

4.3	Level Sets of Example Dead-band Functions ((a) 1-D Dead-band, (b) 2-D Dead-band, (c) 3-D Dead-band), Arrows Indicate Direction of Unrestricted Motion . . . . .	82
4.4	Jacobi Constant versus Time for a Simulated Trajectory under Dead-band Control . . . . .	83
4.5	Example of a $+,+,-$ Simulated Trajectory (motion relative to the zero-velocity surface, dots indicate the predicted region of allowable motion) . . . . .	87
4.6	Escape Trajectory in the Restricted Three-body Problem: Contours are Zero-Velocity Surfaces for Different Initial Energies (vertical dotted lines are the dead-band control boundaries) . . . . .	93
4.7	Hovering Regions Near a Spherical Small-body ( $X$ and $Z$ axes normalized by the resonance radius) . . . . .	97
4.8	Hovering Regions Near Asteroid 433 Eros, $X - Y$ Plane . . . . .	98
4.9	Hovering Regions Near Asteroid 6489 Golevka, $Y - Z$ Plane . . . . .	99
4.10	Hovering Regions in the Restricted Three-Body Problem, $\mu = 0.01$ , $X - Y$ Plane, (coordinates normalized by $R$ , asterisks denote position of primaries) . . . . .	101
4.11	Hovering Regions in the Restricted Three-Body Problem, $\mu = 0.5$ , $X - Y$ Plane, (coordinates normalized by $R$ , asterisks denote position of primaries) . . . . .	102
4.12	Hovering Regions in the Hill Three-Body Problem, (a) $X - Y$ and (b) $X - Z$ Planes (coordinates normalized by the Hill Radius, asterisk denote position of the primary) . . . . .	103
5.1	Relative Orientation of the Altitude Dead-band Boundary $\mathbf{D}$ and the $+,+,-$ Zero-velocity Surface $\mathbf{Z}$ . . . . .	114
5.2	Parameterization Coordinates for (left to right) the One-sheet Hyperboloid, the Quadratic Cone, and the Two-sheet Hyperboloid . . . . .	116
5.3	Boundedness of Hovering with Altimetry in the $+,+,-$ Region above a Sphere, $X - Y$ Plane, Varying Small-body Radius with Constant $\mu_{sb}$ , 100% Open-loop Thrust, $\gamma = 50 m$ . . . . .	121

5.4	Boundedness of Hovering with Altimetry in the $+,+,-$ Region above a $3.5 \times 2.2 \times 1.6 \text{ km}$ Ellipsoid, 100% Open-loop Thrust, $\gamma = 50 \text{ m}$ . . . . .	122
5.5	Boundedness of Hovering with Altimetry in the $+,+,-$ Region above a $3.5 \times 2.2 \times 1.6 \text{ km}$ Ellipsoid, $X - Z$ Plane, Decreasing Open-loop Acceleration Cancellation, $\gamma = 50 \text{ m}$ . . . . .	123
5.6	Boundedness of Hovering with Altimetry in the $+,+,-$ Region above a $3.5 \times 2.2 \times 1.6 \text{ km}$ Ellipsoid, $X - Z$ Plane, 100% Open-loop Thrust, Variable $\gamma$ . . . . .	124
5.7	Numerical Results with GDTS w/OL Body-fixed Hovering Control Overlaid with Altitude Dead-band Sufficiency Condition . . . . .	125
5.8	Optical Navigation Dead-band vs Zero-velocity Surface Orientation . . . . .	127
5.9	General Orientation of Optical Navigation Dead-band and Zero-velocity Surface . . . . .	128
5.10	Position Coefficient for Fuel Usage as a Function of Latitude and Range . . . . .	132
5.11	Required $\Delta V$ vs. Time for Varying Open-loop Thrust Cancellation . . . . .	135
5.12	Trajectory Under Two-dimensional Dead-band Control with Errors in Initial State and Open-loop Thrust with Finite $T_m$ (dead-band and zero-velocity surface boundaries shown in gray) . . . . .	139
5.13	Jacobi Constant Versus Time for a Trajectory Under Two-dimensional Dead-band Control with Finite $T_m$ and Errors in Initial State and Open-loop Thrust . . . . .	140
5.14	Jacobi Constant Versus Time for a Trajectory Under Altitude Dead-band Control with Errors in Initial State and Finite $T_m$ . . . . .	142
5.15	Jacobi Constant Versus Time for a Trajectory Under Altitude Dead-band Control with Errors in Initial State and Finite $T_m$ . . . . .	143
5.16	Trajectory Under Altitude Dead-band Control with Measurement Errors and Finite Sampling Frequency . . . . .	144
5.17	Jacobi Constant Versus Time for a Trajectory Under Altitude Dead-band Control with Measurement Measurement Errors and Finite Sampling Frequency . . . . .	145

5.18	Trajectory Under Altitude Dead-band Control with Fixed Duration Dead-band Thrust . . . . .	146
5.19	Jacobi Constant Versus Time for a Trajectory Under Altitude Dead- band Control with Fixed Duration Dead-band Thrust . . . . .	147
6.1	Miss Distance( $cm$ ) for Translation in the $X - Z$ Plane near Asteroid Itokawa . . . . .	157
6.2	Miss Distance( $cm$ ) for Translation in an $X - Y$ Plane near Asteroid Eros . . . . .	158
6.3	$\sigma$ ( $m$ ) as a Function of Latitude and Longitude for Radial Descent over Asteroid Itokawa . . . . .	166
6.4	809 Vertex Polyhedral Model of the Asteroid Eros . . . . .	168
6.5	$\sigma$ ( $m$ ) as a Function of Latitude and Longitude for Radial Descent over Asteroid Eros . . . . .	169
6.6	$\sigma$ ( $m$ ) as a Function of Latitude and Longitude for Radial Descent over a 289 x 280 x 220 $km$ Ellipsoid . . . . .	171
6.7	Descent to the Surface of Asteroid Eros Using Constant Thrust and Free-drop Control . . . . .	173
6.8	Thruster Plume Geometry . . . . .	176
6.9	Drift for Sliding Dead-band Descent/Ascent Maneuver . . . . .	179
6.10	Miss Distance for Sliding Dead-band Descent . . . . .	180

## LIST OF APPENDICES

### Appendix

A.	Author's Bibliography . . . . .	193
B.	Constant Density Gravity Computations . . . . .	197
	B.1 Potential of a Constant Density Ellipsoid . . . . .	197
	B.2 Potential of a Constant Density Polyhedron . . . . .	199
C.	Use and Outputs of the Small-body Characterization Tool . . . . .	201
D.	Small-body Dynamics Toolbox Description . . . . .	203
E.	Zero-velocity Surfaces near Equilibria in Lagrangian Dynamics . . . . .	207

## LIST OF ABBREVIATIONS

DEEVE	Dynamically Equivalent Equal Volume Ellipsoid
ESA	European Space Agency
GDTS w/OL	Gravitational Direction Thrusting and Sensing with Open-loop
IATNS	Initial Acceleration Thrusting and Normal Sensing
JAXA	Japanese Aerospace Exploration Agency
JHUAPL	John Hopkins University Applied Physics Laboratory
JPL	Jet Propulsion Laboratory
NASA	National Aeronautics and Space Administration
NEAR	Near Earth Asteroid Rendezvous
SBCT	Small-body Characterization Tool
SBDT	Small-body Dynamics Toolbox
SRP	Solar Radiation Pressure

# NOMENCLATURE

(Symbols described in the Section where they first appear)

## 2.1 Small-body Shape Modeling

$a, b, c$	Ellipsoid semi-major axes, $a > b > c > 0$
$\tilde{\rho}$	Position on the small-body surface, groundtrack vector
$E$	3x3 matrix that defines an ellipsoid shape
$\hat{\mathbf{n}}$	Unit normal vector to the small-body surface
$\hat{\mathbf{n}}_i$	Unit normal vector to the i-th polyhedron face
$\tilde{\mathbf{r}}_{i,1}, \tilde{\mathbf{r}}_{i,2}, \tilde{\mathbf{r}}_{i,3}$	Position of the three vertices of the i-th polyhedron face
$C_i$	Scalar constant for the i-th polyhedron face
$\tilde{\rho}_i$	Position on the plane defined by the i-th polyhedron face
$\omega_i$	Solid angle covered by the i-th polyhedron face from the spacecraft point-of-view

## 2.2 Small-body Gravity Modeling

$\Gamma$	Set of positions that define the small-body shape
$U$	Gravitational potential of the small body
$G$	Universal gravitational constant ( $= 6.67 \times 10^{-11} \text{ km}^3 / (\text{kg s}^2)$ )
$\rho$	Mass density
$\tilde{\xi}$	Position of a volume element
$\tilde{\mathbf{r}} = [x, y, z]^T$	Spacecraft position
$dV$	Volume element in the small-body
$M_{sb}$	Mass of the small-body
$C_{nm}, S_{nm}$	Spherical harmonic coefficient sets
$\mu_{sb}$	Gravitational parameter of the small-body
$R_{ref}$	Reference radius for spherical harmonic expansion
$P_{nm}$	Associated Legendre functions
$\phi$	Spacecraft latitude
$\lambda$	Spacecraft longitude

### 2.3.1 Two-body Problem in the Small-body Fixed Frame

$\dot{\mathbf{r}} = [\dot{x}, \dot{y}, \dot{z}]^T$	Spacecraft velocity
$\ddot{\mathbf{r}} = [\ddot{x}, \ddot{y}, \ddot{z}]^T$	Spacecraft acceleration

$\tilde{\omega} = [0, 0, \omega]^T$	Small-body angular velocity vector
$\tilde{\mathbf{T}} = [T_x, T_y, T_z]^T$	Spacecraft thrust vector (per unit spacecraft mass)
$J_{BF}$	Jacobi constant for the two-body problem in the body-fixed frame
$R_r$	Resonance radius
$A$	Linear two-body dynamics matrix
$\mathbf{0}_{m \times n}$	m by n matrix of zeros
$\mathbf{I}_{n \times n}$	n by n identity matrix
$\tilde{\mathbf{f}}$	Linearized two-body dynamics forcing function
$\tilde{\mathbf{r}}_0$	Nominal (hovering) position

### 2.3.2 Circular Restricted Three-body Problem

$\tilde{N} = [0, 0, N]$	Angular velocity of the primaries' mutually circular orbit
$\mu_1, \mu_2$	Gravitational parameter of the first/second primary
$\tilde{\mathbf{r}}_{sc,1}, \tilde{\mathbf{r}}_{sc,2}$	Spacecraft position w.r.t. first/second primary
$\mu \leq \frac{1}{2}$	Ratio of masses
$R(f)$	Distance between primaries
$J_{R3BP}$	Jacobi constant for the circular restricted three-body problem

### 2.3.3 Hill Three-body Problem

$R_{Hill}$	Hill radius
$\beta_{SRP}$	Force parameter for solar radiation pressure
$G_1$	Solar flux constant ( $\approx 1 \text{ E8 } (kg/m^2) (km^3/s^2)$ )
$B$	Spacecraft mass to shadow area ratio
$J_{HILL}$	Jacobi constant for the Hill three-body problem

### 2.3.4 Generalized Elliptic Restricted Three-body Problem

$\dot{f}$	Change in true anomaly w.r.t. time
$\ddot{f}$	Second derivative of true anomaly w.r.t. time
$\mu_{Sun}$	Gravitational parameter of the Sun
$t$	Time
$a_{orb}$	Semi-major axis of small-body orbit
$e_{orb}$	Eccentricity of small-body orbit
$i_{orb}$	Inclination of small-body orbit
$\omega_{orb}$	Argument of periapsis of small-body orbit
$\Omega_{orb}$	Longitude of ascending node of small-body orbit
$T_f$	Rotation matrix from elliptic orbit frame to the rotating three-body frame
$T_{eo}$	Rotation matrix the inertial frame to the elliptic orbit frame
$T_{pole}$	Rotation matrix the inertial frame to the small-body

	rotation pole frame
$\Phi_{pole}$	Latitude of small-body rotation pole
$\Lambda_{pole}$	Longitude of small-body rotation pole
$T_i$	Rotation matrix the small-body rotation pole frame to the small-body fixed frame

## 2.4 Measurement Models

$h$	Spacecraft altitude
$\hat{\mathbf{s}}$	Instrument pointing direction
$h_i$	Altitude between spacecraft and the plane of the i-th face
$\dot{h}$	Altitude rate-of-change, time-of-flight velocimeter measurement

## 3.1 Review of the Results of Sawai *et al.*

$\tilde{\mathbf{T}}_{OL}$	Open-loop component of control thrust
$\alpha_1, \alpha_2, \alpha_3$	Eigenvalues of the Hessian matrix of the gravitational potential
$\hat{\mathbf{v}}_1, \hat{\mathbf{v}}_2, \hat{\mathbf{v}}_3$	Eigenvectors of the Hessian matrix of the gravitational potential
$\tilde{\mathbf{T}}_{DB}$	Dead-band component of control thrust
$T_m$	Constant magnitude of dead-band control thrust
$\hat{\mathbf{c}}$	Dead-band thrust direction
$f_{db}$	Dead-band evaluation function
$\gamma$	Dead-band size parameter

## 3.3.2 Analysis of GDTS w/OL Controller Results

$\hat{\mathbf{n}}_{db}, \hat{\mathbf{t}}_{db}, \hat{\mathbf{z}}$	Unit vectors that define dead-band coordinate frame
$\theta$	Angle between $\hat{\mathbf{n}}_{db}$ and $\hat{\mathbf{c}}$

## 3.4 Other Dead-band Hovering Approaches

$\hat{\mathbf{a}}_0$	Acceleration at the nominal hovering position
$\tilde{\mathbf{r}}_{OI}(t)$	Constant latitude, retrograde, circular orbit
$\phi_0$	Initial latitude
$\lambda_0$	Initial longitude
$\Phi$	State transition matrix
$M$	Monodromy matrix

## 4.1 Zero-velocity Surface Result for Conservative Systems

$V$	Generalized potential function
$\vec{\Omega}$	Frame angular velocity vector
$J$	Jacobi constant

$C_0$	Nominal value of Jacobi constant
$\delta \mathbf{r}$	Deviation in position from nominal
$\delta \dot{\mathbf{r}}$	Deviation in velocity from nominal
$\beta_1, \beta_2, \beta_3$	Eigenvalues of $\partial^2 J / \partial \tilde{\mathbf{r}}^2 _{(\tilde{\mathbf{r}}_0, \mathbf{0}_{3 \times 1})}$
$\hat{\vartheta}_1, \hat{\vartheta}_2, \hat{\vartheta}_3$	Corresponding eigenvectors of $\partial^2 J / \partial \tilde{\mathbf{r}}^2 _{(\tilde{\mathbf{r}}_0, \mathbf{0}_{3 \times 1})}$

## 4.2 Zero-velocity Surfaces and Dead-band Hovering Control

$\delta(x)$	Dirac's delta function
$\hat{\mathbf{v}}_c$	Unit vector defining dead-band orientation
$\mathbf{v}_+$	Spacecraft velocity vector after dead-band thrust activation
$\mathbf{v}_-$	Spacecraft velocity vector before dead-band thrust activation

## 4.3 Effects of Uncertainty on Zero-velocity Surfaces

$C^*$	Value of perturbed Jacobi constant
$\delta \mathbf{r}_0$	Error in initial position vector
$\delta \mathbf{v}_0$	Error in initial velocity vector
$\Delta Z$	Quantifier of zero-velocity surface perturbation
$\Delta J$	Perturbation from nominal Jacobi constant
$\Delta J_{max}$	Largest perturbation from nominal Jacobi constant
$\mathbf{A}$	Set of allowable spacecraft positions (localized formulation)
$r_{max}$	Maximum attainable distance from nominal
$v_{max}$	Maximum attainable spacecraft velocity
$\mathbf{B}$	Set of allowable spacecraft positions (global formulation)
$\mathbf{Z}$	Set of positions on the zero-velocity surface
$\mathbf{D}$	Set of positions on the dead-band surface
$\varkappa$	Function that defines the zero-velocity surface
$d$	Function that defines the dead-band surface
$\Delta J_+, \Delta J_-$	Maximum allowable increase/decrease in Jacobi constant to preserve boundedness
$R_c$	Dead-band surface radius
$\mathbf{r}^* = [x^*, y^*, z^*]^T$	Critical position where dead-band surface and zero-velocity surface are not transverse
$\delta v_{0,max}$	Maximal error in initial velocity that preserves boundedness

## 4.5 Hovering in Non-conservative Systems

$H$	Time-varying Jacobi integral
-----	------------------------------

## 5.1 Generalized Hovering Zero-Velocity Surface Result

$\tilde{\mathbf{a}}_0$	Nominal spacecraft acceleration without thrust
$\delta\tilde{\mathbf{r}}_c = [\delta r_{c,x}, \delta r_{c,y}, \delta r_{c,z}]$	Center of the quadratic zero-velocity surface with respect to the nominal hovering position

## 5.2 Using a Reduced Measurement Set for Control

$\eta$	Angle between $\hat{\mathbf{n}}$ and $\hat{\vartheta}_3$
$h_a, h_b, h_c, h_d$	Four parameters of the zero-velocity hyperboloid
$\delta\tilde{\mathbf{r}}_r = [\delta x_r, \delta y_r, \delta z_r]$	Vector from zero-velocity surface center to points on its surface
$u, v$	Parameterization coordinates
$\kappa_{DB,max}, \kappa_{DB,min}$	Maximum/minimum dead-band surface curvatures
$s$	Sphere radius
$\tilde{\mathbf{r}}_s$	Sphere center
$\tilde{\mathbf{r}}_x = [r_{x,x}, r_{x,y}, r_{x,z}]$	Vector from dead-band sphere center to the zero-velocity surface center
$\phi_m, \lambda_m$	Measured spacecraft latitude/longitude
$Q = \left  \hat{\vartheta}_1 \cdot \hat{\mathbf{r}}_0 \right $	Zero-velocity surface orientation quantifier
$\hat{\mathbf{u}}(v)$	Unit vector along surface of a quadratic cone
$\alpha, \beta$	Angles between the quadratic cone zero-velocity surface and $\hat{\vartheta}_2$ and $\hat{\vartheta}_3$ respectively

## 5.3 Control Application

$\Delta V_{ideal}$	Ideal estimate of hovering fuel cost
$\Delta V_{daily}$	Daily fuel cost of hovering
$\chi$	Normalized hovering distance, $\ \tilde{\mathbf{r}}\ /R_r$
$P$	Position coefficient
$\Pi$	Daily fuel cost coefficient

## 5.4 Simulations

$t_{\Delta V}$	Duration for which dead-band thrust is applied
----------------	--

## 6.2 Free-drop Solution

$t_f$	Time of transfer
-------	------------------

## 6.3 Constant Thrust Solution

$\tilde{\mathbf{r}}_{phantom}$	Artificial translation target position
--------------------------------	--

## 6.4 Sensitivity to Parameter Uncertainty

$\tilde{\mathbf{X}} = [\tilde{\mathbf{r}}, \dot{\tilde{\mathbf{r}}}]^T$	Spacecraft state vector
$\zeta$	Arbitrary system parameter
$\tilde{\mathbf{X}}_f$	Final spacecraft state
$Cov(\tilde{\mathbf{X}})$	Covariance matrix of $\tilde{\mathbf{X}}$
$\sigma$	Quantifies the size of the one-sigma uncertainty ellipsoid at the final spacecraft position
$T_{mag}$	Magnitude of the transfer thrust
$\phi_T, \lambda_T$	Latitude/longitude of the thrust vector

## 6.6 Sliding Dead-band Descent

$d$	Dead-band overshoot distance
$m_{s/c}$	Spacecraft mass
$\psi$	Thruster plume half-angle
$A_T$	Cross-sectional area of the thruster plume on the small-body surface
$p$	Pressure induced by the thruster plume
$r_p$	Radius of a surface particle
$R_{sb}$	Spherical small-body radius

## Appendix E: Zero-velocity Surfaces near Equilibria in Lagrangian Dynamics

$L$	Lagrangian function
$T$	Kinetic energy
$C_L$	Value of Jacobi constant in the Lagrangian formulation
$\tilde{\mathbf{q}}$	System configuration variables
$\tilde{\mathbf{p}}$	Generalized momenta of the system
$(\tilde{\mathbf{q}}_{eqm}, \dot{\tilde{\mathbf{q}}}_{eqm})$	Equilibrium state in Lagrangian formulation

## ABSTRACT

Close Proximity Spacecraft Maneuvers Near Irregularly Shaped Small-bodies:  
Hovering, Translation, and Descent

by

Stephen B. Broschart

Chair: Daniel J. Scheeres

Recently there has been significant interest in sending spacecraft to small-bodies in our solar system, such as asteroids, comets, and small planetary satellites, for the purpose of scientific study. It is believed that the composition of these bodies, unchanged for billions of years, can aid in understanding the formative period of our solar system. However, missions to small-bodies are difficult from a dynamical standpoint, complicated by the irregular shape and gravitational potential of the small-body, strong perturbations from solar radiation pressure and third body gravity, and significant uncertainty in the small-body parameters. This dissertation studies the spacecraft maneuvers required to enable a sampling mission in this unique dynamical environment, including station-keeping (hovering), translation, and descent.

The bulk of this work studies hovering maneuvers, where equilibrium is created at an arbitrary position by using thrusters to null the nominal spacecraft acceleration. Contributions include a numerical study of previous results on the stability of

hovering, a definition of the zero-velocity surface that exists in the vicinity of a hovering spacecraft (for time-invariant dynamics), and a dead-band hovering controller design that ensures the trajectory is bounded within a prescribed region. It is found that bounded hovering near the surface of a small-body can often be achieved using dead-band control on only one direction of motion; altitude measurements alone are often sufficient to implement this control.

A constant thrust strategy for translation and descent maneuvers appropriate for autonomous implementation is also presented and shown to accurately complete maneuvers in the vicinity of the initial position. Sensitivity analysis studies the effects of parameter uncertainty on these maneuvers.

The theory presented within is supported throughout with numerical analysis (software tools are described within) and test cases using models of real small-bodies.

# CHAPTER I

## Introduction

In recent years, there has been significant interest in sending spacecraft to small-bodies in our solar system, such as asteroids and comets, for the purpose of scientific study. Scientists believe that the composition of these bodies, which is likely unchanged over billions of years, can help us to understand the formative period of our solar system. Understanding the structure of these bodies would also be essential to any small-body orbit diversion strategy implemented for planetary protection. Small moons and planetary satellites, also classified as small-bodies, may harbor unique environments of great scientific interest as well. If space exploration continues to expand and become more sophisticated, small-bodies could potentially fill roles as fueling stations, mining sites, or remote observatories.

The interest of the science community is demonstrated by numerous recently executed and currently flying missions. The first comprehensive mission to a small-body was the National Aeronautics and Space Administration (NASA) / Jet Propulsion Laboratory (JPL) / John Hopkins University Applied Physics Laboratory (JHUAPL) Near Earth Asteroid Rendezvous (NEAR) mission to asteroid Eros, which launched in 1996 and completed its mission in 2001. NASA/JPL followed with the 1999 Stardust mission to collect comet outgassing particles, the 2002 Contour comet ren-

dezhvous mission (managed by JHUAPL, failed soon after launch), and the 2005 Deep Impact mission, part of which collided with a comet so the other part could view the dust plume. The Japan Aerospace Exploration Agency (JAXA) Hayabusa mission successfully rendezvoused with the asteroid Itokawa in 2005. As yet, it is unclear whether the goal of obtaining surface material for return to Earth was achieved successfully or not. The European Space Agency (ESA) also launched a mission to study comets, Rosetta, in 2004 that is slated to arrive at comet 67P/Churyumov-Gerasimenko in 2014. Numerous other small-body missions currently are in the proposal or development stages.

Missions to small-bodies have a number of inherent difficulties relative to more traditional space missions to planets and large moons, particularly if touchdown or sampling maneuvers are included. First, the gravity of a small-body is insufficient to pull the mass into a spheroid shape. This results in highly irregular small-body shapes and corresponding arbitrary gravitational potential fields which complicate the spacecraft dynamics increasingly with proximity. The weak gravitational fields near these bodies also allow small accelerations due to tidal forces and solar radiation pressure (SRP) to have tremendous impact on the spacecraft motion, to the point that orbits are almost all unstable near particularly small bodies. Ironically, it is the weak gravitational field that has allowed the elemental composition of these bodies to remain unchanged for so long. Operating a spacecraft near a small-body is further complicated by the uncertainty in the environment prior to arrival. Accurate small-body bulk density estimates are virtually impossible to obtain prior to arrival and shape estimates obtained from Earth-bound radar observations have limited resolution; this adds significant uncertainty to an already complex gravitational field. In addition, the orbit of the small-body is usually insufficiently well known

to navigate a spacecraft in its vicinity using Earth-bound radiometric data. Hence, missions must be equipped with in-situ measurement instruments (such as altimeters or optical cameras) and corresponding filtering techniques to safely navigate the small-body environment. Finally, because of the uncertain dynamics and long travel time for signals to and from Earth, it is desirable for the spacecraft to have significant autonomous capabilities.

In this thesis, control strategies are sought to enable the spacecraft maneuvers in close proximity to a small-body that would be necessary for a sample return mission. Specifically, the dynamics of station-keeping, translation, and descent maneuvers are studied. Due to the difficulties discussed in the previous paragraph specific to small-body missions, the approaches to these maneuvers are necessarily different from those for planetary orbiters. The control methods presented here are designed with the difficulties of the small-body environment in mind and attempt to exploit its peculiarities when possible. Note that the work presented here should be applied cautiously to spacecraft motion near comets for reasons outlined in Section 2.3.5.

One strategy that has been proposed to mitigate some of the difficulties associated with an orbital approach to spacecraft station-keeping in the vicinity of a small-body is hovering[7, 8, 9, 10]. Hovering can be defined broadly as using control thrust continuously to null the total acceleration on the spacecraft, creating an equilibrium at a desired position. This stationary equilibrium (in a particular reference frame) may be an advantageous position for taking high resolution measurements of a particular area, maintaining a fixed communication, solar panel, or sensing geometry, or for maintaining relative orientation to the surface during a descent maneuver. This approach is feasible near small-bodies since the spacecraft's nominal acceleration (and therefore fuel consumed) is small. Hovering also handles third-body perturbations

well, as they are simply an extra small nominal acceleration to cancel.

The bulk of this thesis (Chapters III-V) studies the dynamics of a spacecraft under hovering control near a small-body. In Chapter III, a numerical hovering simulation tool is used to study the stability of hovering trajectories in the small-body fixed frame, where spacecraft position is stationary relative to the small-body surface, and the inertial frame, where the small-body rotates beneath the spacecraft. This chapter also numerically tests the analytical stability criteria for hovering under a dead-band control presented in the previous work by Sawai *et al.*[10]. Chapter IV presents an analytical formulation of the zero-velocity surface that exists in the vicinity of a hovering spacecraft and shows how a dead-band controller can be designed to ensure formal boundedness of a hovering trajectory in an arbitrary potential field. Chapter V studies the implementation of the dead-band control results of Chapter IV.

Translation is the act of moving the spacecraft from one position to another through a combination of thrust and the natural dynamics. Descent is a subset of translation such that the target position lies on the surface of the body. Both of these maneuver types are of critical importance to a small-body sampling mission and are addressed in that context in Chapter VI of this thesis. Ideally, these types of maneuvers should be designed such that a spacecraft is free to move arbitrarily around the small-body to investigate areas of interest and touchdown at a chosen location. A constant thrust translation controller is presented here that is shown to accurately perform translations over short distances. The effects of parameter uncertainty on this class of translations is also studied in a way that can be applied to other maneuvers. The chapter also presents an adaptation of the dead-band hovering strategy for descent where the target hovering altitude is linearly reduced down to the small-body surface.

This work contained here is of interest to people involved in the planning and implementation of small-body missions and those interested in spacecraft dynamics. To a lesser extent, this work may be of interest to scientists who study small-body composition and evolution. It is hoped that the control methodologies and dynamical observations presented here will facilitate small-body exploration missions that are dynamically less restricted and fundamentally less risky than current proposals. By enabling broader scoped small-body missions, this work may also benefit space science. Increased exploration of these bodies could yield information about asteroid collision mechanics, asteroid composition and porosity, the early composition of the solar accretion disk, and asteroid thermal properties. This sort of data will be crucial to any form of future asteroid exploitation.

## 1.1 State of Knowledge Previous to this Research

Close proximity station-keeping operations near small-bodies have primarily been studied from an orbital perspective[11, 12, 13, 14, 15, 16, 17, 18], which is appropriate for small-bodies that are larger than a particular size. For larger bodies, the fuel costs of maintaining hovering become prohibitively large[7, 19]. However, when the small-body is relatively small, orbiting options become very limited since the effects of solar radiation pressure are strong enough to destabilize most orbits in the small-body vicinity and cause impact or escape[14, 20, 17]. For these bodies, hovering requires very little fuel and may be the only option for close proximity investigation of all areas of interest. An orbital station-keeping approach was used throughout the NEAR mission, which was appropriate because of the relatively large size of Eros (about 32 *km* maximum extent)[21]; close-proximity hovering at Eros would cost a few hundred meters per second of  $\Delta V$  per day! On the other hand, the Hayabusa

mission to asteroid Itokawa (about 530  $m$  maximum extent) appropriately chose hovering to keep the spacecraft in Itokawa's vicinity[9] at a cost of a few meters per second or less per day. The choice between these two station-keeping approaches is driven by the small-body size, but ultimately depends on the mission goals. For any landing or sampling mission however, hovering dynamics in the small-body fixed frame must be considered for the final stages of descent if a soft landing with minimal lateral velocity relative to the surface is desired.

This thesis focuses on the hovering approach to station-keeping near small-bodies, which is a relatively new field of study. Hovering near small-bodies was first proposed in the literature by Scheeres[7]. That initial mention was followed by a paper that reported eigenvalue structure as a function of position for hovering in the small-body fixed and inertial reference frames when using an open-loop controller to cancel the spacecraft's nominal acceleration[8]. Subsequent work by Sawai *et al.* added a one-dimensional dead-band control on altitude to the open-loop thrust to suppress deviations from nominal and analytically determined where motion could be stabilized by this controller[10]. Recently, hovering has been studied as a method of slowly changing the orbit of a solar system body[22, 23]. Other contributions in the literature to the study of hovering dynamics from 2003 to 2005 contained in this thesis are given in Appendix A.

The desire to return samples drives current small-body mission proposals. In order to collect a surface sample, the spacecraft needs to be able to maneuver to a chosen location in the small-body fixed frame and descend to the surface (or very close to it). The dynamics of these close proximity translation and descent maneuvers are the second major topic of study in this thesis. The first ever successful descent to an asteroid surface was done by NASA's NEAR mission team using a series of

open-loop thrusts to de-orbit the spacecraft[24]. Theoretical work on descent to small bodies has taken a number of approaches. Guelman and Harel[25] gave an optimal, electric propulsion descent solution from orbit for the spherical body case. Cui and Cui[26] developed a method for descent using feedback control on altitude and thrust modulation. Sawai *et al.* presented a brief study of translation near arbitrarily shaped small-bodies along a constant potential surface[10].

JAXA's Hayabusa sample return mission has given an excellent demonstration of the feasibility of hovering and descent maneuvers in the vicinity of the relatively small asteroid Itokawa. This mission successfully implemented spacecraft hovering in a near-inertial frame for the first time near an asteroid in the fall of 2005. Kubota *et al.*[9] and Kominato *et al.*[27] document their three-dimensional dead-band hovering control approach and success in detail. This mission also made numerous descents to the surface utilizing optical navigation feedback, an altimeter, and a target marker[28, 29, 30, 31]. During these descents, hovering in the small-body fixed frame was also used to eliminate spacecraft motion relative to the surface.

## 1.2 Chapter Preview

Chapter II defines various mathematical models used to describe the small-body environment. Tri-axial ellipsoid and triangular faceted polyhedron small-body shape models are introduced and defined as well as constant density gravity models for each shape type. The spherical harmonic gravity model, often used for small-bodies, is also introduced. Numerous equations of motion that model spacecraft motion near a small-body in different situations are defined as well. Finally, the measurement models for altitude, altitude rate-of-change, and optical navigation measurements that will be used are defined. These definitions in this chapter are the basis of the

analysis and numerical simulations throughout the thesis.

Numerical studies of different spacecraft hovering approaches are presented in Chapter III. First, the analytical stability criteria for hovering under one-dimensional dead-band control in Sawai *et al.*[10] are reviewed. The controller for hovering in the small-body fixed frame suggested in that work is simulated numerically with the HoverSim software (also described in this chapter). Results of these simulations are compared with the stability criteria. The difference between the analytical and numerical results allows an insight on the effect of Coriolis forces on spacecraft dynamics under a one-dimensional dead-band controller to be made; a destabilizing effect is found to exist for hovering above the small-body's leading edge. Another body-fixed hovering controller is suggested to reduce this effect and some advantages of this control are shown numerically. The stability of hovering in an inertial frame, such that the small-body rotates beneath the spacecraft, is also studied in this chapter. Hovering in this way is found to be stable except for when hovering near the small-body "resonance radius" (defined in Eq. (2.16)). This result is supported by numerical simulation. The chapter closes with an application of hovering in the inertial and small-body fixed frames to the asteroid Itokawa, the target of the JAXA Hayabusa mission.

Chapter IV introduces an energetic restriction on the motion of a spacecraft under hovering control in time-invariant dynamical systems. A method for designing dead-band controllers that bound the motion of the spacecraft is developed using knowledge of this energetic bound. The necessary dimensionality of the dead-band controller that bounds hovering is determined via a simple analytic criterion which is easily applied to hovering positions in a known potential field. Results are presented for hovering near small-bodies in the two-body, circular restricted three-body, and

Hill three-body problems. It is found that hovering close to the small-body surface often requires dead-band control on only one direction of motion for boundedness. A significant region also exists where control is required on only two directions of motion for boundedness. The section ends with a brief discussion of extending this method to time-varying dynamics.

Chapter V contains analysis related to implementation of the theoretical ideas on spacecraft hovering in Chapter IV. First, the zero-velocity (energetic) bound result is extended to allow for open-loop thrusts that do not necessarily create an equilibrium at the desired hovering position. This chapter also looks at whether one direction dead-band control can be implemented near the small-body surface using altimeter measurements and finds that indeed it often can be. The feasibility of using optical navigation measurements as the basis of a two-dimensional dead-band control is also studied. It is found that due to the orientation of the zero-velocity surface relative to the small-body surface, this control approach does not create a bounded hovering region. This chapter also addresses fuel consumption and dead-band control application frequency for close proximity hovering in the two-body problem. The last section of the chapter presents numerically integrated hovering trajectories with different error and uncertainties included.

Chapter VI addresses spacecraft translation in an arbitrary potential field such as that near a small-body. Descent maneuvers are a subset of translations where the target position is on the small-body surface. This chapter develops a guidance law for constant thrust translation with error estimation that could be implemented autonomously. A solution for motion without thrust is also presented via linearization of the dynamics. This chapter also presents a covariance study that looks at the effects of errors in initial state, thrust direction and magnitude, small-body ro-

tation state, and the small-body gravitational potential model on constant thrust translation trajectories. Numerical covariance results are presented for descending translations above models of the asteroids Itokawa, Eros, and Vesta. The chapter closes with a numerical validation of using a dead-band hovering control for descent where the target altitude for hovering is linearly varied down to the surface.

The contents of Appendices C and D are also worthy of note. These appendices contain detailed descriptions of two numerical tools used throughout in support of this work: the Small-body Characterization Tool (SBCT) and the Small-body Dynamics Toolbox (SBDT). The SBCT, written in C++, gives a broad assessment of the dynamical environment near a specified small-body applicable to various mission operations including hovering, orbiting, and surface maneuvers. The SBDT is a combination of Matlab and Simulink tools used to simulate dynamics near a small-body. The SBDT is capable of simulating dynamics in the two-body problem, elliptic restricted three-body problem, Hill three-body problem, and the generalized elliptic restricted three-body problem (Section 2.3.4) as well as one-dimensional and linearized motion inside a hovering dead-band. The toolkit also is capable of computing periodic orbits, performing covariance studies, and small-body shape, surface, and gravity characterizations. The SBDT contains many visualization tools as well to help understand its outputs.

### **1.3 Outline of Original Contributions**

This thesis makes numerous original contributions that may be useful to future research and space mission planning. A list of publications that have been made during the course of this research is given in Appendix A.

The most prolific technical contribution in this thesis will likely be the observa-

tion and definition of the zero-velocity surface that exists near a hovering spacecraft (Section 4.1). This bound on the spacecraft motion is fixed in time (for time-invariant systems) and is shown to be a meaningful restriction on the local motion. Knowledge of this built in dynamical “control” allows anyone planning a spacecraft hovering strategy to quickly understand the dynamical possibilities which are otherwise very difficult to understand for the complex dynamics in the small-body environment. The follow-up studies contained here that define the effects of errors in the initial state (Section 4.3) and open-loop thrust (Section 5.1) on the zero-velocity surface, map the zero-velocity surface type as a function of position near small-bodies (Section 4.4), and numerically integrate spacecraft motion to show the validity of the bound (Sections 4.3.1 and 5.4) are all original contributions to the existing body of knowledge.

Contributions are also made to dead-band hovering controller design near small-bodies in light of the zero-velocity surface result. The minimum number of directions of motion that should be restricted by a dead-band control for hovering boundedness is first formulated in Section 4.2. Formal conditions for local and global boundedness are given in Section 4.3. Sufficient conditions for boundedness of hovering under a reduced measurement set (altimetry only or optical navigation only) are also presented here (Section 5.2). These criteria may be useful for planning hovering control strategy and instrument usage during a small-body mission. The IATNS body-fixed dead-band hovering control using altimetry (Section 3.4.1) is also an original contribution. The findings on fuel usage (Section 5.3.2) and thrust application frequency (Section 5.3.3) for a dead-band controller are original contributions that may also assist in dead-band control design for a future mission.

A contribution is also made to the study of inertial hovering through numerical

simulation by validating the instability near the resonance radius and showing that large perturbations from the nominal position exist in the stable region of motion close to the small-body.

The numerical simulation and characterization tools (HoverSim, the SBCT, the SBDT, and other manifestations of these ideas) are also important contributions of this research to future dynamical and mission studies to the small-body environment. Comprehensive tools such as these did not exist publicly at the beginning of this research, though some of the code’s capabilities now exist elsewhere. HoverSim and the SBDT are available for use by others (see Appendix D for contact information). The HoverSim tool was invaluable to this thesis through simulation and validation of hovering techniques. It allowed the previous analytical work of Sawai *et al.*[10] to be tested and the original observations on the effect of Coriolis forces on dead-band dynamics to be discovered (Section 3.3.2). Parts of the SBDT have already been used to support the research of three other graduate students[32][33][34]. Small-body shape and surface characterizations made with the SBDT have contributed to numerous papers on small-body shape models derived from Earth-based radar measurements[35, 36, 37, 38, 39, 40]. The SBCT is the first tool to bring together the results of the existing research on small-body dynamics into one tool useful for mission planning and simulation design. The SBCT is continuing to expand under contract with JPL and its current version (0.03) is available for use by their employees (see Appendix C for contact information).

The measurement models used here for altitude and altitude rate-of-change measurements above ellipsoidal and polyhedral small-bodies used here are also original contributions (Sections 2.4.1 and 2.4.2). These models are currently being used at JPL for internal small-body mission research and development[41].

The constant thrust translation controller is an original contribution (Section 6.3) that could eventually find use as an autonomous path planning algorithm on-board a spacecraft. The free-drop solution (Section 6.2) could find similar use for un-powered descent. The covariance studies on the constant thrust controller are among the first to demonstrate the effects of uncertainty in various parameters on spacecraft motion near a small-body (Section 6.4). The techniques outlined here may help in future covariance studies since they can be applied to any trajectory, not just constant thrust translation. Finally, the “back of the envelope” calculation of the maximum altitude at which particles may be lifted off the small-body surface by thrust in Section 6.6.2 is a useful contribution.

## CHAPTER II

### Model Definitions

This chapter is devoted to defining the mathematical models used throughout the thesis to describe the environment near a small-body. The models include small-body shape descriptions, small-body gravity descriptions, dynamical equations of motion, and spacecraft measurement models. These models serve as the basis for the analysis and numerical simulations in the following chapters. The chapter closes with a brief description of a software implementation that makes use of these models (and others) to compute dynamical parameters of a given small-body environment: the Small-body Characterization Tool (SBCT).

#### 2.1 Small-body Shape Modeling

The most unique characteristic of the environment near a small-body is the irregular shape of the body itself. Small-bodies lack sufficient mass to pull themselves into near spherical, planet-like shapes. Instead, small-bodies take shapes more consistent with the primordial pieces of rock that they are, varying from smooth, near ellipsoidal shapes (for instance Deimos, a moon of Mars, Figure 2.1) to highly irregular shapes (such as asteroids Kleopatra, Figure 2.2, or Golevka, Figure 2.3). Small-body sizes vary widely as well; Kleopatra is about 217 *km* long, while Golevka is only

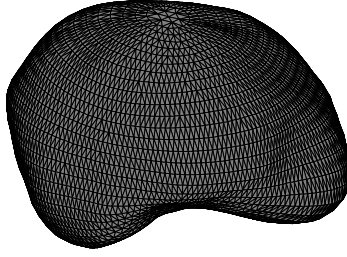


Figure 2.1: Polyhedral Model of the Martian Moon, Deimos[4]

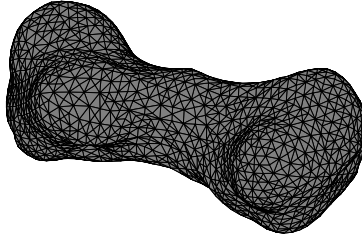


Figure 2.2: Polyhedral Model of Asteroid 216 Kleopatra[5]

about half a kilometer across.

The work in this thesis has adopted two different approaches to modeling small-body shapes: the tri-axial ellipsoid and the triangular-faceted polyhedron. Tri-axial ellipsoids are often reasonable approximations of actual small-body shapes, so using this model may be advantageous when high resolution shape data are not available or first cut approximations are desired. This symmetric quadratic shape is parameterized by its three semi-major axes:  $a > b > c > 0$ . The surface of a tri-axial ellipsoid is defined by the implicit equation  $S_{ellip}(\tilde{\rho}) = 0$ , where

$$S_{ellip}(\tilde{\rho}) = \tilde{\rho}^T E \tilde{\rho} - 1 \quad (2.1)$$

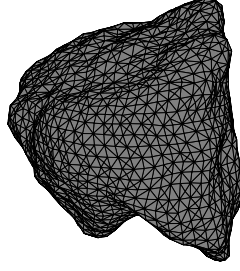


Figure 2.3: Polyhedral Model of Asteroid 6489 Golevka[6]

and

$$E = \begin{bmatrix} \frac{1}{a^2}, & 0, & 0 \\ 0, & \frac{1}{b^2}, & 0 \\ 0, & 0, & \frac{1}{c^2} \end{bmatrix}. \quad (2.2)$$

The unit vector normal to a given point on the surface is defined in Eq. (2.3).

$$\hat{\mathbf{n}} = \frac{E\tilde{\rho}}{\|E\tilde{\rho}\|} \quad (2.3)$$

For a spacecraft position  $\tilde{\mathbf{r}}$ , if  $S_{ellip}(\tilde{\mathbf{r}}) < 0$ , the position is in interior of the ellipsoid and if  $S_{ellip}(\tilde{\mathbf{r}}) > 0$ , the position is outside the body.

More complex small-body geometries are specified as triangular-faceted polyhedrons. Polyhedrons can model a much wider range of shapes than ellipsoids, allowing depressions, ridges, cliffs, caverns, and holes on the model. This type of shape modeling can be very accurate, with resolution increasing with the number of faces used. A triangular-faceted polyhedron is defined by the locations of its  $V$  vertices and a list of which vertices make up each of  $F$  faces. These lists implicitly define  $E = F + V - 2$  edges. Each face of the polyhedron defines a plane with orientation defined by its normal vector,

$$\hat{\mathbf{n}}_i = [(\tilde{\mathbf{r}}_{i,2} - \tilde{\mathbf{r}}_{i,1}) \times (\tilde{\mathbf{r}}_{i,3} - \tilde{\mathbf{r}}_{i,2})] / \|(\tilde{\mathbf{r}}_{i,2} - \tilde{\mathbf{r}}_{i,1}) \times (\tilde{\mathbf{r}}_{i,3} - \tilde{\mathbf{r}}_{i,2})\| \quad (2.4)$$

and location defined by a constant,

$$C_i = \hat{\mathbf{n}}_i \cdot \tilde{\rho}_i \quad (2.5)$$

where  $\tilde{\rho}_i$  is any vector in the plane. The vertices of each face are ordered such that  $\hat{\mathbf{n}}_i$  points outside the body. For a spacecraft position  $\tilde{\mathbf{r}}$ ,

$$S_{poly}(\tilde{\mathbf{r}}) = \sum_{i \in faces} \omega_i = \begin{cases} 2\pi, & \text{if } \tilde{\mathbf{r}} \text{ is on the polyhedron surface,} \\ 4\pi, & \text{if } \tilde{\mathbf{r}} \text{ is inside the polyhedron,} \\ 0, & \text{if } \tilde{\mathbf{r}} \text{ is outside the polyhedron,} \end{cases} \quad (2.6)$$

where

$$\omega_i = 2 \arctan \left( \frac{\tilde{\rho}_{i,1} \cdot \tilde{\rho}_{i,2} \times \tilde{\rho}_{i,3}}{\rho_{i,1}\rho_{i,2}\rho_{i,3} + \rho_{i,1}(\tilde{\rho}_{i,2} \cdot \tilde{\rho}_{i,3}) + \rho_{i,2}(\tilde{\rho}_{i,3} \cdot \tilde{\rho}_{i,1}) + \rho_{i,3}(\tilde{\rho}_{i,1} \cdot \tilde{\rho}_{i,2})} \right) \quad (2.7)$$

$$\tilde{\rho}_{i,1} = \tilde{\mathbf{r}}_{i,1} - \tilde{\mathbf{r}} \quad (2.8)$$

$$\tilde{\rho}_{i,2} = \tilde{\mathbf{r}}_{i,2} - \tilde{\mathbf{r}} \quad (2.9)$$

$$\tilde{\rho}_{i,3} = \tilde{\mathbf{r}}_{i,3} - \tilde{\mathbf{r}} \quad (2.10)$$

and

$$\rho_{i,1} = \|\tilde{\rho}_{i,1}\|, \quad \rho_{i,2} = \|\tilde{\rho}_{i,2}\|, \quad \rho_{i,3} = \|\tilde{\rho}_{i,3}\| \quad [42]. \quad (2.11)$$

Polyhedron models currently exist for a number of real asteroids. A model of the small-body shape can be created from a set of in-situ spacecraft measurements (altimetry or optical measurements for instance[21]) or from terrestrial radar observations using the method of Hudson[43].

## 2.2 Small-body Gravity Modeling

The irregular shapes of small-bodies give rise to equally irregular gravitational environments whose effect on a nearby spacecraft often varies dramatically from that

predicted by a pointmass gravity model. To accurately compute the gravitational potential of an irregular shape, one must begin from first principles. For an irregular (stationary) volume  $\Gamma$ , the potential at  $\tilde{\mathbf{r}}$  can be integrated using Eq. (2.12),

$$U(\tilde{\mathbf{r}}) = G \int_{\Gamma} \frac{\varrho(\tilde{\xi})}{\|\tilde{\mathbf{r}} - \tilde{\xi}\|} dV \quad (2.12)$$

where  $\tilde{\xi}$  is the location in the body of the infinitesimal volume  $dV$ . The gravitational attraction ( $\partial U/\partial\tilde{\mathbf{r}}$ ), Jacobian ( $\partial^2 U/\partial\tilde{\mathbf{r}}^2$ ), and Laplacian ( $\nabla^2 U$ ) are also quantities of interest to our dynamical modeling and can be computed via appropriate derivatives of Eq. (2.12). For the purpose of numerical simulation, it is highly advantageous to have a closed form solution for these gravitational quantities. In the simulations supporting this work, two approaches that give a closed-form solution have been used.

Given a shape model, the first approach assumes uniform density,  $\varrho$ , throughout the body. The literature provides closed form solutions for the gravitational potential, attraction, Jacobian, and Laplacian for ellipsoidal[44][45] and triangular-faceted polyhedral[42] shape models under this assumption. Because these results are fundamental to this research, they are summarized in Appendix B. The results of the NEAR intensive asteroid exploration mission to Eros suggest the assumption of uniform density may be quite applicable for at least some asteroids[21]. Even when the density is not uniform throughout, this approach is not entirely restrictive; solutions still exist if the small-body can be modeled as a finite union of uniform density shapes. Estimates of a small-body's bulk density can be obtained from the radar reflection albedo measured in terrestrial observations.

The other approach available is to use a spherical harmonic expansion[46] to define the small-body gravity. In this method, the gravitational potential (Eq. (2.13)) and

its derivatives are defined by two sets of coefficients ( $C_{nm}$  and  $S_{nm}$ ) and the associated Legendre functions ( $P_{nm}(x)$ ).

$$U = \frac{GM_{sb}}{\|\tilde{\mathbf{r}}\|} \sum_{n=0}^{\infty} \sum_{m=0}^n \left( \frac{R_{ref}}{\|\tilde{\mathbf{r}}\|} \right)^n P_{nm}(\sin \phi) (C_{nm} \cos(m\lambda) + S_{nm} \sin(m\lambda)) \quad (2.13)$$

The implementation of the spherical harmonic potential model used in this work, described in Pines[47], avoids singularities that arise in straightforward differentiation of Eq. (2.13) by using a change of coordinates. Pines goes on to derive recursion relationships for efficient computation of the spherical harmonic gravitational quantities in the new coordinates and Lundberg and Schutz[48] demonstrate which recursions are the most numerically stable. There are two primary drawbacks to using a spherical harmonic representation of the potential. First is that the expansion, which contains an infinite number of terms (it is truncated in the closed-form solution), does not converge for positions inside a sphere that circumscribes the small-body. Thus, a spherical harmonic potential representation is useless for modeling spacecraft dynamics close to the surface of a small-body, as would be necessary to support any sampling or touchdown mission. Secondly, accurate spherical harmonic coefficients for a small-body are impossible to determine without taking in-situ measurements (which could come from a spacecraft or orbiting debris). Since so few missions to small-bodies have been flown, very few such models exist.

For consistency with the equations of motion, the center of mass and principal axes of the small-body shape must be determined. For a constant density ellipsoid model, these quantities are trivially defined due to symmetry. Results for a constant density polyhedral shape are provided by Mirtich[49]. The center of mass and principal axes of a spherical harmonic model can be determined from the first and second order coefficients[50].

## 2.3 Equations of Motion

In this thesis, four typical astrodynamics equations of motion (with appropriate modifications) are used to model the translational spacecraft motion in the vicinity of a small-body. These are the two-body problem (in the small-body fixed rotating frame), the circular restricted three-body problem, the Hill three-body problem, and the generalized elliptic restricted three-body problem. All four sets of equations model the spacecraft as a pointmass whose mass is negligible compared to that of the small-body and a third-body (if present).

### 2.3.1 Two-body Problem in the Small-body Fixed Frame

This formulation defines the spacecraft dynamics in the small-body fixed frame, which spins with the small-body around its rotation pole in inertial space. These equations describe motion relative to the surface of the small-body. This model is applicable to very-close proximity spacecraft operations where only the gravitational attraction of the small-body need be considered<sup>1</sup>.

These equations permit the small-body to have an arbitrary shape and gravitational field (see Sections 2.1 and 2.2). No other perturbing effects (such as planetary tide, solar tide, and solar radiation pressure(SRP)) are included. It is assumed that the small-body rotates uniformly about the principal axis corresponding to the maximum moment of inertia, which is aligned with the  $\hat{\mathbf{z}}$  axis. The  $\hat{\mathbf{x}}$  axis is aligned with the principal axis corresponding to the minimum moment of inertia, and the  $\hat{\mathbf{y}}$  axis completes the right-handed coordinate frame. The only forces present in these dynamics are the gravity of the small-body, inertial forces due to the rotating frame, and the spacecraft thruster forces. The equations of motion for a spacecraft in the

---

<sup>1</sup>A discussion of the region where gravitational force dominates can be found in Scheeres[14]

two-body problem in the small-body fixed frame are given in Eq. (2.14)[10].

$$\ddot{\mathbf{r}} + 2\tilde{\omega} \times \dot{\mathbf{r}} = \frac{\partial U^T}{\partial \tilde{\mathbf{r}}} - \tilde{\omega} \times \tilde{\omega} \times \tilde{\mathbf{r}} + \tilde{\mathbf{T}} \quad (2.14)$$

If the thrust vector  $\tilde{\mathbf{T}}$  is constant (in the rotating small-body fixed frame), then Eq. (2.14) defines a time-invariant conservative Lagrangian system, which means there exists a Jacobi constant of the motion (Eq. (2.15))[51].

$$J_{BF} = \frac{1}{2} \dot{\tilde{\mathbf{r}}}^T \dot{\tilde{\mathbf{r}}} - \frac{1}{2} \omega^2 (x^2 + y^2) - U(\tilde{\mathbf{r}}) - \tilde{\mathbf{T}}^T \tilde{\mathbf{r}} \quad (2.15)$$

The resonance radius (Eq. (2.16)) is an important parameter in the two-body problem which arises frequently in this research[10].

$$R_r = \left( \frac{\mu_{sb}}{\omega^2} \right)^{\frac{1}{3}} \quad (2.16)$$

For a spherical body with the same gravitational parameter as the small-body, the resonance radius is the equilibrium distance from the center of mass in the equatorial plane. This parameter characterizes the approximate location of the important dynamical boundary in the two-body problem between inward and outward acceleration.

### Linearization of the Potential

For the purpose of obtaining a closed form solution to the two-body dynamics, it may be advantageous to linearize the gravitational potential around some nominal position (which makes the entire system linear). This approximation can be used to model hovering dynamics or translation over small distances. The equations of motion for the two-body problem in the small-body fixed frame with a linearized gravitational potential are given in Eq. (2.17),

$$\begin{bmatrix} \dot{\tilde{\mathbf{r}}} \\ \ddot{\tilde{\mathbf{r}}} \end{bmatrix} = A \begin{bmatrix} \tilde{\mathbf{r}} \\ \dot{\tilde{\mathbf{r}}} \end{bmatrix} + \begin{bmatrix} \mathbf{0}_{3 \times 1} \\ \tilde{\mathbf{f}} \end{bmatrix} \quad (2.17)$$

where

$$A = \left[ \begin{array}{cc} \mathbf{0}_{3 \times 3}, & \mathbf{I}_{3 \times 3} \\ \frac{\partial^2 U}{\partial \tilde{\mathbf{r}}^2} \Big|_0 + \begin{bmatrix} \omega^2, & 0, & 0 \\ 0, & \omega^2, & 0 \\ 0, & 0, & 0 \end{bmatrix}, & \begin{bmatrix} 0, & 2\omega, & 0 \\ -2\omega, & 0, & 0 \\ 0, & 0, & 0 \end{bmatrix} \end{array} \right] \quad (2.18)$$

and

$$\tilde{\mathbf{f}} = \tilde{\mathbf{T}} + \frac{\partial U}{\partial \tilde{\mathbf{r}}} \Big|_{\tilde{\mathbf{r}}_0}^T - \frac{\partial^2 U}{\partial \tilde{\mathbf{r}}^2} \Big|_{\tilde{\mathbf{r}}_0} \tilde{\mathbf{r}}_0. \quad (2.19)$$

### 2.3.2 Circular Restricted Three-body Problem

The circular restricted three-body problem expands on the two-body problem by including the gravity of a third body in a mutually circular orbit with the small-body. These equations can be used to model the effects of a small-body's orbit around the Sun on the spacecraft dynamics, a binary asteroid system, or the dynamics of a planetary moon orbiter when the eccentricity of the orbit of the two gravitating primaries is nearly zero. Again here, the only forces considered are those arising from the gravitational attraction of two primaries, the rotating frame, and the spacecraft control system.

In this problem, it is assumed that both primaries have point-mass potential fields so that the equations of motion (without thrust) are time-invariant<sup>2</sup>. The origin of these equations is at the center of mass of the two primaries with the positive  $\hat{\mathbf{x}}$  axis pointing toward the smaller primary (called the “second” primary). The  $\hat{\mathbf{z}}$  axis is normal to the plane of the primaries' mutually circular orbit (aligned with the orbit angular momentum) and the  $\hat{\mathbf{y}}$  axis is defined to complete a right-handed coordinate frame, which is referred to throughout as the rotating three-body frame.

---

<sup>2</sup>More complex gravity fields can be used without destroying this invariance (with some modification of the equations) if the rotation axis and rate of the non-spherical body are equal to the angular momentum direction and mean motion of the mutually circular orbit.

The equations of motion for this dynamical system[52] are given in Eq. (2.20),

$$\ddot{\mathbf{r}} + 2\tilde{\mathbf{N}} \times \dot{\mathbf{r}} = -\mu_1 \frac{\tilde{\mathbf{r}}_{sc,1}}{\|\tilde{\mathbf{r}}_{sc,1}\|^3} - \mu_2 \frac{\tilde{\mathbf{r}}_{sc,2}}{\|\tilde{\mathbf{r}}_{sc,2}\|^3} - \tilde{\mathbf{N}} \times \tilde{\mathbf{N}} \times \tilde{\mathbf{r}} + \tilde{\mathbf{T}} \quad (2.20)$$

where  $\tilde{\mathbf{r}}_{sc,1} = [x + \mu R, y, z]^T$ ,  $\tilde{\mathbf{r}}_{sc,2} = [x - (1 - \mu)R, y, z]^T$ ,  $\mu = \mu_2 / (\mu_1 + \mu_2)$ , and  $N = \sqrt{(\mu_1 + \mu_2) / R^3}$ . The mean motion  $N$  and the orbital radius  $R$  are constant here because of the circular primary orbit. If the spacecraft thrust vector  $\tilde{\mathbf{T}}$  is also constant (in this rotating frame), this is a time-invariant conservative Lagrangian system with the Jacobi constant defined by Eq. (2.21)[52].

$$J_{R3BP} = \frac{1}{2} \dot{\mathbf{r}}^T \dot{\mathbf{r}} - \frac{1}{2} N^2 (x^2 + y^2) - \frac{\mu_1}{|\tilde{\mathbf{r}}_{sc,1}|} - \frac{\mu_2}{|\tilde{\mathbf{r}}_{sc,2}|} - \tilde{\mathbf{T}}^T \tilde{\mathbf{r}} \quad (2.21)$$

### 2.3.3 Hill Three-body Problem

The Hill three-body problem, which is a valid approximation of the circular restricted three-body problem for spacecraft motion near the smaller primary (the “small-body”) when  $\mu$  is small, is now defined. This approximation is valid when spacecraft motion occurs inside the small-body’s Hill sphere, whose radius is given in Eq. (2.22).

$$R_{Hill} = R \left( \frac{\mu}{3} \right)^{\frac{1}{3}} \quad (2.22)$$

The Hill approximation applies well to spacecraft motion near small-bodies in orbit around the Sun or near planetary moons, but generally does not apply to motion near one of the bodies in a binary asteroid system ( $\mu$  is too large). The effects of SRP can be included in this formulation[17]. The frame of these equations is again the rotating three-body frame, centered at the center of mass of the small-body. The larger primary is modeled as a pointmass on the negative  $\hat{\mathbf{x}}$  axis. For the Hill

three-body problem, the equations of motion are given by Eqs. (2.23) - (2.25)[53],

$$\ddot{x} - 2N\dot{y} = 3N^2x + \frac{\partial U(\tilde{\mathbf{r}}, t)}{\partial x} + \frac{\beta_{SRP}}{R^2} + T_x \quad (2.23)$$

$$\ddot{y} + 2N\dot{x} = \frac{\partial U(\tilde{\mathbf{r}}, t)}{\partial y} + T_y \quad (2.24)$$

$$\ddot{z} = -N^2z + \frac{\partial U(\tilde{\mathbf{r}}, t)}{\partial z} + T_z \quad (2.25)$$

where  $\beta_{SRP} = G_1/B$  is a measure of the magnitude of the SRP strength[17]. Here,  $U$  can vary with time which allows these equations to represent dynamics near a general small-body shape with a rotation state that is independent of its orbit with the larger primary.

This system of equations is time-invariant if either the small-body has a pointmass gravitational potential or its angular velocity vector is aligned with the  $\hat{\mathbf{z}}$  axis and has magnitude equivalent to the mean motion of primaries' orbit. If in addition the spacecraft thrust is constant, the Jacobi constant is by Eq. (2.26).

$$J_{Hill} = \frac{1}{2}\dot{\tilde{\mathbf{r}}}^T \dot{\tilde{\mathbf{r}}} - \frac{3}{2}N^2x^2 + \frac{1}{2}N^2z^2 - U(\tilde{\mathbf{r}}) + \frac{\beta_{SRP}x}{R^2} - \tilde{\mathbf{T}}^T \tilde{\mathbf{r}} \quad (2.26)$$

### 2.3.4 Generalized Elliptic Restricted Three-body Problem

The generalized elliptic restricted three-body problem is the least restrictive form of the spacecraft dynamics used in this thesis. These equations expand on the circular restricted three-body problem by allowing for an eccentric primary orbit, an arbitrary small-body potential field, arbitrary (but constant) small-body rotation pole and rate, and SRP.

The equations are given in the three-body rotating frame centered at the small-body center of mass. In this case, the rotation of the frame is non-uniform because of the orbit eccentricity. The equations of motion for this system are given in Eq.

(2.27),

$$\begin{aligned} \ddot{\tilde{\mathbf{r}}} + 2 \left( \dot{f} \hat{\mathbf{z}} \times \dot{\tilde{\mathbf{r}}} \right) = & -\ddot{f} \hat{\mathbf{z}} \times \tilde{\mathbf{r}} - \dot{f} \hat{\mathbf{z}} \times \dot{\tilde{\mathbf{r}}} \times \tilde{\mathbf{r}} - \frac{\mu_{Sun} - \beta_{SRP}}{\|\tilde{\mathbf{r}}_{s/c,Sun}\|^3} \tilde{\mathbf{r}} \\ & - \left[ \frac{\mu_{Sun} - \beta_{SRP}}{\|\tilde{\mathbf{r}}_{s/c,Sun}\|^3} - \frac{\mu_{Sun}}{|R(f)|^3} \right] R(f) \hat{\mathbf{x}} + G_{sb,f}(\tilde{\mathbf{r}}, t) + \tilde{\mathbf{T}} \end{aligned} \quad (2.27)$$

where

$$\tilde{\mathbf{r}}_{s/c,Sun} = \tilde{\mathbf{r}} + [R(f), 0, 0]^T \quad (2.28)$$

$$R(f) = \frac{a_{orb}(1 - e_{orb}^2)}{1 + e_{orb} \cos f} \quad (2.29)$$

$$\dot{f} = \sqrt{\frac{(\mu_{Sun} + \mu_{sb})}{p_{orb}^3}} (1 + e_{orb} \cos f)^2 \quad (2.30)$$

$$\ddot{f} = -2e_{orb} \frac{(\mu_{Sun} + \mu_{sb})}{p_{orb}^3} \sin f (1 + e_{orb} \cos f)^3 \quad (2.31)$$

$$p_{orb} = a_{orb} (1 - e_{orb}^2) \quad (2.32)$$

and  $G_{sb,f}(\tilde{\mathbf{r}}, t)$  returns the gravitational attraction induced by an arbitrary small-body in the frame of these equations of motion. It is defined in terms of the small-body fixed frame potential in Eq. (2.33),

$$G_{sb,f}(\tilde{\mathbf{r}}, t) = T_f T_{eo} T_{pole}^{-1} T_i^{-1} \left. \frac{\partial U}{\partial \tilde{\mathbf{r}}} \right|_{(T_i T_{pole} T_{eo}^{-1} T_f^{-1} \tilde{\mathbf{r}})}^T \quad (2.33)$$

where

$$T_f = \begin{bmatrix} \cos f & \sin f & 0 \\ -\sin f & \cos f & 0 \\ 0 & 0 & 1 \end{bmatrix} \quad (2.34)$$

rotates a vector from the elliptic orbit frame (where  $\hat{\mathbf{x}}$  points to perigee and  $\hat{\mathbf{z}}$  is

parallel to the angular momentum) to the rotating three-body frame,

$$T_{eo} = \begin{bmatrix} \cos \omega_{orb} & \sin \omega_{orb} & 0 \\ -\sin \omega_{orb} & \cos \omega_{orb} & 0 \\ 0 & 0 & 1 \end{bmatrix} \begin{bmatrix} 1 & 0 & 0 \\ 0 & \cos i_{orb} & \sin i_{orb} \\ 0 & -\sin i_{orb} & \cos i_{orb} \end{bmatrix} \begin{bmatrix} \cos \Omega_{orb} & \sin \Omega_{orb} & 0 \\ -\sin \Omega_{orb} & \cos \Omega_{orb} & 0 \\ 0 & 0 & 1 \end{bmatrix} \quad (2.35)$$

rotates a vector from the inertial frame in which the orbital elements are defined (such as EME2000 or EMO2000) to the elliptic orbit frame,

$$T_{pole} = \begin{bmatrix} \sin \Lambda_{pole} & -\cos \Lambda_{pole} & 0 \\ \sin \Phi_{pole} \cos \Lambda_{pole} & \sin \Phi_{pole} \sin \Lambda_{pole} & -\cos \Phi_{pole} \\ \cos \Phi_{pole} \cos \Lambda_{pole} & \cos \Phi_{pole} \sin \Lambda_{pole} & \sin \Phi_{pole} \end{bmatrix} \quad (2.36)$$

rotates a vector from an inertial frame into the small-body rotation pole frame (where  $\hat{\mathbf{z}}$  is aligned with the small-body rotation pole), and

$$T_i = \begin{bmatrix} \cos [\omega (t - t_{0,bf})] & \sin [\omega (t - t_{0,bf})] & 0 \\ -\sin [\omega (t - t_{0,bf})] & \cos [\omega (t - t_{0,bf})] & 0 \\ 0 & 0 & 1 \end{bmatrix} \quad (2.37)$$

rotates a vector from the small-body rotation pole frame into the small-body fixed frame. In Eq. (2.37),  $t_{0,bf}$  is a time at which the small-body fixed frame and small-body rotation pole frame unit vectors are aligned. In inertial coordinates, this corresponds to the time when the  $\hat{\mathbf{x}}$  direction in the body-fixed frame makes a descending transit through the  $X - Y$  plane of the inertial frame. These rotation matrices are also useful for changing coordinates between the specified frames.

This dynamical system is time-varying and therefore has no Jacobi constant.

### 2.3.5 Limitations of the Equations of Motion

As with most analytically tractable equations of motion, none of the preceding equations of motion perfectly define the dynamics that a spacecraft will experience in

the vicinity of a small-body. The most obvious omission is the rotational dynamics of the spacecraft and any coupling between its translational and rotational dynamics. Throughout this work, it is assumed that the effect of any dynamic coupling is negligible and that the required attitude dynamics maneuvers (i.e., pointing in a specified direction or performing a steady slew maneuver) can be implemented with sufficient accuracy.

Though this work is applicable to all types of small-bodies (asteroids, comets, and small-planetary satellites), these equations are most appropriate for an individual asteroid in orbit around the Sun. In the case of comets, the acceleration due to comet outgassing is not modeled by any of these equations of motion. This acceleration is very significant (and quite complex) to the operations of a spacecraft near a comet[32]. For a spacecraft near a planetary satellite, the gravity of the host planet is well modeled by any of the preceding three-body equations of motion, but the gravity and, more importantly, the radiation pressure from the Sun cannot be included and may have a significant effect on the spacecraft motion. If modeling a binary asteroid system, either the circular restricted or the general elliptic restricted three-body problems are appropriate. However, these equations of motions neglect the inevitably irregular shape of one of the primaries and the complex rotational/translational coupling in the non-Keplarian motion of the asteroids themselves[33]. Plus the SRP cannot be included. Finally, all of these equations of motion assume the small-body rotates uniformly around the principal axis corresponding to its largest moment of inertia. This is the case for most of the asteroids for which data exists (with exceptions such as the asteroid Toutatis[15]), but often is not the case for comet nuclei due to torques induced by outgassing jets[11].

There are also a number of accelerations that a spacecraft may experience that

are not modeled in these equations for any type of small-body. If extremely accurate results are desired, as would be needed during mission operations for instance, a dynamics simulator would have to consider accelerations induced by a number of planets, passing asteroids, albedo (reflection off the surface of the body), electromagnetic forces (important for dynamics near comets), the shape and attitude of the spacecraft as a function of time, and numerous other stochastic or un-modeled sources and biases. Because of the many uncertainties involved, a rigorous covariance analysis would also be necessary. The equations of motion defined above strike a balance by including the most significant accelerations a spacecraft would experience near an asteroid, but remaining sufficiently tractable for traditional analysis.

## 2.4 Measurement Models

Missions to small-bodies place difficult demands on navigators for state estimation accuracy. Navigation for a “typical” space mission is done primarily with radiometric Doppler and range measurements taken using large radio telescopes on Earth. These measurements give line-of-sight velocity accuracy to the order of fractions of a millimeter per second and line-of-sight position estimates to within a few meters. However, the small-body state is usually uncertain to tens of kilometers in position and to a few millimeters per second in velocity. For a mission to a small-body, which may be only a few hundred meters in size, this level of measurement accuracy (particularly in position) is not sufficient for safe and effective relative navigation. Further, because of the tremendous distances between the majority of small-bodies and the Earth, there is a significant time lag associated with these measurements. Clearly, if a spacecraft is to operate in close-proximity to the surface of a small-body, additional measurements are necessary.

The most effective solution to these problems comes in the form of in-situ measurements. These are direct measurements of the spacecraft state relative to the small-body which deliver greatly improved position, velocity, and attitude measurements to the spacecraft in real-time. Altimeters and optical cameras have typically been used on small-body missions to obtain in-situ measurements. This study will consider three in-situ measurement types: single beam altimetry, time-of-flight velocimetry, and optical navigation. A discussion of the mathematical modeling of these measurements follows. Since this work is concerned primarily with close proximity operations, these measurements are defined in the small-body fixed frame where the surface of the small-body is stationary (though they can be adapted to other frames without too much difficulty).

Additional information on the altimetry and time-of-flight velocimetry measurements used here, including measurement partials with respect to spacecraft position, velocity, instrument orientation, and angular velocity, as well as a software class implementation written in MPython, a variant of Python written at JPL as part of the MONTE navigation software set, can be found in Broschart[41].

#### **2.4.1 Altimetry Measurements**

An altimetry measurement specifies the distance between the spacecraft and surface of the small-body in a specified direction. Numerous types of altimeters are available including radar altimeters, laser altimeters, and multi-beam altimeters. Here a simple altimeter that returns the range between the spacecraft and the surface of the small-body in a particular direction is considered. This type of measurement most closely resembles that of a laser altimeter.

On an actual spacecraft, altitude information would be given to the spacecraft

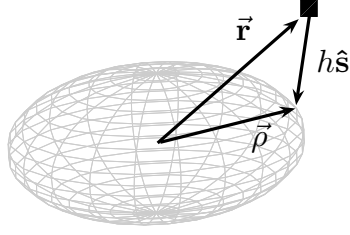


Figure 2.4: Altitude Measurement Geometry

by an altimeter pointing in the appropriate direction. For the sake of numerical simulation, knowledge of the spacecraft position in the body-fixed frame and a small-body shape model is sufficient to determine the altitude. The problem geometry is shown in Figure 2.4. Here, the spacecraft position  $\tilde{\mathbf{r}}$  is given by the simulation integrator,  $\tilde{\rho}$  specifies the point on the surface that the altimeter intersects,  $h$  is the spacecraft altitude, and  $\hat{\mathbf{s}}$  is the normalized altimeter pointing direction. From this diagram, the following relation is derived.

$$\tilde{\rho} = \tilde{\mathbf{r}} + h\hat{\mathbf{s}} \quad (2.38)$$

For an ellipsoidal shape model,  $\tilde{\rho}$  must lie on its surface and therefore is a solution to  $S_{ellip}(\tilde{\rho}) = 0$  (Eq. (2.1)). Substituting Eq. (2.38) into Eq. (2.1) yields Eq. (2.39) since  $E$  is symmetric.

$$(\hat{\mathbf{s}}E\hat{\mathbf{s}}^T)h^2 + (2\hat{\mathbf{s}}E\tilde{\mathbf{r}}^T)h + (\tilde{\mathbf{r}}E\tilde{\mathbf{r}}^T - 1) = 0 \quad (2.39)$$

As one would expect, this quadratic gives two solutions for the altitude  $h$  in general, one intersection on either side of the ellipsoid (a double root is obtained if  $\hat{\mathbf{s}}$  is tangent to the surface). Assuming that the altimeter pointing direction has been chosen such that both solutions for  $h$  are positive real, the smaller solution of the two (Eq. (2.40)), corresponding to the side of the ellipsoid closest to the spacecraft,

is the correct range solution.

$$h = \frac{-\hat{\mathbf{s}}E\tilde{\mathbf{r}}^T - \sqrt{(\hat{\mathbf{s}}E\tilde{\mathbf{r}}^T)^2 - (\hat{\mathbf{s}}E\hat{\mathbf{s}}^T)(\tilde{\mathbf{r}}E\tilde{\mathbf{r}}^T - 1)}}{\hat{\mathbf{s}}E\hat{\mathbf{s}}^T} \quad (2.40)$$

If there are no real solutions, the sensing direction does not intersect the body.

The calculation of altitude above the polyhedral shape is fundamentally different, as the surface is described by not one, but many equations. To determine the correct altitude, range is computed to the plane defined by each facet, then the results are sorted.

In addition to the constraint in Eq. (2.38), the groundtrack vector must lie on the surface of the plane defined by a particular facet. Thus, Eq. (2.5) must hold. Eqs. (2.38) and (2.5) are combined to find that

$$\hat{\mathbf{n}}_i \cdot (\tilde{\mathbf{r}} + h_i\hat{\mathbf{s}}) = C_i \quad (2.41)$$

and thus,

$$h_i = \frac{C_i - \hat{\mathbf{n}}_i \cdot \tilde{\mathbf{r}}}{\hat{\mathbf{n}}_i \cdot \hat{\mathbf{s}}}. \quad (2.42)$$

Eq. (2.42) defines the altitude above each of the polyhedron's infinitely extended planar facets. Next, it must be determined which of these solutions for  $\tilde{\rho}_i$  lie on the actual surface of the body. Given  $h_i$  and  $\tilde{\mathbf{r}}$ , Eq. (2.38) allows computation of  $\tilde{\rho}_i$ . For the altitude to be valid,  $\tilde{\rho}_i$  must lie inside the area defined by that face's three vertex vectors. Further, the intersection must occur on the correct side of the body, so it is required that  $\tilde{\mathbf{r}} \cdot \hat{\mathbf{n}}_i > 0$ . Applying these two filters leaves only valid intersections with facets facing in the proper direction. Because the polyhedral shape can be quite arbitrary, this set can include multiple solutions. As in the ellipsoidal case, the smallest altitude from this set of valid solutions is the correct one. There may be no valid altitude, which means the sensing direction does not intersect the body.

The number of faces in a polyhedral model can be very large, necessitating a heavy computational load to perform this altitude computation for all the body's faces each time an altitude measurement is needed. This load is lessened by creating a temporary, revised face list which includes only faces that are in the vicinity of the current spacecraft groundtrack and have surface normals in the proper direction. Because the spacecraft moves in a continuous manner, it can be assumed that subsequent altitude measurements will fall on this same set of faces. If the simulation is unable to find a satisfactory altitude from this set of faces, which could occur if the spacecraft has traveled outside the area, a new set of faces based on the spacecraft's current position are chosen. A Matlab implementation of this technique, as well as groundtrack computation, is found in Broschart[54].

#### 2.4.2 Time-of-flight Velocimeter Measurements

A time-of-flight velocimeter measures the full time derivative of the range to the body at a given time, as would be calculated by differencing two subsequent altitude measurements. Using knowledge of the spacecraft position, velocity, and surface geometry, the rate-of-change in spacecraft altitude in a fixed measurement sensing direction  $\hat{\mathbf{s}}$  can be computed (the formulation in Broschart[41] allows the sensing direction to vary). This measurement includes components arising from both the spacecraft velocity and changes in the topography of the small-body's surface.

The altitude rate-of-change for the ellipsoid or polyhedron shape models is determined in the following way. The system geometry is the same as in the altimeter formulation (Figure 2.4), but these nominal vectors are propagated forward to their values after a small time step,  $\Delta t$ . Nominal values are noted using a subscript 0.

From the figure,

$$\tilde{\mathbf{r}}_0 + h_0 \hat{\mathbf{s}} = \tilde{\rho}_0. \quad (2.43)$$

Also, for a small change in the groundtrack vector  $\tilde{\rho}$ ,

$$(\tilde{\rho} - \tilde{\rho}_0) \cdot \hat{\mathbf{n}} = 0. \quad (2.44)$$

After a small timestep,

$$(\tilde{\mathbf{r}}_0 + \dot{\tilde{\mathbf{r}}}_0 \Delta t) + (h_0 + \Delta h) \hat{\mathbf{s}} = \tilde{\rho}. \quad (2.45)$$

Subtract  $\tilde{\rho}_0$  from both sides, dot with  $\hat{\mathbf{n}}$ , and rearrange to obtain the altitude rate-of-change (Eq. (2.46)).

$$\dot{h} = \frac{\Delta h}{\Delta t} = - \frac{\dot{\tilde{\mathbf{r}}}_0 \cdot \hat{\mathbf{n}}}{\hat{\mathbf{s}} \cdot \hat{\mathbf{n}}} \quad (2.46)$$

### 2.4.3 Optical Navigation Measurements

Optical navigation measurements are widely accepted as a critical component of a small-body navigation system. Computation of optical navigation measurements is generally complicated involving complex computer vision algorithms that extract, recognize, and match features from a series of pictures of the small-body surface. There are a number of techniques used ranging from simple to very complex. These include centroid computation[55], landmark tracking[56], paired feature tracking[56], limb tracking, shadow measurements, and others. The ultimate goal of all of these measurement types is to provide in-situ navigation data.

The mathematical model used here for optical navigation measurements is relatively simple. It is assumed that the measurement gives the unit vector  $\hat{\mathbf{o}}$  that points from the center of mass of the small-body toward the spacecraft. Equivalently, it can be said that the measurement gives the latitude and longitude, but not the range, of the spacecraft with respect to the small-body. This is most consistent with the

information obtained by a surface feature tracking optical navigation technique, such as landmark tracking or paired feature tracking.

## 2.5 Small-body Characterization Tool

The SBCT is a stand alone software tool (written in *C++*) designed to give an overview of the dynamic environment near a small-body. Development up to the current release, version 0.03, has been sponsored by JPL. The advantage of this tool is that it gives a broad overview of the dynamic environment near a small-body nearly instantaneously. Users can quickly get the “big [dynamics] picture” for a specified close-proximity mission profile. The validity of the user’s assumptions, plausibility of a mission concept, and the effects of parameter tweaking can quickly be assessed.

SBCT is very useful at a mission planning level, but is useful for simulation design in this research for many of the same reasons. It gives a method to quickly check if the equations of motion being used are appropriate. It can be very helpful in choosing appropriate initial conditions to obtain the desired motion in simulation and it gives quick answers to a wide range of questions in one place (“Can this orbit escape?”, “Where are the equilibria?”, “What is the acceleration and escape speed at this point on the surface?”, etc.). The SBCT brings together previously disparate tools and research (nothing of its kind for small-body dynamics existed previously) and is a useful tool for small-body dynamics work such as this. A brief overview of the use and outputs of the SBCT can be found in Appendix C.

## CHAPTER III

# Numerical Validation of Hovering

The first goal of this research project was to numerically validate the existing theory on controlling hovering spacecraft put forth in Sawai *et al.*[10] and Scheeres[8]. To do this, a first of its kind numerical hovering simulation tool, HoverSim, was developed. This chapter details the HoverSim tool and the how it was used to test the previously existing theory on hovering in the small-body fixed and inertial reference frames. Results and discussions of this comparison are included. The HoverSim tool is also used to perform a case study of hovering above asteroid Itokawa, the target of JAXA’s Hayabusa mission<sup>1</sup>.

These results of this chapter are also detailed in Broschart and Scheeres[58].

### 3.1 Review of the Results of Sawai *et al.*

Sawai *et al.*[10] considers a closed-loop strategy for hovering in the two-body problem. Hovering in this frame, which rotates with the small-body, is called “body-fixed hovering”. Body-fixed hovering (equilibrium) is ideally implemented at a nominal

---

<sup>1</sup>The study presented here was completed in advance of Hayabusa’s successful rendezvous and hovering campaign at Itokawa. Improved dynamical models of the shape and gravity of Itokawa now exist[57] that should be used as the basis of any future analysis.

hovering position  $\tilde{\mathbf{r}}_0$  by applying thrust  $\tilde{\mathbf{T}} = \tilde{\mathbf{T}}_{OL}$ , where

$$\tilde{\mathbf{T}}_{OL} = - \left. \frac{\partial U}{\partial \tilde{\mathbf{r}}} \right|_{\tilde{\mathbf{r}}_0}^T + \tilde{\omega} \times \tilde{\omega} \times \tilde{\mathbf{r}}_0 \quad (3.1)$$

in the two-body problem<sup>2</sup>. In addition to this open-loop cancellation of the nominal acceleration, Sawai *et al.* add a closed-loop control component to handle perturbations that completely restricts motion in a chosen direction.

By removing the dynamics in one direction from the equations of motion, stability criteria for the remaining two-dimensional motion are derived analytically from the linearized two-body equations of motion (Section 2.3.1). For an arbitrary potential  $U$ , the three criteria for stability derived in Sawai *et al.*[10] are given in Eqs. (3.2) - (3.4),

$$3\omega^2 \hat{v}_{3z}^2 + \omega^2 - (\alpha_1 + \omega^2) - (\alpha_2 + \omega^2) \geq 0 \quad (3.2)$$

$$(\alpha_1 + \omega^2)(\alpha_2 + \omega^2) - \omega^2 \hat{v}_{1z}^2 (\alpha_2 + \omega^2) - \omega^2 \hat{v}_{2z}^2 (\alpha_1 + \omega^2) \geq 0 \quad (3.3)$$

$$(\alpha_1 - \alpha_2 - \omega^2)^2 + 3\omega^4 \hat{v}_{3z}^2 (\hat{v}_{3z}^2 + 2) - 8\omega^2 \hat{v}_{3z}^2 \{(\alpha_1 + \omega^2) + (\alpha_2 + \omega^2)\} > 0 \quad (3.4)$$

where  $\alpha_1, \alpha_2, \alpha_3$  are the three eigenvalues of the Hessian matrix of the gravitational potential ( $\partial^2 U / \partial \tilde{\mathbf{r}}^2$ ) at the nominal hovering point, and  $\hat{\mathbf{v}}_1, \hat{\mathbf{v}}_2, \hat{\mathbf{v}}_3$  are the corresponding eigenvectors (subscripts  $x, y$ , and  $z$  refer to the Cartesian components of these vectors). The eigenvectors and eigenvalues are arranged such that the third set refers to the eigenvector ‘nearly’ aligned with the gravitational attraction direction (pointing away from the body). Of the remaining two, the eigenvector/eigenvalue pair with the largest eigenvalue is considered the first set. These three criteria define a region above an arbitrarily-shaped body where hovering in the small-body fixed frame is theoretically stable under this control. This region is roughly approximated by the locus of initial hovering points inside the body’s resonance radius (Eq.

---

<sup>2</sup>The stability of hovering under this open-loop control is investigated by Scheeres[8].

(2.16)). Illustrations of the region defined by these sufficiency criteria for spherical and ellipsoidal small-bodies, as well as the real asteroid Castalia, can be found in [10].

Implementation of the open-loop portion of the control requires a constant thrust that cancels the nominal acceleration on the spacecraft in the small-body fixed frame, given in Eq. (3.1)<sup>3</sup>. Note that this is a constant thrust vector in a rotating frame and thus, actual implementation would require an attitude controller or thrust vectoring system.

The closed-loop portion of the proposed control perfectly restricts motion along  $\hat{\mathbf{v}}_3$ , such that  $\dot{\mathbf{r}}^T \hat{\mathbf{v}}_3 \equiv 0$ . A spacecraft with an internal model of the small-body could compute the Hessian matrix of the potential and determine  $\hat{\mathbf{v}}_3$  on board. However, the assumption of such an “infinitely tight” control is not realistic, as it is impossible for an actual spacecraft control system to implement. [10] suggests an approximation to this control would be achieved by a dead-band thrust control based on altitude measurements, which confines the spacecraft movement to a band of positions around a target altitude. Eq. (3.5) gives a general formulation of a dead-band thrust control,

$$\tilde{\mathbf{T}}_{DB} = \begin{cases} -T_m \hat{\mathbf{c}}(\tilde{\mathbf{r}}), & \text{if } f_{db}(\tilde{\mathbf{r}}) \geq \gamma; \\ 0, & \text{otherwise.} \end{cases} \quad (3.5)$$

where for an altitude dead-band,  $f_{db}$  is defined in Eq. (3.6),

$$f_{db}(\tilde{\mathbf{r}}) = |h(\tilde{\mathbf{r}}) - h_0| \quad (3.6)$$

and for this controller,  $\hat{\mathbf{c}} = \text{sgn}(h - h_0) \hat{\mathbf{v}}_3$ . In the idealized controller used for the

---

<sup>3</sup>In [10], it is suggested that in implementation the open-loop control need only cancel the centrifugal force on the spacecraft. However, this research uses the open-loop control to null the full nominal acceleration on the spacecraft, as proposed in [8] to closer approximate the dynamics used to develop the theory. Full cancellation is found to more tightly confine the spacecraft’s range of motion. A more detailed look at the difference between full and partial cancellation of the nominal acceleration is found in Chapter V.

analytical model, the dead-band size,  $\gamma$ , would be zero. Hereafter, this implementation (Eqs. (3.1), (3.5), and (3.6)) of the idealized control proposed by Sawai *et al.* where,

$$\tilde{\mathbf{T}} = \tilde{\mathbf{T}}_{OL} + \tilde{\mathbf{T}}_{DB} \quad (3.7)$$

is known as the Gravitational Direction Thrusting and Sensing with Open-loop (GDTS w/OL) body-fixed hovering controller.

## 3.2 HoverSim Simulation Tool

HoverSim is a software tool, written in Matlab and Simulink, that was developed to simulate hovering under dead-band control based on altimetry measurements. The purpose of building this tool was to test the theoretical results of Sawai *et al.*[10] and serve as a platform for testing other dead-band control ideas. The basic function of the code is to integrate the spacecraft equations of motion in an arbitrary gravitational potential field subject to a chosen control law. Control laws can be implemented for body-fixed hovering, inertial hovering, or ballistic flight.

The simulation was designed to work with the polyhedron or tri-axial ellipsoid shape models with a constant density gravitational potential (Sections 2.1 and 2.2). The spacecraft dynamics are defined by the two-body equations of motion in the small-body fixed frame (Section 2.3.1), though the option exists to add the time-varying disturbance caused by the solar tide and SRP (as in Section 2.3.4, but in the small-body fixed frame).

Over the years, HoverSim has evolved into the more comprehensive Small-body Dynamics Toolkit (SBDT) which facilitates numerical simulation and investigation of additional dynamics and spacecraft motions near small-bodies. A more comprehensive description of the capabilities of the SBDT is found in Appendix D.

### 3.2.1 Thrust Control Options

In HoverSim, the spacecraft thrust  $\tilde{\mathbf{T}}$  is determined by the control law chosen by the user. The simulation includes three different types of control that can be applied to the spacecraft. These include a dead-band control on altimetry measurements (Eqs. (3.5),(3.6), and Section 2.4.1), a dead-band control on velocimetry (Eq. (3.5) and Section 2.4.2), where

$$f_{db}(\tilde{\mathbf{r}}) = \begin{cases} |\dot{h}|, & \text{if } |h(\tilde{\mathbf{r}}) - h_0| \geq \gamma_{(altitude)}; \\ 0, & \text{otherwise} \end{cases} \quad (3.8)$$

and an open-loop constant thrust controller (Eq. (3.1)). The simulation can be run using any combination of these three controllers. It is also possible to specify the instrument sensing direction  $\hat{\mathbf{s}}$  and dead-band control thrust application direction  $\hat{\mathbf{c}}$ .

When using the altitude dead-band controller, the user specifies a target altitude  $h_0$  for the spacecraft and a tolerance factor  $\gamma$ . If the spacecraft altitude is within  $\gamma$  of the target altitude, no thrust is added. If the spacecraft leaves this region, a thrust is applied along  $\hat{\mathbf{c}}(\tilde{\mathbf{r}})$  to return the spacecraft to the target altitude band. The magnitude of this thrust  $T_m$  is also specified as a simulation input. It is possible to implement only one ‘side’ of the dead band controller, i.e., thrusters are only fired when the spacecraft altitude is less than (greater than) the desired altitude.

The velocimetry dead-band controller is active only when the spacecraft is inside the altitude dead-band and fires the spacecraft thrusters when the spacecraft changes altitude faster than the specified rate limit  $\gamma$ . This control has a damping effect, reducing the magnitude of oscillations in altitude inside an altimetry dead-band.

The final controller available in HoverSim is the open-loop controller. This constant control thrust nulls gravitational and centripetal accelerations in the two-body

problem at the prescribed hovering point.

### 3.2.2 HoverSim Output

Upon completion of the simulation, the system parameters and time-stamped histories of spacecraft position, velocity, altimetry measurements, velocimeter measurements, and thrust are given to the user. These outputs fully define the spacecraft motion and system geometry and can be used to compute any desired additional quantities. To obtain data for a range of initial conditions, the simulation can also be run iteratively as described in a Matlab script file. Any of the HoverSim outputs can be saved for each iteration.

### 3.2.3 Simulation Verification

In order to assure that the simulation works as intended, a series of tests with known results were completed and compared with the expected behavior. First, a trajectory was computed above a spherical body with no thrust applied. The spacecraft's angular momentum and energy were computed from the simulation output and it was found that energy was conserved, the angular momentum vector had constant magnitude, and it was rotated from its initial direction by  $\omega\Delta t$  around the rotation axis as predicted by the analytical theory.

The next test was designed to verify that the simulation was computing the correct body forces on the spacecraft. This was done by solving analytically for the forces on the spacecraft at a given position, then adding an open-loop thrust of equal magnitude and opposite direction to the spacecraft. If the simulation computes the forces on the spacecraft correctly, this open-loop thrust should cancel those forces perfectly and the spacecraft should not move. The simulation was found to correctly produce this result for numerous test positions.

The final verification test was done to ensure that the dead-band controllers were working as intended. This was determined by looking at the thrust, altitude, and altitude rate of change vs. time output. Thrust should be enabled in the proper direction whenever the dead-band condition is violated. This test was performed for a number of initial conditions and the dead-band controllers were found to be working as expected.

### 3.3 Numerical Investigation of the Sawai *et al.* Results

The difference between the idealized closed-loop hovering controller used in the derivation of Sawai *et al.*'s stability criteria (Eqs. (3.2)-(3.4)), which completely restricts motion in a chosen direction, and its practical implementation, which allows motion across a finite band of altitude in the same direction, is significant enough to warrant study. For one, the allowable region of motion in the ideal case is a flat plane in space, while the implementation with altimetry creates a region that curves in space with the contours of the small-body surface. Also, the cumulative effect of Coriolis forces on the trajectory in the two unrestricted directions is very different in three-dimensional motion across a finite dead-band than the effect of simply canceling the out-of-plane component of the Coriolis force has on the planar dynamics. Thus, an analysis using the full nonlinear equations of motion under the GDTS w/OL thrust control is necessary to validate the theoretical results of Sawai *et al.*[10].

This chapter furthers the previous work by numerically simulating the nonlinear equations of motion with HoverSim to study one-dimensional dead-band hovering via altimetry with realistic control constraints. The results of the numerical study are compared and contrasted with the previous findings to determine in which regions

the analytical stability criteria (Eqs. (3.2)-(3.4)) produce valid results.

Determining stability characteristics of a trajectory from numerical data is inherently difficult. With finite-time simulation data, it is impossible to verify true stability or instability. In this chapter, a quantifiable numerical definition of stability which is suitable to evaluate finite-time trajectories will be used. Beginning with a perturbation from equilibrium smaller than a given magnitude, stability is quantified by the size of the region around the initial hovering point that contains the entire trajectory for a given simulation time. The results presented here quantify the size of this region by the maximum angular deviation from the nominal hovering position as viewed from the small-body center of mass. Angular deviation may be a more relevant parameter to a mission than absolute distance deviation if the spacecraft is trying to point at a specific location on the surface of the body. Instability is defined not as unbounded motion, but as motion outside a specified region during the simulation time. Due to potentially long time constants of instability, this analysis seeks only to verify stability for a fixed duration in the regions predicted by the analytical stability criteria and not to verify instability in the complimentary space.

### 3.3.1 Hovering with GDTS w/OL Control

The GDTS w/OL hovering controller is defined by a target altitude,  $h_0$ , and a dead-band width parameter,  $\gamma$ . If the spacecraft's altitude (measured along  $\hat{\mathbf{s}} = -\hat{\mathbf{v}}_3$ ) is outside the 'band' defined by  $h_0 \pm \gamma$ , thrust is enabled to return the spacecraft into the dead-band (where  $\hat{\mathbf{c}} = \text{sgn}(h - h_0) \hat{\mathbf{v}}_3$ ).

Using an ellipsoidal small-body shape model, HoverSim was used to simulate motion under the GDTS w/OL controller for random initial positions in the body's three symmetric planes ( $X - Y$ ,  $X - Z$ , and  $Y - Z$ ). The ellipsoid used in these

simulations was  $15 \times 7 \times 6 \text{ km}$ , a rough approximation of the size of asteroid (433)Eros that was visited during NASA/JPL's NEAR mission. A bulk density of  $3 \text{ g/cm}^3$  and a ten hour rotation period were used, which are not consistent with Eros, but were chosen to move the resonance radius further from the body for clarity<sup>4</sup>. The dead-band width parameter,  $\gamma$ , was 10 meters. For each initial spacecraft position, the simulation was run ten times with different initial velocity errors each time. Each Cartesian component of velocity error was chosen randomly from a uniform distribution between  $-1$  and  $1 \text{ cm/s}$ .

Data were collected from independent simulations of two different durations, 20000 and 50000 seconds (roughly 5.5 and 13.9 *hrs* respectively). These relatively short simulation times (on the order of one rotation period) are justified by noting that a spacecraft operating in the body-fixed frame very near the surface would have little reason to remain in one position for long periods of time. This type of maneuver would likely be used during a descent or a translation across the surface, while longer term hovering station-keeping maneuvers would more likely be carried out in the inertial frame.

In the following figures, each data point represents the average size over ten trials of the smallest solid angle such that the entire trajectory is contained within it. For this analysis, averages of less than  $0.4^\circ$  are considered to be stable. The region inside the bold line is the locus of initial positions satisfying the analytical stability criteria (Eqs. (3.2)-(3.4)). Note that for an ellipsoidal shape model, the equations of motion exhibit a longitudinal symmetry, i.e., results are the same for any two points  $180^\circ$  longitude apart.

These simulations show that in the  $X - Z$  and  $Y - Z$  planes the analytical criteria

---

<sup>4</sup>With Eros' true rotation period of 5.27 *hrs* and bulk density of  $2.4 \text{ g/cm}^3$ , the resonance radius is roughly  $15.7 \text{ km}$ , barely beyond the long end of the body.

for stability were well supported by the numerical results. There were no regions of numerically unstable motion (large angular deviation) that encroached upon the predicted region of stability. Numerical stability (tightly bound motion) extended to some regions outside the area defined by the stability criteria in these planes, but these trajectories are not necessarily stable in the long term and therefore, do not suggest error in the stability conditions. Figures 3.1 and 3.2 show the results in the  $X - Z$  plane after 20000 and 50000 seconds respectively. The  $Y - Z$  results are essentially identical, the difference being that the boundary of the predicted stability region is closer to the body at low latitudes and, hence, so is the onset of instability (just outside that region). It can be noted that large angular deviations arise most quickly for hovering outside the predicted stability zone at low latitudes in the  $X - Z$  and  $Y - Z$  planes.

Figures 3.3 and 3.4 present results from simulations in the body's  $X - Y$  (equatorial) plane for simulation durations of 20000 and 50000 seconds respectively. In the  $X - Y$  plane figures, the results do not correspond as well with the analytical stability criteria as in the others. Here, instabilities arise above the body's leading edges inside of the region that satisfies the stability conditions. The leading edges are defined as the two quadrants of longitude on the body's surface that extend from the tip of the largest semi-major axis of the ellipsoid to the intermediate semi-major axis in the direction of  $\hat{\mathbf{z}} \times \hat{\mathbf{x}}$ . As the simulation duration increases from 20000 to 50000 seconds, the area of instability encroaches further upon the region satisfying the stability criteria. On the other hand, the region of predicted stability above the body's trailing edge is unaffected and remains stable. The region of stability off the trailing edge actually is significantly expanded for shorter duration (20000 second) hovering.

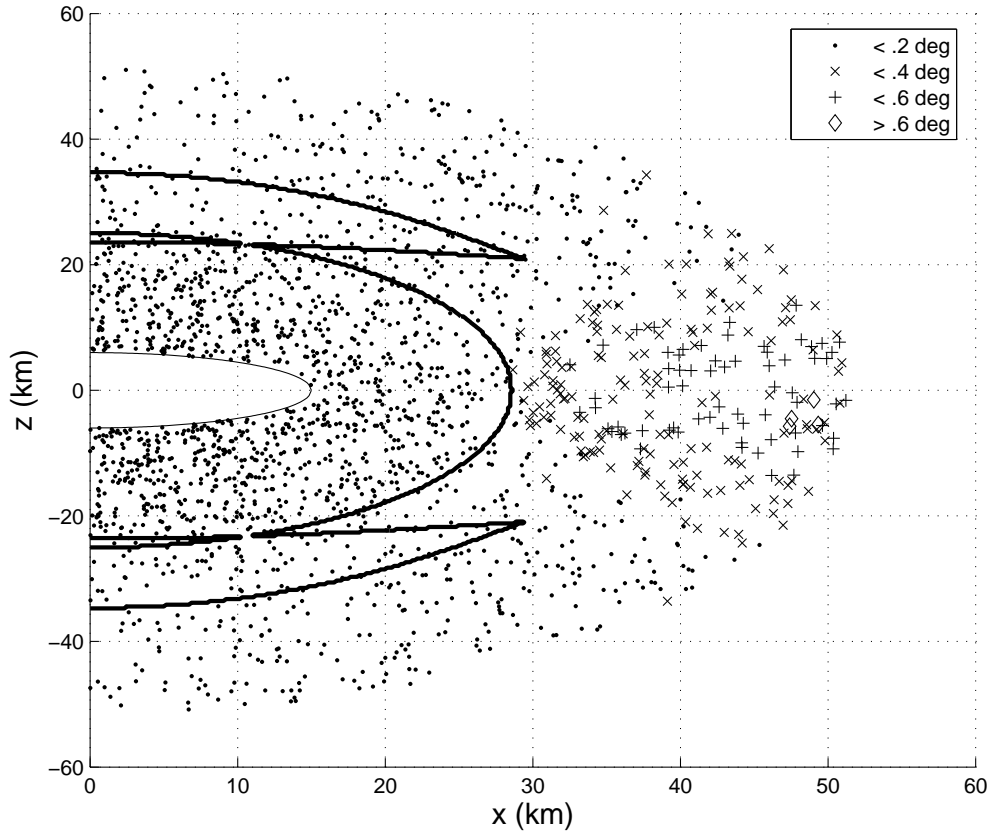


Figure 3.1: Angular Deviation for GDTS w/OL Body-fixed Hovering Controller, 20000 s ( $X - Z$  plane)

### 3.3.2 Analysis of GDTS w/OL Controller Results

The discrepancy between the ideal region of stability and the numerical findings in the  $X - Y$  plane can be attributed to the Coriolis accelerations introduced when the assumption of infinitely tight control in the gravitational direction is relaxed. An interaction between the dead-band orientation, the control thrust application direction, and the Coriolis accelerations causes the degradation of numerical stability above the ellipsoid leading edges and the improvement in stability above the trailing edge seen in the simulation data.

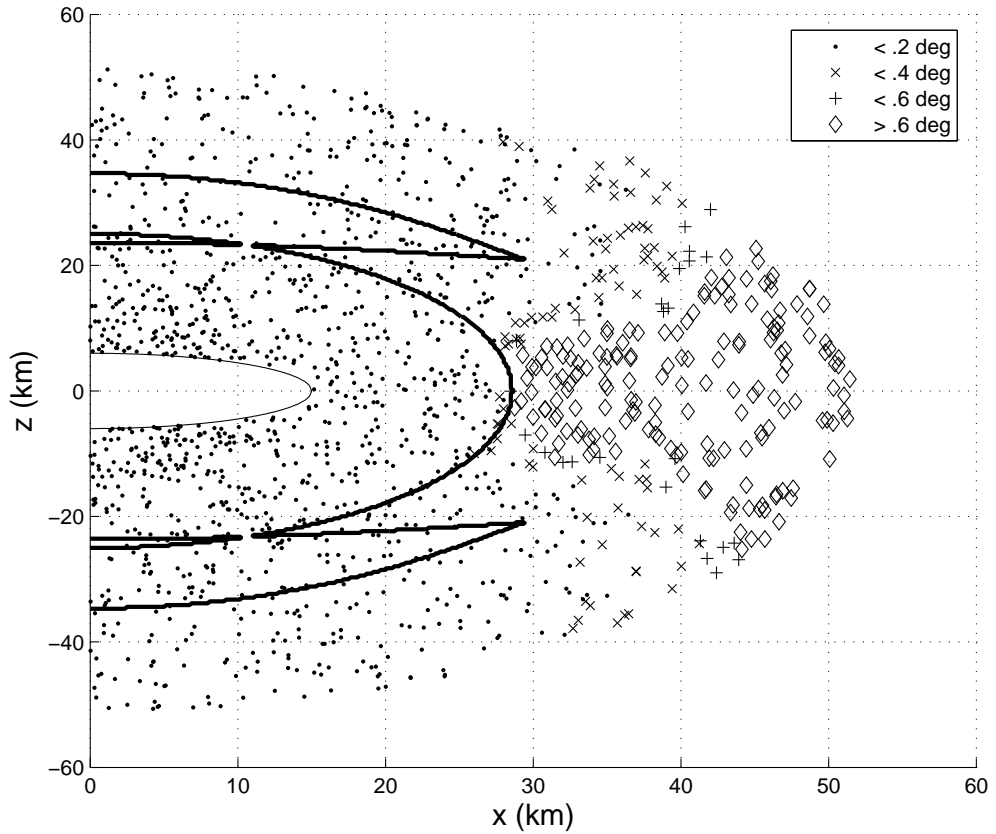


Figure 3.2: Angular Deviation for GDTS w/OL Body-fixed Hovering Controller, 50000 s ( $X - Z$  plane)

The orientation of the dead-band region for hovering in the  $X - Y$  plane is shown in Figure 3.5. A coordinate system can be defined for the dead-band dynamics consisting of the normal vector to the dead-band boundary,  $\hat{\mathbf{n}}_{db}$ , the unit vector along the rotation axis,  $\hat{\mathbf{z}}$ , and the unit vector transverse to the dead-band boundary,  $\hat{\mathbf{t}}_{db} = \hat{\mathbf{z}} \times \hat{\mathbf{n}}_{db}$ . The surface normal where  $\hat{\mathbf{s}}$ , intersects the body's surface defines  $\hat{\mathbf{n}}_{db}$ , the local orientation of the dead-band. This direction is not aligned with the control direction,  $\hat{\mathbf{c}}$ , in general. Therefore, when dead-band control thrust is applied, it will have some component along  $\hat{\mathbf{t}}_{db}$ . This transverse thrust component will be equal and opposite at the two dead-band boundaries. If the spacecraft hits both boundaries

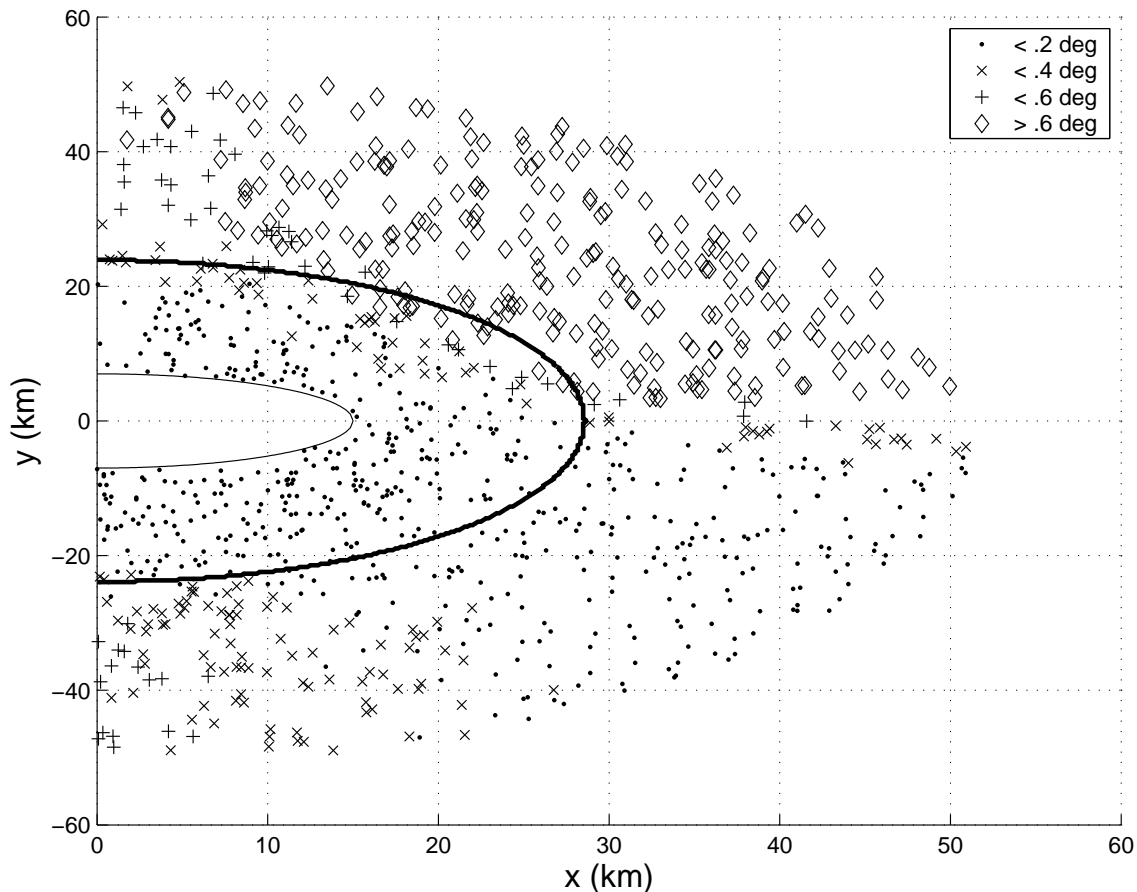


Figure 3.3: Angular Deviation for GDTS w/OL Body-fixed Hovering Controller, 20000 s ( $X - Y$  plane)

an equal number of times, this transverse acceleration will have no net effect on the spacecraft's motion along the dead-band. However, due to Coriolis forces which effectively rotate the spacecraft velocity vector, this may not be the case. This rotation coupled with the control thrust component along the dead-band can either cause the spacecraft to repeatedly hit one boundary of the dead-band or encourage it to bounce back and forth between the boundaries.

Figure 3.6(a) illustrates the dynamics above the leading edge. Above an ellipsoid's leading edge subject to GDTS w/OL hovering control, the relative orientation of  $\hat{\mathbf{n}}_{db}$  and  $\hat{\mathbf{c}}$  is such that at the minimum altitude boundary of the dead-band, a component

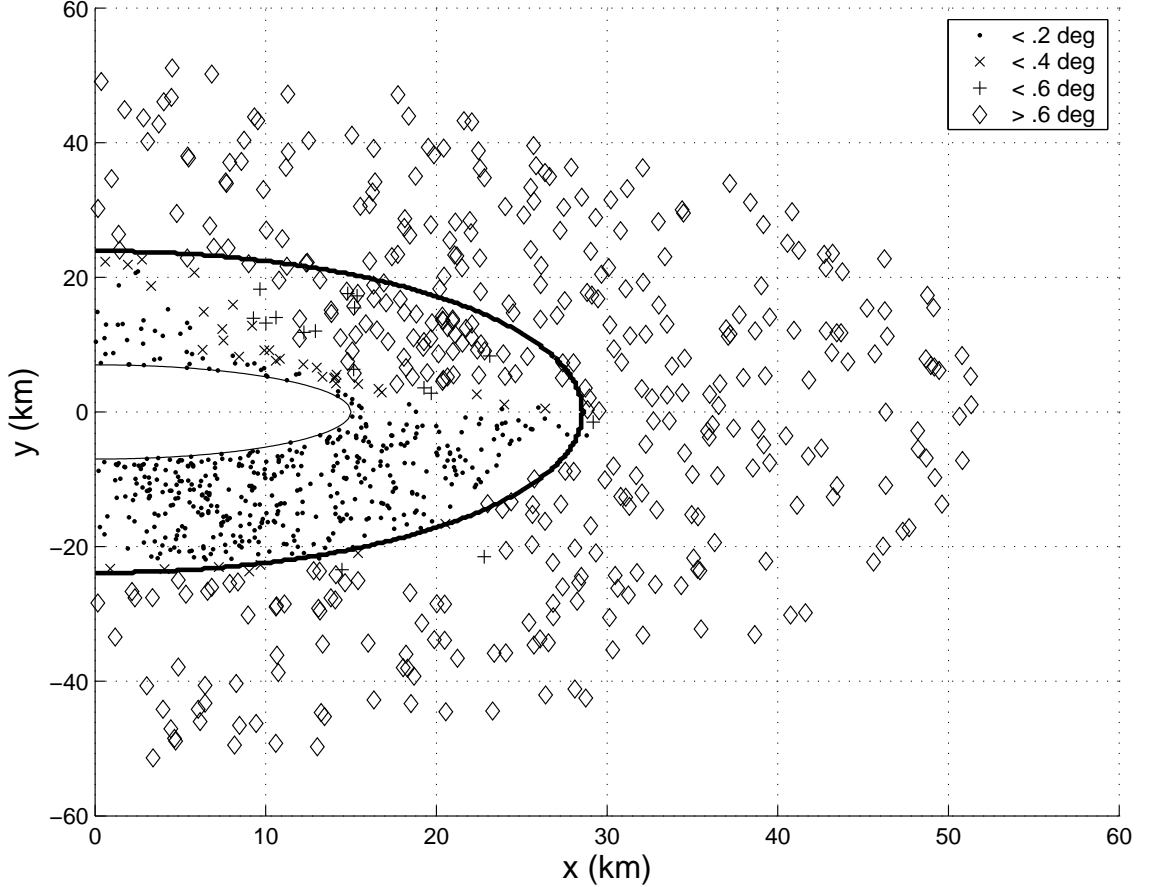


Figure 3.4: Angular Deviation for GDTS w/OL Body-fixed Hovering Controller, 50000 s ( $X - Y$  plane)

of the control thrust is applied in the negative  $\hat{\mathbf{t}}_{db}$  direction and at the maximum altitude boundary, thrust is applied in the positive  $\hat{\mathbf{t}}_{db}$  direction. The Coriolis force acting on the spacecraft,  $F_c = -2\omega(\hat{\mathbf{z}} \times \dot{\hat{\mathbf{r}}})$ , effectively rotates the spacecraft's velocity vector clockwise in the plane defined by  $\hat{\mathbf{n}}_{db}$  and  $\hat{\mathbf{t}}_{db}$ . When the spacecraft reaches a boundary, the component of control thrust along  $\hat{\mathbf{t}}_{db}$  will effectively rotate the return velocity vector clockwise from the direction it would have been if there were no thrust component along  $\hat{\mathbf{t}}_{db}$ . As the spacecraft moves toward its next boundary crossing, Coriolis forces will rotate the velocity in the same clockwise direction. Once transients due to initial velocity errors wear off, the combination of these two effects

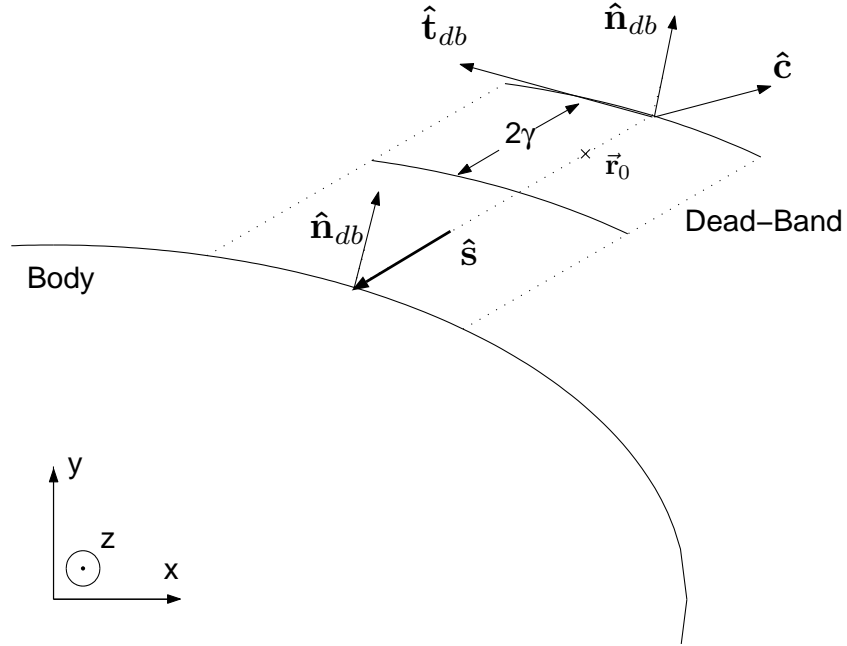


Figure 3.5: Dead-band Orientation Diagram

will cause the spacecraft to hit the same boundary on successive occasions until the non-linear effects of gravity and changes in dead-band orientation eventually turn it around. This successive ‘bouncing’ motion leads to large oscillations from the nominal hovering point. Examination of numerical simulations show that this “bouncing” movement always takes over in the steady-state for hovering in a small dead-band above the leading edge of an ellipsoid subject to the GDTS w/OL controller.

Figure 3.6(b) illustrates the dynamics above the trailing edge. Above the body’s trailing edge, the relative orientation of  $\hat{\mathbf{n}}_{db}$  and  $\hat{\mathbf{c}}$  is the opposite. At the minimum altitude boundary, a component of the control thrust is applied in the positive  $\hat{\mathbf{t}}_{db}$

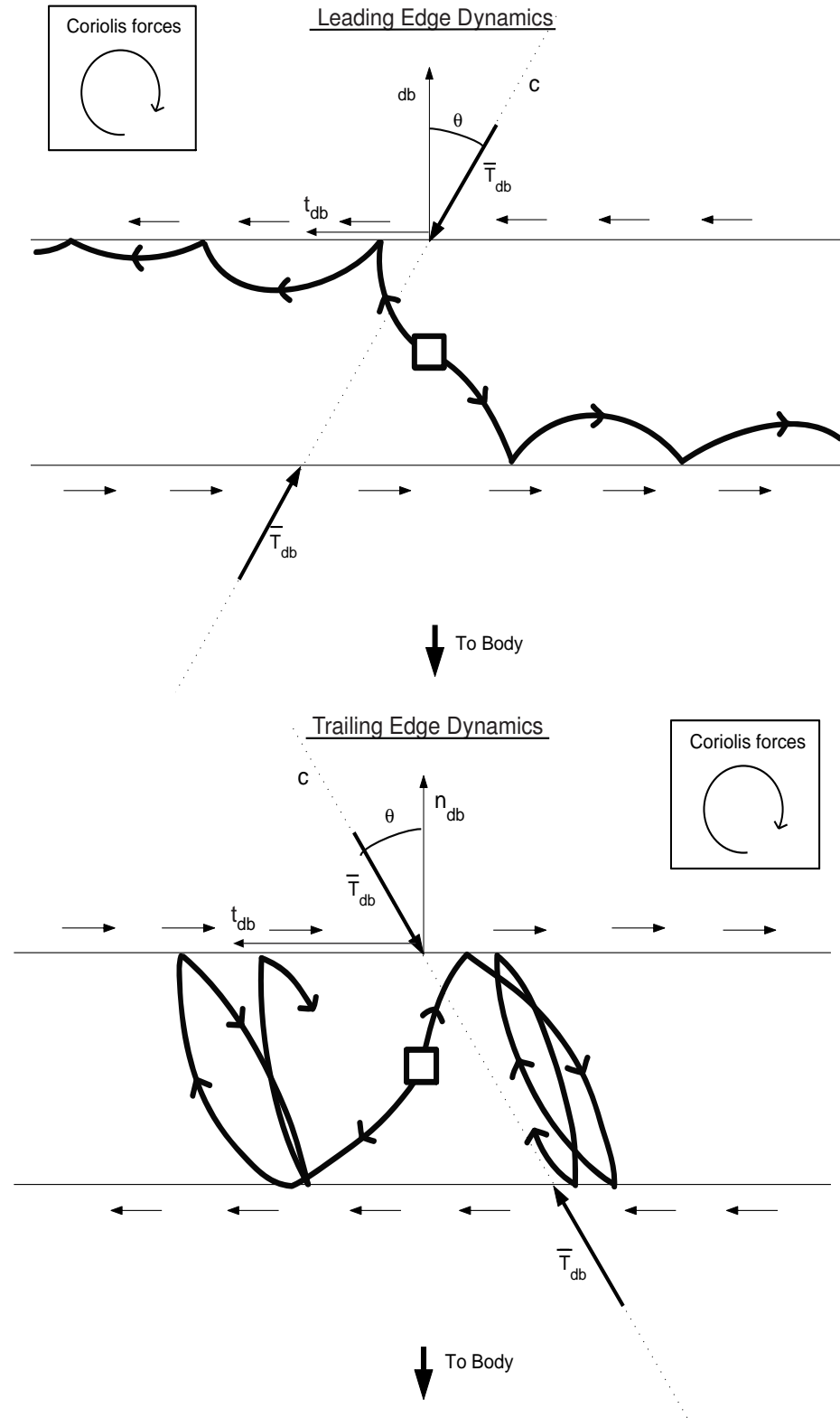


Figure 3.6: Dead-band Dynamics Above an Ellipsoid under GDTS w/OL Control, (a)Leading and (b)Trailing Edges

direction and at the maximum altitude boundary, thrust is applied in the negative  $\hat{\mathbf{t}}_{db}$  direction. As opposed to above the leading edge, the thrust component along  $\hat{\mathbf{t}}_{db}$  in this configuration causes the velocity vector reflected off the dead-band boundary to be rotated counter-clockwise from where it would have been if there were no transverse thrust component. In this case, the clockwise rotation of the velocity vector caused by the Coriolis force will counter the effect of the control thrust, encouraging the spacecraft to move toward the other dead-band boundary. Again, in the steady state, this motion always takes over above an ellipsoid's trailing edge for small dead-band sizes, causing a 'chattering' effect, where the spacecraft never hits the same boundary on successive occasions. This 'chattering' has a focusing effect that keeps the spacecraft close to the initial hovering point.

The analysis here is done in the equatorial plane for the sake of simplicity, but this effect occurs with weakening strength (meaning the leading and trailing edge results differ less) all the way to the body's  $X - Z$  and  $Y - Z$  planes. In these planes, thrust transverse to the dead-band and Coriolis accelerations never work together to push the spacecraft in a consistent direction. Also, the Coriolis accelerations only act in the unrestricted plane of motion, so their effect is not canceled at all when the motion along  $\hat{\mathbf{v}}_3$  is removed. This is why the numerical results in the  $X - Z$  and  $Y - Z$  planes agree well with the analytical predictions.

The strength of this Coriolis effect above either the leading or trailing edge is determined by  $\omega$ ,  $\gamma$ , and the angle between  $\hat{\mathbf{n}}_{db}$  and  $\hat{\mathbf{c}}$ . Let  $\theta$  be this angle, measured from  $\hat{\mathbf{n}}_{db}$  and positive for orientations such that  $\hat{\mathbf{c}} \cdot \hat{\mathbf{t}}_{db} > 0$ . Sufficiently positive values of  $\theta$  will result in a focusing "chattering" effect and sufficiently negative values result in the destabilizing "bouncing" effect. The sufficient values and the  $\theta$  that produces the tightest focusing effect are functions of  $\tilde{\mathbf{r}}_0$ ,  $\omega$ , and  $\gamma$ . If a symmetric, universal

method of choosing control direction is used, such as gravitational direction or initial acceleration, some optimal control law may exist which will adequately focus the leading edge dynamics, while not weakening the focusing effect off the trailing edge too much.

These results suggest that ideally, a spacecraft should use a method of choosing control direction above the leading and trailing edges such that the angle  $\theta$  is always positive. Simulations have shown that shifting the control direction above the leading edge so that  $\theta$  is positive does indeed produce the desired stabilizing effect. It should be noted that  $\theta$  should never approach  $\pm 90^\circ$  since there will then be no thrust in the direction normal to the dead-band to maintain the spacecraft's altitude.

### 3.4 Other Dead-band Hovering Approaches

During the course of the investigation of the results of Sawai *et al.*, HoverSim was used to look at some alternative approaches to hovering. First, the Initial Acceleration Thrusting and Normal Sensing (IATNS) controller for body-fixed hovering is studied. This controller is a variant on the dead-band control approach of Sawai *et al.* in Section 3.1. Hovering in an inertial frame, where the small-body rotates beneath the spacecraft, is also investigated numerically.

#### 3.4.1 Body-fixed Hovering with IATNS Control

The performance of another implementation of the body-fixed hovering solution, the IATNS controller, was also evaluated numerically. This controller also utilizes a dead-band control based on altimeter readings (Eqs. (3.5) and (3.6)), but it has no open-loop component. Also for IATNS control, the direction of the dead-band control thrust is changed to be aligned with the nominal acceleration vector  $\hat{\mathbf{a}}_0$  (Eq. (3.9)), such that  $\hat{\mathbf{c}} = -\text{sgn}(h - h_0) \hat{\mathbf{a}}_0$ . This should more directly counter the natural

motion of the spacecraft.  $\hat{\mathbf{s}}$  is also changed to measure altitude in the direction that is normal to the small-body surface. This is the most robust direction to measure altitude since the component that changes with the surface topography is minimized for small deviations in spacecraft position.

$$\hat{\mathbf{a}}_0 = \frac{\partial U / \partial \tilde{\mathbf{r}}|_{\tilde{\mathbf{r}}_0}^T - \tilde{\omega} \times \tilde{\omega} \times \tilde{\mathbf{r}}_0}{\left\| \partial U / \partial \tilde{\mathbf{r}}|_{\tilde{\mathbf{r}}_0}^T - \tilde{\omega} \times \tilde{\omega} \times \tilde{\mathbf{r}}_0 \right\|} \quad (3.9)$$

The IATNS controller may offer advantages over the GDTS w/OL controller. By sensing altitude in the direction normal to the surface at the initial hovering point, the magnitude of the angle  $\theta$  between the dead-band orientation vector  $\hat{\mathbf{n}}_{db}$  and the control direction  $\hat{\mathbf{v}}_c$  is smaller for ellipsoids, which the analysis suggests should improve performance above the body's leading edge. Also, removing the open-loop causes the spacecraft's motion to proceed very closely along the initial acceleration direction from the initial hovering point. This lessens the deviation from the initial hovering point due to transient effects caused by initial velocity errors, as the spacecraft will more quickly move into steady-state motion in the dead-band. Fuel savings may result as well (see Chapter V).

With some thought, it is clear that the IATNS controller will fail catastrophically near (and beyond) the resonance radius of the body. As the spacecraft hovering point approaches the resonance radius, the initial acceleration vector,  $\hat{\mathbf{a}}_0$  will turn  $180^\circ$  as the nominal acceleration transitions from pointing toward the body to away due to centrifugal force. Therefore, this controller will be limited to use inside the body's resonance radius or near the rotation axis.

Using the same ellipsoidal small-body and system parameters used in the simulations for the GDTS w/OL controller, spacecraft motion subject to the IATNS controller has been simulated in the  $X - Y$ ,  $X - Z$ , and  $Y - Z$  planes. Here again,

ten different simulations with random velocity errors were conducted at each initial hovering point.

The IATNS body-fixed hovering controller was found to work well at altitudes inside the resonance radius. As expected, the controller quickly becomes less stable as the initial position nears the area where the initial acceleration rotates away from the body. In all three planes, initial positions inside this destabilizing threshold are found to be numerically stable.

Figures 3.7 and 3.8 show the results of simulations in the  $X - Y$  plane after 20000 and 50000 seconds respectively. In the  $X - Y$  plane, the analytical stability conditions define the threshold where the initial acceleration vector turns away from the body. The bold line in the figures outlines this region. As hoped, the IATNS controller reduces the deviations associated with the Coriolis forces discussed in the Section 3.3.2 above the body's leading edge compared to the GDTS w/OL controller. By reducing  $\theta$ , the instability related to Coriolis forces above the leading edge is weakened and develops more slowly. In the 50000 second figure, a slight degradation of stability is just beginning to appear above the leading edge. In the data from the 20000 second runs, this degradation of stability cannot be seen. Similarly, the stabilizing effect above the trailing edge could be slightly weakened due to the realignment of the vector  $\hat{\mathbf{n}}_{db}$  for this controller. However, the angle  $\theta$  is still negative and therefore, a focusing effect remains, as demonstrated by these numerical results.

For comparison with the GDTS w/OL control, Figures 3.9 and 3.10 show the results of simulations in the  $X - Z$  plane after 20000 and 50000 seconds respectively. Again, the results in the  $Y - Z$  plane are qualitatively similar.

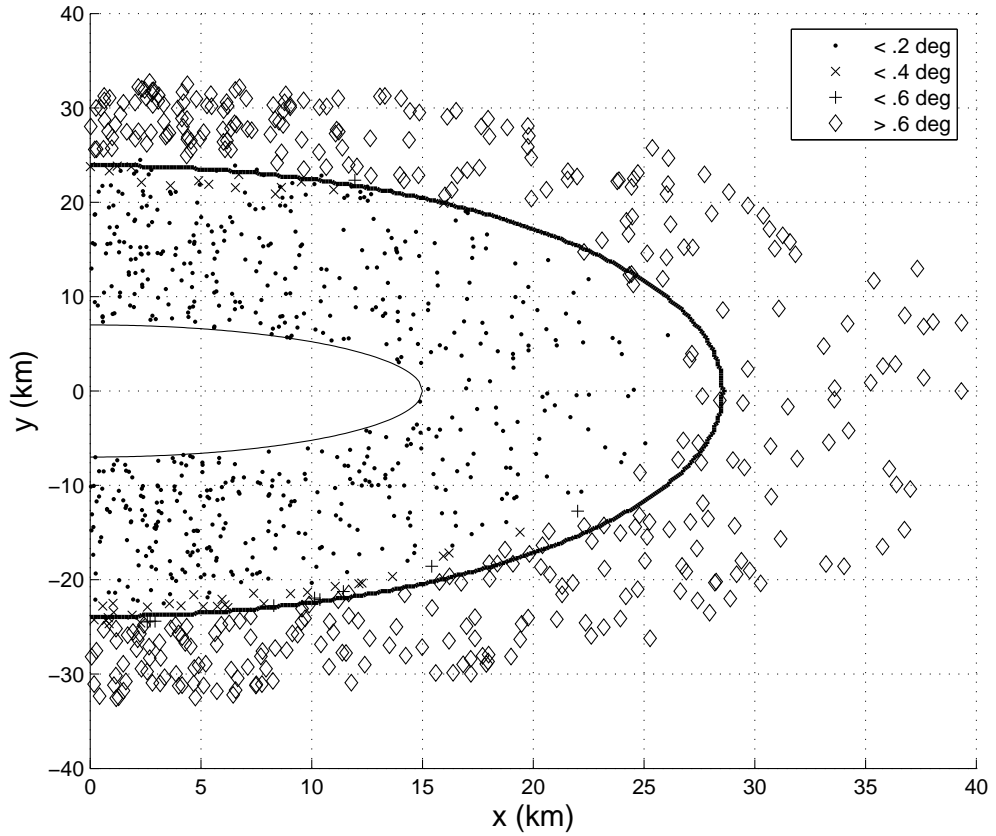


Figure 3.7: Angular Deviation for IATNS Body-fixed Hovering Controller, 20000 s  
( $X - Y$  plane)

### 3.4.2 Inertial Hovering

This section looks at a second solution to the two-body equations of motion in the small-body fixed frame (Eq. (2.14)). This solution is a retrograde, constant latitude, circular orbit whose orbital period is equal to the small-body's rotation period. In this “inertial hovering” solution, the spacecraft position remains fixed in inertial space while the small-body rotates beneath it. In the small-body fixed frame, this solution is specified in Eqs. (3.10) and (3.11),

$$\tilde{\mathbf{r}}_{0I}(t) = \|\tilde{\mathbf{r}}_{0I}(0)\| \begin{bmatrix} \cos \phi_0 \cos(\omega t + \lambda_0), & -\cos \phi_0 \sin(\omega t + \lambda_0), & \sin \phi_0 \end{bmatrix}^T \quad (3.10)$$

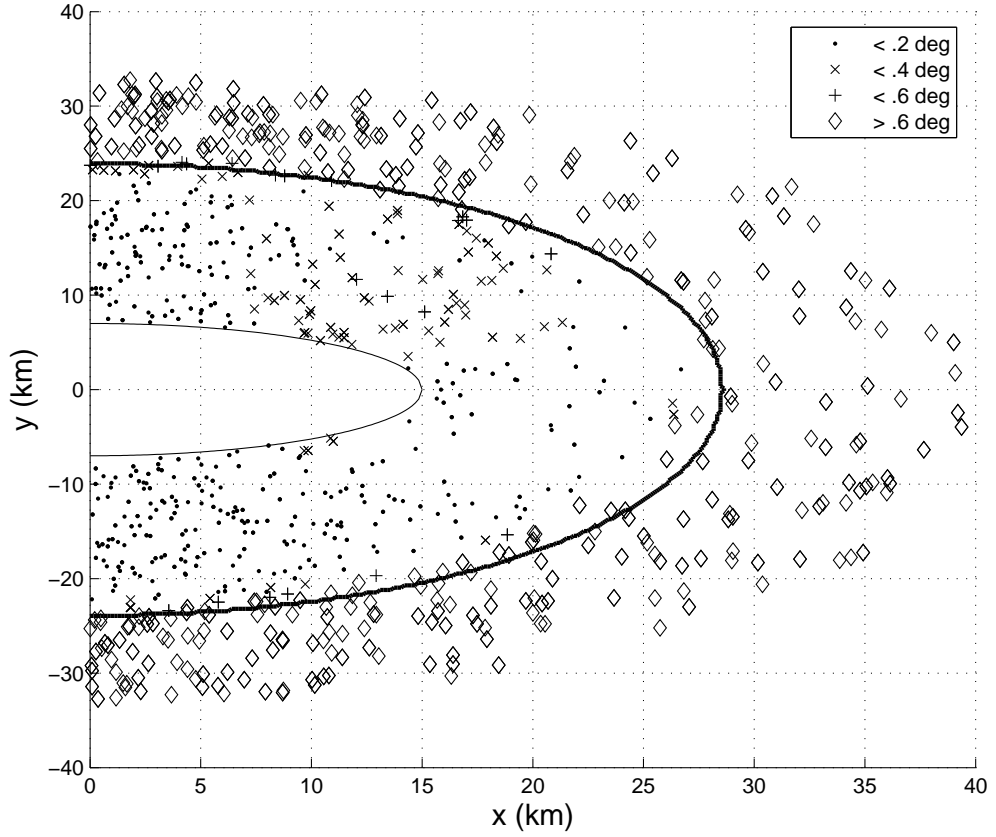


Figure 3.8: Angular Deviation for IATNS Body-fixed Hovering Controller, 50000  $s$  ( $X - Y$  plane)

$$\ddot{\tilde{\mathbf{r}}}_{0I}(t) = -\omega \|\tilde{\mathbf{r}}_{0I}(0)\| \begin{bmatrix} \cos \phi_0 \sin(\omega t + \lambda_0) \\ \cos \phi_0 \cos(\omega t + \lambda_0) \\ 0 \end{bmatrix}^T \quad (3.11)$$

where  $\phi_0$  and  $\lambda_0$  are the initial latitude and longitude (measured from the positive  $\hat{\mathbf{x}}$  axis), respectively. For inertial hovering, Eq. (3.12) defines the thrust necessary to make this circular orbit a solution to the equations of motion.

$$\tilde{\mathbf{T}}(t) = -\left. \frac{\partial U}{\partial \tilde{\mathbf{r}}} \right|_{\tilde{\mathbf{r}}_{0I}(t)}^T \quad (3.12)$$

If the two-body equations of motion are linearized about the inertial hovering

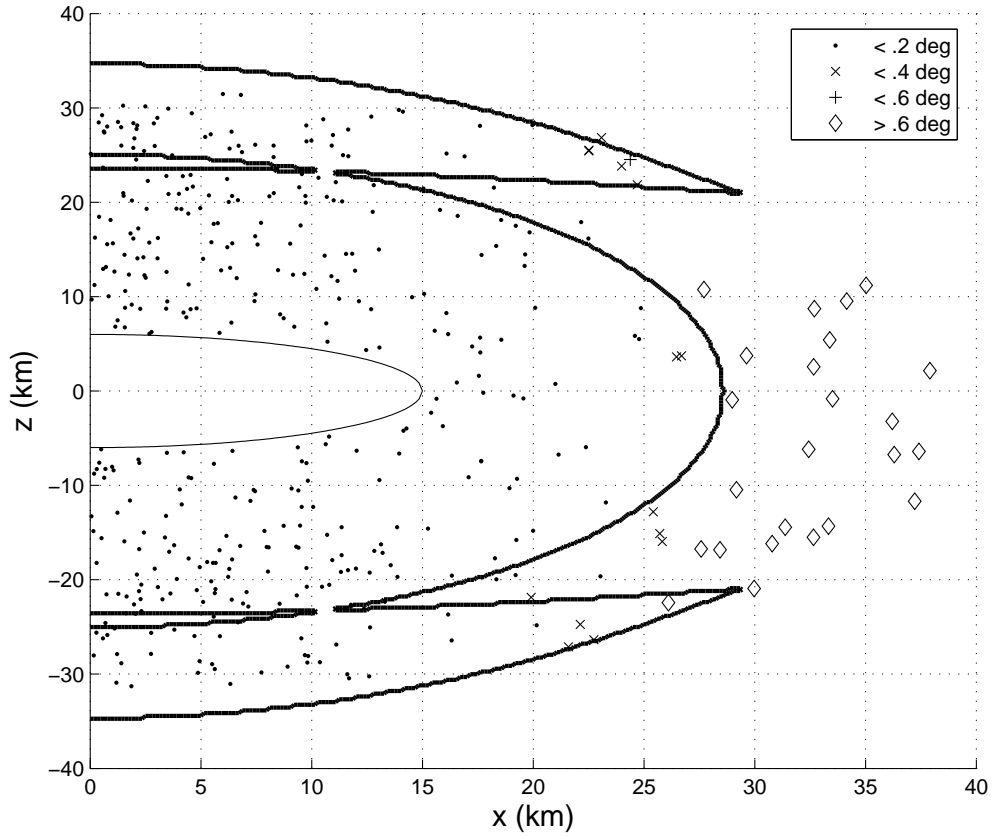


Figure 3.9: Angular Deviation for IATNS Body-fixed Hovering Controller, 20000 s ( $X - Z$  plane)

solution (Eqs. (3.10) and (3.11)), the perturbation equations (Eq. (3.13)) are found.

$$\delta\ddot{\mathbf{r}} + 2\tilde{\omega} \times \delta\dot{\mathbf{r}} = \left. \frac{\partial^2 U}{\partial \tilde{\mathbf{r}}^2} \right|_{\tilde{\mathbf{r}}_{0I}(t)} \delta\tilde{\mathbf{r}} - \tilde{\omega} \times \tilde{\omega} \times \delta\tilde{\mathbf{r}} \quad (3.13)$$

This is a periodic, time-varying linear system. The stability of this system can be determined using Floquet theory, which says that the state transition matrix is of the form,

$$\Phi(t) = P(t) e^{Mt} \quad (3.14)$$

where  $P(t)$  is a periodic matrix and  $M$  is the constant monodromy matrix. The stability of the system is determined by the eigenvalues of  $M$ . This is done by eval-

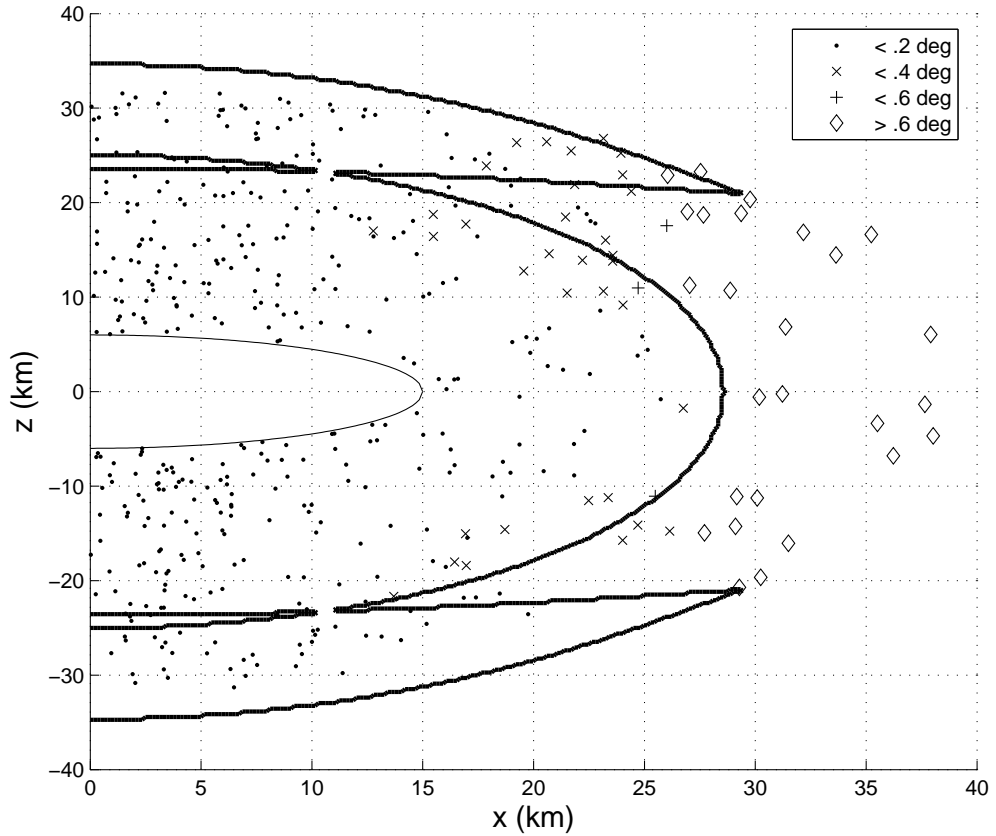


Figure 3.10: Angular Deviation for IATNS Body-fixed Hovering Controller, 50000  $s$  ( $X - Z$  plane)

uating the state transition matrix after one period of motion, i.e., when  $P$  is the identity matrix. The state transition matrix can be calculated numerically for an arbitrary gravity model using Matlab tools in the SBDT. Further, this is a Hamiltonian system, and thus, the eigenvalues of  $\Phi$  after one period, or Floquet multipliers, must come in complex conjugate and inverse pairs. This means that for stability, the Floquet multipliers of the system must all lie on the unit circle in the complex plane. Multipliers with magnitude larger than unity imply instability. Previous work in Scheeres[8] gives the types of eigenvalues of the inertial hovering dynamics (Eq. (3.13)) as a function of hovering radius and latitude.

Without performing any calculations, one would expect that the system will have at least one unstable pair of multipliers corresponding to motion in roughly the radial direction. If there are some perturbations in this direction, the gravitational attraction the spacecraft feels will either increase or decrease in the same manner that the nominal thrust will be inaccurate, resulting in an unchecked acceleration. This observation is confirmed analytically in Scheeres[8] for a pointmass and the numerical results given for more general shapes all have at least one such hyperbolic unstable mode (or pair of eigenvalues).

In fact, for the pointmass gravity field, inertial hovering at all distances and latitudes has exactly one hyperbolic unstable mode and two stable oscillation modes[8]. So at a minimum, a controller is necessary to stabilize motion in the radial direction. The following results assume a controller that stabilizes radial motion (such as a dead-band thrust control) exists and focus on the character of the two remaining modes.

For the ellipsoidal shape case, the perturbation equations (Eq. (3.13)) have been numerically integrated for one period of motion and the eigenvalues of the state transition matrix have been determined for a range of hovering radii and latitudes. The initial longitude of the hovering position has no effect on the eigenvalues of the monodromy matrix, though it does effect the eigenvectors[8]. Integrations were performed using Matlab with a relative tolerance of  $10^{-8}$  ( $m$ ) and an absolute tolerance of  $10^{-11}$  ( $m$ ).

It was found that inertial-frame hovering dynamics, excluding the hyperbolic unstable mode in the radial direction, are stable at most radial distances and inclinations. The exception to this is a region near the resonance radius that extends around the body, forming a nearly-spherical shell of instability. The cross-hatched regions in

Figure 3.11 show the shape of this unstable region, which is axially symmetric about  $\hat{z}$ , for different rotation rates around an ellipsoidal body measuring  $15 \times 7 \times 6 \text{ km}$  with a density of  $2.3 \text{ g/cm}^3$ <sup>5</sup>. The resonance radius corresponding to each rotation rate is shown as a vertical dashed line. It can be seen that the region of instability moves

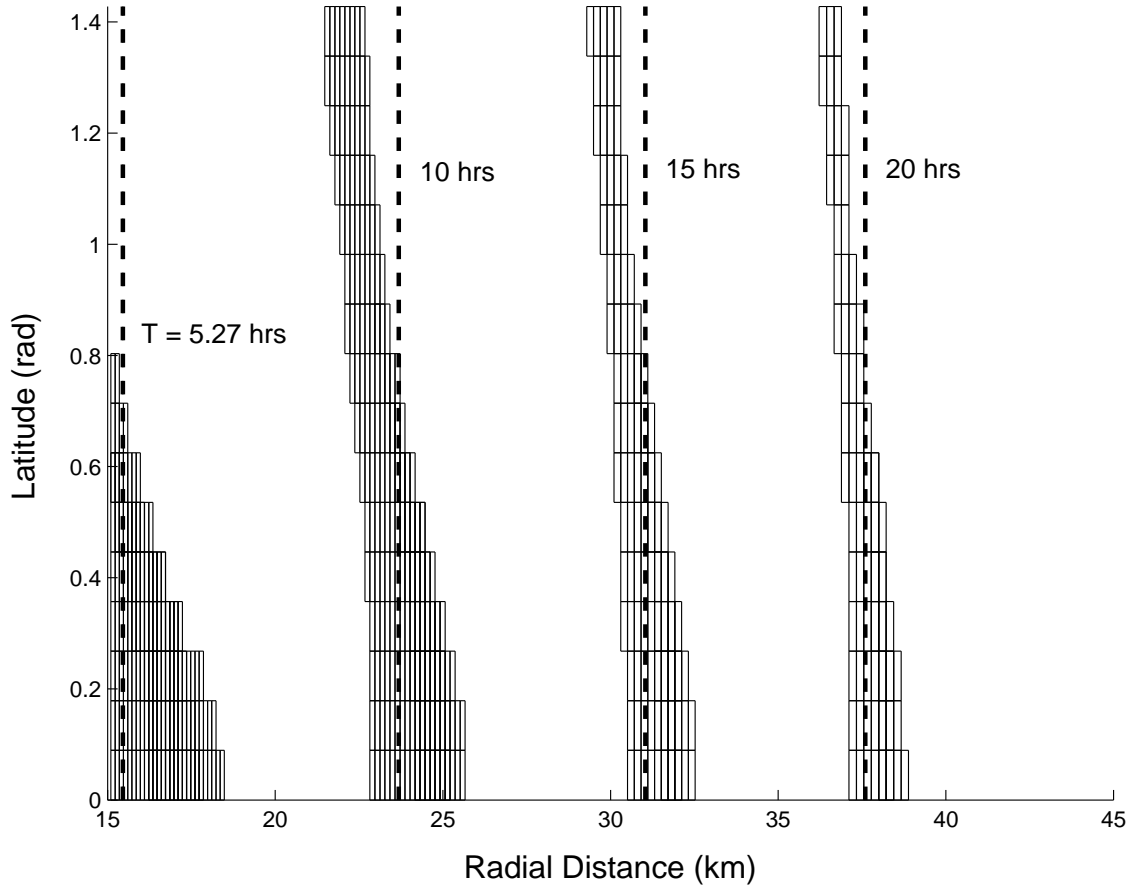


Figure 3.11: Regions of Instability for Inertial Hovering above a  $15 \times 7 \times 6$  Ellipsoid for Various Rotation Rates,  $T_{Eros} = 5.27 \text{ hrs}$

with the changing resonance radius (Eq. (2.16)), a function of rotation rate. As latitude of hovering increases, the radius of unstable hovering becomes smaller and the strength of the instability is marginally decreased. The range of radial distances

<sup>5</sup>These parameters roughly approximate the size and mass of asteroid Eros.

covered by the instability also decreases as the rotation rate decreases. Figure 3.12 shows the magnitude of the four transverse eigenvalues (corresponding to the two transverse directions in position space) versus radius in the equatorial plane for selected rotation rates. Again, the correlation between the primary instability and the resonance radius is clear. This figure also shows that the magnitude of the instability increases for faster rotation rates. Note that the magnitude of the instabilities that exist near the resonance radii is small, generally  $< 2$  except very near the small-body. Beyond the instability at the body's resonance radius, inertial hovering is found to be stable in all cases up to the point where the two-body assumptions break down and third-body effects of the sun become an issue. The qualitative properties of this ellipsoidal example are reflective of the other ellipsoidal shapes tested.

One may expect there to be instabilities near other harmonics of the rotation rate. The data suggests that relatively weak instabilities may exist inside the resonance radius at these secondary resonances. However, as the ratio of hovering radius to resonance radius decreases, the condition number of the state transition matrix that gives us the stability result increases exponentially. The secondary harmonic instabilities found for the ellipsoidal body case lie too far inside the resonance radius to be considered numerically accurate. Therefore, the stability of hovering well inside the resonance radius remains unknown. No secondary harmonics outside of the resonance radius, where the result is numerically tractable, were found in this study.

### **Numerical Support**

The analytical result for stability of inertial hovering described above is well supported in numerical simulations. For these simulations, constant density ellipsoidal shape and gravity models were used with an ideal dead-band control that restricted

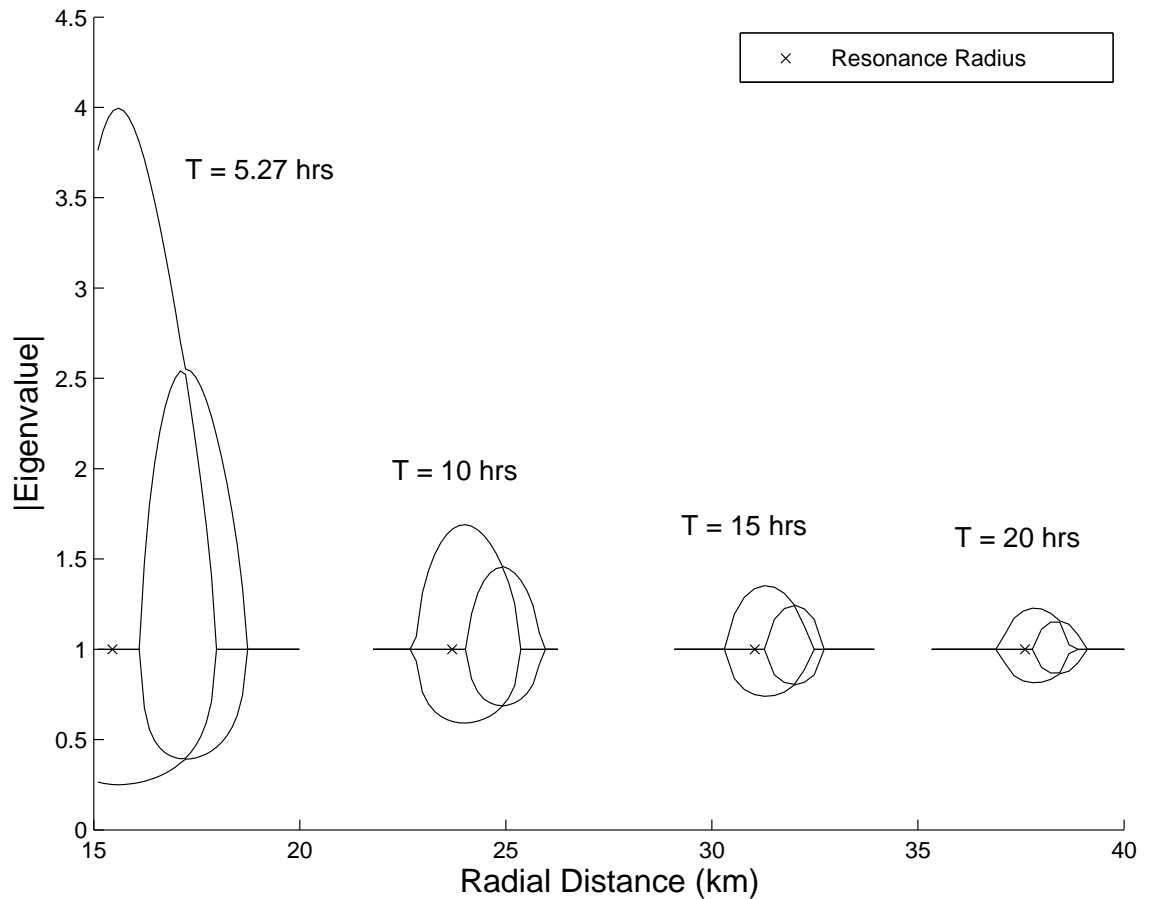


Figure 3.12: Magnitude of Floquet Multipliers for Inertial Hovering above a 15x7x6 Ellipsoid for Various Rotation Rates, Latitude =  $0^\circ$

motion to the plane passing through  $\tilde{\mathbf{r}}_0$  defined by the vectors  $\hat{\mathbf{z}}$  and  $\tilde{\mathbf{r}}_0 \times \hat{\mathbf{z}}$  in the small-body rotation pole (inertial) frame. The control direction was defined as being constant and parallel to the direction of the initial hovering point.

Because the control direction is constant and the dead-band control confines the motion of the spacecraft to a plane perpendicular to  $\tilde{\mathbf{r}}_0$ , all inertial hovering trajectories will ultimately have bounded time responses, assuming the thrusters have adequate authority to enforce the dead-band. That is, as the spacecraft moves far from the initial point, the gravitational attraction will increasingly pull the spacecraft back toward the nominal position. This phenomena is not apparent in the linearized

analysis, but is ultimately true in the full non-linear case. However, oscillations of this magnitude generally would not be acceptable during a mission to a small-body. For the purposes of analyzing the linearized result of the Section 3.4.2, let instability not be represented by unbounded motion, but by growth in the quasi-periodic oscillation of the spacecraft about the nominal point over time.

Using the same ellipsoidal shape model used in Figures 3.11 and 3.12 (15x7x6  $km$ ,  $\rho = 2.3 g/cm^3$ ), simulations of inertial hovering trajectories were performed at a range of radial distances in the equatorial plane. Figure 3.13 shows the maximum deviation from nominal in the  $\hat{y}$  direction (since in the equatorial plane,  $z \equiv 0$ ) for simulations of one to five small-body rotation periods. The primary feature of the previous results, instability near the resonance radius, is clearly shown for trajectories with a target radius near the resonance radius (23.7  $km$ ). Over time, the largest magnitude oscillations arise for the part of the unstable region closest to the body. Numerical simulation also confirms that the linear stability analysis for hovering outside the resonance radius produced accurate results; that is, inertial hovering is stable orbit over orbit at all radii beyond the resonance radius instability. Other simulations showed that the oscillations in position of the spacecraft in these regions were consistent over relatively long simulation times (35 days). Figure 3.13 also shows that in regions very near the body, oscillations from the nominal point were large in magnitude, though bounded in the long term. In general, the bound on the spacecraft's oscillations about the nominal point for stable hovering radii became larger as radius decreases.

Recall the analytical work did not yield insight into the stability of inertial hovering very near the body. These numerical results show inertial hovering to be non-linearly stable very near the body, but with large oscillations in position. There

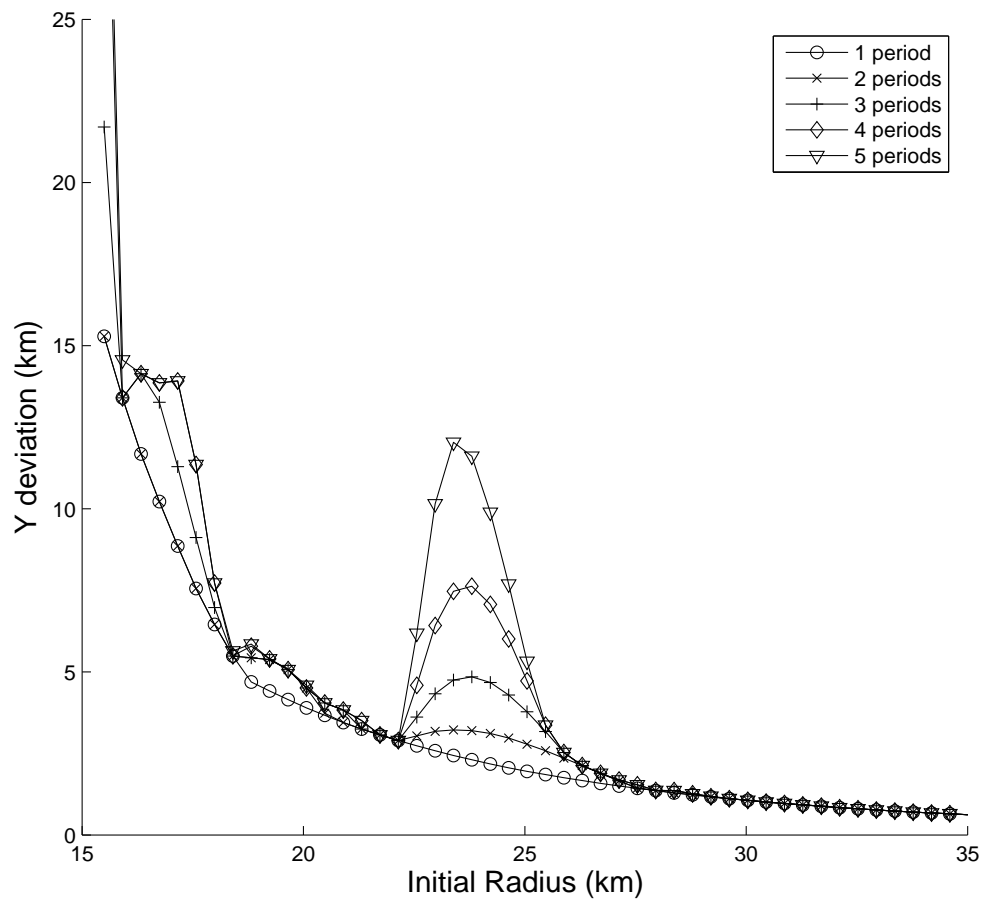


Figure 3.13: Deviation from Nominal for Inertial Hovering above a 15x7x6 Ellipsoid, Latitude =  $0^\circ$

is growth in the oscillation size between 15 and 20  $km$  period over period, which continues for longer simulation times. This may be attributable to a three circular orbits to two rotation period resonance at 18.1  $km$ .

### 3.5 Hovering above Asteroid 25143 Itokawa

On May 9, 2003, JAXA successfully launched the MUSES-C spacecraft, renamed Hayabusa after launch, toward asteroid (25143)Itokawa[59]. In this mission, the spacecraft eventually rendezvoused with the asteroid, spent some time inertial hov-

ering, then descended to the surface to attempt regolith sample collection for return to Earth. Because of the applicability of the work in this chapter to this mission, this section presents numerical stability results for a spacecraft hovering near Itokawa subject to the control strategies in this chapter. The simulations were conducted before Hayabusa’s rendezvous and use the system parameters available at that time. Simulations for both body-fixed and inertial hovering scenarios use the 6098–vertex polyhedral shape model of Itokawa developed by Ostro *et. al.*[35]. The body-fixed simulations assume a bulk density of  $2.3\text{g}/\text{cm}^3$  and rotation period of  $12.12\text{hrs}$ , while the inertial hovering simulations use updated estimates: a bulk density of  $2.5\text{g}/\text{cm}^3$  and a rotation period of  $12.132\text{hrs}$ . Improvements to both parameter sets were obtained from Hayabusa’s in-situ measurements[57].

### 3.5.1 Body-fixed Hovering

To verify that the qualitative results found for the ellipsoidal case apply to more realistic small-body shapes, simulations of body-fixed hovering above Itokawa subject to the two controllers discussed earlier (GDTS w/OL and IATNS) were performed with a  $\gamma$  of  $5\text{m}$ . The approach here was to use initial positions at a range of altitudes along various radial lines extending from the center of the body to test if the qualitative stability properties of body-fixed hovering above an ellipsoid applied to this polyhedral shape. Again, numerical stability is quantified by average maximum angular deviation over ten simulation runs with different initial velocity errors.

Recall that for ellipsoids, the GDTS w/OL controller agreed well with the analytical stability criteria of Sawai *et al.* in the  $X - Z$  and  $Y - Z$  planes. In the equatorial plane, numerically unstable regions were found above the body’s leading edge that satisfied the stability criteria and the numerically stable region was extended above

the trailing edge for shorter duration hovering. This asymmetry was attributed to an interaction between Coriolis forces and the dead-band thrust. It was suggested that these leading and trailing edge effects are present at all latitudes, weakening as the hovering position moves away from the equator. This analysis is supported by numerical simulations of GDTS w/OL hovering above Itokawa.

Figure 3.14 shows angular deviation versus radius for GDTS w/OL hovering at  $5^\circ$  latitude and  $45^\circ$  longitude (measured from the positive x axis), i.e., above the leading edge near the equatorial plane. The radii satisfying the analytical stability criteria are indicated with squares at the bottom of the plot. It can be seen that the average deviation starts to increase somewhat inside the region satisfying the sufficiency criteria for the 20000 second runs. For the 50000 second runs, the effect is more dramatic; destabilization occurs well inside the analytical stability limit and causes large deviations from the hovering position. These findings support the results found in the ellipsoidal analysis where leading edge performance was degraded by an interaction between Coriolis forces and the control thrust direction.

For the radial line extending at  $30^\circ$  latitude and  $45^\circ$  longitude, body-fixed hovering with the GDTS w/OL controller is found to behave largely in line with the stability criteria (Figure 3.15). There is a clearly visible increase in the average angular deviation at both 20000 and 50000 seconds when the initial radius moves beyond the region satisfying the stability criteria. As the initial radius approaches the limit of the analytically stable region, a slow increase in average deviation is found, which can be attributed to the weakened, out-of-plane, leading edge effect.

Simulations for the radial line at  $0^\circ$  latitude and  $-30^\circ$  longitude, i.e., off the trailing edge, show a region of stability extending well beyond the threshold suggested by the analytical stability criteria after 20000 seconds (Figure 3.16). In the 50000

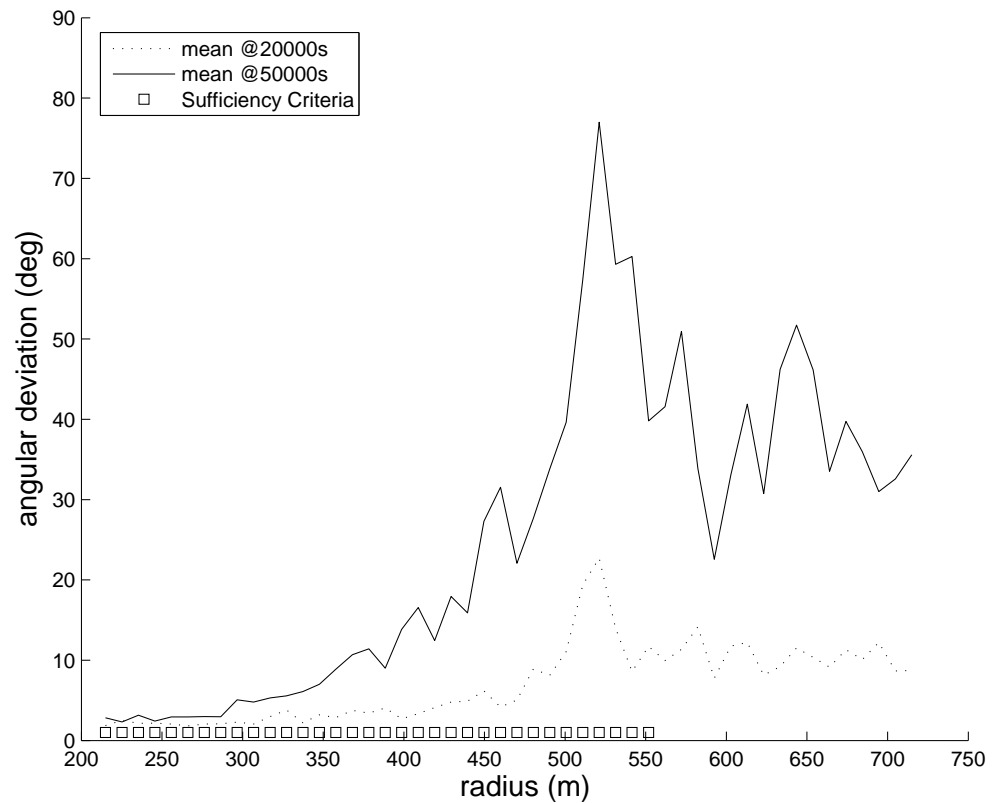


Figure 3.14: Angular Deviation of Body-Fixed Hovering above Asteroid (25143)Itokawa as a Function of Radius, GDTS w/OL Controller ( $5^\circ$  latitude,  $45^\circ$  longitude)

second case, the angular deviation begins to increase just inside the limit of the region of predicted stability. Beyond the analytical stability threshold, deviations are noticeably smaller than in the unstable regions of the other two cases.

Simulations of body-fixed hovering above Itokawa with the IATNS controller were also run. Again, the results were found to be in agreement with the findings in the ellipsoidal case. That is, the IATNS controller is consistently numerically stable for 20000 and 50000 second simulations in all directions in a region near the body extending almost to the analytical stability threshold. Beyond this point, the controller becomes very unstable. Figures 3.17, 3.18, and 3.19 show results

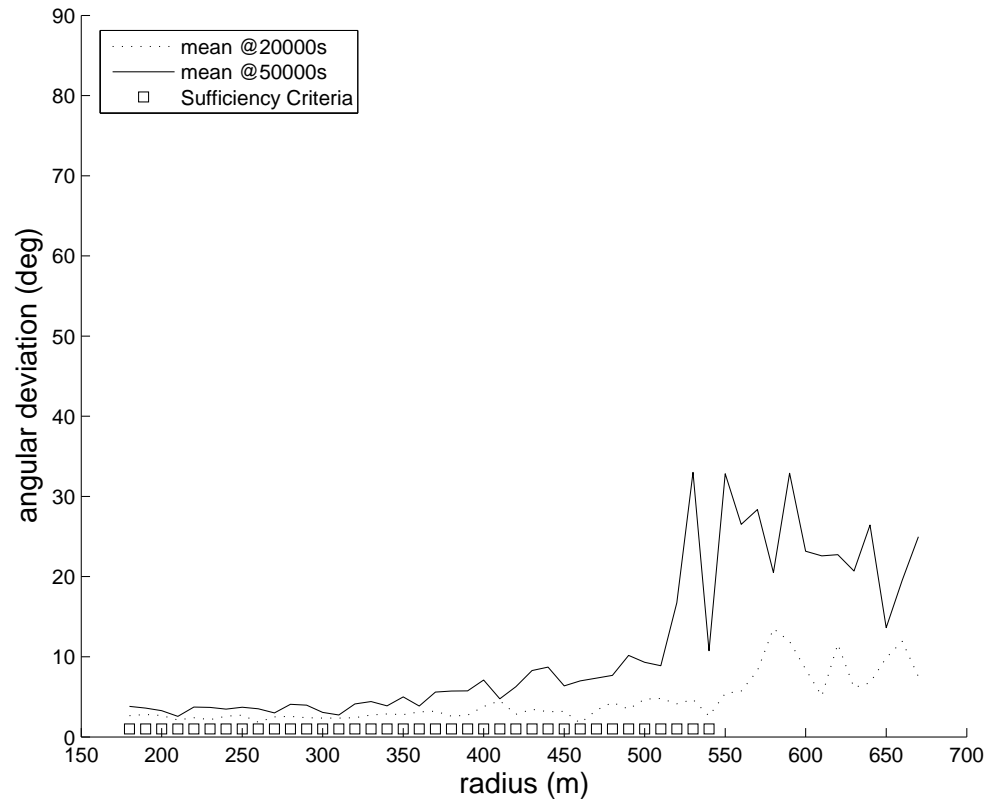


Figure 3.15: Angular Deviation of Body-Fixed Hovering above Asteroid (25143)Itokawa as a Function of Radius, GDTS w/OL Controller ( $30^\circ$  latitude,  $45^\circ$  longitude)

for the same three radial lines presented above for the GDTS w/OL controller for comparison.

### 3.5.2 Inertial-Frame Hovering

A large portion of the Hayabusa mission was dedicated to inertial hovering, during which instrumentation onboard the spacecraft was used to map the asteroid's surface. For this phase of the mission, Hayabusa implemented a controller consisting of three orthogonally-oriented position dead-band controllers to maintain spacecraft position[9]. This type of control effectively forms a 'box' in position space that

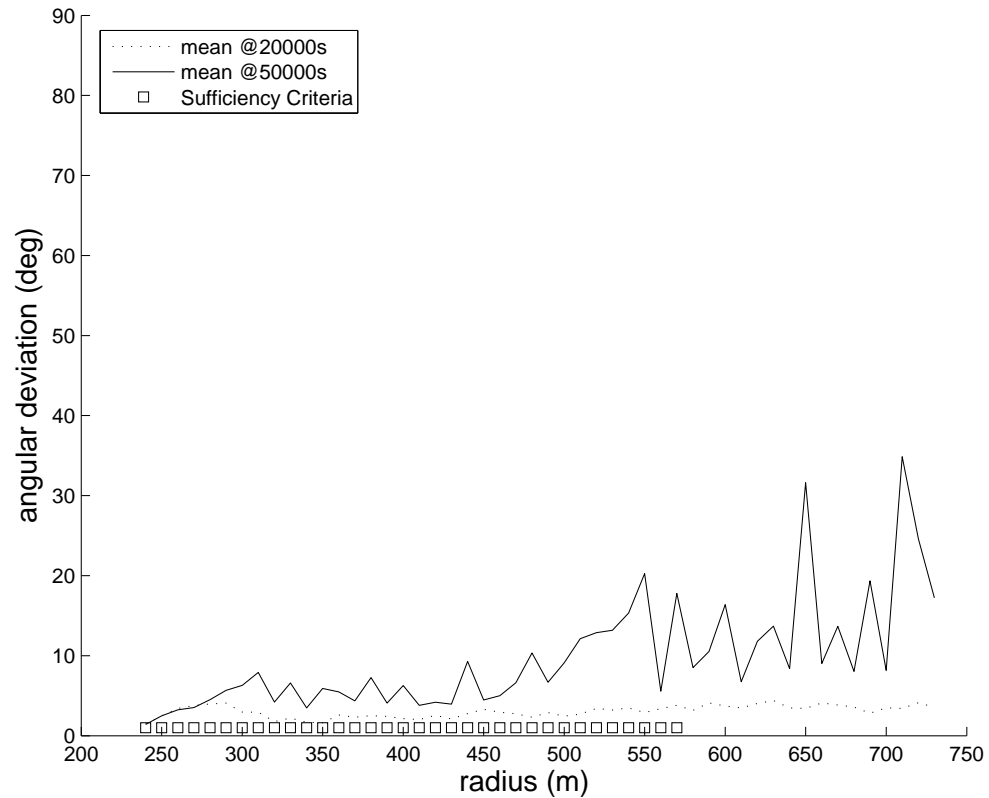


Figure 3.16: Angular Deviation of Body-Fixed Hovering above Asteroid (25143)Itokawa as a Function of Radius, GDTS w/OL Controller ( $0^\circ$  latitude,  $-30^\circ$  longitude)

contains the spacecraft's trajectory.

The analysis in Section 3.4.2 suggests that the spacecraft can maintain position in inertial space with only a single dimensional controller at altitudes outside the body's resonance radius. If this is the case, it could result in improved fuel efficiency and operational simplicity for this part of the Hayabusa mission. The plan at the time of this experiment was for the Hayabusa spacecraft to hover at an altitude of approximately 20 km over Itokawa[60], well outside the resonance radius. The results presented here predict that inertial hovering at this altitude is stable.

For this data to be as accurate (and useful) as possible, it was necessary to

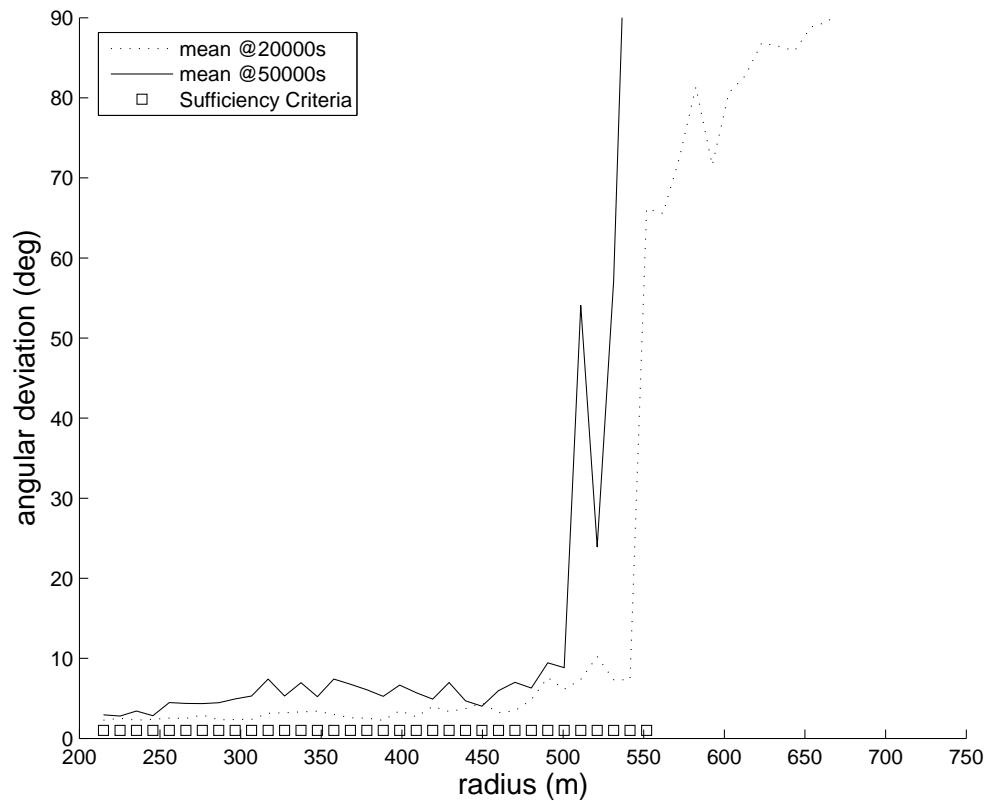


Figure 3.17: Angular Deviation of Body-Fixed Hovering above Asteroid (25143)Itokawa as a Function of Radius, IATNS Controller ( $5^\circ$  latitude,  $45^\circ$  longitude)

compute the appropriate latitude at which the spacecraft would be hovering. The plan was for the spacecraft to hover in the vicinity of the Earth-asteroid line for purposes of communication. Given the orbit of Itokawa and the appropriate mission data (Table 3.1), the Earth-asteroid line is calculated to move between  $14.8^\circ$  latitude upon the spacecraft's arrival and  $16.8^\circ$  at departure in the small-body fixed frame. This analysis is performed at  $15^\circ$  latitude.

Figure 3.20 shows the analytical stability results obtained by examining the eigenvalues of the state transition matrix after one period of inertial hovering at  $15^\circ$  latitude over Itokawa for a range of radial distances. As expected, the primary instability

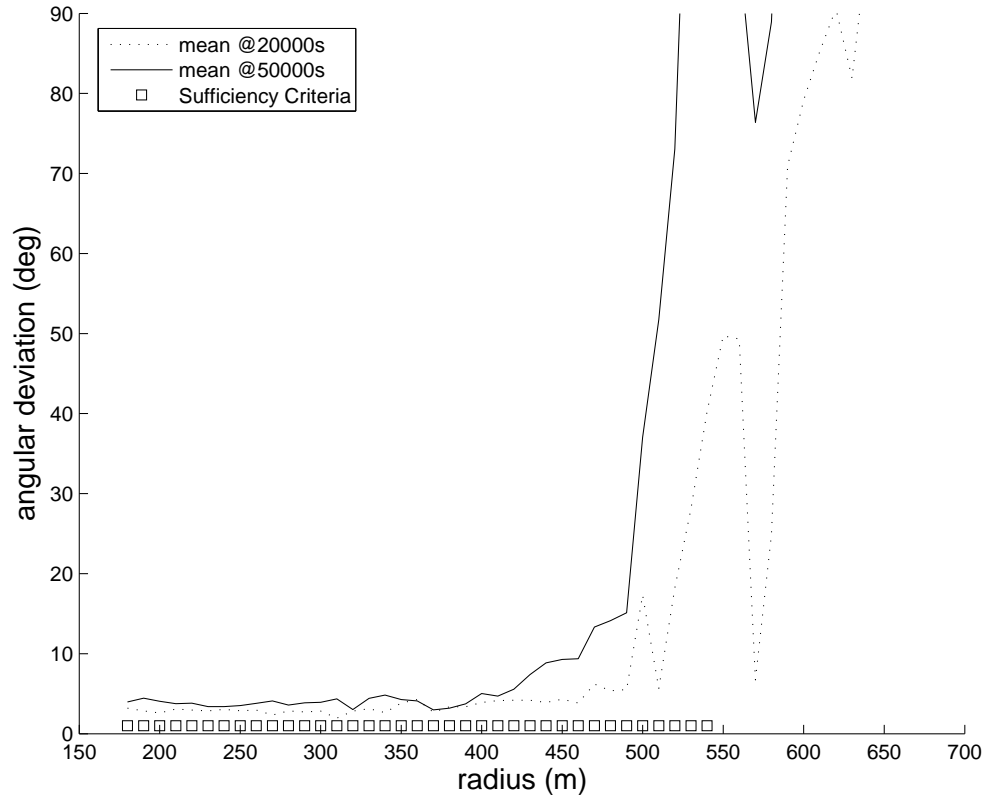


Figure 3.18: Angular Deviation of Body-Fixed Hovering above Asteroid (25143)Itokawa as a Function of Radius, IATNS Controller ( $30^\circ$  latitude,  $45^\circ$  longitude)

exists in the region near the body's resonance radius of  $579\text{ m}$ . Again, note that the magnitude of this instability is reasonably small. Interestingly, two secondary instabilities near  $450\text{ m}$  radius appear in this case. These results are numerically valid, as opposed to the secondary instabilities seen in the ellipsoidal case. However, without a more general result, it is difficult to say if these results validate the idea of secondary harmonic instabilities suggested in the ellipsoidal case or if they exist only due to a specific parameter of this model's shape. Beyond the resonance radius, all inertial hovering is stable. It is concluded that the Hayabusa mission plan to inertially hover at an altitude of  $20\text{ km}$  is safely within the region of stable inertial hovering subject

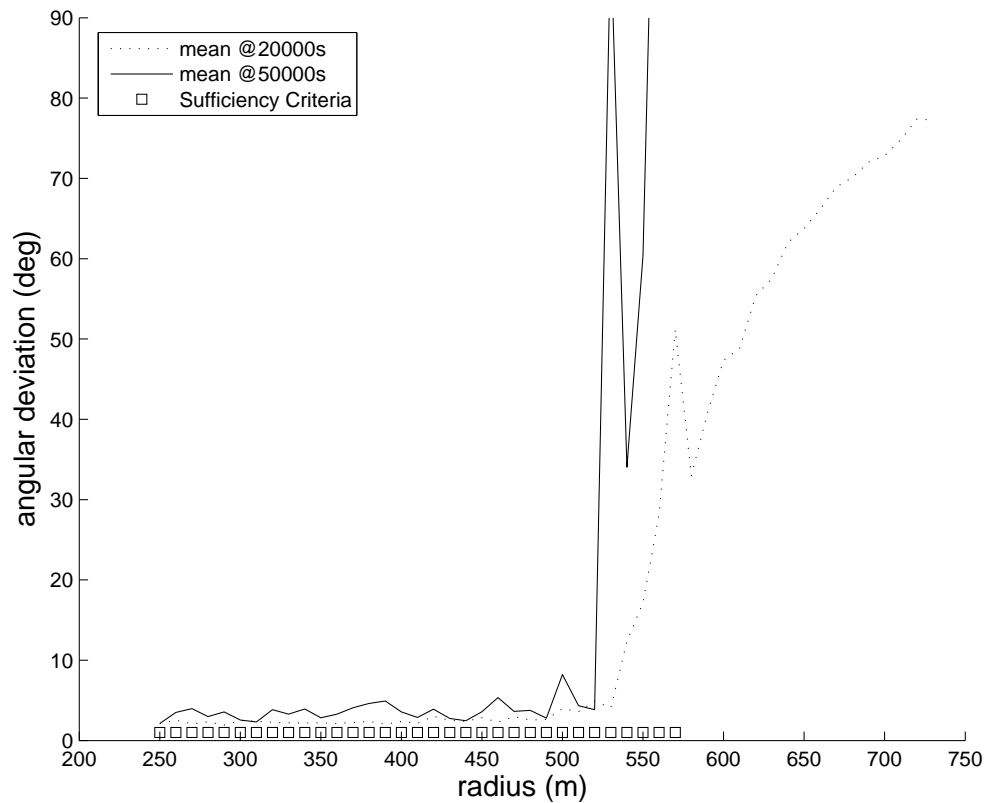


Figure 3.19: Angular Deviation of Body-Fixed Hovering above Asteroid (25143)Itokawa as a Function of Radius, IATNS Controller ( $0^\circ$  latitude,  $-30^\circ$  longitude)

to one-dimensional control when solar gravitation and solar radiation pressure are ignored. The effect of these perturbations is quite significant though and can be addressed using the Hill equations (Section 2.3.3) and the results of Chapter IV.

### 3.6 Discussion

In this chapter, body-fixed hovering subject to a combination of dead-band control on altitude and open-loop control was numerically simulated with the HoverSim software. This simulation capability is fundamental here and for the work on hovering in the next two chapters. Using this capability, we were able to compare the

Orbital inclination	1.728°
Long. of ascending node	70.921°
Orbital eccentricity	0.280
Orbital period	1.521 Julian yrs
Periapsis passage	2001-May-4.601
Argument of periapsis	161.029°
Orbital semi-major axis	1.323 AU
Rotation period	12.132 hrs[35]
Rotation pole	355°, -84°[61]
Hayabusa time of arrival (s/c)	6-15-05
Hayabusa time of departure (s/c)	11-2-05

Table 3.1: Asteroid (25143)Itokawa and Hayabusa Mission Parameters[1][2]

analytical stability results of Sawai *et al.* for idealized dead-band hovering to numerical simulation data under a realistic dead-band implementation (GDTS w/OL). The results were mixed. The one-dimensional control technique is shown to be quite plausible by the simulations and the stability criteria correspond well with the actual spacecraft motion in the  $X - Z$  and  $Y - Z$  planes. But the assumptions in the analytical theory restrict the effect of the Coriolis forces on the dynamics, which turns out to poorly model motion across a finite dead-band. We found that without the assumption of infinitely-tight dead-band control, Coriolis accelerations destabilize hovering above the leading edges of ellipsoidal small-bodies in the equatorial plane with weakening effect up to the polar planes. This is an important observation for body-fixed hovering with dead-band control which came as a result of our numerical simulation capability. The alternative IATNS control demonstrates that this Coriolis effect can be reduced by decreasing the magnitude of  $\theta$ . As mentioned previously,  $\theta$  would be positive at all hovering points in an ideal implementation.

We found inertial hovering above an ellipsoidal body to be linearly stable (not including the (roughly) radial direction which is always unstable) at most latitudes

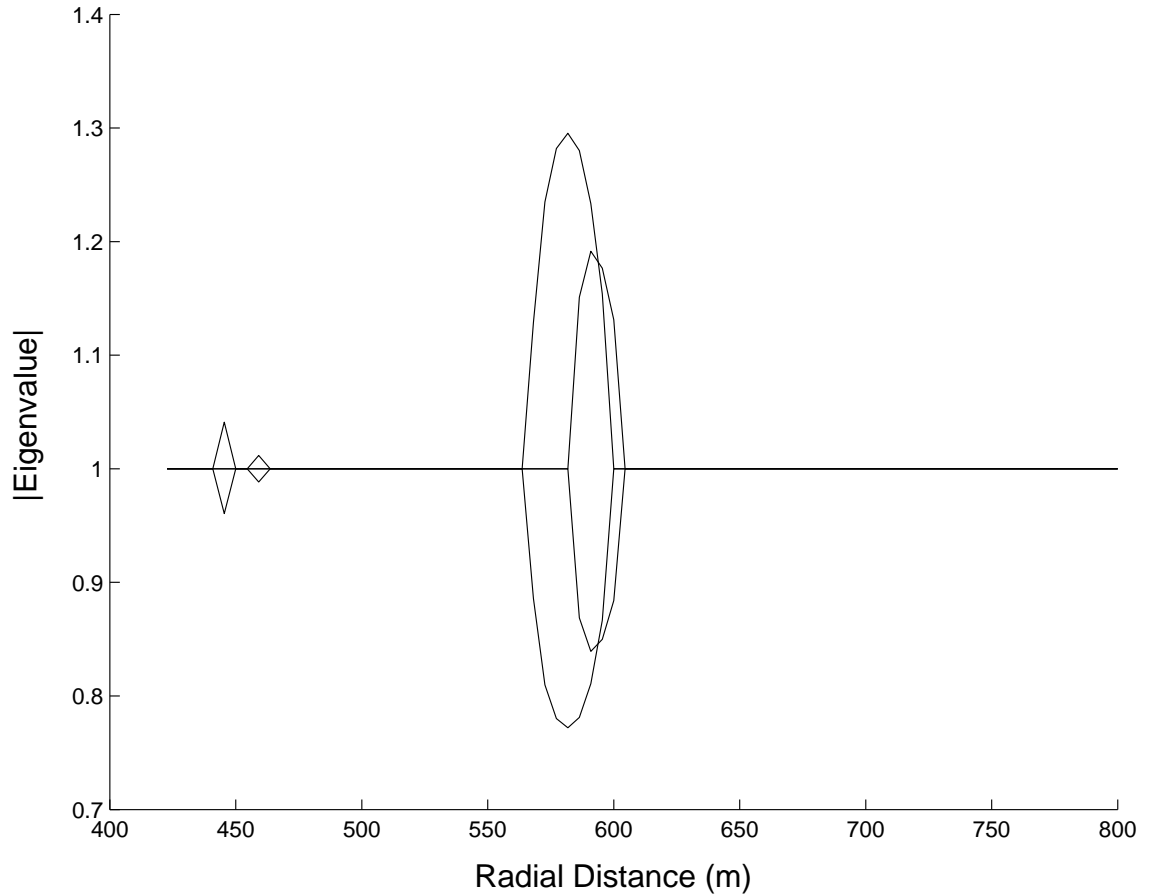


Figure 3.20: Magnitude of Floquet Multipliers for Inertial Hovering above Asteroid (25143)Itokawa,  $15^\circ$  Latitude

and radial distances. The exceptions were in a ‘shell’ of unstable hovering positions around the small-body at a distance near the body’s resonance radius. This was the first work to look at the strength of this instability, which is strongest in the equatorial plane and strengthens with increasing rotation rates. In most cases, however, the strength of this instability remains mild and it would likely be possible for a spacecraft to safely move across the region under hovering control. This was also the first work to numerically simulate inertial hovering and we found the theoretical results were supported very well. These numerical results seemed to confirm the existence of secondary resonances close to the body which could not be determined definitively

in the linear analysis. They also showed that though many positions close to the body are linearly stable, the oscillations in position can be quite large.

The simulations of body-fixed and inertial hovering above asteroid Itokawa were interesting case-studies for a current mission, but they also served another purpose. The results suggest that the qualitative properties of the findings for body-fixed hovering above ellipsoidal bodies (for both the GDTS w/OL and IATNS controllers) can be extended to hovering over real small-body shapes. This makes sense actually since for the purpose of computing initial accelerations and gravity gradients, a dipole gravity field (such as a constant density ellipsoid) will approximate these quantities very well for arbitrary shapes if the evaluation points are sufficiently far from the surface. The other half of the control is defined by surface topography, which can be quite arbitrary, but in some average sense, the qualitative results of the ellipsoid simulations will hold.

## CHAPTER IV

# Zero-velocity Surfaces and Hovering

This chapter furthers the work on hovering with an analytical result for boundedness of hovering that applies for any conservative system, including the two-body problem, circular restricted three-body problem, and the Hill three-body problem. Using the existence of a Jacobi constant in these systems, the zero-velocity surface is defined for a hovering spacecraft. With knowledge of the zero-velocity surface, dead-band control can be designed appropriately so that the hovering trajectory is energetically bounded. Sections of this chapter address this result in the context of initial state uncertainties, define the zero-velocity surface type as a function of position for different applications, and look at how the result can be extended to non-conservative systems.

The majority of the results presented in this chapter can also be found in Broschart and Scheeres[62].

### 4.1 Zero-velocity Surface Result for Conservative Systems

The equations of motion for a spacecraft in a uniformly rotating coordinate frame subject to accelerations derived from a potential function  $V$  and a constant thrust

(in the rotating frame) can be written in the form of Eq. (4.1),

$$\ddot{\tilde{\mathbf{r}}} + 2(\tilde{\boldsymbol{\Omega}} \times \dot{\tilde{\mathbf{r}}}) = \frac{\partial V(\tilde{\mathbf{r}}, t)^T}{\partial \tilde{\mathbf{r}}} + \tilde{\mathbf{T}} \quad (4.1)$$

where the angular velocity of the reference frame with respect to inertial space,  $\tilde{\boldsymbol{\Omega}}$ , is assumed to be constant. In this form, the centrifugal acceleration term,  $-\tilde{\boldsymbol{\Omega}} \times \tilde{\boldsymbol{\Omega}} \times \tilde{\mathbf{r}}$ , is derived from the potential function  $V$ . The two-body problem in the small-body fixed frame (Section 2.3.1), the circular restricted three-body problem (Section 2.3.2), and the Hill three-body problem (Section 2.3.3) can be written in the form of Eq. (4.1). If both sides of Eq. (4.1) are multiplied by  $\dot{\tilde{\mathbf{r}}}$ ,

$$\frac{d}{dt} \left[ \frac{1}{2} \dot{\tilde{\mathbf{r}}}^T \dot{\tilde{\mathbf{r}}} - V(\tilde{\mathbf{r}}, t) - \tilde{\mathbf{T}}^T \tilde{\mathbf{r}} \right] = -\frac{\partial V}{\partial t}. \quad (4.2)$$

If the reference frame is chosen such that  $V$  is not an explicit function of time (i.e.,  $\partial V/\partial t = 0$ ), then Eq. (4.3) defines the general Jacobi constant form for a conservative system.

$$J(\tilde{\mathbf{r}}, \dot{\tilde{\mathbf{r}}}) = \frac{1}{2} \dot{\tilde{\mathbf{r}}}^T \dot{\tilde{\mathbf{r}}} - V(\tilde{\mathbf{r}}) - \tilde{\mathbf{T}}^T \tilde{\mathbf{r}} \quad (4.3)$$

Eq. (4.3) maintains its value for the duration of any trajectory following the equations of motion (Eq. (4.1)).

If the thrust is chosen such that  $\tilde{\mathbf{T}} = -\partial V(\tilde{\mathbf{r}})/\partial \tilde{\mathbf{r}}|_{\tilde{\mathbf{r}}_0}^T$ , then the right hand side of Eq. (4.1) equals zero at  $\tilde{\mathbf{r}}_0$ . If  $\dot{\tilde{\mathbf{r}}}$  is also zero, then  $\tilde{\mathbf{r}}_0$  is an equilibrium point. This is precisely the approach that is used in spacecraft hovering under open-loop thrust control.

For a trajectory initialized at an equilibrium state  $(\tilde{\mathbf{r}}, \dot{\tilde{\mathbf{r}}}) = (\tilde{\mathbf{r}}_0, \mathbf{0}_{3x1})$ , all states on a valid trajectory must satisfy Eq. (4.4).

$$J(\tilde{\mathbf{r}}, \dot{\tilde{\mathbf{r}}}) = J(\tilde{\mathbf{r}}_0, \mathbf{0}_{3x1}) = C_0, \quad \forall t \quad (4.4)$$

Expand the left-hand side in a Taylor series in position and velocity deviations from the equilibrium state to second order to obtain the condition in Eq. (4.5) on allowable states in the vicinity of the equilibrium,

$$\delta\tilde{\mathbf{r}}^T \frac{\partial^2 J}{\partial\tilde{\mathbf{r}}^2} \Big|_{(\tilde{\mathbf{r}}_0, \mathbf{0}_{3x1})} \delta\tilde{\mathbf{r}} = -\delta\dot{\tilde{\mathbf{r}}}^T \delta\dot{\tilde{\mathbf{r}}} \leq 0 \quad (4.5)$$

where  $\delta\tilde{\mathbf{r}} = \tilde{\mathbf{r}}(t) - \tilde{\mathbf{r}}_0$  and  $\delta\dot{\tilde{\mathbf{r}}} = \dot{\tilde{\mathbf{r}}}(t)$ . Note that  $\partial J/\partial\tilde{\mathbf{r}}|_{(\tilde{\mathbf{r}}_0, \mathbf{0}_{3x1})} = \partial J/\partial\dot{\tilde{\mathbf{r}}}|_{(\tilde{\mathbf{r}}_0, \mathbf{0}_{3x1})} = \mathbf{0}_{1x3}$  at an equilibrium point. It is clear that for real values of  $\delta\dot{\tilde{\mathbf{r}}}$ , the right hand side must be less than or equal to zero. The inequality in Eq. (4.5) defines the local region of allowable motion in position space of the system. The boundary of this region (Eq. (4.6)) defines a quadratic ‘zero-velocity surface’ as a function of  $\delta\tilde{\mathbf{r}}$  that cannot be crossed by a real-valued system.

$$\delta\tilde{\mathbf{r}}^T \frac{\partial^2 J}{\partial\tilde{\mathbf{r}}^2} \Big|_{(\tilde{\mathbf{r}}_0, \mathbf{0}_{3x1})} \delta\tilde{\mathbf{r}} = 0 \quad (4.6)$$

This result for the zero-velocity surface near equilibrium is general and applies to any time-invariant conservative Lagrangian system. A more general formulation is given in Appendix E.

Let the eigenvalues of the matrix  $\partial^2 J/\partial\tilde{\mathbf{r}}^2|_{(\tilde{\mathbf{r}}_0, \mathbf{0}_{3x1})}$  be  $\beta_1$ ,  $\beta_2$ , and  $\beta_3$  (such that  $\beta_1 > \beta_2 > \beta_3$ ) with corresponding eigenvectors  $\hat{v}_1$ ,  $\hat{v}_2$ , and  $\hat{v}_3$ . Depending on the signs of these eigenvalues, this local boundary has one of the quadratic shapes described in Table 4.1 and shown in Figure 4.1.

Sign of Eigenvalues	Zero-Velocity Surface	$\ \dot{\tilde{\mathbf{r}}}\  > 0$ Surface
+,+,+	Imaginary Quadratic Cone	Imaginary Ellipsoid
+,+,-	Real Quadratic Cone	Two-Sheet Hyperboloid
+,-,-	Real Quadratic Cone	One-Sheet Hyperboloid
-,,-,-	Imaginary Quadratic Cone	Real Ellipsoid

Table 4.1: Shape of the Nominal Local Zero-Velocity Surface for Hovering[3]

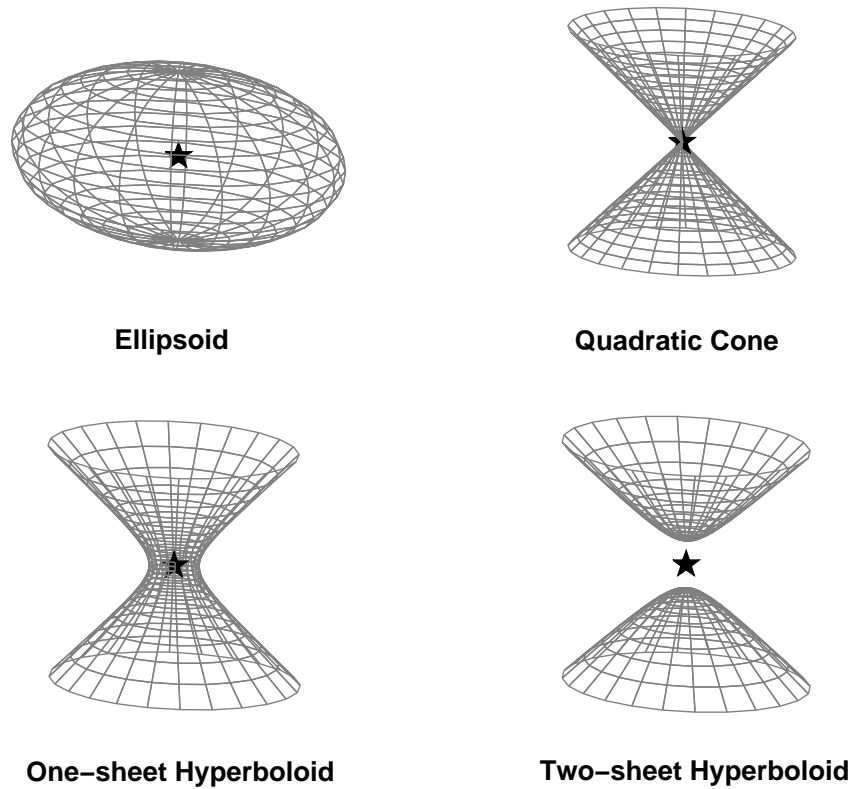


Figure 4.1: Quadratic Zero-velocity Boundaries

In simple terms, Table 4.1 means the following. If all three eigenvalues are negative, then there are no local restrictions on where the spacecraft can go, as all (real) displacements from nominal result in a negative left hand side of Eq. (4.5). Conversely, if all eigenvalues are positive, then no (real) displacements from the nominal state are permitted. For both of the mixed eigenvalue cases, the zero-velocity surface is a real quadratic cone in  $\delta\tilde{\mathbf{r}}$  where the two bounding cones touch at the equilibrium point. For a real  $\delta\dot{\tilde{\mathbf{r}}}$ , motion is restricted to hyperboloid surfaces on the outside of these cones in the  $+, -, -$  case and on the inside of the cones for the  $+, +, -$  case. The shaded regions in Fig. 4.2 illustrate the allowable region of motion for each case in two dimensions. Each shaded contour represents allowable positions for some

$$\|\dot{\mathbf{r}}\| \geq 0.$$

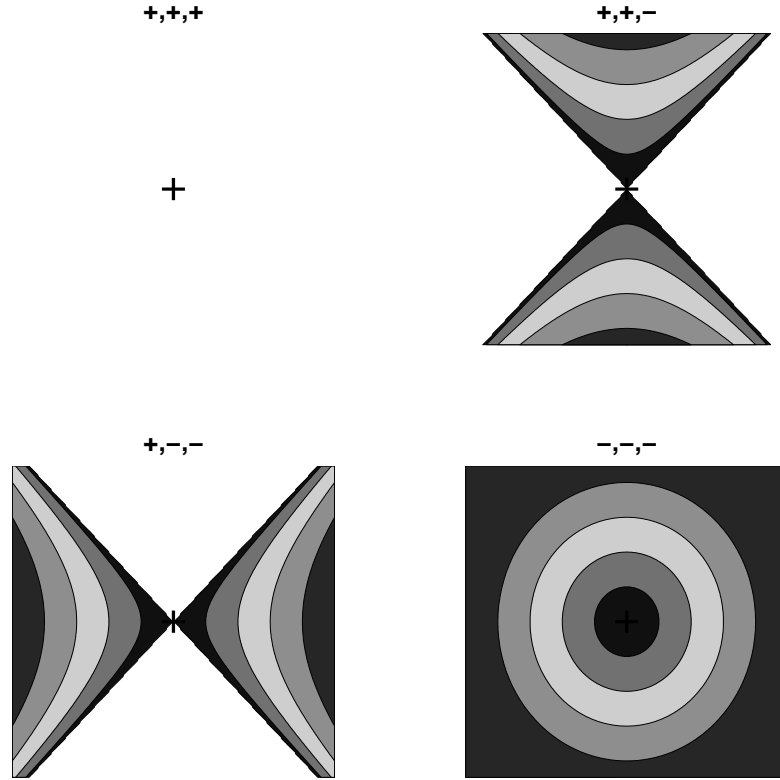


Figure 4.2: Allowable Regions of Motion for Different Eigenvalue Sets (shaded regions), Each Contour Represents Allowable Positions for some Non-negative Velocity Magnitude

## 4.2 Zero-velocity Surfaces and Dead-band Hovering Control

The existence and geometry of the different zero-velocity surfaces induced by an open-loop hovering thrust control (Eq. (4.7)) suggest a dead-band controller (Eq. (3.5)) may be appropriate for controlling perturbations from the nominal position.

$$\tilde{\mathbf{T}}_{OL} = - \left. \frac{\partial V}{\partial \tilde{\mathbf{r}}} \right|_{(\tilde{\mathbf{r}}_0, \mathbf{0}_{3 \times 1})}^T \quad (4.7)$$

It can be shown that the dynamics of spacecraft operating under a combination of open-loop and dead-band thrust controls maintain their conservative property and

thus, the zero-velocity surface bound on motion. It will be shown that the combination of the energetic zero-velocity surface restriction and the restriction induced by the dead-band can be used to bound the spacecraft motion for all time.

For a dead-band controller (Eq. (3.5)), if  $T_m$  is sufficiently large, the small acceleration derived from  $V(\tilde{\mathbf{r}})$  can be ignored when the spacecraft is outside the dead-band (when  $f_{db}(\tilde{\mathbf{r}}) \geq \gamma$ ). Such a large thrust assumption is reasonable for operation near small-bodies and typically used for spacecraft applications. This assumption allows a closed form solution for the  $\Delta V$  applied to the spacecraft between subsequent dead-band crossings as a function of incoming velocity. If the dead-band thrust direction is normal to the dead-band boundary ( $\hat{\mathbf{c}}(\tilde{\mathbf{r}}) = \nabla \hat{f}_{db}(\tilde{\mathbf{r}})$ ), the form of the dead-band thrust component in Eq. (4.8) is obtained.

$$\tilde{\mathbf{T}}_{DB} = - \left[ \left( 2\dot{\tilde{\mathbf{r}}}^T \nabla \hat{f}_{db}(\tilde{\mathbf{r}}) \right) \nabla \hat{f}_{db}(\tilde{\mathbf{r}}) \right] \delta(f_{db}(\tilde{\mathbf{r}}) - \gamma) \quad (4.8)$$

The dead-band function  $f_{db}$  can be chosen to constrain the spacecraft motion in an arbitrary number of directions. The following examples of the function  $f_{db}$  would restrict spacecraft motion in one (Eq. (4.9)), two (Eq. (4.10)), or three (Eq. (4.11)) dimensions.

$$f_{db}(\tilde{\mathbf{r}}) = \left| (\tilde{\mathbf{r}} - \tilde{\mathbf{r}}_0)^T \hat{\mathbf{v}}_c \right| \quad (4.9)$$

$$f_{db}(\tilde{\mathbf{r}}) = \left\| (I - \hat{\mathbf{v}}_c \hat{\mathbf{v}}_c^T) (\tilde{\mathbf{r}} - \tilde{\mathbf{r}}_0) \right\| \quad (4.10)$$

$$f_{db}(\tilde{\mathbf{r}}) = \left\| (\tilde{\mathbf{r}} - \tilde{\mathbf{r}}_0) \right\| \quad (4.11)$$

Level sets for each of these examples are shown in Figure 4.3.  $f_{db}$  can be formulated an infinite number of ways to create the desired dead-band boundary using whatever state estimates or measurements are available; Eq. (3.6) is an example using altimetry measurements. The function should be smooth at the boundary  $f_{db}(\tilde{\mathbf{r}}) = \gamma$  so that  $\nabla f_{db}$  is well-defined.

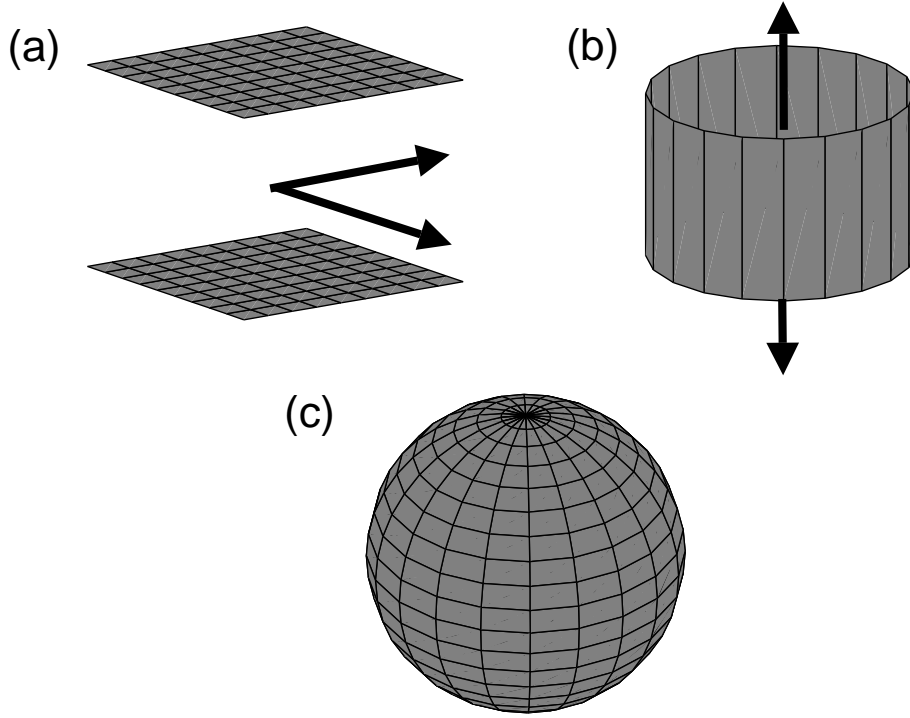


Figure 4.3: Level Sets of Example Dead-band Functions ((a) 1-D Dead-band, (b) 2-D Dead-band, (c) 3-D Dead-band), Arrows Indicate Direction of Unrestricted Motion

#### 4.2.1 Conservation of the Jacobi Constant under Dead-band Thrust Control

The formulation for the Jacobi constant (Eq. (4.3)) already allows for a constant thrust, so the conservative properties of this system are not violated for the  $\tilde{\mathbf{T}}_{OL}$  component of the hovering control. It is easily shown that the same Jacobi constant is preserved in the presence of the idealized dead-band thrust  $\tilde{\mathbf{T}}_{DB}$  (Eq. (4.8)) as well. This impulsive thrust “reflects” the velocity vector of the spacecraft off the boundary  $f_{db}(\tilde{\mathbf{r}}) = \gamma$  such that

$$\dot{\tilde{\mathbf{r}}}_+ = \dot{\tilde{\mathbf{r}}}_- - 2 \left( \dot{\tilde{\mathbf{r}}}_-^T \hat{\mathbf{c}} \right) \hat{\mathbf{c}}. \quad (4.12)$$

It is easily shown that the magnitude of the velocities before and after the burn are equal. Since the Jacobi constant depends only on the magnitude of  $\dot{\mathbf{r}}$ , the addition of the impulsive control thrust  $\tilde{\mathbf{T}}_{DB}$  does not destroy the conservative nature of this class of dynamical systems.

Figure 4.4 shows the Jacobi constant as a function of time for a typical simulated trajectory under one-dimensional dead-band control with a finite  $T_m$  in the two-body problem. The magnitude of  $T_m$  was approximately 90 times that of the acceleration due to  $V$  in this case. It can be seen that the Jacobi constant is indeed well preserved over time under dead-band control. The instantaneous spikes in the Jacobi constant correspond to the times when the dead-band thrust is active (when the spacecraft is outside the dead-band).

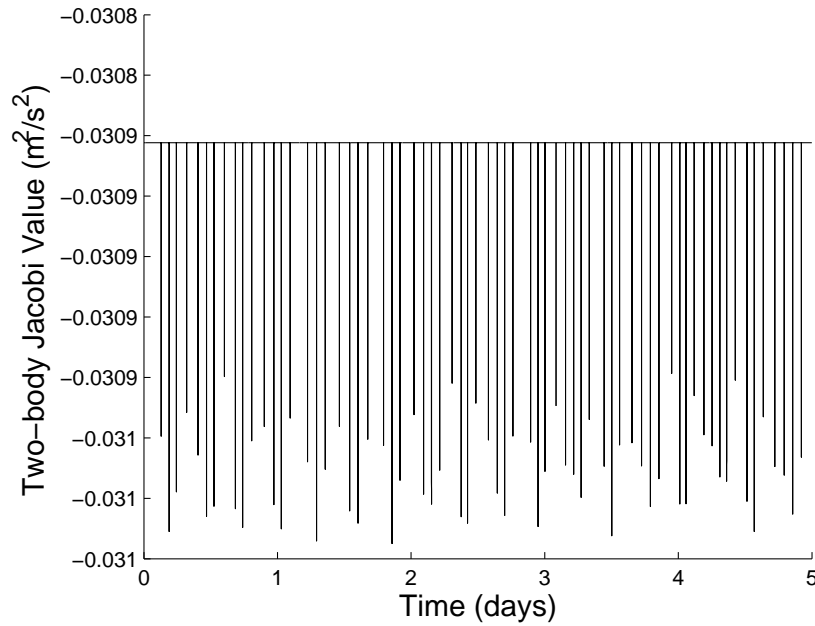


Figure 4.4: Jacobi Constant versus Time for a Simulated Trajectory under Dead-band Control

### 4.2.2 Dead-band Hovering Controller Design in Conservative Systems

Since dead-band hovering control does not destroy the Jacobi constant of the system, knowledge of zero-velocity surfaces (Eq. (4.6) and Table 4.1) can be applied to design a controller that ensures boundedness of a hovering trajectory for all time. The idea is to use dead-band thrust to control motion in the directions not naturally restricted by the zero-velocity surface. The general rule for hovering dead-band design is that the chosen controller must restrict motion in at least as many dimensions as the zero-velocity surface allows unrestricted motion and be oriented such that the spacecraft trajectory is trapped inside a bounded region defined by the zero-velocity surface and the dead band surface (where  $f_{ab} = \gamma$ ).

For instance, say hovering is implemented at a position where the Hessian matrix of the Jacobi constant with respect to position has one negative and two positive eigenvalues (+,+,- case). Then if a one-dimensional dead-band control of the form in Eq. (4.9) is implemented such that  $\hat{\mathbf{v}}_c$  is sufficiently close to the eigenvector  $\hat{\mathbf{v}}_3$  (assumed to point away from the small-body), the spacecraft trajectory is known to be bounded for all future time. Geometrically, the +,+,- zero-velocity surface defines a quadratic cone that restricts the spacecraft motion in two dimensions and the dead-band control defines two bounding planes that place “caps” on these cones. This creates a three-dimensional hourglass shaped region of space to which the spacecraft is energetically restricted. Similarly in the +,-,- case, where the zero-velocity surface restricts motion in one dimension, a two-dimensional dead-band control, such as Eq. (4.10) with  $\hat{\mathbf{v}}_c$  adequately close to the eigenvector  $\hat{\mathbf{v}}_1$ , is sufficient to bound the nominal trajectory in three dimensions. In the -,-,- case, a dead-band control that bounds the trajectory in three dimensions, such as Eq. (4.11), would be necessary. Motion near equilibrium in the +,+,+ case is stable without any control, but

generally does not occur at practical positions in astrodynamics systems.

### 4.3 Effects of Uncertainty on Zero-Velocity Surfaces

Of course this idea works for the nominal system since there is no motion away from the equilibrium anyway. The following sections show that this idea remains valid when uncertainties in the initial state and thrust are considered.

#### 4.3.1 Local Result

First, the effects of small errors in the initial state and control thrust on our localized zero-velocity surface result are determined. The zero-velocity surface for hovering with small perturbations in initial position and velocity is defined via a Taylor expansion. In this way, the true value of the Jacobi constant can be approximated to second order as in Eq. (4.13).

$$J\left(\tilde{\mathbf{r}}_0 + \delta\tilde{\mathbf{r}}_0, \delta\dot{\tilde{\mathbf{r}}}_0\right) = C^* \approx C_0 + \frac{1}{2}\delta\tilde{\mathbf{r}}_0^T \frac{\partial^2 J}{\partial \tilde{\mathbf{r}}^2} \Bigg|_{(\tilde{\mathbf{r}}_0, \mathbf{0}_{3x1})} \delta\tilde{\mathbf{r}}_0 + \frac{1}{2}\delta\dot{\tilde{\mathbf{r}}}_0^T \delta\dot{\tilde{\mathbf{r}}}_0 \quad (4.13)$$

Note that the true perturbation in  $J$  due to  $\delta\dot{\tilde{\mathbf{r}}}_0$  is quadratic and therefore, Eq. (4.13) is not approximate for perturbations in velocity. For dynamically valid future motion,

$$J\left(\tilde{\mathbf{r}}_0 + \delta\tilde{\mathbf{r}}, \delta\dot{\tilde{\mathbf{r}}}\right) = J\left(\tilde{\mathbf{r}}_0 + \delta\tilde{\mathbf{r}}_0, \delta\dot{\tilde{\mathbf{r}}}_0\right) = C^* \quad (4.14)$$

and thus,

$$\delta\tilde{\mathbf{r}}^T \frac{\partial^2 J}{\partial \tilde{\mathbf{r}}^2} \Bigg|_{(\tilde{\mathbf{r}}_0, \mathbf{0}_{3x1})} \delta\tilde{\mathbf{r}} \approx -\delta\dot{\tilde{\mathbf{r}}}_0^T \delta\dot{\tilde{\mathbf{r}}}_0 + 2(C^* - C_0). \quad (4.15)$$

The zero-velocity surface for the system under small-perturbations is defined in Eq. (4.16).

$$\delta\tilde{\mathbf{r}}^T \frac{\partial^2 J}{\partial \tilde{\mathbf{r}}^2} \Bigg|_{(\tilde{\mathbf{r}}_0, \mathbf{0}_{3x1})} \delta\tilde{\mathbf{r}} = 2(C^* - C_0) = \Delta Z \quad (4.16)$$

In general, the quantity  $\Delta Z$  can be positive or negative. The shape of the perturbed zero-velocity surface for all eigenvalue cases is given in Table 4.2. See Figure 4.1 for illustration.

Sign of Eigenvalues	$\Delta Z > 0$	$\Delta Z < 0$
+,+,+	Real Ellipsoid	N/A
+,+,-	One-Sheet Hyperboloid	Two-Sheet Hyperboloid
+,-,-	Two-Sheet Hyperboloid	One-Sheet Hyperboloid
-,-,-	Imaginary Ellipsoid	Real Ellipsoid

Table 4.2: Shape of the Perturbed Zero-velocity Surface[3]

In all eigenvalue cases, the number of dimensions restricted by the zero-velocity surface and its orientation (eigenvectors) is not changed by small perturbations in initial state. This means that a dead-band control that bounds the nominal trajectory still has the dimensionality and the proper orientation to bound the perturbed trajectory (assuming small perturbations). For instance, in the +,+,- case, the zero-velocity surface is either a one-sheet or two-sheet hyperboloid (Figure 4.1). Hovering in either of these cases would still be bounded by a one-dimensional dead-band control designed for the nominal state (with quadratic cone zero-velocity surface). This analytical result is verified by numerical simulation. Figure 4.5 shows an integrated hovering trajectory in the +,+,- region above a sphere and the predicted perturbed zero-velocity surface (dotted region). The trajectory remains contained in the predicted region for the full integration time ( $\approx 1$  day) under the nominally selected one-dimensional dead-band control.

Next, a more general statement of the zero-velocity surface for a perturbed initial state is given without assuming small error. If the control is designed for hovering at  $(\tilde{\mathbf{r}}, \mathbf{0}_{3x1})$  but, in actuality, the initial state is  $(\tilde{\mathbf{r}} + \delta\tilde{\mathbf{r}}_0, \delta\dot{\tilde{\mathbf{r}}}_0)$ , the equation for the

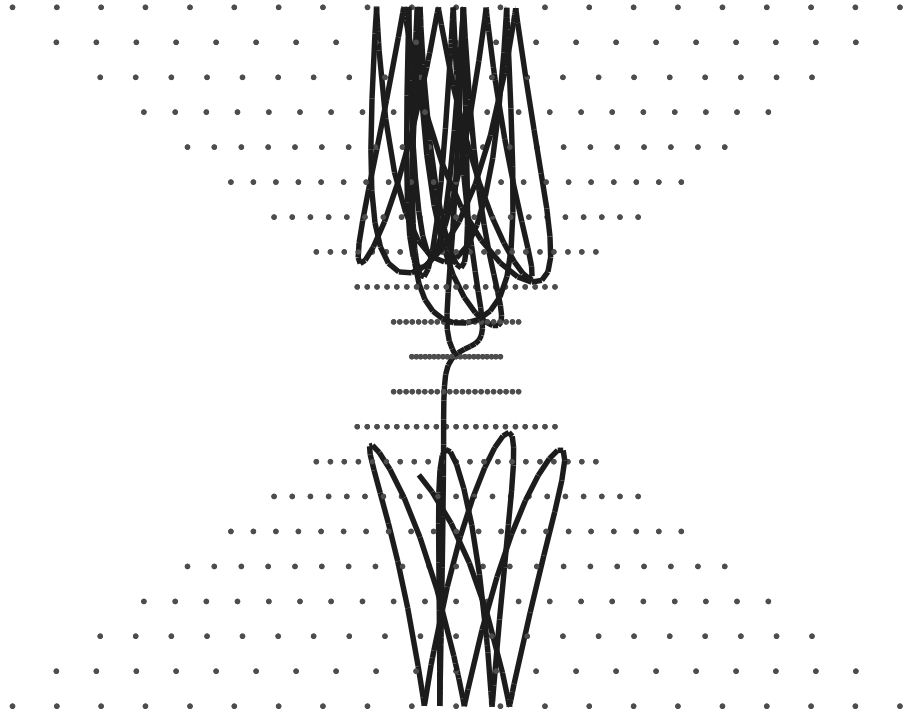


Figure 4.5: Example of a  $+,+,-$  Simulated Trajectory (motion relative to the zero-velocity surface, dots indicate the predicted region of allowable motion)

local bounding zero-velocity surface is given in Eq. (4.17),

$$(\delta\tilde{\mathbf{r}} - \delta\tilde{\mathbf{r}}_0)^T \frac{\partial^2 J}{\partial \tilde{\mathbf{r}}^2} \Big|_{(\tilde{\mathbf{r}}+\delta\tilde{\mathbf{r}}_0, \delta\dot{\tilde{\mathbf{r}}}_0)} (\delta\tilde{\mathbf{r}} - \delta\tilde{\mathbf{r}}_0) + 2 \frac{\partial J}{\partial \tilde{\mathbf{r}}} \Big|_{(\tilde{\mathbf{r}}+\delta\tilde{\mathbf{r}}_0, \delta\dot{\tilde{\mathbf{r}}}_0)} (\delta\tilde{\mathbf{r}} - \delta\tilde{\mathbf{r}}_0) = \delta\dot{\tilde{\mathbf{r}}}_0^T \delta\dot{\tilde{\mathbf{r}}}_0 \quad (4.17)$$

where  $\partial J / \partial \tilde{\mathbf{r}}|_{(\tilde{\mathbf{r}}+\delta\tilde{\mathbf{r}}_0, \mathbf{0}_{3 \times 1})} \neq \mathbf{0}_{1 \times 3}$  since  $\tilde{\mathbf{T}}_{OL}(\tilde{\mathbf{r}})$  does not create an equilibrium point. In general, this quadratic is not centered at  $\tilde{\mathbf{r}} + \delta\tilde{\mathbf{r}}_0$ . The center and  $\Delta Z$ , which is not zero in general, can be found by completing the square. The shape of the zero-velocity surface still depends solely on the eigenvalues of the matrix  $\partial^2 J / \partial \tilde{\mathbf{r}}^2|_{(\tilde{\mathbf{r}}+\delta\tilde{\mathbf{r}}_0, \delta\dot{\tilde{\mathbf{r}}}_0)}$ , and can be found in Table 4.2. Therefore, for the perturbed system to be bounded under dead-band hovering control, the actual initial position of the spacecraft must have the same eigenvalue signs as the nominal position. In addition, the eigenvectors that

describe the true zero-velocity surface (linearized about  $\tilde{\mathbf{r}} + \delta\tilde{\mathbf{r}}_0$ ) must be sufficiently close to the nominal so that the nominal dead-band still bounds the motion in three dimensions. Thus, it is concluded that hovering near a “border” between different eigenvalue regions with a minimal dead-band control would risk unbounded behavior.

The effect of open-loop thrust application errors on the zero-velocity surface can be analyzed similarly. Both thrust and position errors cause  $\partial J/\partial\tilde{\mathbf{r}}|_{(\tilde{\mathbf{r}}_0, \mathbf{0}_{3 \times 1})}$  to be non-zero, which changes the center of the bounding surface as well as its shape. However, the signs of the eigenvalues of  $\partial^2 J/\partial\tilde{\mathbf{r}}^2|_{(\tilde{\mathbf{r}}_0, \mathbf{0}_{3 \times 1})}$  and the orientation of the zero-velocity surface do not change from nominal, so the nominal controller will still bound the perturbed system.

### 4.3.2 Formal Local Boundary Definition

Formally, (uniform) boundedness of the perturbed trajectory under idealized dead-band control (Eq. (4.8)) can be shown using the definition of Khalil[63]. It states that the solutions of a dynamical system under a chosen hovering thrust control law are:

- uniformly bounded if there exists a positive constant  $c$ , independent of  $t_0 \geq 0$ , and for every  $a \in (0, c)$ , there is  $\beta = \beta(a) > 0$ , independent of  $t_0$ , such that if  $\|x(t_0)\| \leq a$ , then  $\|x(t)\| \leq \beta, \forall t \geq t_0$ .

Since this system is time-invariant, the conditions regarding uniformity are automatically satisfied. For the proof, utilize the standard norm and let  $c = \gamma$ , the parameter of the chosen dead-band. In the initial condition ball of measure  $a$ , first compute the largest change in  $J$  induced by any initial state,

$$\Delta J_{max} = \max_{(\tilde{\mathbf{r}}, \dot{\tilde{\mathbf{r}}}) \in B_a} \left( J(\tilde{\mathbf{r}}, \dot{\tilde{\mathbf{r}}}) - C_0 \right), \quad (4.18)$$

then use it to compute the maximum allowable deviation in position and velocity from the nominal. Formally, if

$$\mathbf{A} = \left\{ \tilde{\mathbf{r}} \in \mathfrak{R}^3 \mid \delta\tilde{\mathbf{r}}^T \frac{\partial^2 J}{\partial \tilde{\mathbf{r}}^2} \Big|_{(\tilde{\mathbf{r}}_0, \mathbf{0}_{3 \times 1})} \delta\tilde{\mathbf{r}} \leq 2\Delta J_{max} \quad \& \quad f_{db}(\tilde{\mathbf{r}}) \leq \gamma \right\}, \quad (4.19)$$

then

$$r_{max} = \max_{\tilde{\mathbf{r}} \in Bd(\mathbf{A})} \|\tilde{\mathbf{r}} - \tilde{\mathbf{r}}_0\| \quad (4.20)$$

and

$$v_{max} = \sqrt{2 \left( J_0 + \Delta J_{max} + \max_{\tilde{\mathbf{r}} \in \mathbf{A}} \left[ V(\tilde{\mathbf{r}}) + \tilde{\mathbf{T}}_{OL}^T \tilde{\mathbf{r}} \right] \right)}. \quad (4.21)$$

If both  $r_{max}$  and  $v_{max}$  are finite, which is implied by the condition that the dead-band must be properly oriented, then the system is bounded with  $\beta(a) = r_{max} + v_{max}$ .

Thus, a sufficient condition for boundedness of trajectories in the vicinity of the hovering position is that the chosen controller must restrict motion in at least as many dimensions as the zero-velocity surface allows unrestricted motion and be oriented such that the spacecraft trajectory is trapped inside a bounded region defined by the zero-velocity surface and the dead band surface. To get this result, it was assumed that  $T_m$  is sufficiently large so that our impulsive approximation is valid (which makes the level set  $f_{db} = \gamma$  an inviolable boundary) and that  $\gamma$  is sufficiently small so that our second order approximation of the zero-velocity surface is valid. Also, nothing here (except performance of the thruster) prevents using a very small  $\gamma$  to force  $\mathbf{A}$  to be arbitrarily small.

For particular cases, computing  $r_{max}$  and  $v_{max}$  is simple algebra. For example, if the one-dimensional dead-band function in Eq. (4.9) with  $\hat{\mathbf{v}}_c = \hat{\mathbf{v}}_3$  is used at a hovering position with  $+, +, -$  eigenvalue structure,

$$r_{max} = \sqrt{\gamma^2 \left( 1 - \frac{\alpha_3}{\alpha_2} \right) + \frac{\Delta J_{max}}{\alpha_2}} \quad (4.22)$$

and

$$v_{max} = \sqrt{2(\Delta J_{max} + \gamma^2 \alpha_3^2)}. \quad (4.23)$$

The localized system can be misleading due to its second order nature as it allows for arbitrarily large increases in the nominal Jacobi constant without destroying boundedness. This is not the case in general as is shown in the next section.

### 4.3.3 Formal Global Boundary Definition

Now, boundedness of hovering trajectories with perturbations in the initial state is shown in a global formulation. This result would be more applicable than the localized result when using a dead-band with a large  $\gamma$ . The argument is intuitive and simply states that for a trajectory to be bounded, its region of allowable motion must be finite.

In the formal boundedness definition (Theorem 4.3.2), let  $c = \gamma$  and  $\Delta J_{max}$  be defined as in Eq. (4.18). The allowable region of motion is defined by the set  $\mathbf{B}$ , where

$$\mathbf{B} = \{ \tilde{\mathbf{r}} \in \mathfrak{R}^3 \mid f_{db}(\tilde{\mathbf{r}}) \leq \gamma \quad \& \quad - (V(\tilde{\mathbf{r}}) + \mathbf{T}_{OL}^T \tilde{\mathbf{r}}) \leq (C_0 + \Delta J_{max}) \\ \& \quad \exists \text{ a path from } \tilde{\mathbf{r}} \text{ to } \tilde{\mathbf{r}}_0 \}. \quad (4.24)$$

$r_{max}$  and  $v_{max}$  are defined similarly to the local case (Eqs. (4.22), (4.23)) by substituting the set  $B$  for  $A$ . Computation of  $r_{max}$  and  $v_{max}$  in the global case involves solving simultaneous implicit equations and is generally more complicated than obtaining the localized result. If the dead-band is of sufficient dimension and oriented properly such that these values are finite, then the function  $\beta(a) = r_{max} + v_{max}$  satisfies the condition for boundedness.

#### 4.3.4 Maximum Allowable Perturbations in Initial State

The largest perturbations in initial state that a spacecraft subject to hovering control designed for a particular position can withstand and have the future motion remain bounded is now formulated for the global result. Unlike the linearized result, there are two limits for  $\Delta J$ : a maximal decrease that can only be achieved by errors in position, and a maximal increase, achievable by a combination of errors in position and velocity. The following formulation applies only to hovering trajectories that are nominally bounded.

Without approximation, the zero-velocity surface is defined in Eq. (4.25).

$$\mathbf{Z} = \{\tilde{\mathbf{r}} \in \mathfrak{R}^3 \mid \varkappa(\tilde{\mathbf{r}}) = J(\tilde{\mathbf{r}}, \mathbf{0}_{3x1}) - C^* = 0\} \quad (4.25)$$

The bounding surface(s) created by the dead-band control boundary can be defined by Eq. (4.26).

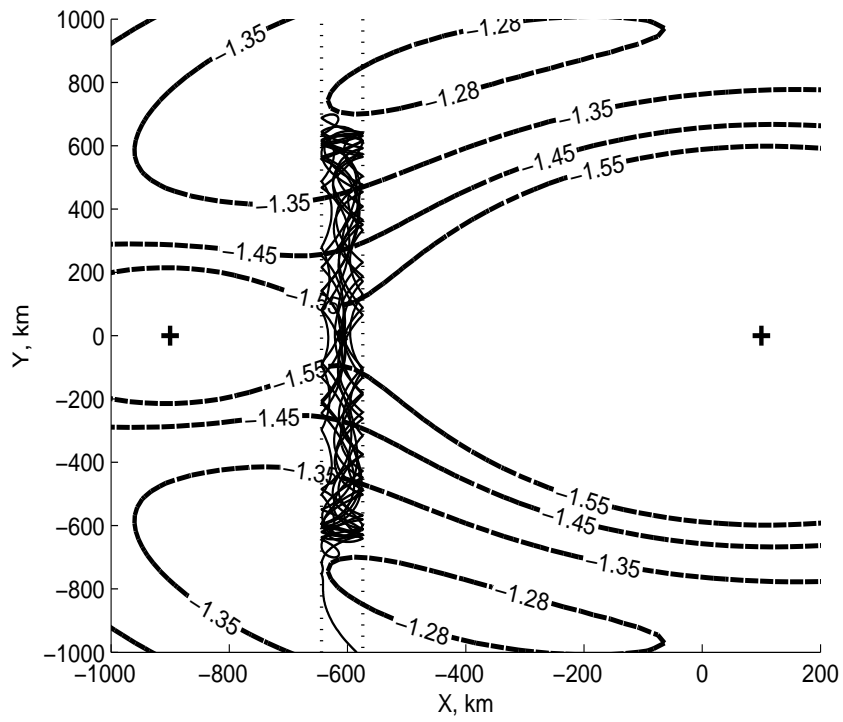
$$\mathbf{D} = \{\tilde{\mathbf{r}} \in \mathfrak{R}^3 \mid d(\tilde{\mathbf{r}}) = f_{ab}(\tilde{\mathbf{r}}) - \gamma = 0\} \quad (4.26)$$

For boundedness to be preserved,  $C^*$  must be such that these surfaces fully enclose the permitted motion from the nominal hovering position. The critical values of  $C^*$  where hovering becomes unbounded occur when the zero-velocity surface and the control surfaces no longer intersect transversely, i.e., when there first exists a position  $\tilde{\mathbf{r}} \in (\mathbf{Z} \cap \mathbf{D})$  such that  $\nabla \varkappa(\tilde{\mathbf{r}})$  and  $\nabla d(\tilde{\mathbf{r}})$  are collinear. Finding this critical point under the assumption that  $\Delta J > 0$  yields the maximal allowable increase in Jacobi constant and assuming  $\Delta J < 0$  gives the maximal decrease in Jacobi constant.  $\Delta J_+$  and  $\Delta J_-$  can be found analytically in simplified cases and numerically in general.

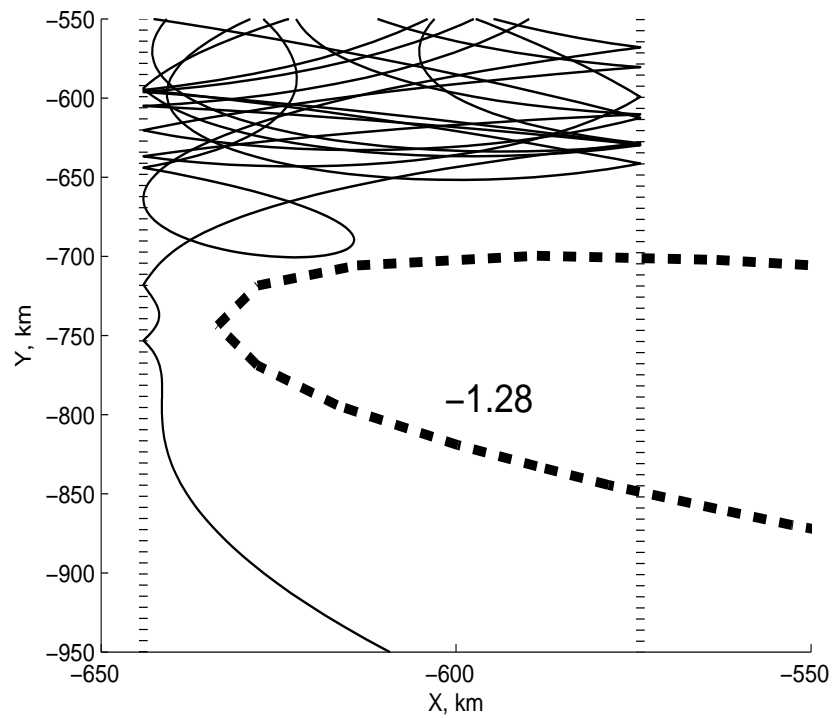
This concept may be best demonstrated visually. Figures 4.6(a) and (b) show a series of zero-velocity surfaces,  $\mathbf{Z}$ , for different values of the Jacobi constant in the planar, circular-restricted three-body problem (Section 2.3.2) as dashed contour

lines. Here, the spacecraft is “hovering” at the  $L1$  Lagrange point ( $X \approx -609$  km,  $Y = 0$  km) which requires no thrust since it is a natural equilibrium of the system. The control surfaces for a one-dimensional dead-band,  $\mathbf{D}$ , are shown as vertical dotted lines. In this plot, a spacecraft’s motion is restricted to areas where  $J(\tilde{\mathbf{r}}, \mathbf{0}_{3x1})$  (equivalent to the negative of the potential  $V(\mathbf{r})$  since there is no open-loop thrust) is less than the initial Jacobi constant. Beginning with the nominal energy at the hovering point ( $\approx -1.57$ ), it can be seen that if the spacecraft energy is increased to  $-1.35$  (by increasing the initial velocity), the allowable region of motion created by the zero-velocity surface and the control surfaces expands but the allowable trajectory remains enclosed. It can be seen in the figure that at  $-1.28$ ,  $\Delta J_+$  has been exceeded; the zero-velocity contour and the control surface no longer intersect transversely. This means that the trajectory of a spacecraft that starts at the  $L1$  Lagrange point of this system with an energy of  $-1.28$  is not guaranteed to be bounded. An example of an unbounded trajectory with a Jacobi constant of  $-1.28$  is shown as a solid line in the figures. Figure 4.6(b) shows a zoomed-in view of the trajectory escaping out of the open bottleneck between the zero-velocity and control surfaces.

Now, an example analytical calculation of  $\Delta J_+$  and  $\Delta J_-$  is given for spacecraft motion under a one-sided (thrust is only applied for the dead-band boundary closest to the body), one-dimensional dead-band control (without the open-loop thrust component) near a spherical body in the two-body problem (Section 2.3.1). Here, it is assumed that the nominal position is of the form  $\tilde{\mathbf{r}}_0 = [x_0, 0, z_0]$  without loss of generality. The zero-velocity surface and dead-band control surfaces are defined in



a)



b)

Figure 4.6: Escape Trajectory in the Restricted Three-body Problem: Contours are Zero-Velocity Surfaces for Different Initial Energies (vertical dotted lines are the dead-band control boundaries)

Eqs. (4.27) and (4.28).

$$\mathbf{Z} = \left\{ \tilde{\mathbf{r}} \in \mathfrak{R}^3 \mid \varkappa(\tilde{\mathbf{r}}) = -\frac{1}{2}\omega^2(x^2 + y^2) - \frac{\mu_{sb}}{|\tilde{\mathbf{r}}|} - C^* = 0 \right\} \quad (4.27)$$

$$\mathbf{D} = \{ \tilde{\mathbf{r}} \in \mathfrak{R}^3 \mid d(\tilde{\mathbf{r}}) = x - R_c = 0 \} \quad (4.28)$$

For a trajectory in this system to be nominally bounded under one-dimensional control,  $R_c < |\tilde{\mathbf{r}}_0| < R_r$ . The applicable gradients are given in Eqs. (4.29) and (4.30).

$$\nabla \varkappa(\tilde{\mathbf{r}}) = \left[ -\omega^2 x + \mu_{sb} \frac{x}{|\tilde{\mathbf{r}}|^3}, -\omega^2 y + \mu_{sb} \frac{y}{|\tilde{\mathbf{r}}|^3}, \mu_{sb} \frac{z}{|\tilde{\mathbf{r}}|^3} \right]^T \quad (4.29)$$

$$\nabla d(\tilde{\mathbf{r}}) = [1, 0, 0]^T \quad (4.30)$$

The Jacobi constant at the critical position  $\tilde{\mathbf{r}}^* \in (\mathbf{Z} \cap \mathbf{D})$  where  $\nabla \varkappa(\tilde{\mathbf{r}}^*)$  and  $\nabla d(\tilde{\mathbf{r}}^*)$  are collinear is sought. It is immediately seen that  $z^* = 0$  and  $x^* = R_c$ . There are three possible solutions for the  $y^*$  coordinate,  $y^* = 0, \pm \sqrt{R_r^2 - R_c^2}$ . The solution  $[x^*, y^*, z^*] = [R_c, 0, 0]$  defines the largest allowable decrease in the Jacobi constant,  $\Delta J_- = J([R_c, 0, 0]^T, \mathbf{0}_{3x1}) - C_0$ . This bound can only be violated by an error initial position such that the spacecraft is initially outside the dead-band. The largest allowable increase in initial Jacobi constant is defined by the other two solutions for  $y^*$  where  $\Delta J_+ = J([R_c, \pm \sqrt{R_r^2 - R_c^2}, 0]^T, \mathbf{0}_{3x1}) - C_0$ . If only errors in initial velocity are considered,

$$\delta v_{0,max} = \sqrt{2\Delta J_+} \quad (4.31)$$

is the maximal allowable error in initial velocity such that the trajectory remains bounded. For hovering positions outside of the resonance radius, these solutions are not applicable because the hovering trajectory is not nominally bounded by this dead-band control.

## 4.4 Particular Case Studies Applicable to Small-Bodies

It has been shown that a dead-band controller can be used to maintain hovering in a conservative system. A number of time-invariant systems can be discussed that occur in spacecraft dynamics with equations of motion of the form in Eq. (4.1). In this section, boundedness of hovering is considered in three systems commonly used to model dynamics near small-bodies: the two-body problem in a rotating frame (Section 2.3.1), the circular restricted three-body problem (Section 2.3.2), and the Hill three-body problem (Section 2.3.3). Since  $J$  is well-defined and twice differentiable at all physically relevant positions in these problems, the necessary type of dead-band control to bound hovering can be mapped as a function of hovering position. Unbounded or problematic hovering areas (i.e., near a boundary of the eigenvalue regions) for a particular controller can easily be identified and avoided.

### 4.4.1 Hovering in the Body-Fixed Frame (Two-body Problem)

First, the control type necessary to bound hovering for the two-body problem is determined. It may be desirable to hover in the small-body fixed frame for purposes of taking high-resolution measurements of a particular area of the surface or during a landing or sampling maneuver. The time-invariant equations of motion for this system are given in Eq. (2.14) and the resulting Jacobi constant is given by Eq. (2.15) where  $\tilde{\mathbf{T}} = \tilde{\mathbf{T}}_{OL}$ . The generalized potential for the two-body problem is defined in Eq. (4.32).

$$V(\tilde{\mathbf{r}}) = U(\tilde{\mathbf{r}}) + \frac{1}{2}\omega^2(x^2 + y^2) \quad (4.32)$$

The Hessian partial matrix with respect to position of  $J_{bf}$  is given by Eq. (4.33).

$$\left. \frac{\partial^2 J_{bf}}{\partial \tilde{\mathbf{r}}^2} \right|_{(\tilde{\mathbf{r}}_0, \mathbf{0}_{3x1})} = \begin{bmatrix} -\omega^2, & 0, & 0 \\ 0, & -\omega^2, & 0 \\ 0, & 0, & 0 \end{bmatrix} - \left. \frac{\partial^2 U}{\partial \tilde{\mathbf{r}}^2} \right|_{\tilde{\mathbf{r}}_0} \quad (4.33)$$

The signs of the eigenvalues of this matrix, and hence, the type of dead-band controller necessary for bounded hovering in the body-fixed two-body problem, can be mapped out for any well-defined gravitational potential field. Figure 4.7 shows the different eigenvalue regions for hovering positions above a spherical body in the  $X-Z$  plane, normalized by the resonance radius. The equations of motion are rotationally symmetric about  $\hat{\mathbf{z}}$ , so this figure fully characterizes the three-dimensional space around the body. Using the Routh criterion, it can be shown analytically that the boundary between the  $+,+,-$  and the  $+,-,-$  regions is precisely defined by a sphere at the center of mass with radius equal to the resonance radius (Eq. (2.16)). That is, all hovering positions near a spherical body with  $|\tilde{\mathbf{r}}| < R_r$  have the  $+,+,-$  eigenvalue structure and therefore, can be bounded by a hovering controller with an appropriate one-dimensional dead-band. Similarly, the boundary between the  $-,-,-$  and  $+,-,-$  regions is defined as a function of  $|\tilde{\mathbf{r}}|$  for  $|\tilde{\mathbf{r}}| > R_r$  by Eqs. (4.34) and (4.35).

$$\left( \frac{x}{R_r} \right)^2 = \frac{2}{3} \left( \frac{|\tilde{\mathbf{r}}|}{R_r} \right)^2 - \frac{2}{3} \left( \frac{R_r}{|\tilde{\mathbf{r}}|} \right) \quad (4.34)$$

$$\left( \frac{z}{R_r} \right)^2 = \frac{1}{3} \left( \frac{|\tilde{\mathbf{r}}|}{R_r} \right)^2 + \frac{2}{3} \left( \frac{R_r}{|\tilde{\mathbf{r}}|} \right) \quad (4.35)$$

Since no  $+,+,+$  regions exist in this problem, the shape of the zero-velocity surface for hovering near a sphere has been fully mapped analytically as a function of position. Nothing in this analysis limits the results to small-bodies; the eigenvalue regions defined in Figure 4.7 apply equally well to dynamics near spherical planetary bodies. However, on the planetary scale, the necessary thrust to hover is large and the

oscillations from nominal allowed under a bounding controller may be too large for some applications.

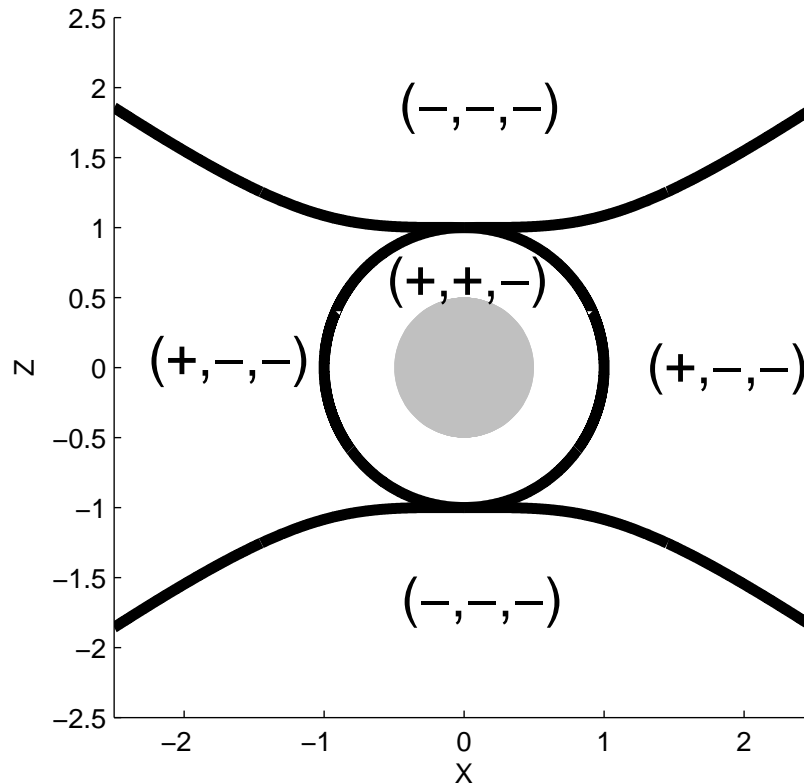


Figure 4.7: Hovering Regions Near a Spherical Small-body ( $X$  and  $Z$  axes normalized by the resonance radius)

The eigenvalue regions are more complex to define for real small-body shapes. Because the term “small-body” covers a wide range of irregular gravitational fields, the shapes of the eigenvalue regions are unique to each. Figure 4.8 shows the sufficient dead-band for bounded hovering in the equatorial plane near a polyhedral model of the asteroid 433 Eros ( $3.0 \text{ g/cm}^3$  density, 5.27 hr period[21]). Because of Eros’ elongated shape, the  $+,+,-$  hovering region here is divided into two lobes. Hovering above the small-body equator requires a one-dimensional dead-band near the elongated ends of the body and requires two dimensions of dead-band control

near its midsection. Figure 4.9 shows the different hovering regions near a polyhedral model of the asteroid 6489 Golevka ( $5.0 \text{ g/cm}^3$  density, 6.0289 hr period[6]). This is also interesting because of the  $+, -, -$  region inside the large canyon that runs across Golevka's south pole.

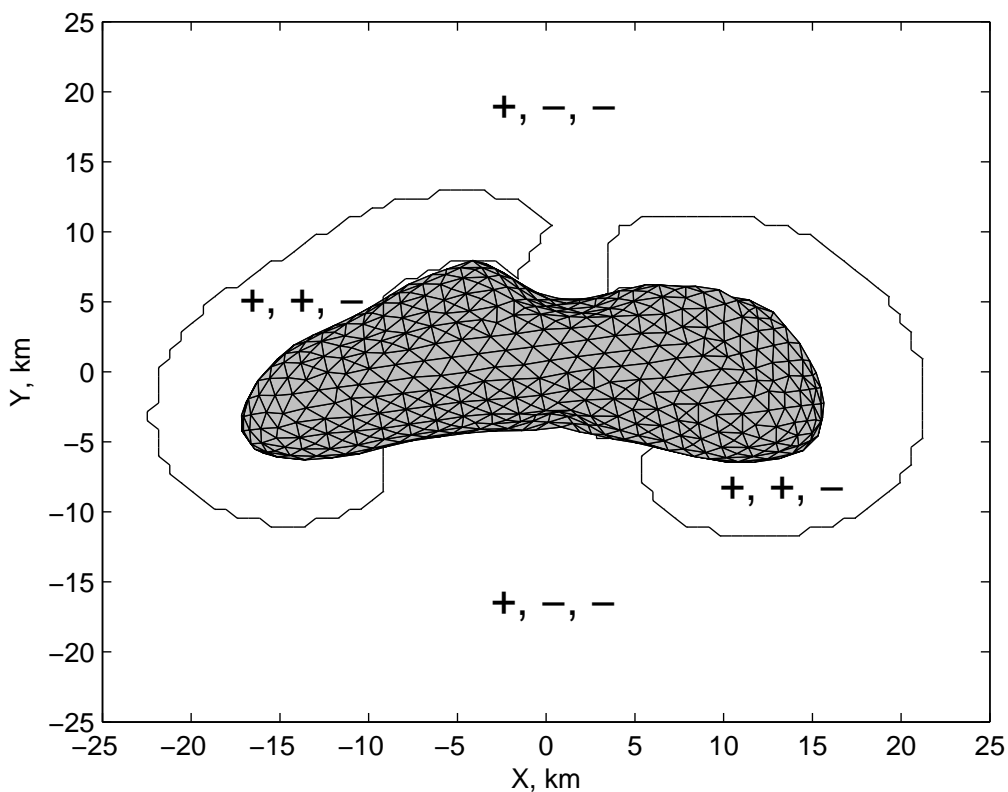
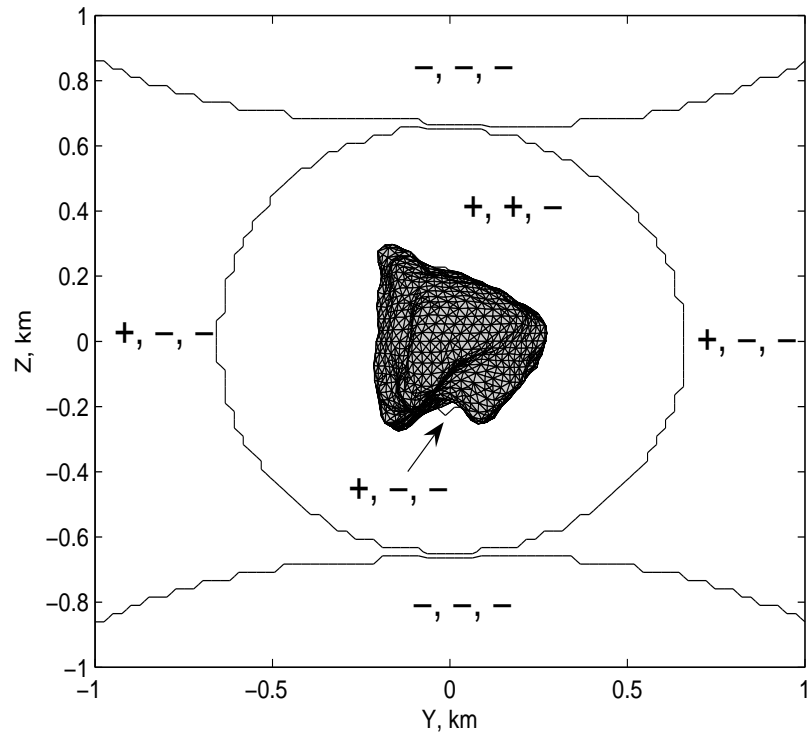


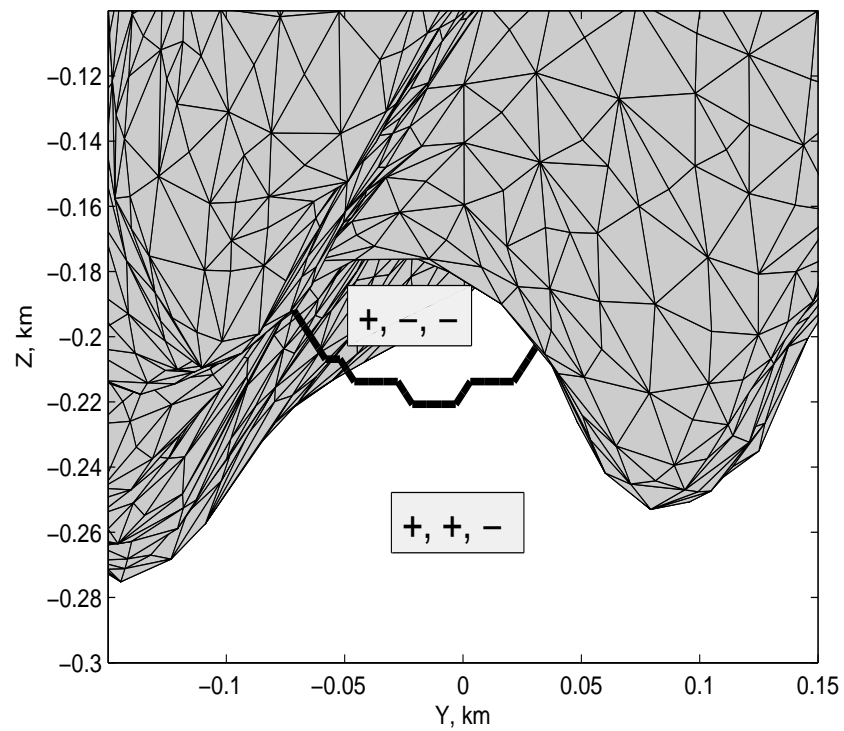
Figure 4.8: Hovering Regions Near Asteroid 433 Eros,  $X - Y$  Plane

#### 4.4.2 Hovering in the Circular Restricted Three-body Problem

Next, hovering in the circular restricted three-body problem (Section 2.3.2) is studied. It may be advantageous to hover in this frame, which rotates with the small-body around the sun, for the purpose of keeping a fixed communication, sensing, or solar panel geometry. These dynamics can be applied to hovering in the small-body-Sun system, a planet-moon system, or a binary asteroid system. The time-invariant



a)



b)

Figure 4.9: Hovering Regions Near Asteroid 6489 Golevka,  $Y - Z$  Plane

equations of motion for this system are given in Eq. (2.20) and the resulting Jacobi constant is given by Eq. (2.21) where  $\tilde{\mathbf{T}} = \tilde{\mathbf{T}}_{OL}$ . The generalized potential for the circular restricted three-body problem is defined in Eq. (4.36).

$$V(\tilde{\mathbf{r}}) = \frac{\mu_1}{|\tilde{\mathbf{r}}_{sc,1}|} + \frac{\mu_2}{|\tilde{\mathbf{r}}_{sc,2}|} + \frac{1}{2}N^2(x^2 + y^2) \quad (4.36)$$

Using the methodology discussed previously, the dead-band control sufficient to bound hovering in the restricted three-body problem can be mapped as a function of position. Figure 4.10 shows the shape of the eigenvalue regions in the vicinity of the two primaries for  $\mu = 0.01$ , a value typical for a planet-moon system. It is seen that each primary has an area in its immediate vicinity proportional to its mass where hovering requires one-dimensional perturbation control. If the  $\mu = 0.5$  case is considered, representative of a binary asteroid system,  $+,+,-$  and  $+,-,-$  regions are found in the  $X - Y$  plane as shown in Fig. 4.11. Here, a lobe of  $+,+,-$  dynamics is found around each equal mass primary. This region of one-dimensional dynamics is slightly larger on the outside of the primaries' orbit than on the inside.

#### 4.4.3 Hovering in the Hill Three-body Problem

The last conservative system presented here is the Hill three-body problem (Section 2.3.3), which is a valid approximation of the circular restricted three-body problem for hovering near the smaller primary when  $\mu$  is small. The Hill approximation does not generally apply to binary asteroid systems. The time-invariant equations of motion for this system are given in Eqs. (2.23) - (2.25) and the resulting Jacobi constant is given by Eq. (2.26) where  $\tilde{\mathbf{T}} = \tilde{\mathbf{T}}_{OL}$ . The generalized potential for the Hill three-body problem is defined in Eq. (4.37).

$$V(\tilde{\mathbf{r}}) = U(\tilde{\mathbf{r}}) + \frac{3}{2}N^2x^2 - \frac{1}{2}N^2z^2 - \frac{\beta_{SRP}x}{R^2} \quad (4.37)$$

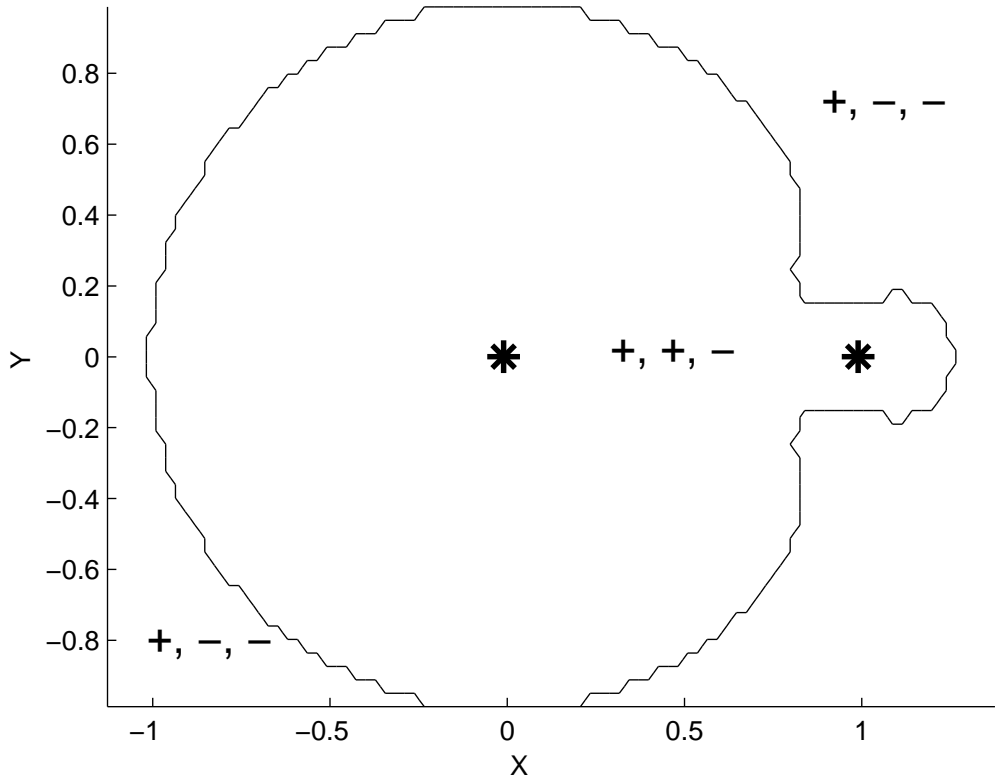


Figure 4.10: Hovering Regions in the Restricted Three-Body Problem,  $\mu = 0.01$ ,  $X - Y$  Plane, (coordinates normalized by  $R$ , asterisks denote position of primaries)

The sufficient dead-band type to bound hovering near the small-body is mapped the same way as done in the previous sections. When  $|\tilde{\mathbf{r}}| < R_{Hill}$  (Eq. (2.22)), the results are identical to those obtained in the circular restricted three-body problem. Figure 4.12 shows the eigenvalue regions for hovering near the small-body in the  $X - Z$  plane of the Hill problem. It can be noted that the addition of SRP has no effect on the sufficient dead-band since the potential associated with it is linear under Hill's approximations. The only difference in the necessary control is in  $\mathbf{T}_{OL}$ , which must null the nominal acceleration due to solar radiation pressure.

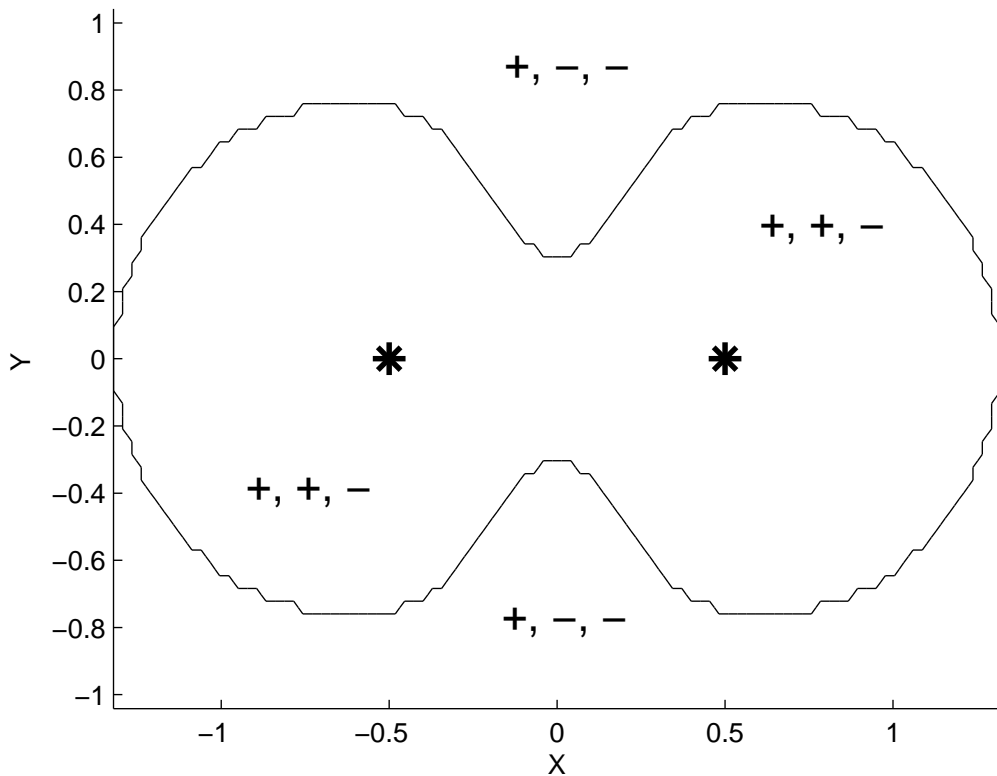
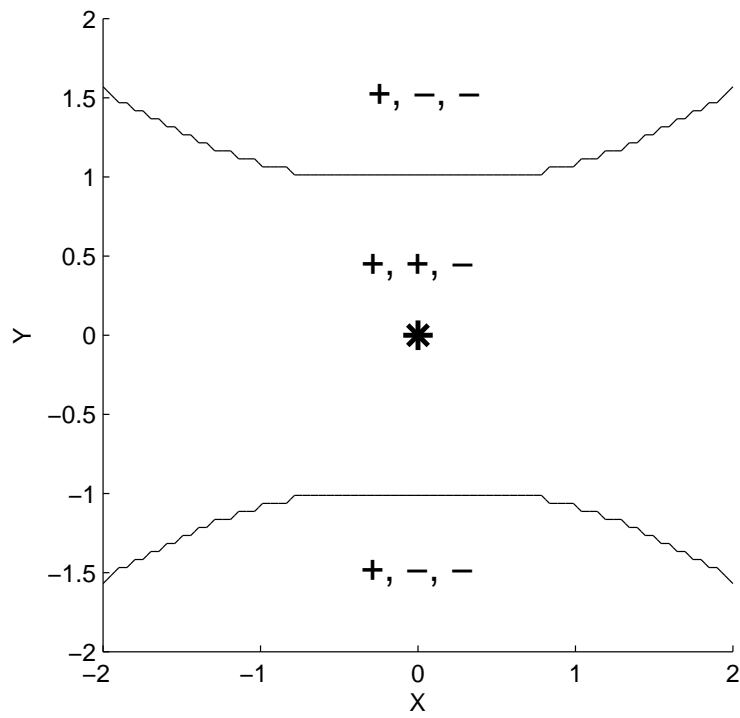


Figure 4.11: Hovering Regions in the Restricted Three-Body Problem,  $\mu = 0.5$ ,  $X - Y$  Plane, (coordinates normalized by  $R$ , asterisks denote position of primaries)

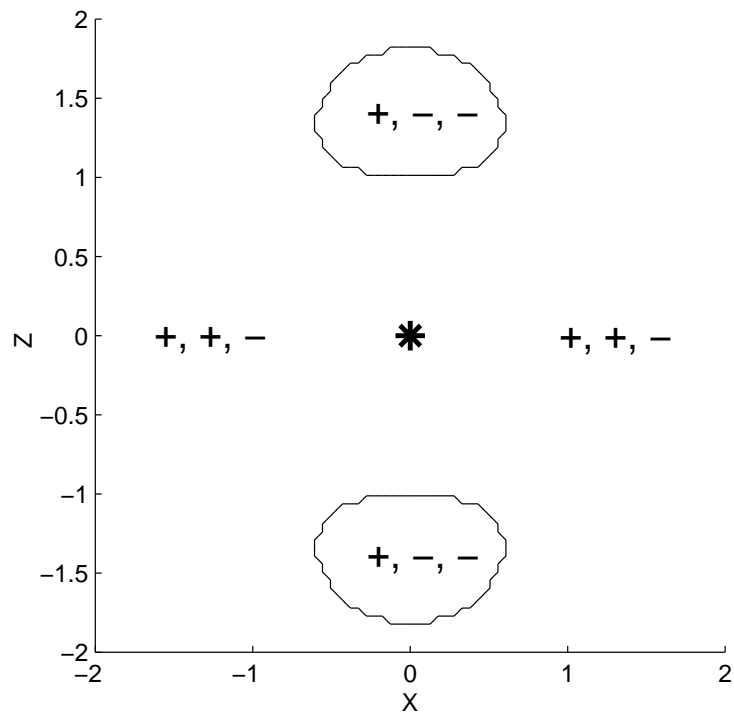
## 4.5 Hovering in Non-conservative Systems

When hovering in a non-conservative system, the Jacobi constant is no longer an integral of motion and therefore, if the zero-velocity surface exists, it becomes a function of time. In reality, all systems have this non-conservative property, caused by accelerations un-modeled in the idealized conservative dynamical systems (Eqs. (2.14), (2.20), and (2.23) - (2.25)). It is shown (and believed) that the approach developed for the conservative systems can still be useful in more realistic, non-conservative models.

The basis of the study here is the generalized elliptic restricted three-body prob-



a)



b)

Figure 4.12: Hovering Regions in the Hill Three-Body Problem, (a)  $X - Y$  and (b)  $X - Z$  Planes (coordinates normalized by the Hill Radius, asterisk denote position of the primary)

lem (Section 2.3.4), which includes the most fundamental time-varying perturbations: an elliptic small-body orbit around the Sun and arbitrary rotation of an arbitrarily shaped small-body. For this problem,  $V(\tilde{\mathbf{r}}, t)$  can be defined by Eq. (4.38)

$$V(\tilde{\mathbf{r}}, t) = U(T_i T_{pole} T_{eo}^{-1} T_f^{-1} \tilde{\mathbf{r}}) + 0.5 \dot{f}^2 (x^2 + y^2) + \frac{\mu_{Sun} x}{|R(f)|^2} + \frac{\mu_{Sun} - \beta_{SRP}}{\|\tilde{\mathbf{r}}_{s/c, Sun}\|} \quad (4.38)$$

and the equations of motion can be manipulated into the form in Eq. (4.39),

$$\frac{d}{dt} \left[ H(\tilde{\mathbf{r}}, \dot{\tilde{\mathbf{r}}}, t) \right] = -\frac{\partial V}{\partial t} - (\ddot{f} \hat{\mathbf{z}} \times \tilde{\mathbf{r}}) \cdot \dot{\tilde{\mathbf{r}}} - \frac{\partial \tilde{\mathbf{T}}^T}{\partial t} \tilde{\mathbf{r}} \quad (4.39)$$

where

$$H(\tilde{\mathbf{r}}, \dot{\tilde{\mathbf{r}}}, t) = \frac{1}{2} \dot{\tilde{\mathbf{r}}}^T \dot{\tilde{\mathbf{r}}} - V(\tilde{\mathbf{r}}, t) - \tilde{\mathbf{T}}^T \tilde{\mathbf{r}} \quad (4.40)$$

is the time-varying Jacobi integral. Eq. (4.39) is very similar to Eq. (4.2). The difference is that it allows a non-uniformly rotating coordinate frame and  $\tilde{\mathbf{T}}$  is allowed to change with time, represented by the extra terms on the right hand side. The open-loop thrust necessary to make a nominal hovering state stationary in this case is given by Eq. (4.41),

$$\tilde{\mathbf{T}}_{OL}(t) = - \left. \frac{\partial V(\tilde{\mathbf{r}}, t)}{\partial \tilde{\mathbf{r}}} \right|_{(\tilde{\mathbf{r}}_0, t)}^T + \ddot{f} \hat{\mathbf{z}} \times \tilde{\mathbf{r}}_0 \quad (4.41)$$

which is time-varying.

#### 4.5.1 Circular Orbit with Arbitrary Small-body Rotation

First, the case where  $e_{orb} = 0$  is considered. This allows the small-body to have arbitrary pole and rotation rate, but requires that its orbit around the Sun be circular. In this case,  $R(f)$  (Eq. (2.29)) and  $\dot{f}$  (Eq. (2.30)) are constant and  $\ddot{f} = 0$  (Eq. (2.31)). It can be shown that for virtual displacements in state (displacements without passage of time[64]) consistent with the equations of motion at any particular instant of time,  $H(\tilde{\mathbf{r}}, \dot{\tilde{\mathbf{r}}}, t)$  is conserved, that is,

$$\frac{\partial H}{\partial \tilde{\mathbf{r}}} \dot{\tilde{\mathbf{r}}} + \frac{\partial H}{\partial \dot{\tilde{\mathbf{r}}}} \ddot{\tilde{\mathbf{r}}} = 0. \quad (4.42)$$

This is equivalent to saying the dynamics would conserve  $H$  if the orientation of the small-body was frozen at a particular time. If open-loop hovering control is applied (Eq. (4.41)), equilibrium is induced at the nominal hovering position and thus,  $\partial H/\partial \tilde{\mathbf{r}}|_{(\tilde{\mathbf{r}}_0, \mathbf{0}_{3x1}, t)} = \partial H/\partial \dot{\tilde{\mathbf{r}}}|_{(\tilde{\mathbf{r}}_0, \mathbf{0}_{3x1}, t)} = \mathbf{0}_{1x3}$ . The region of allowable motion in the vicinity of the nominal state is then defined via second order Taylor expansion in Eq. (4.43)

$$\delta \tilde{\mathbf{r}}^T \frac{\partial^2 H}{\partial \tilde{\mathbf{r}}^2} \Big|_{(\tilde{\mathbf{r}}_0, \mathbf{0}_{3x1}, t)} \delta \tilde{\mathbf{r}} = -\delta \dot{\tilde{\mathbf{r}}}^T \delta \dot{\tilde{\mathbf{r}}} \leq 0 \quad (4.43)$$

and the local zero-velocity surface is defined at any instant of time by Eq. (4.44).

$$\delta \tilde{\mathbf{r}}^T \frac{\partial^2 H}{\partial \tilde{\mathbf{r}}^2} \Big|_{(\tilde{\mathbf{r}}_0, \mathbf{0}_{3x1}, t)} \delta \tilde{\mathbf{r}} = 0 \quad (4.44)$$

The quantity  $\partial^2 H/\partial \tilde{\mathbf{r}}^2|_{(\tilde{\mathbf{r}}_0, \mathbf{0}_{3x1}, t)}$  varies periodically at the rotation rate of the small-body in the three-body rotating frame. Given a dead-band hovering control, boundedness of the trajectory can be determined by evaluating whether the time-varying zero-velocity surface and the dead-band surface create an enclosed region around the nominal hovering position at all times over one period of motion. Note, this may be achieved by a time-varying dead-band. Also, the signs of the eigenvalues of  $\partial^2 H/\partial \tilde{\mathbf{r}}^2|_{(\tilde{\mathbf{r}}_0, \mathbf{0}_{3x1}, t)}$ , and therefore, the type of zero-velocity surface may change over time

Of course, this approach is limited to giving information about the general character of the zero-velocity surface as a function of time, as it is impractical to assume that the spacecraft will stay exactly at the nominal state for all time. There are two ways to approach a perturbed trajectory. One way is to assume the perturbations are small and linearize about the nominal state to determine the zero-velocity surface for each state (or possible state) on the trajectory for the time of concern (such as was done in the first part of Section 4.3.1). The resulting zero-velocity sur-

faces can be checked against the dead-band control to determine boundedness. For this method,  $\partial^2 H / \partial \tilde{\mathbf{r}}^2|_{(\tilde{\mathbf{r}}_0, \mathbf{0}_{3 \times 1}, t)}$  must be evaluated and stored for only one period of nominal motion.

Another approach evaluates the local zero-velocity surface at each point on the actual trajectory, similar to what is done in Eq. (4.17). The trajectory is bounded if the zero-velocity surface and dead-band create a bounded region at all times in the duration of interest. However, the usefulness of this approach is limited since the perturbed state is not known until it has already happened (at least). This method is more suitable to planned motion away from the hovering position (i.e., a translation maneuver). Then a linear perturbation method could be used to evaluate the effects of uncertainty along that nominal trajectory.

#### 4.5.2 Hovering in the Generalized Elliptic-restricted Three-body Problem

When the circular small-body orbit restriction is lifted, things become more difficult. Now, if the system parameters are frozen in time, Eq. (4.45) shows  $H$  is still not conserved.

$$\frac{\partial H}{\partial \tilde{\mathbf{r}}} \dot{\tilde{\mathbf{r}}} + \frac{\partial H}{\partial \dot{\tilde{\mathbf{r}}}} \ddot{\tilde{\mathbf{r}}} = - \left( \ddot{f} \hat{\mathbf{z}} \times \tilde{\mathbf{r}} \right) \cdot \dot{\tilde{\mathbf{r}}} \quad (4.45)$$

This means that the zero-velocity surface cannot be defined at any time using  $H$  and may not exist at all.

Scheeres[17] uses a “pulsating” frame, where the coordinates are scaled by the distance between the Sun and the small-body and derivatives are taken with respect to  $f$ , to address this issue in the context of escape orbits. The pulsating frame is probably not appropriate for evaluating hovering at a stationary position in real space, unfortunately. Also, this approach evaluates  $H$  along a given trajectory and compares it with a constant escape value in the equatorial plane, where constant

zero-velocity surface boundaries exist. It is observed that the possibility of escape first appears in the equatorial plane, so this is a valid approach. For that work,  $H$  need not be constant for permissible motion (which is required here to obtain the instantaneous zero-velocity surface), it must only remain larger than the constant threshold value.

The term  $\ddot{f}$  is quite small in general (especially for nearly circular small-body orbits), which may allow treatment of the zero-velocity surfaces under “small variations” in the value of  $H$ . Figuring out how to treat such small variations is crucial to learning how to apply this result to real systems where other such time-varying perturbations exist. This is a topic of future work.

## 4.6 Discussion

The main result here is not that the spacecraft trajectory can be bounded by dead-band control (that is achieved trivially by a three-dimensional dead-band), but that it can often be done by a reduced order controller. In Figures 4.7, 4.8, and 4.9, we see that hovering in close proximity to a small-body, as may be necessary for a sampling or landing maneuver, can often be bounded by a one-dimensional dead-band controller, since the zero-velocity surface frequently has a  $+,+,-$  structure. Positions a little further from the body often have  $+,-,-$  zero-velocity surfaces, which requires only two-dimensions of control. The next chapter will look at using altimetry and optical navigation measurements as a basis of the control for these two cases respectively.

For safety purposes, it may be desirable to have three-dimensional control of the spacecraft motion as on the Hayabusa spacecraft[28]. This could be achieved by a three-dimensional dead-band controller, or more cleverly, by a combination of a

one-dimensional (such as Eq. (4.9)) and a two-dimensional dead-band control (Eq. (4.10)). Depending on where the spacecraft hovers, the  $\gamma$  parameter of each thrust control could be adjusted so that the minimal dimension controller bounds the spacecraft and the secondary controller, which has a larger  $\gamma$  value, provides a safety net. Measurements for the secondary dead-band could be performed less frequently, which would conserve spacecraft resources.

This sufficient condition for boundedness is more useful than the conditions for linear stability on the manifold for one-dimensional dead-band control (Eqs. (3.2)-(3.4)) presented in the previous literature[10] because it does not neglect the Coriolis forces on the spacecraft, nor artificially restrict the spacecraft motion in any way. However, it is interesting to note that the region where that work predicts stability when motion along  $\hat{\mathbf{v}}_3$  is restricted corresponds closely with the  $+,+,-$  zero-velocity surface region. This makes sense for slowly rotating small-bodies since the results in this chapter demonstrate energetically bounded motion perpendicular to  $\hat{\mathbf{v}}_3$  (the direction corresponding to the negative eigenvalue of  $-\partial^2 U/\partial \tilde{\mathbf{r}}^2 - \text{diag}(\omega^2, \omega^2, 0)$ ), which is close to  $\hat{\mathbf{v}}_3$  (the eigenvector corresponding to the positive eigenvalue of  $\partial^2 U/\partial \tilde{\mathbf{r}}^2$ ). Implementation of the control law in Sawai *et al.* via an altimetry dead-band however is fundamentally different from restricting motion along  $\hat{\mathbf{v}}_3$ , as will be seen in Chapter V. This boundedness test is also preferable to the numerical approach of the previous chapter since it ensures bounded motion for all time. Also, determining the sufficient dead-band type requires only that the eigenvalues of a single matrix be determined, as opposed to numerical integration.

This result is a sufficient condition however; a trajectory may be Lyapunov stable without any control, but not satisfy this boundedness condition. For instance, Scheeres[8] predicts stable dynamics under open-loop control in the two-body prob-

lem in areas with  $+, -, -$  (two free directions) eigenvalue structure. This work does not disagree that result; it says the spacecraft has the energy to move far away from nominal in two directions, but says nothing about the dynamics ever taking it there. They are two different ways of approaching the same problem, but the results are similar. The  $+, +, -$  (one free direction) area inside the resonance radius corresponds very closely with the region with one hyperbolic unstable mode in Scheeres[8]. Interestingly, the  $-, -, -$  region above the small-body poles in the two-body problem also corresponds to a region with one hyperbolic unstable mode of the open-loop dynamics; this suggests that the spacecraft is energetically free to move in any direction, but will actually only move far from the initial position in one.

## CHAPTER V

# Hovering Implementation Issues and Simulations

In this chapter, some practical issues related to hovering under dead-band control are addressed in the context of the zero-velocity surface result of the last chapter. First, the zero-velocity surface result is generalized to allow for varying levels of open-loop thrust. The next section derives criteria for boundedness of hovering under dead-band control based on altimetry or optical navigation measurements. Fuel usage during hovering is addressed both analytically and via numerical simulations with HoverSim and a method for determining the time between subsequent dead-band crossings without integration is also given. The final section of this chapter presents HoverSim simulations to demonstrate the results of this chapter and Chapter IV as well as to investigate the effects of measurement uncertainty and finite measurement sampling frequencies.

### 5.1 Generalized Hovering Zero-Velocity Surface Result

In the previous chapter, the quadratic zero-velocity surface in the vicinity of a spacecraft operating under hovering control was defined for time-invariant systems of the form in Eq. (4.1). For a constant applied thrust, this dynamical system has a Jacobi constant of the form in Eq. (4.3).

It can be noted that the magnitude and direction of the open-loop thrust does not matter for the purpose of preserving the conservative nature of the system, so long as it is constant. Here, the zero-velocity surface result in Section 4.1 is generalized to allow for any constant thrust (in the frame of interest), not just one that creates an equilibrium at the nominal position. This formulation allows no open-loop thrust to be used (such as in the IATNS body-fixed hovering controller) or partial cancellation of the nominal acceleration (such as canceling centrifugal acceleration only[10]).

Using a quadratic expansion of the Jacobi constant around the nominal hovering state  $(\tilde{\mathbf{r}}_0, \mathbf{0}_{3x1})$ , the condition in Eq. (5.1) applies to states in the vicinity of the nominal for all times  $t$ ,

$$J(\tilde{\mathbf{r}}_0 + \delta\tilde{\mathbf{r}}, \delta\dot{\tilde{\mathbf{r}}}) = J(\tilde{\mathbf{r}}_0, \mathbf{0}_{3x1}) - (\tilde{\mathbf{a}}_0 + \tilde{\mathbf{T}})^T \delta\tilde{\mathbf{r}} + \frac{1}{2} \delta\tilde{\mathbf{r}}^T \left. \frac{\partial^2 J}{\partial \tilde{\mathbf{r}}^2} \right|_{(\tilde{\mathbf{r}}_0, \mathbf{0}_{3x1})} \delta\tilde{\mathbf{r}} + \frac{1}{2} \delta\dot{\tilde{\mathbf{r}}}^T \delta\dot{\tilde{\mathbf{r}}} \quad (5.1)$$

where

$$\tilde{\mathbf{a}}_0 = \left. \frac{\partial V}{\partial \tilde{\mathbf{r}}} \right|_{\tilde{\mathbf{r}}_0}^T \quad (5.2)$$

is the nominal acceleration on the spacecraft without thrust;  $(\tilde{\mathbf{a}}_0 + \tilde{\mathbf{T}})$  is null if open-loop thrust is applied to create an equilibrium at the nominal position. Eq. (5.1) can be rearranged to give a more general form of the zero-velocity surface restriction than in Eq. (4.6).

$$\delta\tilde{\mathbf{r}}^T \left. \frac{\partial^2 J}{\partial \tilde{\mathbf{r}}^2} \right|_{(\tilde{\mathbf{r}}_0, \mathbf{0}_{3x1})} \delta\tilde{\mathbf{r}} = 2 (\tilde{\mathbf{a}}_0 + \tilde{\mathbf{T}})^T \delta\tilde{\mathbf{r}} \quad (5.3)$$

By completing the square and moving the coordinate center, the above equation can be put into the form of Eq. (5.4),

$$(\delta\tilde{\mathbf{r}} - \delta\tilde{\mathbf{r}}_c)^T \left. \frac{\partial^2 J}{\partial \tilde{\mathbf{r}}^2} \right|_{(\tilde{\mathbf{r}}_0, \mathbf{0}_{3x1})} (\delta\tilde{\mathbf{r}} - \delta\tilde{\mathbf{r}}_c) = \Delta Z \quad (5.4)$$

where

$$\delta\tilde{\mathbf{r}}_c = \left( \left. \frac{\partial^2 J}{\partial \tilde{\mathbf{r}}^2} \right|_{(\tilde{\mathbf{r}}_0, \mathbf{0}_{3x1})} \right)^{-1} (\tilde{\mathbf{a}}_0 + \tilde{\mathbf{T}}) \quad (5.5)$$

and

$$\Delta Z = \left( \tilde{\mathbf{a}}_0 + \tilde{\mathbf{T}} \right)^T \left( \frac{\partial^2 J}{\partial \tilde{\mathbf{r}}^2} \Big|_{(\tilde{\mathbf{r}}_0, \mathbf{0}_{3 \times 1})} \right)^{-1} \left( \tilde{\mathbf{a}}_0 + \tilde{\mathbf{T}} \right). \quad (5.6)$$

It should be noted that  $\delta \tilde{\mathbf{r}}_c$  may be very large, which means care should be taken when using a quadratic expansion of the zero-velocity surface near  $\tilde{\mathbf{r}}_0$ . This nominal bound has identical form to the perturbed zero-velocity surface given in Eq. (4.16). Table 4.2 and Figure 4.1 can be referenced to determine the shape of the local zero-velocity surface. In the figure, the star now represents the location  $\tilde{\mathbf{r}}_0 + \delta \tilde{\mathbf{r}}_c$ . Depending on the eigenvalues and the sign of  $\Delta Z$ , spacecraft motion may be restricted to the outside or the inside of these shapes.

## 5.2 Using a Reduced Measurement Set for Control

Chapter IV demonstrates that boundedness of a hovering trajectory can be ensured using a reduced order dead-band controller (Eq. (3.5)); that is, motion may only need to be controlled in one or two directions for boundedness. This result suggests it may be possible to implement bounded hovering using a limited measurement set. Here, simple altimetry measurements (Section 2.4.1) are considered as a basis for a one-dimensional dead-band controller and optical navigation measurements (Section 2.4.3) are considered as a basis for a two-dimensional dead-band.

### 5.2.1 Altimetry Measurements

Since the region of space closest to the small-body often only requires one-dimensional dead-band control for boundedness (see the  $+,+,-$  regions in Figures 4.7, 4.8, and 4.9), it is natural to wonder if altimetry measurements alone can be used to maintain hovering in these situations. Here this question is considered using a dead-band control on altitude with  $f_{ab}(\tilde{\mathbf{r}})$  defined by Eq. (3.6).

Simply stated, the local condition for boundedness is that the union of the zero-velocity surface  $\mathbf{Z}$  (Eq. (4.25)) and the dead-band surface  $\mathbf{D}$  (Eq. (4.26)) must fully enclose the initial position in  $\mathfrak{R}^3$ . Boundedness under an altitude dead-band control is different from under the one-dimensional control presented in the previous chapter (Eq. (4.9)) because now the topography of the small-body surface defines the dead-band limiting surface instead of a simple flat plane. Figure 5.1 depicts the relative orientation of the dead-band and zero-velocity surfaces graphically. It is clear that using altimetry measurements as the basis of the dead-band control (curved bounding surface  $\mathbf{D}$ ) instead of full position estimates (flat plat bounding surface  $\mathbf{D}$ ) will reduce the set of positions where one-dimensional dead-band control bounds hovering. This is because the surface of the small-body is (usually) convex and its surface normal generally will not be aligned with  $\hat{v}_3$  (the eigenvector corresponding to the negative eigenvalue of the  $+,+,-$  zero-velocity surface). Thus, if the curvature of the surface of the small-body or the angle  $\eta$  between  $\hat{\mathbf{n}}$  and  $\hat{v}_3$  is too large at the nominal sub-altimeter point  $\tilde{\rho}_0$ , the hovering trajectory may not be bounded.

In this section, analytical criteria for boundedness of hovering under an altitude dead-band controller (Eq. (3.6)) in the  $+,+,-$  region are sought using the zero-velocity surface knowledge gained in Chapter IV. For this analysis, only ellipsoidal small-body shape models are considered; the boundedness of altitude dead-band hovering above a polyhedron is a topic for future study. This restriction reduces the problem to evaluating the intersection set of two arbitrarily oriented quadratics: a hyperboloid ( $+,+,-$  zero-velocity surface) and an ellipsoid (dead-band surface). This is actually a very challenging geometry problem which has been solved numerically by Dupont *et al.*[65]. In addition to being numerical, the resulting solution is prohibitively complex. With some simplification of the problem, analytical sufficient

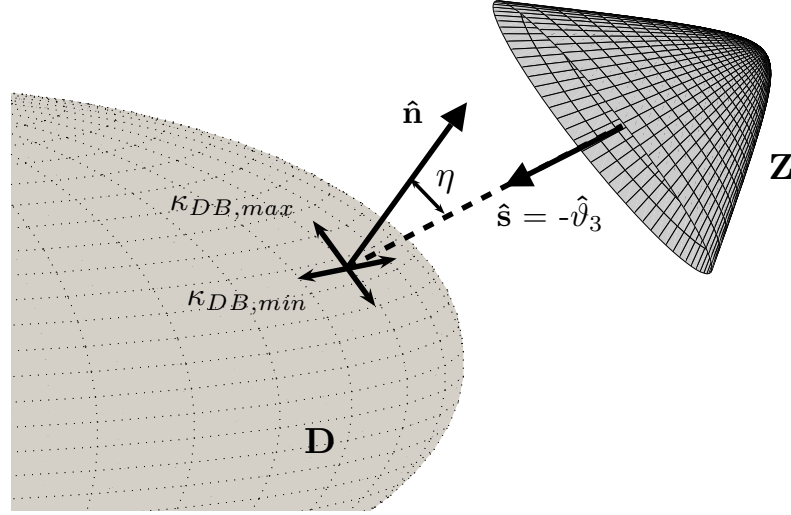


Figure 5.1: Relative Orientation of the Altitude Dead-band Boundary **D** and the  $+,+,-$  Zero-velocity Surface **Z**

conditions for boundedness are derived here.

In the hyperboloid coordinate frame (whose unit vectors are  $\hat{\vartheta}_2$ ,  $\hat{\vartheta}_1$ , and  $\hat{\vartheta}_3$ ), Eq. (5.7) defines the local zero-velocity hyperboloid, which is a two-sheet hyperboloid if  $h_d > 0$ , a quadratic cone if  $h_d = 0$ , and a one-sheet hyperboloid if  $h_d < 0$  (Figure 4.1).

$$H(\delta\tilde{\mathbf{r}}_r) = \frac{\delta x_r^2}{h_a^2} + \frac{\delta y_r^2}{h_b^2} - \frac{\delta z_r^2}{h_c^2} + h_d = 0 \quad (5.7)$$

Here,  $h_a > h_b$  and coordinates are measured from the zero-velocity surface center so that  $\delta\tilde{\mathbf{r}}_r = \tilde{\mathbf{r}} - (\tilde{\mathbf{r}}_0 + \delta\tilde{\mathbf{r}}_c)$ . To simplify the analysis, let the zero-velocity surface be a hyperboloid of revolution about  $\hat{\vartheta}$  with  $h_b = h_a$ . This effectively widens the zero-velocity surface; if it bounds the motion, then the real zero-velocity surface will

as well. Under this assumption, a parameterization of the solution to Eq. (5.7) is given in Eq. (5.8) when  $h_d > 0$ ,

$$\delta\tilde{\mathbf{r}}_r = \left[ h_a\sqrt{h_d}\sinh u \cos v, \quad h_a\sqrt{h_d}\sinh u \sin v, \quad \pm h_c\sqrt{h_d}\cosh u \right]^T \quad (5.8)$$

where  $u \in (-\infty, \infty)$  and  $v \in [0, \pi)$ . The positive third term applies to the “upper lobe” sheet of the hyperboloid (the one further from the small-body) and the negative term refers to the “lower lobe” sheet. Eq. (5.9) is the parameterization for the quadratic cone solution (when  $h_d = 0$ ),

$$\delta\tilde{\mathbf{r}}_r = \left[ h_a u \cos v, \quad h_a u \sin v, \quad h_c u \right]^T \quad (5.9)$$

where  $u \in (-\infty, \infty)$  and  $v \in [0, 2\pi)$ . Eq. (5.10) is the solution parameterization for when  $h_d < 0$  (one-sheet hyperboloid),

$$\delta\tilde{\mathbf{r}}_r = \left[ h_a\sqrt{-h_d}\cosh u \cos v, \quad h_a\sqrt{-h_d}\cosh u \sin v, \quad h_c\sqrt{-h_d}\sinh u \right]^T \quad (5.10)$$

where  $u \in (-\infty, \infty)$  and  $v \in [0, 2\pi)$ [66]. Figure 5.2 shows the parameterization coordinates  $u$  and  $v$  on these three hyperboloid surfaces.

The local character of the surface of an ellipsoid at  $\tilde{\rho}_0$  (and therefore, of the dead-band surface  $\mathbf{D}$ ) can be characterized by three parameters: the normal vector to the surface  $\hat{\mathbf{n}}$  (Eq. (2.3)), the maximum principal curvature of the surface  $\kappa_{DB,max}$ , and the minimum principal curvature  $\kappa_{DB,min}$ . The principal curvatures of the surface of a tri-axial ellipsoid at any point can be computed using the method described in Cipolla and Giblin[67]. Let the the problem be simplified by reducing the ellipsoidal dead-band surface to a sphere with both principal curvatures equal to  $\kappa_{DB,max}$ . The radius of the sphere  $s$  is the inverse of this curvature. This sphere fits inside of the original best-fit ellipsoid and thus, if the spherical surface “caps” the zero-velocity

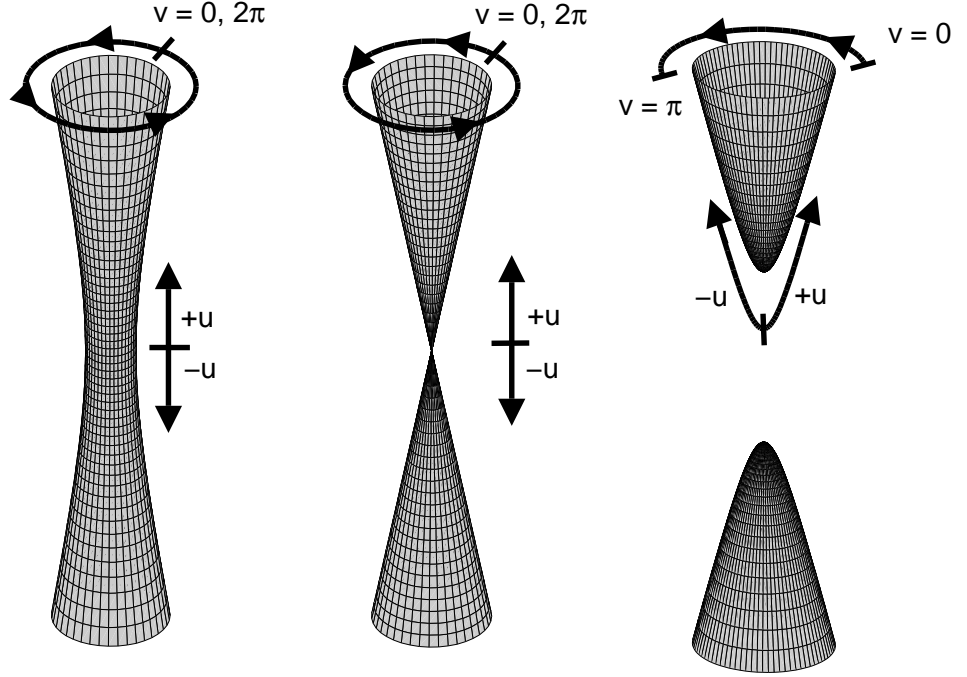


Figure 5.2: Parameterization Coordinates for (left to right) the One-sheet Hyperboloid, the Quadratic Cone, and the Two-sheet Hyperboloid

hyperboloid, then so does the ellipsoid. This sphere is defined by  $S(\tilde{\mathbf{r}}) = 0$ , where

$$S(\tilde{\mathbf{r}}) = \frac{1}{s^2} (\tilde{\mathbf{r}} - \tilde{\mathbf{r}}_s)^T (\tilde{\mathbf{r}}_r - \tilde{\mathbf{r}}_s) - 1. \quad (5.11)$$

For points inside the sphere  $S(\tilde{\mathbf{r}}) < 0$  and for points outside the sphere  $S(\tilde{\mathbf{r}}) > 0$ .

The center of the sphere  $\tilde{\mathbf{r}}_s$  is defined as a function of  $\gamma$  and the small-body surface in Eqs. (5.12) and (5.13),

$$\tilde{\mathbf{r}}_{s,top} = \tilde{\mathbf{r}}_0 - \gamma \hat{\mathbf{s}} - s \hat{\mathbf{n}}(\tilde{\rho}_0) \quad (5.12)$$

$$\tilde{\mathbf{r}}_{s,bot} = \tilde{\mathbf{r}}_0 + \gamma \hat{\mathbf{s}} - s \hat{\mathbf{n}}(\tilde{\rho}_0) \quad (5.13)$$

where  $\tilde{\mathbf{r}}_{s,top}$  corresponds to the dead-band surface at the upper altitude limit and  $\tilde{\mathbf{r}}_{s,bot}$  corresponds to the dead-band surface at the lower altitude limit. Let  $\tilde{\mathbf{r}}_{x,top}$  (Eq.

(5.14)) and  $\tilde{\mathbf{r}}_{x,bot}$  (Eq. (5.15)) be the vectors from the respective sphere center to the hyperboloid center with Cartesian components  $r_{x,x}$ ,  $r_{x,y}$ , and  $r_{x,z}$ .

$$\tilde{\mathbf{r}}_{x,top} = \delta\tilde{\mathbf{r}}_c + \gamma\hat{\mathbf{s}} + s\hat{\mathbf{n}}(\tilde{\rho}) \quad (5.14)$$

$$\tilde{\mathbf{r}}_{x,bot} = \delta\tilde{\mathbf{r}}_c - \gamma\hat{\mathbf{s}} + s\hat{\mathbf{n}}(\tilde{\rho}) \quad (5.15)$$

For hovering to be bound above the minimum altitude limit, there must exist a complete circuit around the zero-velocity hyperboloid in  $v$  (see Figure 5.2) that is entirely contained by the minimum altitude dead-band sphere (such that  $S(\tilde{\mathbf{r}}) \leq 0 \forall (u, v)$  on the circuit). Similarly, for hovering to be bound below the maximum altitude limit there must exist a complete circuit in  $v$  entirely outside the maximum altitude dead-band sphere (such that  $S(\tilde{\mathbf{r}}) \geq 0 \forall (u, v)$  on the circuit). The approach here is to search for such a circuit with constant  $|u|$ . The criteria developed under this restriction on  $(u, v)$  correctly predict boundedness in all but the most degenerate situations.

For each  $+,+,-$  zero-velocity surface shape, the parameterization of the hyperboloid solution (Eqs. (5.8), (5.9), and (5.10)) can be substituted into Eq. (5.11) with the appropriate sign condition to derive sufficient conditions for boundedness of the hovering trajectory with altitude dead-band control. The variables can be separated so that the resulting inequality can be evaluated by separate functions of  $u$  and  $v$ .

For the  $h_d = 0$  case (quadratic cone zero-velocity surface), the initial position is at  $u_0 = 0$  and must be bounded by both the upper and lower dead-band surfaces; that is, there must exist a  $u \geq 0$  such that  $S(\tilde{\mathbf{r}}(u, v)) \geq 0$  and a  $u \leq 0$  such that  $S(\tilde{\mathbf{r}}(u, v)) \leq 0$  for all  $v \in [0, 2\pi)$ . These conditions can be stated as in Eqs. (5.16)

and (5.17) respectively,

$$\min_{u \in [0, \infty)} f_{qc}(u; \tilde{\mathbf{r}}_{x,top}) \leq \min_{v \in [0, 2\pi)} g(v; \tilde{\mathbf{r}}_{x,top}) \quad (5.16)$$

$$\min_{u \in (-\infty, 0]} f_{qc}(u; \tilde{\mathbf{r}}_{x,bot}) \leq \min_{v \in [0, 2\pi)} g(v; \tilde{\mathbf{r}}_{x,bot}) \quad (5.17)$$

where

$$f_{qc}(u; \tilde{\mathbf{r}}_x) = \frac{1}{2h_a u} (s^2 - \tilde{\mathbf{r}}_x^T \tilde{\mathbf{r}}_x - u^2 (h_a^2 + h_c^2)) - \frac{h_c}{h_a} r_{x,z} \quad (5.18)$$

and

$$g(v; \tilde{\mathbf{r}}_x) = r_{x,x} \cos v + r_{x,y} \sin v. \quad (5.19)$$

For the  $h_d > 0$  case, the two-sheet hyperboloid zero-velocity surface (Figure 4.1) only allows escape on one side for a trajectory contained by a given sheet. Therefore, only the side of the dead-band corresponding to this sheet must “cap” the zero-velocity surface. Let  $|u_0|$  be defined by Eq. (5.20),

$$|u_0| = \operatorname{arccosh} \left( \frac{|\delta r_{c,z}|}{h_c \sqrt{h_d}} \right) \quad (5.20)$$

where  $\delta \tilde{\mathbf{r}}_c$  is defined in the hyperboloid frame. If  $\delta r_{c,z} < 0$ , the initial hovering position is in the upper lobe and the condition for boundedness is given in Eq. (5.21),

$$\min_{|u| \in [u_0, \infty)} f_{ts,top}(|u|) \leq - \max_{v \in [0, \pi)} |g(v; \tilde{\mathbf{r}}_{x,top})| \quad (5.21)$$

where

$$\begin{aligned} f_{ts,top}(u) &= -\frac{h_c}{h_a} r_{x,top,z} \coth u \\ &+ \frac{1}{2h_a \sqrt{h_d} \sinh u} [s^2 - \tilde{\mathbf{r}}_{x,top}^T \tilde{\mathbf{r}}_{x,top} - h_d (h_a^2 \sinh^2 u + h_c^2 \cosh^2 u)]. \end{aligned} \quad (5.22)$$

Conversely, if  $\delta r_{c,z} > 0$ , the initial hovering position is in the lower lobe and the condition for boundedness is given in Eq. (5.23),

$$\max_{|u| \in [u_0, \infty)} f_{ts,bot}(|u|) \geq \max_{v \in [0, \pi)} |g(v; \tilde{\mathbf{r}}_{x,bot})| \quad (5.23)$$

where

$$f_{ts,bot}(u) = \frac{h_c}{h_a} r_{x,bot,z} \coth u + \frac{1}{2h_a\sqrt{h_d}\sinh u} [s^2 - \tilde{\mathbf{r}}_{x,bot}^T \tilde{\mathbf{r}}_{x,bot} - h_d (h_a^2 \sinh^2 u + h_c^2 \cosh^2 u)]. \quad (5.24)$$

Finally, for the  $h_d < 0$  case (one-sheet hyperboloid zero-velocity surface), the initial position must be bounded by both the upper and lower dead-band surfaces. For this case,  $u_0$  is defined in Eq. (5.25),

$$|u_0| = \operatorname{arcsinh} \left( \frac{|\delta r_{c,z}|}{h_c\sqrt{-h_d}} \right) \quad (5.25)$$

where  $\delta\tilde{\mathbf{r}}_c$  is again defined in the hyperboloid frame. The sufficient conditions for boundedness in this case are stated in Eqs. (5.26) and (5.27) respectively,

$$\min_{u \in [u_0, \infty)} f_{os}(u; \tilde{\mathbf{r}}_{x,top}) \leq \min_{v \in [0, 2\pi)} g(v; \tilde{\mathbf{r}}_{x,top}) \quad (5.26)$$

$$\max_{u \in (-\infty, u_0]} f_{os}(u; \tilde{\mathbf{r}}_{x,bot}) \geq \max_{v \in [0, 2\pi)} g(v; \tilde{\mathbf{r}}_{x,bot}) \quad (5.27)$$

where

$$f_{os}(u; \tilde{\mathbf{r}}_x) = -\frac{h_c}{h_a} r_{x,z} \tanh u + \frac{1}{2h_a\sqrt{-h_d}\cosh u} [s^2 - \tilde{\mathbf{r}}_x^T \tilde{\mathbf{r}}_x + h_d (h_a^2 \cosh^2 u + h_c^2 \sinh^2 u)]. \quad (5.28)$$

It must also be ensured for all cases that the initial position is outside of the lower bounding sphere and inside of the upper bounding sphere (so that the spacecraft is initially inside the dead-band). These conditions are somewhat less interesting though because motion in the upper lobe of the hyperboloid is almost always bounded by an altimetry dead-band since the dead-band surface is generally convex.

## Examples of Bounded Hovering Regions under Altitude Dead-band Control

This sufficient conditions for boundedness at a given hovering position under an altitude dead-band in Section 5.2.1 (Eqs. (5.16), (5.17), (5.21), (5.23), (5.26), and (5.26)) are functions of the surface topography, the initial spacecraft energy (determines  $h_d$ ), and  $\gamma$  (comes in through  $\tilde{\mathbf{r}}_x$ ). Eqs. (4.16) and (5.4) show that the initial spacecraft energy is a function of the initial state error and the applied open-loop thrust. Here, examples of the region where hovering is bounded using a one-dimensional dead-band controller based on altimetry are presented to demonstrate the effects of the surface curvature, the surface normal, the dead-band size, and the open-loop thrust on this region.

First, the effect of the surface curvature is examined. Figure 5.3 shows hovering positions in the  $X - Y$  plane above a sphere that satisfy the sufficient conditions for bounded hovering with an altitude dead-band and open-loop controller. Here,  $\mu_{sb}$  is constant so that the small-body radius varies from 0.667 to 1.5  $km$  as the density varies from 5.74 to 0.50  $g/cm^3$ . The dead-band size is 50  $m$  for all cases. Two things are worthy of noting here. The region where hovering under altitude dead-band control is bounded is a subset of the  $+,+,-$  region (union of the “YES” and “NO” regions) consisting of points inside a particular radius. The area labeled “N/A” requires a dead-band on more than one direction of motion to stabilize. Second, the change in surface curvature over the range of realistic small-body densities has only a small-effect on the bounded hovering region. The region of bounded hovering in the  $X - Z$  plane above a sphere is similar in size, though not perfectly circular.

Figure 5.4 shows the bounded region in the three principal axis planes above a 3.5 x 2.2 x 1.6  $km$  ellipsoid with  $\rho = 2.5 g/cm^3$  and a rotation period of 7.5  $hrs$ . Full

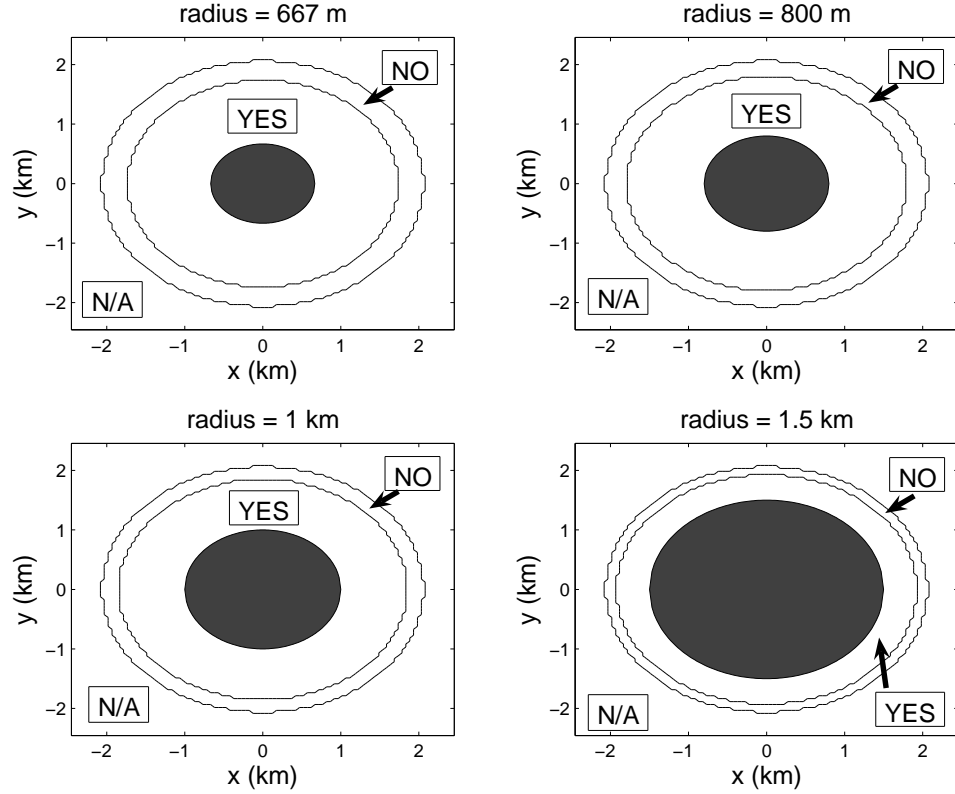


Figure 5.3: Boundedness of Hovering with Altimetry in the  $+,+,-$  Region above a Sphere,  $X - Y$  Plane, Varying Small-body Radius with Constant  $\mu_{sb}$ , 100% Open-loop Thrust,  $\gamma = 50 m$

open-loop cancellation of the nominal acceleration is applied and  $\gamma = 50 m$  in all three cases. For an ellipsoid, the surface curvature is not constant and the surface normal is not aligned with  $\hat{v}_3$  in general. Here, it can be seen that hovering under an altitude dead-band is more likely to be bounded above the “flatter” parts of the surface (where  $\kappa_{DB,max}$  is small) and near the axes where  $\eta$  is small. The results here are qualitatively typical of an ellipsoidal small-body.

Figure 5.5 shows the effect of changing the open-loop thrust in the  $X - Z$  plane of the same ellipsoid. Here the open-loop thrust is modulated to cancel 90%, 80%, 70%, and 50% of the nominal acceleration (left to right, top to bottom). The figures

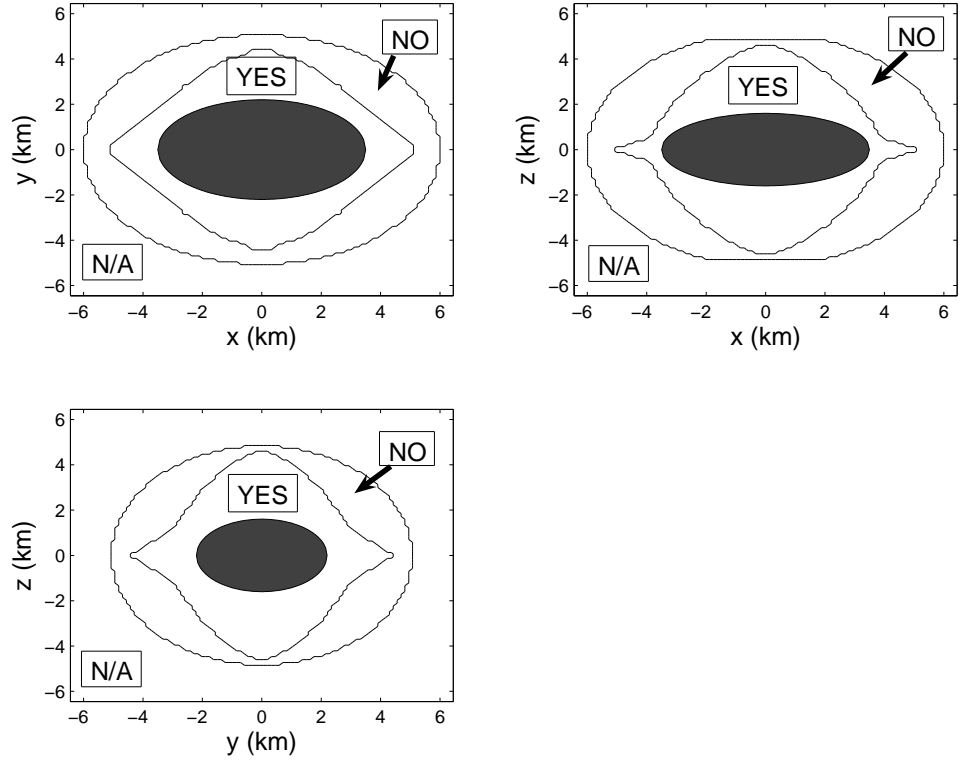


Figure 5.4: Boundedness of Hovering with Altimetry in the  $+,+,-$  Region above a  $3.5 \times 2.2 \times 1.6 \text{ km}$  Ellipsoid, 100% Open-loop Thrust,  $\gamma = 50 \text{ m}$

are symmetric about  $x = 0$  and  $z = 0$ . Decreasing the open-loop thrust (generally) has the effect of decreasing a negative  $\Delta Z$ , which widens the zero-velocity hyperboloid. As the surface becomes progressively wider the trajectory is less likely to be bounded under altitude dead-band control. As open-loop thrust decreases, boundedness remains longest above the flat areas along the principal axes of the body. A small area of stable hovering near the one-dimensional hovering boundary above the small-body's longest axis is also found. In this area, the spacecraft is nominally trapped by the upper boundary of the dead-band in the top lobe of a two-sheet hyperboloid.

Finally, the size of the dead-band  $\gamma$  plays a significant role in boundedness. Figure

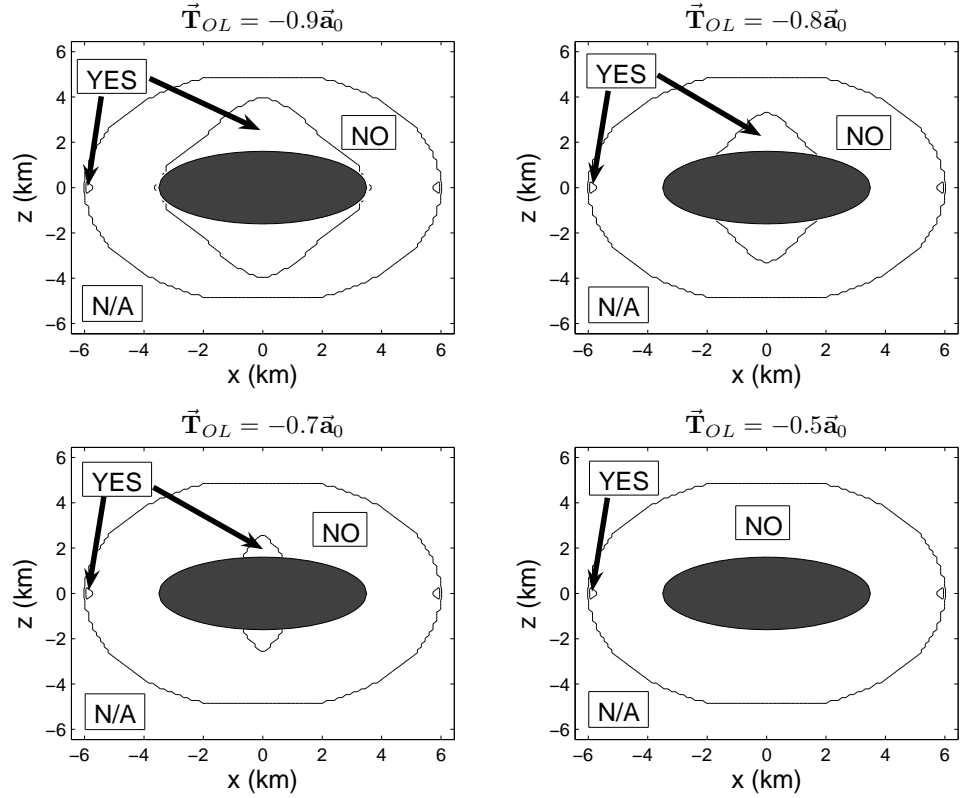


Figure 5.5: Boundedness of Hovering with Altimetry in the  $+, +, -$  Region above a  $3.5 \times 2.2 \times 1.6 \text{ km}$  Ellipsoid,  $X - Z$  Plane, Decreasing Open-loop Acceleration Cancellation,  $\gamma = 50 \text{ m}$

5.6 shows the bounded region for the  $3.5 \times 2.2 \times 1.6 \text{ km}$  ellipsoid in the  $Y - Z$  plane for  $\gamma = 5, 20, 100,$  and  $200 \text{ m}$ . Here, full open-loop cancellation of the nominal acceleration is applied. As the dead-band size increases, the set of positions where hovering is bounded under an altitude dead-band gets smaller.

The sufficient condition for boundedness in this chapter is also appropriate to predict the performance of the altitude dead-band controllers investigated numerically in Chapter III (GDTS w/OL and IATNS). For the GDTS w/OL body-fixed hovering controller (full open-loop cancellation of the nominal acceleration and  $\hat{\mathbf{s}} = -\hat{\mathbf{v}}_3$ ), positions inside the solid line in Figure 5.7 satisfy the sufficient conditions for bounded

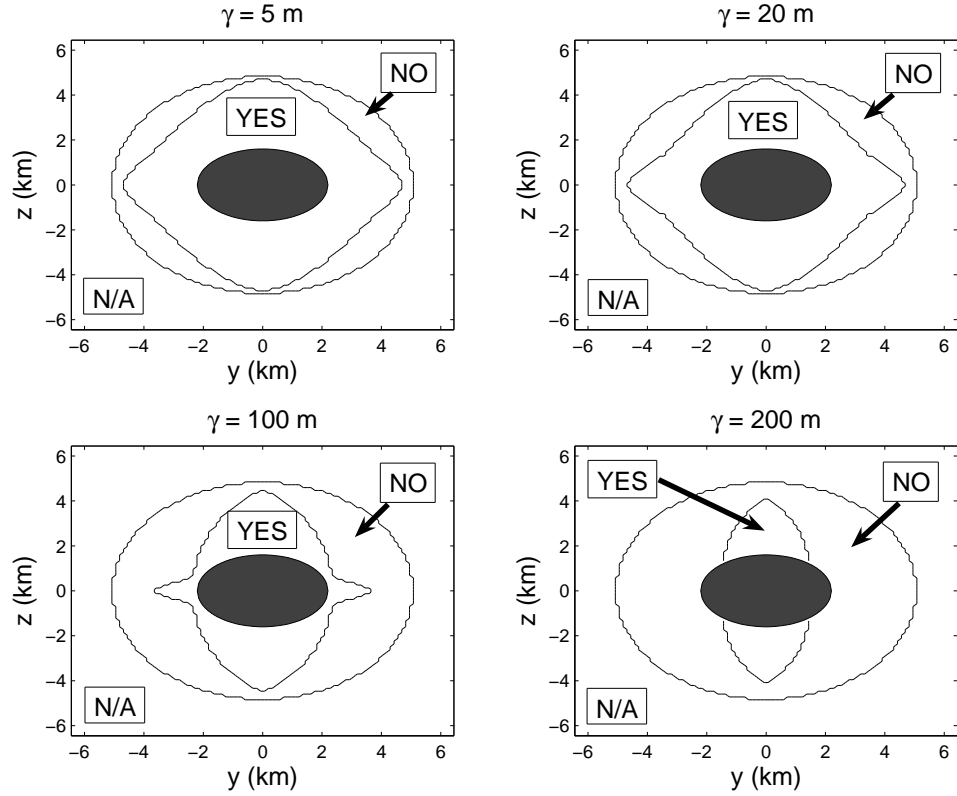


Figure 5.6: Boundedness of Hovering with Altimetry in the  $+,+,-$  Region above a  $3.5 \times 2.2 \times 1.6$  km Ellipsoid,  $X - Z$  Plane, 100% Open-loop Thrust, Variable  $\gamma$

body-fixed hovering above a  $15 \times 7 \times 6$  km ellipsoid with  $\rho = 3 \text{ g/cm}^3$ ,  $\gamma = 10$  m, and a ten hour rotation period. These are the same parameters used for the simulation results in Figure 3.4, which are plotted here for comparison. It can be seen that boundedness is not guaranteed for the majority of the area of large angular deviations that satisfies the stability criteria of Sawai *et al.* (Eqs. (3.2)-(3.4)), indicated by the dotted line. On the other hand, the regions with large (and small) deviations inside the solid line can be guaranteed to ultimately be bounded. The bound on angular deviation for some of these positions is apparently larger than the  $0.6^\circ$  numerical threshold, but it does exist. The positions above the trailing edge that do

not satisfy the sufficient condition are probably not technically bounded, but angular deviation is kept small by the Coriolis effect discussed in Section 3.3.2.

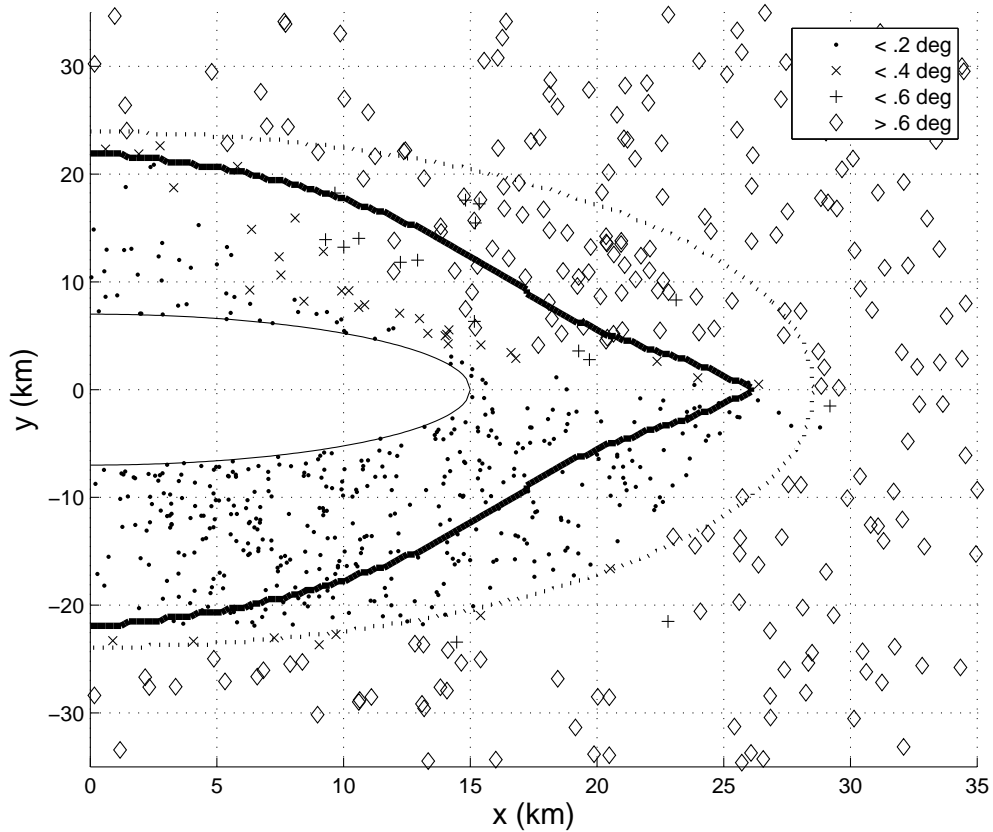


Figure 5.7: Numerical Results with GDTs w/OL Body-fixed Hovering Control Overlaid with Altitude Dead-band Sufficiency Condition

### 5.2.2 Optical Navigation Measurements

Optical navigation measurements give information about the lateral position of the spacecraft with respect to the small-body center of mass, but not the range (in general). In this section, these measurements are considered as the basis for a two-dimensional dead-band control that bounds motion in the  $+, -, -$  region of the two-body problem close to a small-body (see Figures 4.7, 4.8, and 4.9).

The simple characterization of an optical navigation measurement  $\hat{\mathbf{o}}$  as the unit vector from the small-body center of mass to the spacecraft in Section 2.4.3 is employed in this analysis. Eq. (5.29) is a dead-band function that could be used for this type of measurement,

$$f_{db}(\tilde{\mathbf{r}}) = \sqrt{(\phi_m(\tilde{\mathbf{r}}) - \phi_0)^2 + \cos^2 \phi_0 (\lambda_m(\tilde{\mathbf{r}}) - \lambda_0)^2} \quad (5.29)$$

where

$$\phi_m = \arcsin(o_z), \quad \phi_m \in \left[-\frac{\pi}{2}, \frac{\pi}{2}\right] \quad (5.30)$$

$$\lambda_m = \arctan2(o_y, o_x), \quad \lambda_m \in [-\pi, \pi]. \quad (5.31)$$

This dead-band defines a conical boundary that allows a maximum angular deviation of size  $\gamma$  from the nominal latitude and longitude.

First, a simple argument about boundedness of hovering in the  $+,-,-$  region under this type of dead-band is made. Assume that the zero-velocity surface is a quadratic cone ( $h_d = 0$ ) where motion is not allowed along  $\hat{\vartheta}_1$  and let  $Q = \left| \hat{\vartheta}_1 \cdot \hat{\mathbf{r}}_0 \right|$ . Figure 5.8 shows two simple cases. If  $Q = 1$  and the cone is sufficiently wide, then the union of the dead-band boundary and the zero-velocity surface will fully enclose the motion as is seen for the zero-velocity surface configuration on the left (motion is bounded on the outside of the zero-velocity surface and inside the gray conical dead-band surface). Conversely, if  $Q = 0$ , then it will never be bounded as seen in the right hand configuration. For a spherical small-body, it turns out that  $Q$  is identically zero for all points in the equatorial plane. Recall that the  $+,-,-$  region for a sphere in the two-body problem consists of points outside the resonance radius within a band of latitudes around the equatorial plane (Figure 4.7).  $Q$  is largest at the maximum latitude boundaries, but its value remains modest with a minimum angle between  $\hat{\vartheta}_1$  and  $\hat{\mathbf{r}}_0$  of about  $60^\circ$  within five resonance radii of the body ( $\hat{\vartheta}_1$  is

assumed to have some component pointing away from the small-body). This simple analysis for a spherical small-body suggests optical navigation measurements used in this way are unlikely to bound hovering in the two-body problem.

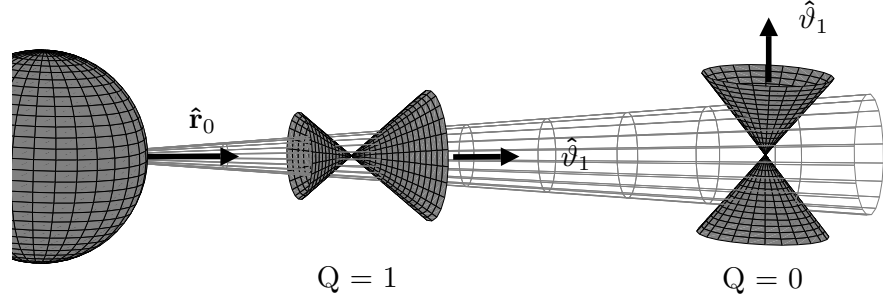


Figure 5.8: Optical Navigation Dead-band vs Zero-velocity Surface Orientation

A more precise approach is to use the unit vectors extending from  $\tilde{\mathbf{r}}_0$  that define the zero-velocity surface to determine intersection with the conical dead-band. Only the portion of the zero-velocity surface with  $\delta z_r > 0$  need be considered as if this side forms an enclosed region, the  $\delta z_r < 0$  side will as well. Figure 5.9 shows a general orientation of the quadratic cone zero-velocity surface with respect to the dead-band surface. Boundedness is ensured if  $\hat{\mathbf{r}}_0$  points in a forbidden direction of motion with respect to the zero-velocity surface and the angle between the zero-velocity surface boundary and  $\hat{\mathbf{r}}_0$  is greater than  $\gamma$  for all  $v \in [0, 2\pi)$ . If this is true, the component of the zero-velocity surface perpendicular to  $\hat{\mathbf{r}}_0$  grows more quickly than the corresponding component of the dead-band surface as radial distance from the body increases for all  $v$  and thus, bounding intersection will occur. Therefore, the necessary and sufficient conditions in Eqs. (5.32) and (5.33) must be satisfied for boundedness of hovering using the optical navigation measurement dead-band

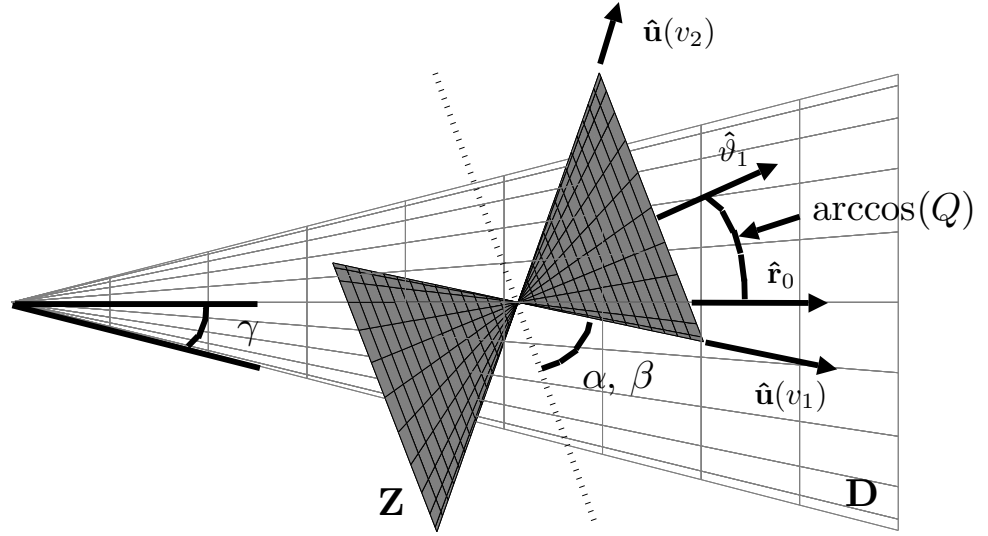


Figure 5.9: General Orientation of Optical Navigation Dead-band and Zero-velocity Surface

discussed here,

$$\min_{v \in [0, 2\pi)} \arccos(\hat{\mathbf{u}}(v) \cdot \hat{\mathbf{r}}_0) > \gamma \quad (5.32)$$

$$h_c^2 \left( \frac{x_0^2}{z_0^2 h_a^2} + \frac{y_0^2}{z_0^2 h_b^2} \right) < 1 \quad (5.33)$$

where  $\hat{\mathbf{r}}_0$  is expressed in hyperboloid frame and

$$\hat{\mathbf{u}}(v) = \frac{[h_a \cos v, h_b \sin v, h_c]^T}{\sqrt{h_a^2 \cos^2 v + h_b^2 \sin^2 v + h_c^2}} \quad (5.34)$$

is the unit vector that defines the quadratic cone at  $v$ . To clarify, Eq. (5.32) formulates the condition on the angle between the zero-velocity surface and  $\hat{\mathbf{r}}_0$  and Eq. (5.33) determines whether  $\hat{\mathbf{r}}_0$  points in a direction where motion is forbidden. Unfortunately the  $v$  such that  $\arccos(\hat{\mathbf{u}}(v) \cdot \hat{\mathbf{r}}_0)$  is minimized is not easily found analytically, so either the value must be numerically computed over  $[0, 2\pi)$  or the critical value of  $v$  must be found numerically.

It may not be necessary to go to that trouble since analytical sufficient forms of Eq. (5.32) seem adequate to determine boundedness or un-boundedness of hovering in real systems. Boundedness is guaranteed if the quadratic cone of revolution where  $h_a = h_b$  (which forbids motion in a smaller region than the actual zero-velocity surface) intersects the dead-band surface for all  $v$ , or equivalently, satisfies Eq. (5.32). This condition can be reduced to Eq. (5.35),

$$\beta \leq \frac{\pi}{2} - \gamma - \arccos(Q) \quad (5.35)$$

where  $\beta = \arctan(h_c/h_b)$  is the largest angle between the quadratic cone zero-velocity surface and the plane defined by  $\hat{v}_2$  and  $\hat{v}_3$  (these are the independent directions of unrestricted motion). A sufficient condition for boundedness is that Eqs. (5.35) and (5.33) are satisfied.

Similarly, the zero-velocity surface is guaranteed not to intersect the dead-band surface for all  $v$  if the quadratic cone of revolution where  $h_b = h_a$  (which forbids motion in a larger region than the actual zero-velocity surface) does not satisfy Eq. (5.32). This condition can be reduced to the sufficient condition in Eq. (5.36),

$$\alpha > \frac{\pi}{2} - \gamma - \arccos(Q) \quad (5.36)$$

where  $\alpha = \arctan(h_c/h_a)$  is the smallest angle between the quadratic cone zero-velocity surface and the plane defined by  $\hat{v}_2$  and  $\hat{v}_3$ . The trajectory is certainly not bounded by the union of the dead-band surface and the zero-velocity surface if Eq. (5.36) is satisfied or Eq. (5.33) is not satisfied. This sufficient condition for non-intersection is not a sufficient or necessary condition for dynamical unboundedness of the trajectory; it does not preclude the possibility that the trajectory is bounded by the dynamics and it is not a necessary condition for incomplete intersection of the two bounding surfaces.

These two sufficient conditions can be easily applied to any given body as a function of position. For the ellipsoidal and realistic polyhedral shapes examined in this research, the sufficient condition for the trajectory to not be enclosed by the union of the dead-band and zero-velocity surfaces (satisfying Eq. (5.36) or not Eq. (5.33)) is satisfied at all locations in the  $+,-,-$  hovering region. The areas “closest” to not satisfying this sufficient condition were found near the border with the  $+,+,-$  region above the shortest extents of the body. This does not mean that the spacecraft motion is certainly unbounded, but the region of energetically allowable motion is not finite.

It can be concluded from these criteria that using a dead-band control of the form in Eq. (5.29) based on optical navigation measurements that give information about the spacecraft longitude and latitude is not an effective means of ensuring boundedness of a hovering trajectory in the  $+,-,-$  region close to a small-body. However, some optical navigation techniques yield some information about the altitude of the spacecraft. Future work should look at the use of these optical measurements as a basis for a bounding dead-band hovering control. Future work could also look at applying these criteria in the circular-restricted and Hill three-body problems to determine if optical navigation measurements are an effective basis of a dead-band further from the small-body. Even if this is possible, care would have to be taken to be sure that fourth body effects from nearby planets or passing small-bodies do not destroy the boundedness during the applicable time frame.

### 5.3 Control Application

This section presents a brief analysis of the practical implementation issues of fuel use and the frequency of dead-band thrust activation.

### 5.3.1 Ideal Fuel Cost of Hovering

An ideal estimate of the  $\Delta V$  required to maintain hovering at a given position can be obtained by multiplying the nominal acceleration (without thrust) at the hovering position by the duration of hovering (Eq. (5.37))[7].

$$\Delta V_{ideal} = \|\tilde{\mathbf{a}}_0\| \Delta t \quad (5.37)$$

For the two-body problem in the small-body fixed frame, the daily  $\Delta V$  requirement for hovering near a spherical body can be computed using Eq. (5.38),

$$\Delta V_{daily}(\chi, \phi) = \chi^{-2} P(\chi, \phi) \Pi \quad (5.38)$$

where  $\chi = \|\tilde{\mathbf{r}}\|/R_r$  is the normalized hovering distance,  $P(\chi, \phi) = \sqrt{|1 + (\chi^6 - 2\chi^3) \cos^2 \phi|}$  is the position coefficient, a function of hovering latitude, and  $\Pi = (86400 s) \mu_{sb}/R_r^2$  is the daily fuel cost coefficient. This formula gives a reasonable “back of the envelope” prediction for hovering in arbitrary potential fields. Note that Eq. (5.38) should only be used for hovering positions close to the small-body where the two-body assumptions are valid. It does not include accelerations due to solar effects which become increasingly relevant as  $\chi$  increases[14].

Values of the position coefficient are shown in Figure 5.10. For hovering above the equator, ideal fuel cost goes to zero at the resonance radius since it is an equilibrium for spherical bodies. As the hovering distance is increased further, the coefficient value rises as a cubic. For inertial frame hovering (Section 3.4.2),  $P(\chi, \phi) \equiv 1$ . Note that when  $\chi = \sqrt[3]{2}$ , the fuel cost of hovering is the same at all latitudes.

Table 5.1 gives the daily fuel cost coefficient for various real small-bodies (modeled as pointmass potentials). The required  $\Delta V_{daily}$  spans several orders of magnitude across the spectrum of objects under the classification of small-body. These numbers

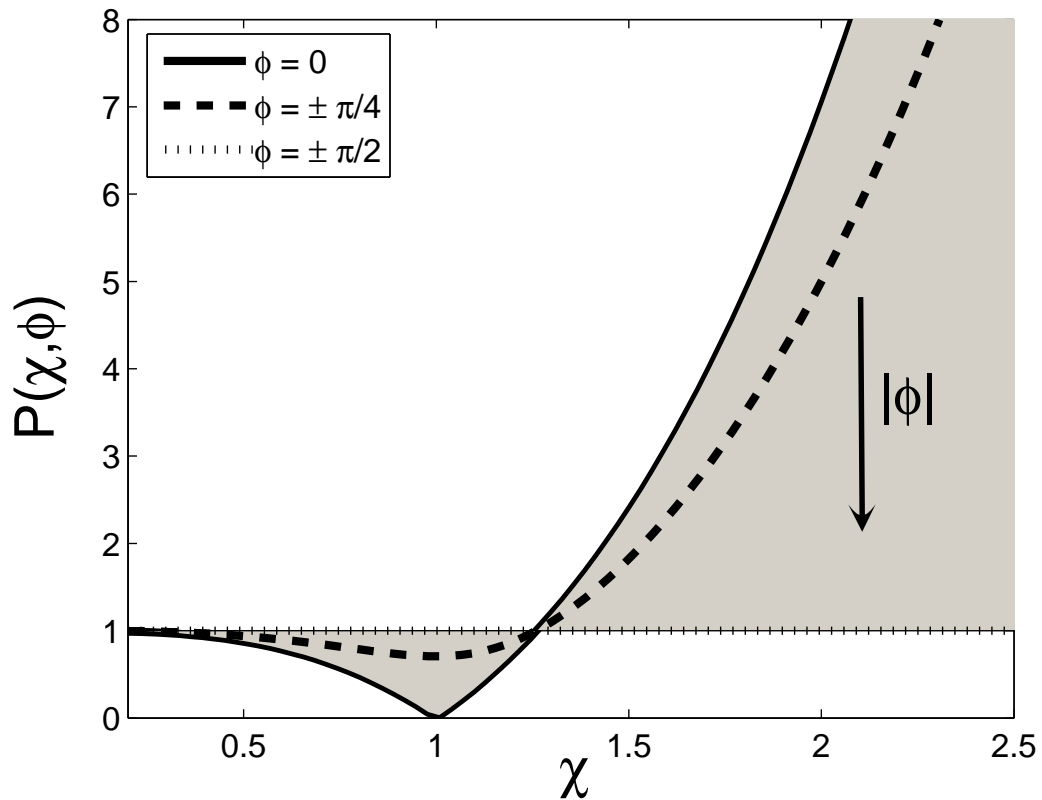


Figure 5.10: Position Coefficient for Fuel Usage as a Function of Latitude and Range demonstrate one reason why hovering is considered a viable strategy only for smaller small-bodies; hovering near the large asteroid Vesta generally requires many  $km/s$  of  $\Delta V$  per day (unless hovering near an equilibrium)! On the other hand, hovering near Itokawa (which was done in the inertial frame by Hayabusa<sup>1</sup>) is very feasible from a fuel cost point-of-view, requiring on the order of only a  $m/s$  of  $\Delta V$  or less per day.

<sup>1</sup>For the range at which inertial hovering was used during the Hayabusa mission, the SRP was the dominate acceleration so Eq. (5.38) is not appropriate for calculation of the required daily  $\Delta V$ .

Small-body	$\mu_{sb}$ ( $km^3/s^2$ )	Rotation period ( <i>hrs</i> )	$R_r$ ( <i>km</i> )	$\Pi$ ( <i>m/s</i> )
Itokawa[68]	$2.39 E - 9$	12.13	0.487	0.87
Deimos[69]	$9.8 E - 5$	30.29	30.90	8.87
Eros[21]	$4.46 E - 4$	5.27	15.96	151
Vesta[70]	17.8	5.34	550	5080

Table 5.1: Daily Fuel Cost Coefficient for Several Small-bodies

### 5.3.2 Fuel Usage Under Dead-band Control

HoverSim can be used to determine the accuracy of the ideal  $\Delta V$  solution (Eq. (5.37)) for hovering under dead-band control. The simulation computes the fuel used via the simple integration in Eq. (5.39).

$$\Delta V(t) = \int_0^t \left\| \tilde{\mathbf{T}}_{OL} + \tilde{\mathbf{T}}_{DB} \right\| dt \quad (5.39)$$

Here it is assumed that spacecraft can apply  $\tilde{\mathbf{T}} = \tilde{\mathbf{T}}_{OL} + \tilde{\mathbf{T}}_{DB}$  in an arbitrary direction without any cancellation. This formulation is minimum bound on  $\Delta V$  since a spacecraft would likely use a combination of thrusters to achieve  $\tilde{\mathbf{T}}$  that would generally involve some cancellation between thrusters.

It is clear from Eq. (5.40) that if full cancellation of the nominal acceleration is applied via open-loop thrust, then the actual  $\Delta V$  must be larger than predicted by Eq. (5.37) if  $T_m > \left\| \tilde{\mathbf{T}}_{OL} \right\|$  for a perturbed case.

$$\Delta V(t) = \int_0^t \sqrt{\|\tilde{\mathbf{a}}_0\|^2 + T_m^2 + 2T_m \|\tilde{\mathbf{a}}_0\| (\hat{\mathbf{c}} \cdot \hat{\mathbf{a}}_0)} dt \quad (5.40)$$

The assumption that  $T_m$  is large is an important part of the argument that the Jacobi constant is preserved under dead-band control, so this would be the case for hovering in this manner.

For one-dimensional hovering, it can be seen in Eq. (5.40) that a trajectory which repeatedly hits the dead-band boundary where the open-loop thrust and dead-band

thrust are in opposition ( $\tilde{\mathbf{T}}_{OL}^T \tilde{\mathbf{T}}_{DB} < 0$  or  $\hat{\mathbf{c}} \cdot \hat{\mathbf{a}}_0 < 0$ ) will be more fuel efficient than a trajectory that repeatedly hits the opposite boundary. This can be said because the linearized dynamics are symmetric with respect to both dead-band boundaries and predict an equal number of dead-band thrusts for both sides (see Section 5.3.3). For the typical one-dimensional hovering setup where the radial distance to the more fuel efficient boundary is larger than to the other boundary, this effect is strengthened in the non-linear dynamics (for a pointmass gravity field, but generally applicable) since the actual acceleration due to gravity is larger than predicted by the linear model on both sides of the nominal position. This means that the time between dead-band thrusts is shorter than predicted by the linear dynamics when  $\|\tilde{\mathbf{r}}\| < \|\tilde{\mathbf{r}}_0\|$  and longer when  $\|\tilde{\mathbf{r}}\| > \|\tilde{\mathbf{r}}_0\|$ . This assertion is supported by numerical simulations, but the actual fuel savings are not drastic.

Fuel efficiency for a given one-dimensional hovering position can also be improved by adjusting the open-loop component of the control such that it only cancels nominal acceleration in the  $\hat{\vartheta}_3$  direction. This can be shown by substituting  $\tilde{\mathbf{T}}_{OL} = -(\tilde{\mathbf{a}}_0 \cdot \hat{\vartheta}_3) \hat{\vartheta}_3$  into Eq. (5.40) and defining the dead-band as in Eq. (4.9) such that  $\hat{\mathbf{v}}_c = \hat{\vartheta}_3$  and  $\hat{\mathbf{c}} = \pm \hat{\vartheta}_3$  so that  $\Delta V$  is defined by Eq. (5.41).

$$\Delta V(t) = \int_0^t \sqrt{\|\tilde{\mathbf{a}}_0\|^2 (\hat{\mathbf{a}}_0 \cdot \hat{\vartheta}_3)^2 + T_m^2 \pm 2T_m \|\tilde{\mathbf{a}}_0\| (\hat{\mathbf{a}}_0 \cdot \hat{\vartheta}_3)} dt \quad (5.41)$$

The integrand here is clearly smaller than in Eq. (5.40) so the fuel use with this type of dead-band control will be less if the number of dead-band activations is the same. The linear dynamics in this case still have the same acceleration along  $\hat{\vartheta}_3$  as in the nominal case, so the number of dead-band activations should remain the same. For the full non-linear dynamics, numerical simulation supports this assertion and shows that changing the open-loop thrust in this manner seems to always result in less fuel

usage than in the nominal case.

Finally, an observation can be made from the numerical simulation data. As the magnitude of the open-loop thrust is reduced for a particular position (as studied in Sections 5.1 and 5.2.1), the total  $\Delta V$  required tends to decrease. Figure 5.11 shows the  $\Delta V$  used as a function of time for various levels of open-loop thrust under one-dimensional dead-band control at  $\tilde{\mathbf{r}}_0 = [294, 294, -240]$  m above a 350 x 180 x 170 m ellipsoid with  $\rho = 2.0$  g/cm<sup>3</sup> and a 12.132 hr rotation period. If using altitude

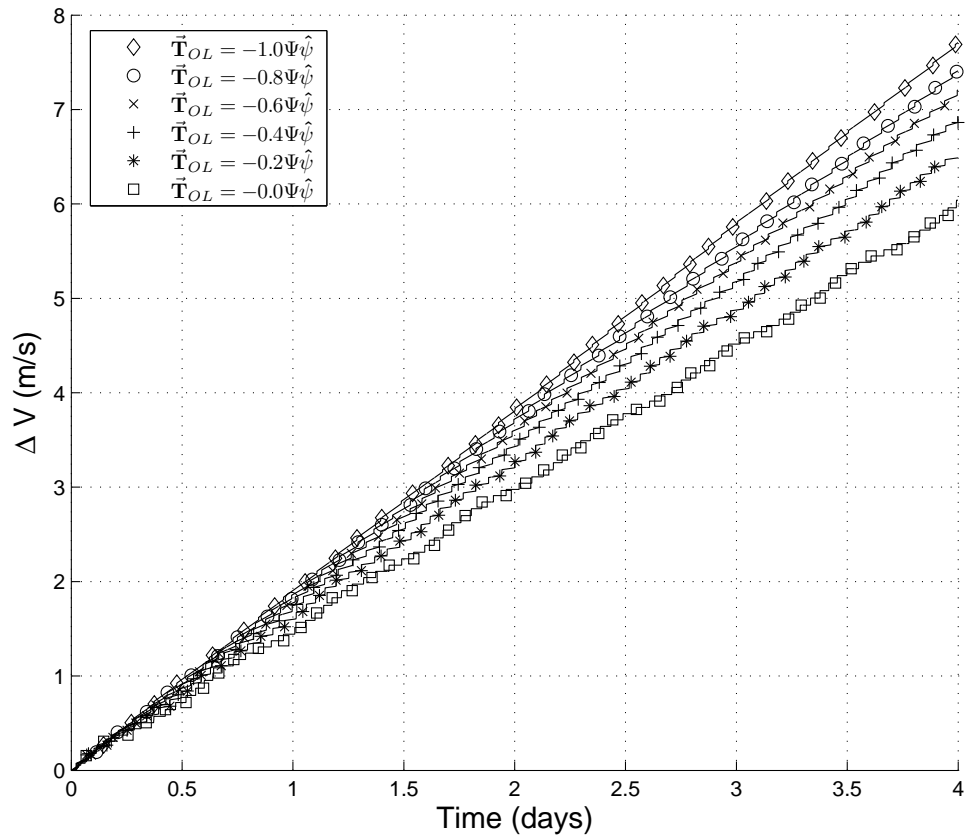


Figure 5.11: Required  $\Delta V$  vs. Time for Varying Open-loop Thrust Cancellation

measurements to define the dead-band in a one-dimensional hovering region, this observation sets up a trade between maximal fuel economy and boundedness (see

Figure 5.5). In some cases (such as in Figure 5.11 where  $\Delta V_{ideal} = 6.67 \text{ m/s}$ ), the required  $\Delta V$  is actually less than the ideal prediction in Eq. (5.37) for reduced levels of open-loop thrust.

### 5.3.3 Dead-band Control Application Frequency

An estimate of the time between subsequent dead-band thrust activations can be obtained by linearizing the dynamics around the nominal hovering position so that a closed form solution exists. Section 2.3.1 gives the linearized dynamics in the two-body problem, which are used here as an example. If  $A$  (Eq. (2.18) or the equivalent matrix for other time-invariant linear systems) is invertible and  $\tilde{\mathbf{T}}$  is constant, the identity in Eq. (5.42) holds,

$$\int_0^t e^{A(t-\tau)} \begin{bmatrix} \mathbf{0}_{3 \times 1} \\ \tilde{\mathbf{f}} \end{bmatrix} d\tau = A^{-1} [e^{At} - I_{6 \times 6}] \begin{bmatrix} \mathbf{0}_{3 \times 1} \\ \tilde{\mathbf{f}} \end{bmatrix} \quad (5.42)$$

and therefore, the linear equations of motion have the exact solution in Eq. (5.43).

$$\begin{bmatrix} \tilde{\mathbf{r}}(t) \\ \dot{\tilde{\mathbf{r}}}(t) \end{bmatrix} = e^{At} \begin{bmatrix} \tilde{\mathbf{r}}_0 \\ \dot{\tilde{\mathbf{r}}}_0 \end{bmatrix} + A^{-1} [e^{At} - I_{6 \times 6}] \begin{bmatrix} \mathbf{0}_{3 \times 1} \\ \tilde{\mathbf{f}} \end{bmatrix} \quad (5.43)$$

The condition that  $A$  be invertible is equivalent to requiring that  $\partial^2 J_{bf} / \partial \tilde{\mathbf{r}}^2|_0$  be invertible. Chapter IV showed that this condition is met everywhere except on the boundary between hovering regions (i.e., between the  $+,+,-$  and  $+,-,-$  or the  $+,-,-$  and  $-,-,-$  regions).

For a known state at a some initial time, Eq. (5.43) can be used in conjunction with  $f_{db}$  to estimate the time until  $f_{db} = \gamma$  numerically. If a one-dimensional dead-band of the form in Eq. (4.9) is assumed, then solving the implicit Eq. (5.44) for  $t$  gives the time of the next intersection.

$$|\hat{\mathbf{v}}_c \cdot (\tilde{\mathbf{r}}(t) - \tilde{\mathbf{r}}_0)| - \gamma = 0 \quad (5.44)$$

Since the dynamics are linear and time-invariant, a large initial guess is always appropriate to avoid converging to the trivial solution  $t = 0$ .

This approach approximates the transit time between any state and the next dead-band crossing in the full non-linear equations of motion well if  $\gamma$  is sufficiently small so that the linear approximation is reasonable across the region of possible motion. As such, for a fixed dead-band size, this approximation is more accurate further from the body where the linear approximation of the gravitational potential is accurate for a larger region of space.

## 5.4 Simulations

This section presents numerical simulations to demonstrate the effects of some common uncertainties relevant dead-band hovering control implementation on a real spacecraft. The effects of errors in the open-loop thrust magnitude and direction, errors in initial state estimate, finite dead-band thrust magnitude, errors in measurements values, errors in the small-body density estimate, and finite measurement sampling frequencies are examined here.

The Jacobi constant is the primary measure of how well the theory holds under these perturbations. It is desirable for the Jacobi constant to remain close to the nominal value over time with minimal oscillations. This means that the zero-velocity surface remains near its nominal configuration and will continue to effectively bound the spacecraft motion assuming adequate dead-band control authority. At worst, the Jacobi constant must stay within the allowable range for global boundedness (Section 4.3.4). A second way to evaluate the effectiveness of the theory is to look at the trajectory and see if it stays within the predicted region. If it does, that suggests the second order expansion of the zero-velocity surface is valid for the given

dead-band size.

#### 5.4.1 Hovering with Small Errors in Initial State and Realistic Thrusters

Theoretical results on the effects of small-errors in initial position and changing open-loop thrust have been presented in Sections 4.3.1 and 5.1 respectively. Figure 4.5 qualitatively presents simulation data that shows how the predicted zero-velocity surface (adjusted for a small error in initial state) properly contains the trajectory. Here, simulation results that demonstrate the combined effects of small errors in initial state, open-loop thrust errors (constant in time), and a finite  $T_m$  are presented quantitatively. Except for the effect of finite  $T_m$ , the errors addressed here are relatively benign since they only change the initial value of the Jacobi constant. After the initial perturbation, the zero-velocity surface continues to apply for the remainder of the trajectory.

Figure 5.12 shows a trajectory (heavy black line) integrated for a 5 day hovering duration under two-dimensional dead-band control (Eq. (4.10),  $\gamma = 40 m$ ) with open-loop cancellation of  $\tilde{\mathbf{a}}_0$  (nominally). The central body for this simulation is a polyhedral shape of Itokawa (Ostro *et al.* rough model[36]) with  $\rho = 1.9 g/cm^3$  and a rotation period of 12.132hrs. The nominal hovering position is  $[550, -310, -140]^T m$  with  $\delta\tilde{\mathbf{r}}_0 = [10, -5, -5]^T m$  and  $\delta\dot{\tilde{\mathbf{r}}}_0 = [1, 0, 2]^T mm/s$ . Each Cartesian component of the error in the open-loop thrust was chosen from a zero-mean normal distribution with standard deviation of  $0.01 \|\tilde{\mathbf{a}}_0\|$ .  $T_m$  is finite here with magnitude of  $3 E-3 m/s^2$ , about 580 times the nominal acceleration magnitude without thrust.

The figure clearly shows that the spacecraft trajectory stays inside the region predicted by the theory in this thesis. Here, the bounding surfaces are in gray; the zero-velocity surface is the hourglass shaped hyperboloid and the dead-band surface

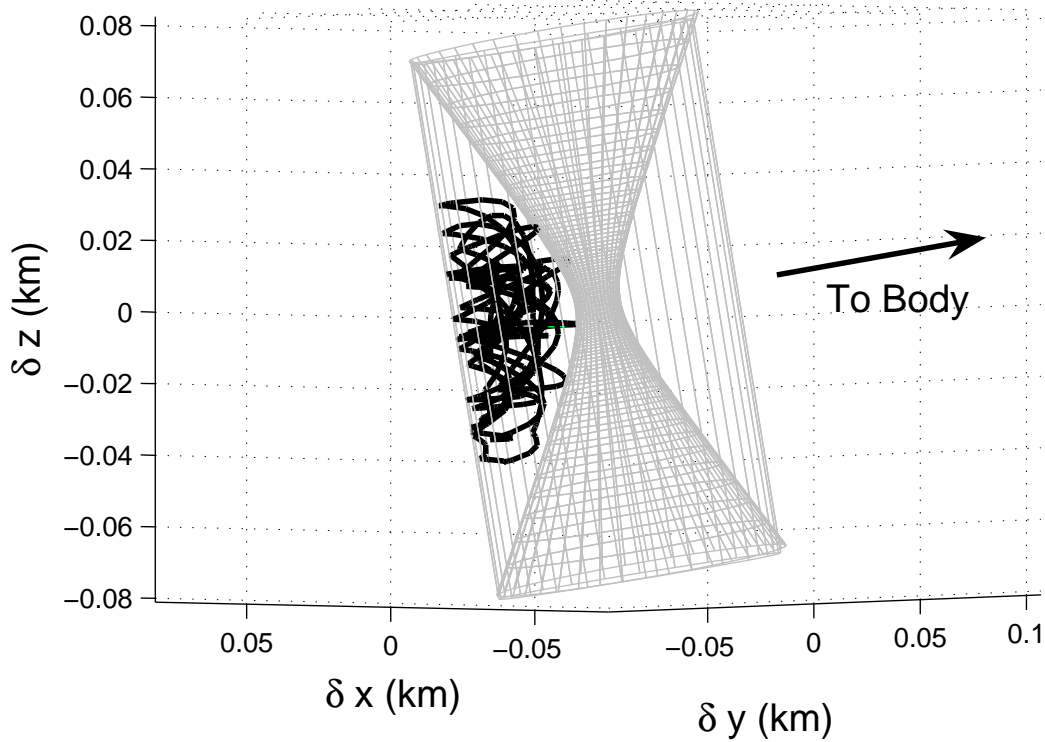


Figure 5.12: Trajectory Under Two-dimensional Dead-band Control with Errors in Initial State and Open-loop Thrust with Finite  $T_m$  (dead-band and zero-velocity surface boundaries shown in gray)

is the cylinder. The zero-velocity surface seems to correspond well with the actual spacecraft motion which suggests the quadratic expansion of the Jacobi constant is valid for this dead-band size. The longest dimension of the Itokawa model is about  $590\text{ m}$ , so showing the quadratic zero-velocity surface theory holds in a region approximately  $140 \times 80 \times 80\text{ m}$  is encouraging and may represent a reasonable space for operations.

Figure 5.13 shows the value of the Jacobi constant versus time for this trajectory. The initial value of  $J$  is preserved very well over the duration of the simulation. This means that the idealized thrust assumption used in Section 4.2 to show that the

Jacobi constant is preserved under dead-band control was a good one for large  $T_m$ . The brief spikes in the Jacobi constant value represent times when the spacecraft is outside the dead-band and dead-band thrust is active.

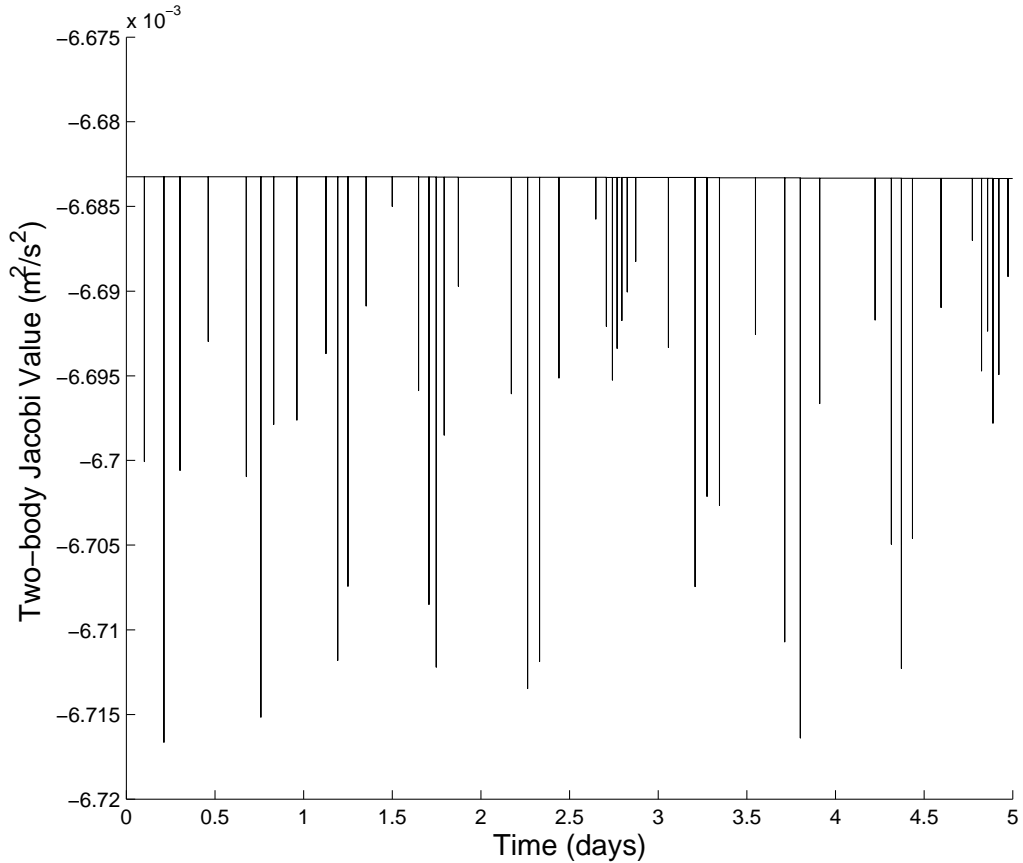


Figure 5.13: Jacobi Constant Versus Time for a Trajectory Under Two-dimensional Dead-band Control with Finite  $T_m$  and Errors in Initial State and Open-loop Thrust

#### 5.4.2 Hovering with Measurement Errors and Finite Sampling Frequencies

Next, the effects of an altimeter sampling frequency and measurement errors are shown via simulation of one-dimensional altitude dead-band hovering above an oblate  $10 \times 10 \times 8 \text{ km}$  ellipsoid with  $\rho = 3.0 \text{ g/cm}^3$  and a rotation period of  $7.5 \text{ hrs}$ .

For these simulations, the initial position of  $[10.5, 7.5, 2.5]^T$  km is well within the bounded region for this altitude dead band where  $\gamma = 30$  m and  $\hat{\mathbf{s}} = -\hat{\mathbf{v}}_3$ ; the surface of the small-body is almost flat in the vicinity of  $\tilde{\rho}_0$ .

Figure 5.14 demonstrates the boundedness of hovering under this altitude dead-band with full open-loop cancellation of the nominal acceleration. For this plot, there are no errors in the altitude measurement nor does the altimeter have a delay between measurements. There are only errors in initial position and velocity ( $\delta\tilde{\mathbf{r}}_0 = [-15, 5, -10]^T$  m and  $\delta\dot{\tilde{\mathbf{r}}}_0 = [0, -2, 1]^T$  cm/s) and a finite  $T_m$  ( $\approx 87 \|\tilde{\mathbf{a}}_0\|$ ). The spacecraft trajectory can be seen to remain inside of the predicted zero-velocity surface (in gray) for the 5 day simulation duration. Figure 5.15 shows the Jacobi constant of this trajectory versus time. It varies only slightly on account of the finite  $T_m$  and the integration tolerances. These figures demonstrate the validity of the boundedness criteria for altimeter dead-band control as well as the perturbed zero-velocity surface result.

However, when altitude measurements occur only every 0.5 seconds and each measurement is given a random error (from a normal distribution with standard deviation of 1 m, nominal altitude here is 3.24 km), the behavior of this trajectory changes dramatically. Figures 5.16 and 5.17 show the trajectory with the predicted initial zero-velocity surface and the Jacobi constant versus time respectively for an integration period of 1hr. It can be seen that the Jacobi constant is not well preserved at all, even over this relatively short period of time, and by effect, the predicted zero-velocity surface poorly predicts the allowable region of motion. In fact, the velocity of the spacecraft grows large enough so that the dead-band thrust is no longer effective (and decreasingly so) at quickly returning the spacecraft to the dead-band.

The Jacobi constant is not preserved through dead-band thrust activation here

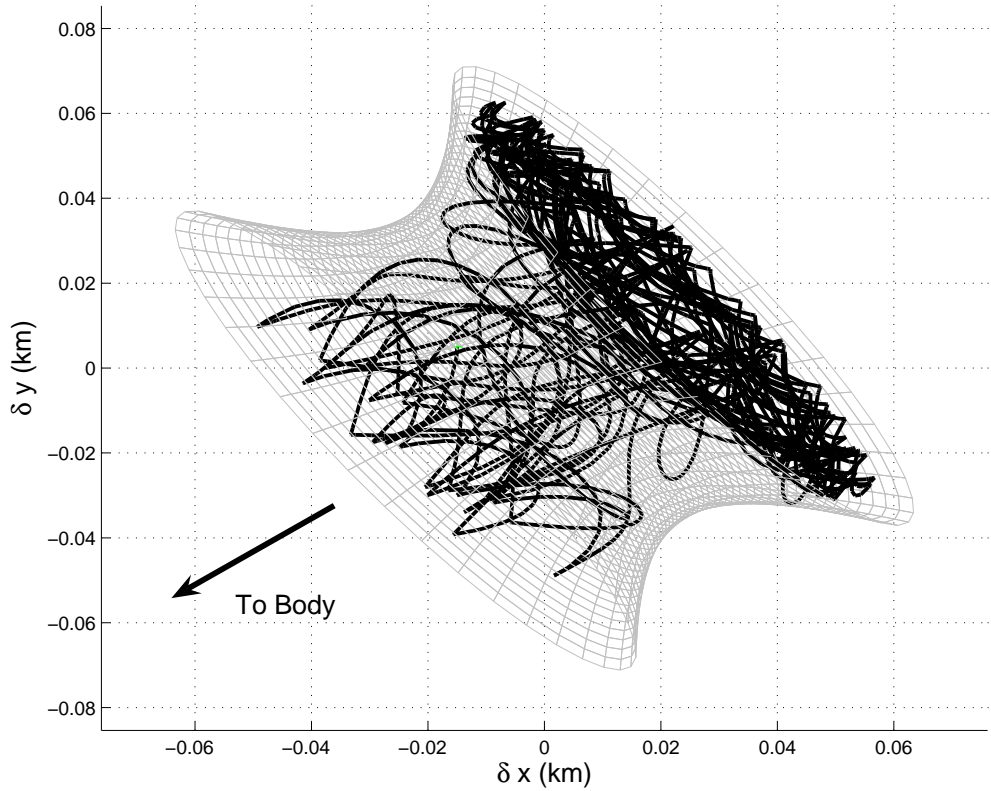


Figure 5.14: Jacobi Constant Versus Time for a Trajectory Under Altitude Dead-band Control with Errors in Initial State and Finite  $T_m$

because of the errors in altitude measurement and the altimeter sampling frequency. Uncertainty in altitude can cause the dead-band thrust to activate and turn off too early or too late. This should cause a random positive or negative variation in the magnitude of the spacecraft speed normal to the boundary after the dead-band crossing ( $\dot{\mathbf{r}}_+ \cdot \hat{\nu}_3$ ) with respect to the normal entry speed ( $\dot{\mathbf{r}}_- \cdot \hat{\nu}_3$ ). This change in magnitude of  $\dot{\mathbf{r}}$  gives a corresponding change in Jacobi constant.

The effect of a finite measurement sampling frequency is the real problem here. The dead-band thrust is not activated until the spacecraft knows that  $f_{db}(\tilde{\mathbf{r}}) > \gamma$  and it is not shut off until the spacecraft knows that  $f_{db}(\tilde{\mathbf{r}}) < \gamma$ . Thus, thrust will

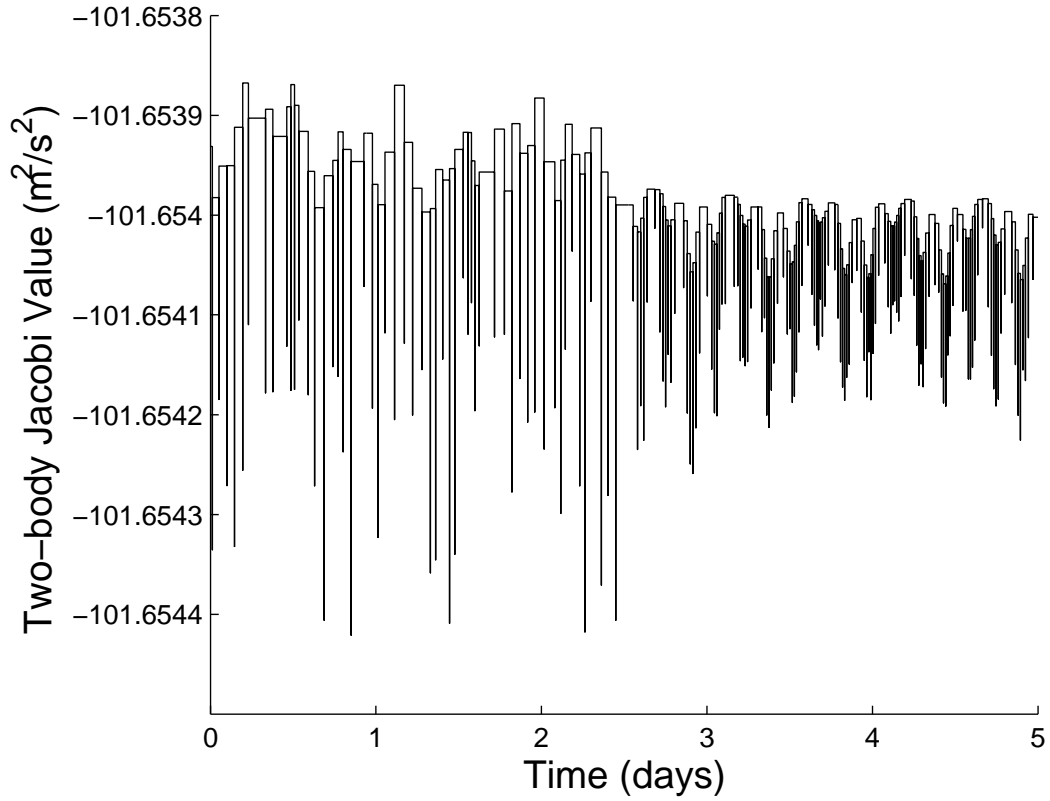


Figure 5.15: Jacobi Constant Versus Time for a Trajectory Under Altitude Dead-band Control with Errors in Initial State and Finite  $T_m$

always be turned on later than (or equal to in the best case) the time assumed in the theory and will be turned off later than the proper cut-off time. Both mis-timings result in an increase in the magnitude of  $\dot{\tilde{\mathbf{r}}}_+$ . When thrust cuts on late, the incoming velocity at  $f_{db}(\tilde{\mathbf{r}}) = \gamma_1^* > \gamma$  has increased beyond its nominal value. If a constant acceleration is assumed outside of the dead-band, the late thrust activation already means the velocity magnitude will be larger still at  $f_{db}(\tilde{\mathbf{r}}) = \gamma$  upon return to the dead-band since it will be equal to the increased incoming value at  $f_{db}(\tilde{\mathbf{r}}) = \gamma_1^*$  (since it is ballistic motion in a constant gravity field), then continue to increase. The velocity is augmented further until thrust is shut off at  $f_{db}(\tilde{\mathbf{r}}) = \gamma_2^* < \gamma$ . Finite measurement frequency causes a uniform increase in the Jacobi constant which will

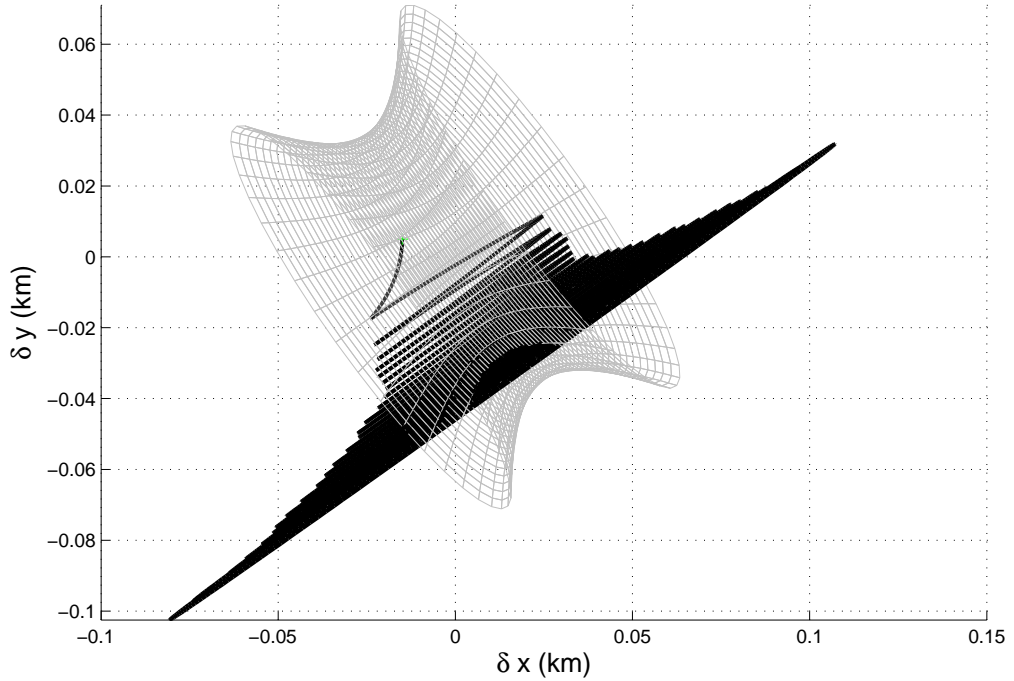


Figure 5.16: Trajectory Under Altitude Dead-band Control with Measurement Errors and Finite Sampling Frequency

eventually lead to escape or impact with the small-body. Figure 5.17 suggests this may happen in a relatively short period of time. This effect occurs for all types of dead-band control where activation is based on measurement values and must be addressed when implementing a controller that relies on the Jacobi constant (the zero-velocity surface) being maintained.

In order for this effect to be manageable, the mean value of  $\left(\left\|\dot{\mathbf{r}}_{-}\right\| - \left\|\dot{\mathbf{r}}_{+}\right\|\right)$  over all the dead-band crossings (proportional to the change in  $J$ ) must be zero. One approach to achieving this goal is to apply dead-band thrust for a specific amount of time based on the state at the initial dead-band crossing. This approach eliminates

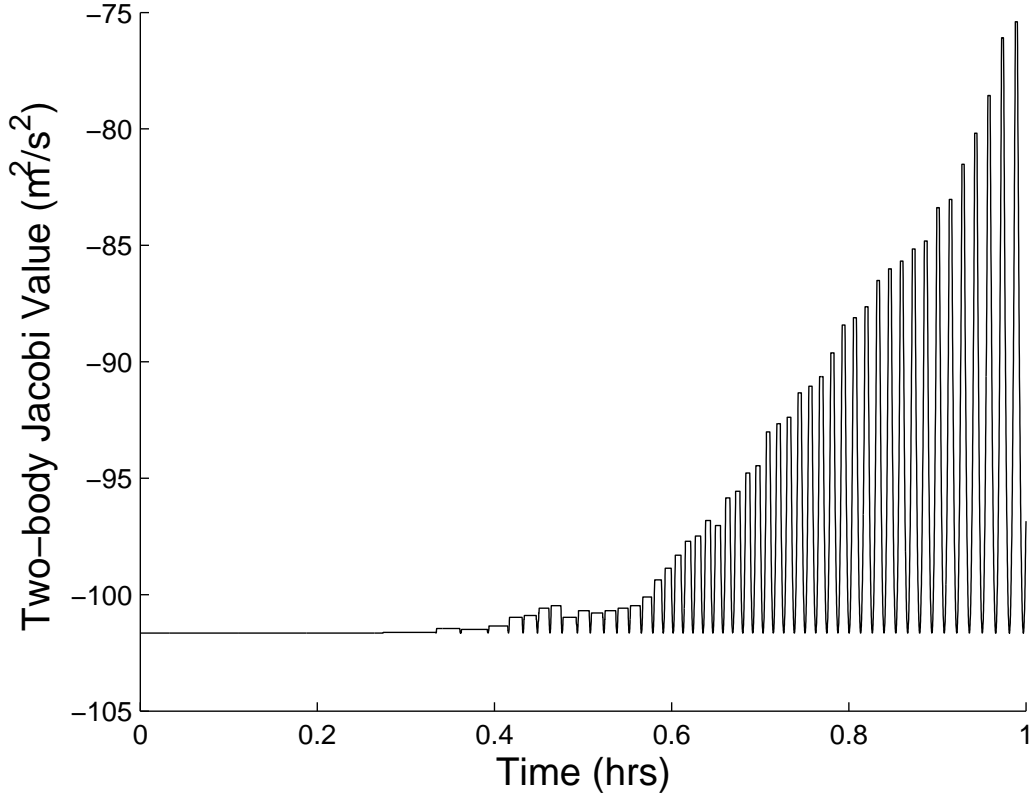


Figure 5.17: Jacobi Constant Versus Time for a Trajectory Under Altitude Dead-band Control with Measurement Measurement Errors and Finite Sampling Frequency

the error induced by the thrust cut off time. In simulation this can be achieved by integrating the trajectory until the spacecraft reaches the dead-band boundary, then using the impulsive  $\Delta V$  assumption (Eq. (4.8)) to compute the duration the dead-band thrust should be fired,  $t_{\Delta V}$  (Eq. (5.45)), from the current state<sup>2</sup>.

$$t_{\Delta V} = \frac{2 \left| \dot{\mathbf{r}}_- \cdot \hat{\vartheta}_3 \right|}{T_m} \quad (5.45)$$

---

<sup>2</sup>If the spacecraft acceleration is constant across the range of motion outside the dead-band, applying thrust for this time preserves the Jacobi constant perfectly. For a realistic gravity field, applying thrust for this time causes a slow drift in Jacobi constant proportional to the distance traveled outside the dead-band (inversely proportional to  $T_m/||\hat{\mathbf{a}}_0||$ ). For large  $T_m$ , such that  $t_{\Delta V}$  is small, the rate of change in  $J$  due to this approximation is shown to be small by numerical simulation. Nonetheless, an occasional corrective maneuver may be necessary if the induced change in  $J$  approaches  $\Delta J_+$  or  $\Delta J_-$ .

A random error in  $\left(\left\|\dot{\mathbf{r}}_{-}\right\| - \left\|\dot{\mathbf{r}}_{+}\right\|\right)$  is achieved by adding random error to  $t_{\Delta V}$  with zero mean.

Such an approach is demonstrated by the simulation results in Figures 5.18 and 5.19. The parameters of this simulation are the same as used previous previously (Figures 5.14 and 5.16) and the random error in  $t_{\Delta V}$  is drawn from a normal distribution with a 1 *ms* standard deviation (nominal  $t_{\Delta V}$  is between 0.1 and 0.2 seconds for this case). The Jacobi constant in this case exhibits sufficiently small random

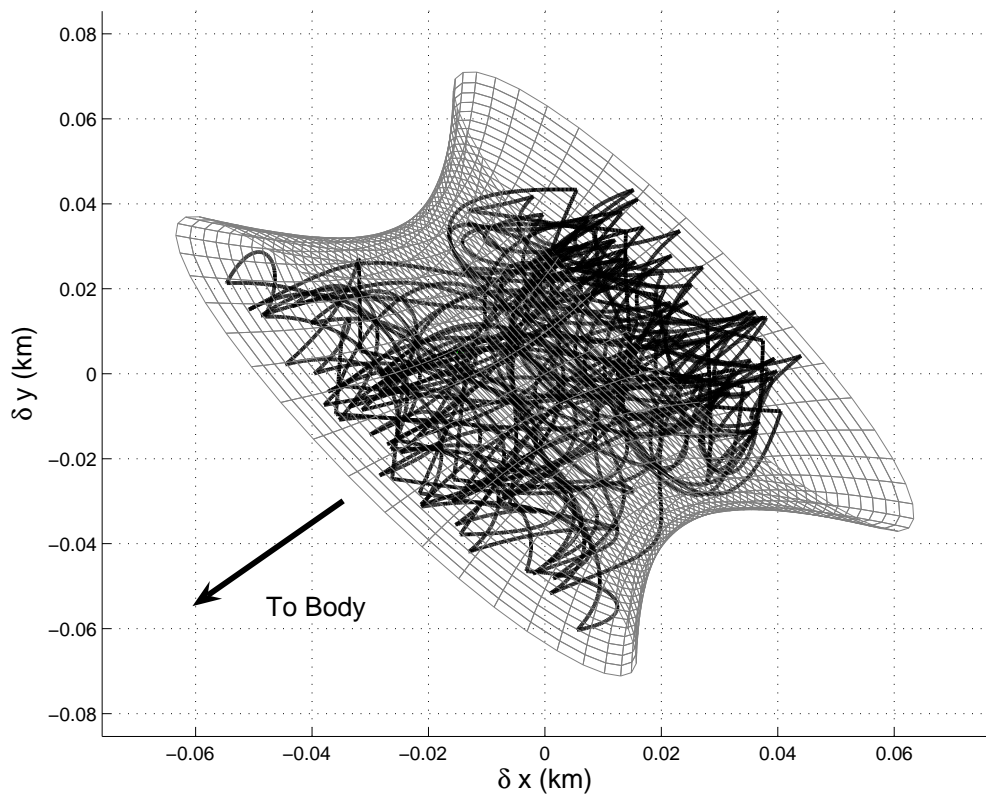


Figure 5.18: Trajectory Under Altitude Dead-band Control with Fixed Duration Dead-band Thrust

variations about the nominal value such that the trajectory is well contained in the

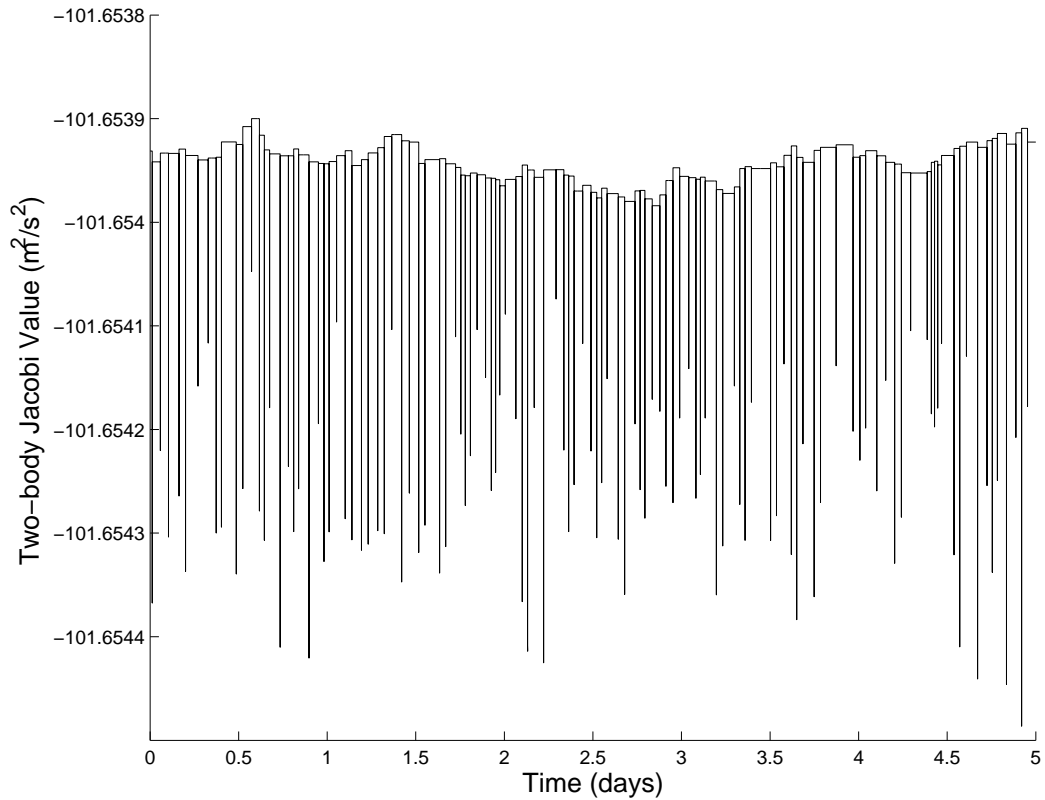


Figure 5.19: Jacobi Constant Versus Time for a Trajectory Under Altitude Dead-band Control with Fixed Duration Dead-band Thrust

predicted region over the 5 day simulation time<sup>3</sup>.

Applying thrust for a fixed duration based on the state when the spacecraft leaves the dead-band seems to be a good approach to mitigating the change in Jacobi constant due to dead-band thrust on/off timing. Of course, in a realistic implementation, there would be some error in the turn on time, but if  $t_{\Delta V}$  is computed from the state at that time, the error in burn time is the only source of error. For a finite measurement frequency, the state (or even just  $h$  and  $\dot{h}$ ) and time of the dead-band crossing could be predicted by a measurement filter and an appropriate model of the

---

<sup>3</sup>The change in Jacobi constant induced by error in the impulsive assumption is about  $-1 E - 5 m^2/s^2$  after 5 days here.

dynamics.

Future work will implement this approach with the thrust turn on time and duration predicted by a measurement filter. Other methods of implementing the dead-band control such that the Jacobi constant is preserved should also be investigated in future studies.

## 5.5 Discussion

This chapter takes some of the first steps in bridging the gap between the bounded hovering theory that has been developed in the preceding chapters and its implementation in a real space mission. The discussion and simulations in Section 5.4.2 have shown us that this job is far from complete; a realistic method of implementing the dead-band control that does not significantly change the Jacobi constant over time must be found before this theory can be applied in a small-body mission.

Important theoretical results were presented in this chapter on the feasibility of using a dead-band control based on altimetry or optical navigation measurements. If station-keeping could be reduced to monitoring a single measurement type, it would be advantageous to a small-body mission through reduced instrument cost and operational complexity of the mission.

We found that, theoretically, hovering near the surface of an ellipsoidal small-body in the  $+, +, -$  zero-velocity surface region can often be maintained with altitude measurements only. For an arbitrarily shaped small-body, the formulation is more complex, but the qualitative results should be similar; changes in dead-band size, open-loop thrust, and the surface curvature should have similar effects as in the ellipsoidal case (Section 5.2.1) and we can expect that hovering closer to the surface or the smaller semi-major axes is more likely to be bounded than at other positions.

This is an important result for close proximity operations that could reduce the controller complexity during descent and touchdown maneuvers.

We were able to conclude that measurements of the unit vector from the small-body center of mass to the spacecraft are not an effective basis of a bounding dead-band control in the  $+, -, -$  zero-velocity surface region in the two-body problem. This would have been a very useful result if it were positive but the sufficient condition for incomplete intersection of the zero-velocity and dead-band surfaces was satisfied everywhere we looked.

Finally, simulations were presented in this chapter that verify the previous analytical work. Our numerical simulation capabilities (HoverSim and SBDT) continue to serve as a very useful laboratory for testing theory and observing hovering dynamics.

## CHAPTER VI

# Translation and Descent

In this chapter, the spacecraft translation and descent maneuvers are considered in an arbitrary gravitational field such as that near a small-body. Linearized dynamics are used here to give a closed form solution to the dynamics under a constant thrust. This solution is used to define a constant thrust control that moves the spacecraft between two arbitrary positions in a chosen time. A method for improving the performance of this controller by estimating the error associated with the linearization is also described. Numerical studies of the controller performance are presented for translations above asteroids Itokawa and Eros. A descent without thrust solution is also derived from the linearized equations which gives the locus of initial states that result in touchdown at a chosen position. A sensitivity study of constant thrust translation maneuvers to various model parameters is described with numerical covariance results given for maneuvers near models of the asteroids Itokawa, Eros, and Vesta. A multi-leg descent scenario to asteroid Eros is also described in detail. Finally, results of numerical simulations of descent under a sliding dead-band control are discussed.

## 6.1 Problem Formulation

The problem of translation is addressed here as an interception problem; determine the necessary maneuvers to arrive at a specified position regardless of final velocity. The guidance laws presented here are intended to be implemented autonomously; it is therefore implicitly assumed that the spacecraft has an on-board model of the small-body shape and estimates of rotation state and density.

The work in this chapter assumes the translation and descent maneuvers take place in close proximity to the small-body surface. As such, the dynamics of the two-body problem in the small-body fixed frame (Section 2.3.1) are used throughout, though the approaches presented can be extended to other time-invariant dynamics. The two-body equations of motion (Eq. (2.14)) are linear except for the attraction terms derived from the potential. If the attraction vector is linearized about its value at the nominal initial position, the linear equations of motion in Eq. (2.17) are found.

If only constant thrust (in the rotating frame) maneuvers are sought and the matrix  $\partial^2 J_{bf}/\partial \tilde{\mathbf{r}}^2|_{\tilde{\mathbf{r}}_0}$  is invertible, the identity in Eq. (5.42) holds which gives the closed form solution for the state at time  $t = t_f$  in Eq. (5.43). Now, there are six linear equations with sixteen potential variables (initial state, final state, time of transfer ( $t_f$ ), and thrust) that define the spacecraft motion. Given a set of known variables, this formulation can be cast as a solution for a number of different situations. One such solution was the time between dead-band crossings presented in Section 5.3.3. In this chapter, Eq. (5.43) is used to find solutions to two other problems: the free-drop and constant thrust translation problems.

## 6.2 Free-drop Solution

For a mission studying small-body composition, it is desirable to cut off spacecraft thrusters before reaching the surface to avoid contamination. Because of the small gravitational accelerations induced by these bodies, un-powered ‘free-drop’ descents are possible without excessive impact velocity. By rearranging the solution of the linearized dynamics in Eq. (5.43), the locus of initial states that result in impact at a given surface position without thrust (thrust is constant here with  $\tilde{\mathbf{T}} \equiv \mathbf{0}_{3 \times 1}$ ) are defined by Eq. (6.1) (note that the second derivatives of the small-body potential in matrix  $A$  are evaluated at  $\tilde{\mathbf{r}}(t_f)$  here).

$$\begin{bmatrix} \tilde{\mathbf{r}}_0 \\ \dot{\tilde{\mathbf{r}}}_0 \end{bmatrix} = e^{-At_f} \left( \begin{bmatrix} \tilde{\mathbf{r}}(t_f) \\ \dot{\tilde{\mathbf{r}}}(t_f) \end{bmatrix} - A^{-1} (e^{At_f} - \mathbf{I}_{6 \times 6}) \begin{bmatrix} \mathbf{0}_{3 \times 1} \\ \left. \frac{\partial U}{\partial \tilde{\mathbf{r}}} \right|_{\tilde{\mathbf{r}}(t_f)}^T - \left. \frac{\partial^2 U}{\partial \tilde{\mathbf{r}}^2} \right|_{\tilde{\mathbf{r}}(t_f)} \tilde{\mathbf{r}}(t_f) \end{bmatrix} \right) \quad (6.1)$$

For the free-drop problem, the surface target position and time of transfer are specified. If touchdown velocity is neglected, Eq. (6.1) yields three equations and six unknowns. This defines a three dimensional manifold of initial states in six dimensional phase space that result in touchdown at the target for the chosen transfer time (in the linear dynamics). If an initial velocity is specified (zero for instance), a line of qualifying initial positions parameterized by  $t_f$  is defined. The manifold of initial states defined by the free-drop solution is useful as a target space for the preceding transfers.

## 6.3 Constant Thrust Solution

The general interception problem can be solved by applying a constant thrust in Eq. (5.43). In this formulation, an initial state, final position, and transfer time are specified and the appropriate thrust to complete the transfer is determined. By

rearranging Eq. (5.43), this necessary thrust is found (Eq. (6.2)),

$$\tilde{\mathbf{T}} = G(4 : 6, :) \left( \begin{bmatrix} \tilde{\mathbf{r}}(t_f) \\ \dot{\tilde{\mathbf{r}}}(t_f) \end{bmatrix} - e^{At_f} \begin{bmatrix} \tilde{\mathbf{r}}_0 \\ \dot{\tilde{\mathbf{r}}}_0 \end{bmatrix} \right) - \frac{\partial U}{\partial \tilde{\mathbf{r}}} \Big|_{\tilde{\mathbf{r}}_0}^T + \frac{\partial^2 U}{\partial \tilde{\mathbf{r}}^2} \Big|_{\tilde{\mathbf{r}}_0} \tilde{\mathbf{r}}_0 \quad (6.2)$$

as well as a linear estimate of the resulting final velocity (Eq. (6.3)),

$$\dot{\tilde{\mathbf{r}}}(t_f) = G^{-1}(1 : 3, 4 : 6) \left( G(1 : 3, :) e^{At_f} \begin{bmatrix} \tilde{\mathbf{r}}_0 \\ \dot{\tilde{\mathbf{r}}}_0 \end{bmatrix} - G(1 : 3, 1 : 3) \tilde{\mathbf{r}}(t_f) \right) \quad (6.3)$$

where

$$G = [e^{At_f} - \mathbf{I}_{6 \times 6}]^{-1} A. \quad (6.4)$$

The notation  $G(a : b, c : d)$  represents the  $a$ -th through  $b$ -th rows and  $c$ -th through  $d$ -th columns of matrix  $G$  (equivalent to the notation used in Matlab). A colon alone indicates all rows or columns are included. This thrust solution completes the transfer exactly in the linearized system. Errors arise in the true system due to the nonlinearity of the potential field.

### 6.3.1 Estimate of Linear Error

The error induced by nonlinearity of the potential in the constant thrust solution can be computed by comparing the linearized dynamics with the true dynamics. The solution to the non-linear two-body equations of motion (Eq. (2.14)) is given by Eq. (6.5),

$$\begin{bmatrix} \tilde{\mathbf{r}}(t) \\ \dot{\tilde{\mathbf{r}}}(t) \end{bmatrix}_{true} = e^{A_0 t} \begin{bmatrix} \tilde{\mathbf{r}}_0 \\ \dot{\tilde{\mathbf{r}}}_0 \end{bmatrix} + \int_0^t e^{A_0(t-\tau)} \begin{bmatrix} \mathbf{0}_{3 \times 1} \\ \frac{\partial U}{\partial \tilde{\mathbf{r}}} \Big|_{\tilde{\mathbf{r}}_{true}(\tau)}^T + \tilde{\mathbf{T}} \end{bmatrix} d\tau \quad (6.5)$$

where

$$A_0 = \begin{bmatrix} \mathbf{0}_{3 \times 1}, & \mathbf{I}_{3 \times 3} \\ \begin{bmatrix} \omega^2 & 0 & 0 \\ 0 & \omega^2 & 0 \\ 0 & 0 & 0 \end{bmatrix}, & \begin{bmatrix} 0 & 2\omega & 0 \\ -2\omega & 0 & 0 \\ 0 & 0 & 0 \end{bmatrix} \end{bmatrix}. \quad (6.6)$$

Error is computed in Eq. (6.7) by subtracting the solution to the linear dynamics.

$$\begin{aligned}
\mathbf{E}(t) &= \begin{bmatrix} \tilde{\mathbf{r}}(t) \\ \dot{\tilde{\mathbf{r}}}(t) \end{bmatrix}_{true} - \begin{bmatrix} \tilde{\mathbf{r}}(t) \\ \dot{\tilde{\mathbf{r}}}(t) \end{bmatrix}_{linear} \\
&= (e^{A_0 t} - e^{At}) \begin{bmatrix} \tilde{\mathbf{r}}_0 \\ \dot{\tilde{\mathbf{r}}}_0 \end{bmatrix}_{true} + e^{A_0 t} \int_0^t e^{-A_0 \tau} \begin{bmatrix} \mathbf{0}_{3 \times 1} \\ \frac{\partial U}{\partial \tilde{\mathbf{r}}} \Big|_{\tilde{\mathbf{r}}_{true}(\tau)}^T + \tilde{\mathbf{T}} \end{bmatrix} d\tau \\
&\quad - A^{-1} (e^{At} - \mathbf{I}_{6 \times 6}) \begin{bmatrix} \mathbf{0}_{3 \times 1} \\ \frac{\partial U}{\partial \mathbf{r}} \Big|_{\tilde{\mathbf{r}}_0}^T + \tilde{\mathbf{T}} - \frac{\partial^2 U}{\partial \mathbf{r}^2} \Big|_{\tilde{\mathbf{r}}_0} \tilde{\mathbf{r}}_0 \end{bmatrix}
\end{aligned} \tag{6.7}$$

Because of the integral involving the true path of the spacecraft, the error cannot be evaluated without explicitly integrating the non-linear equations of motion. However, if it is assumed that the nominal constant thrust solution derived from the linear dynamics is ‘close’ to the actual path, the integral can be evaluated along the linearized path to obtain a suitable approximation.

If it is further assumed that all paths near the true path have similar  $\partial U / \partial \tilde{\mathbf{r}}$  profiles over time, then the error vector can be assumed to be nearly the same since the integral is the only path dependent part of the error. If the magnitude of this error is sufficiently small, a phantom target position, defined in Eq. (6.8), can be chosen such that if Eq. (6.2) is used to calculate thrust to arrive at the phantom target, roughly the same error is invoked, and therefore, the spacecraft arrives very near the desired target.

$$\tilde{\mathbf{r}}_{phantom} = \tilde{\mathbf{r}}_{target} - \mathbf{E}(t_f) (1 : 3) \tag{6.8}$$

This method also yields an improved estimate of the final velocity by adding the velocity error in Eq. (6.7) with the predicted velocity in Eq. (6.3).

Using this error estimate approach, the original constant thrust translation controller is made more accurate without numerically integrating the equations of mo-

tion. Further, a closed form solution for the necessary transfer thrust and a well-defined nominal trajectory are maintained.

### 6.3.2 Accuracy of Translation Controller

Using an appropriate phantom target, the constant thrust controller can be shown numerically to be very accurate for translations inside a fairly large domain around the initial position. An idea of the limits of the accurate domain can be obtained by considering the case of translations in a point-mass potential field. The erroneous assumption in the derivation is that the attraction vector changes in a linear manner as the spacecraft position deviates from the initial position. In actuality, for a change of position in the radial direction, percentage error in this approximation grows as a cubic of the ratio of initial radius to final radius. If a line of constant radius along either a constant latitude or longitude line is traversed, the attraction vector changes as the cosine function. This suggests the linearity assumption is only valid for translations that involve small changes in latitude or longitude. Generally, translations across the same distance are more accurate further from the body since both the angular deviation and the ratio of initial radius to final radius change more slowly. This type of analysis closely predicts the error in the original controller formulation (Eq. (6.2)) before the error estimate is included. The qualitative properties of the error remain the same for the phantom target formulation; the domain of accurate translation is bounded by a maximum allowable angular deviation and a maximum radial deviation.

Contour plots in Figures 6.1 and 6.2 show numerical results for the nominal miss distances (difference between the target and numerically integrated final position) associated with a class of translations above asteroids Itokawa and Eros, respectively.

Figure 6.1 shows the nominal miss distance, in centimeters, for translations from a stationary initial position  $\tilde{\mathbf{r}}_0 = [300, 0, -150] \text{ m}$  (denoted by ‘+’) to targets in Itokawa’s  $X - Z$  plane with a transfer time of 1200 s. A rotation period of 12.132 hrs and a density of  $2.5 \text{ g/cm}^3$  are assumed for the polyhedral model of Itokawa[35]. The constant thrust controller misses the desired target by less than 8 cm for the translations on the order of a few hundred meters shown here. Figure 6.2 shows translations to points in the plane  $z = 5 \text{ km}$  from the initial position  $\tilde{\mathbf{r}}_0 = [16, 0, 5] \text{ km}$  above a polyhedral model of the asteroid Eros[21] with rotation period of 5.27 hours and density  $3.0 \text{ g/cm}^3$ . Errors here are on the order of a few centimeters for translation distances on the order of a kilometer. These examples are typical of the miss distances and domain of accuracy seen for this controller in general.

It should be noted that the time of transfer must be kept adequately small to ensure accuracy of the control. If the time of transfer becomes too large, the actual path will deviate significantly from the predicted linearized path and the error estimate will be inaccurate.

## 6.4 Sensitivity to Parameter Uncertainty

Parameter uncertainty is an inevitable part of any space mission. Here, the effects of parameter uncertainty on the open-loop, constant-thrust translation controller are characterized. The final state in Eq. (5.43) is dependent on the initial state, rotation rate, thrust, and gravitational potential, and can be characterized as in Eq. (6.9).

$$\begin{bmatrix} \tilde{\mathbf{r}}(t_f) \\ \dot{\tilde{\mathbf{r}}}(t_f) \end{bmatrix} = g(\tilde{\mathbf{r}}_0, \dot{\tilde{\mathbf{r}}}_0, \omega, \tilde{\mathbf{T}}, M_{sb}, C_{nm}, S_{nm}) \quad (6.9)$$

The parameters  $M_{sb}$ ,  $C_{nm}$ , and  $S_{nm}$  represent the small-body mass and spherical harmonic gravity coefficients as defined in Eq. (2.13). There is uncertainty associated

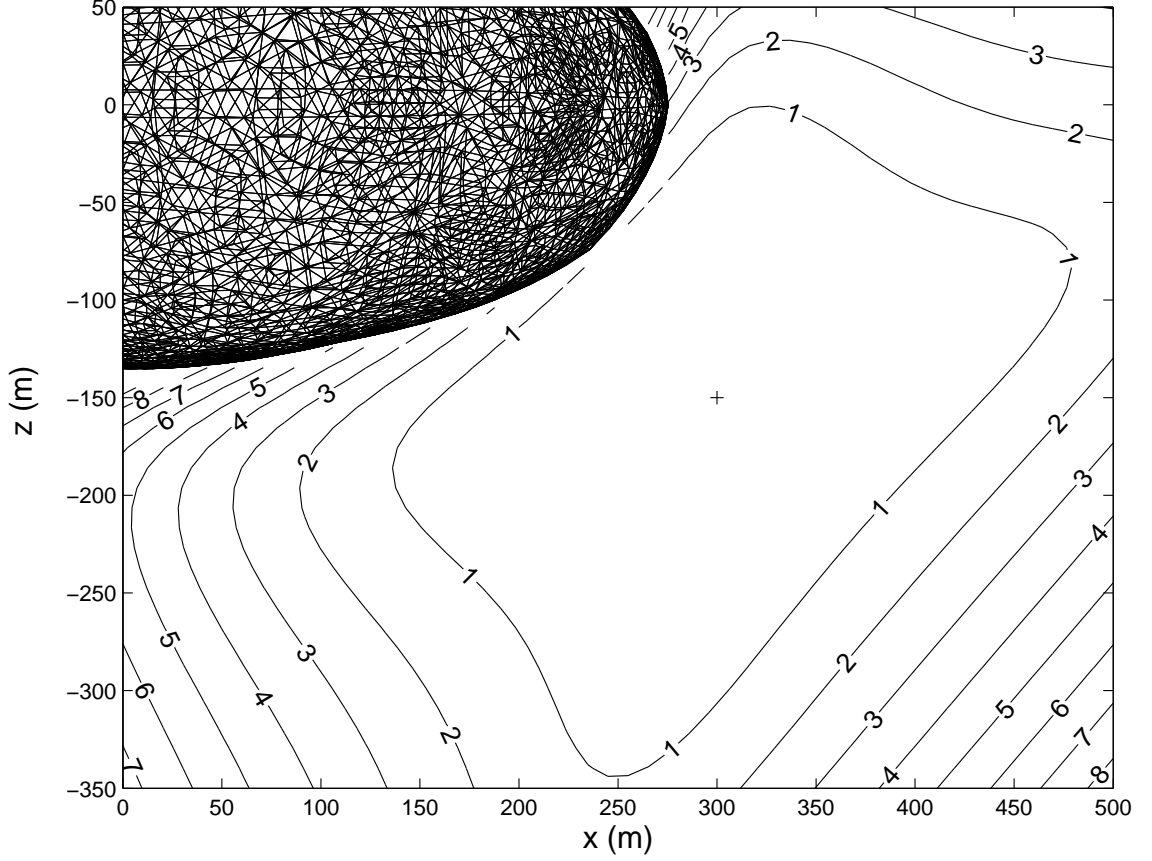


Figure 6.1: Miss Distance(*cm*) for Translation in the  $X - Z$  Plane near Asteroid Itokawa

with each of these system parameters. Expanding the perturbed system in a Taylor series, gives Eq. (6.10).

$$\begin{aligned} \begin{bmatrix} \delta\tilde{\mathbf{r}}(t_f) \\ \delta\dot{\tilde{\mathbf{r}}}(t_f) \end{bmatrix} &= \frac{\partial g}{\partial \tilde{\mathbf{r}}_0} \delta\tilde{\mathbf{r}}_0 + \frac{\partial g}{\partial \dot{\tilde{\mathbf{r}}}_0} \delta\dot{\tilde{\mathbf{r}}}_0 + \frac{\partial g}{\partial \omega} \delta\omega + \frac{\partial g}{\partial \tilde{\mathbf{T}}} \delta\tilde{\mathbf{T}} + \\ &\quad \frac{\partial g}{\partial M_{sb}} \delta M_{sb} + \sum_{n=1}^{\infty} \sum_{m=0}^n \left( \frac{\partial g}{\partial C_{nm}} \delta C_{nm} + \frac{\partial g}{\partial S_{nm}} \delta S_{nm} \right) + \dots \quad (6.10) \end{aligned}$$

The partial derivatives in Eq. (6.10), called sensitivity matrices, can be evaluated numerically using standard sensitivity analysis[50]. If the equations of motion are

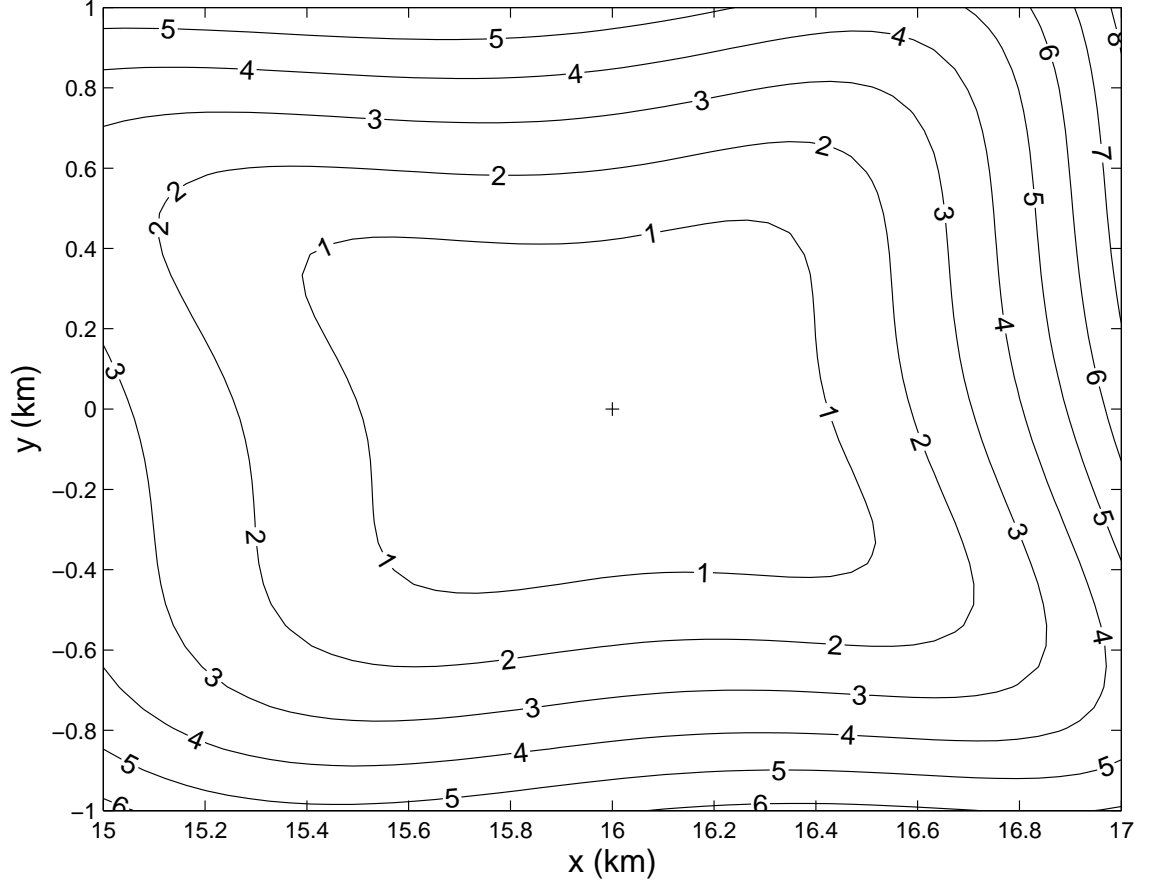


Figure 6.2: Miss Distance( $cm$ ) for Translation in an  $X - Y$  Plane near Asteroid Eros defined by Eq. (6.11)

$$\begin{bmatrix} \dot{\tilde{\mathbf{r}}} \\ \ddot{\tilde{\mathbf{r}}} \end{bmatrix} = f(\tilde{\mathbf{r}}, \dot{\tilde{\mathbf{r}}}, \omega, \tilde{\mathbf{T}}, M_{sb}, C_{nm}, S_{nm}) \quad (6.11)$$

and  $\zeta$  is one of the parameters, then the dynamics of the sensitivity matrices are given in Eq. (6.12),

$$\frac{d}{dt} \left( \frac{\partial \tilde{\mathbf{X}}}{\partial \zeta} \right) = \frac{\partial f}{\partial \tilde{\mathbf{X}}} \frac{\partial \tilde{\mathbf{X}}}{\partial \zeta} + \frac{\partial f}{\partial \zeta} \quad (6.12)$$

where  $\tilde{\mathbf{X}}$  is the state vector and

$$\left. \frac{\partial \tilde{\mathbf{X}}}{\partial \zeta} \right|_{(\tilde{\mathbf{r}}_0, \dot{\tilde{\mathbf{r}}}_0)} = \mathbf{0}_{6 \times n} \quad (6.13)$$

except in the case of sensitivity to initial state, where

$$\left. \frac{\partial \tilde{\mathbf{X}}}{\partial \tilde{\mathbf{X}}_0} \right|_{(\tilde{\mathbf{r}}_0, \dot{\tilde{\mathbf{r}}}_0)} = \mathbf{I}_{6 \times 6}. \quad (6.14)$$

Once the sensitivity matrices are known, the linear covariance of the final state is computed by Eq. (6.15) given the initial covariances of the various parameters,

$$Cov(\tilde{\mathbf{X}}_f) = \Phi(t_f, 0)Cov(\mathbf{X}_0)\Phi(t_f, 0)^T + \sum_{i=1}^k \left. \frac{\partial \tilde{\mathbf{X}}}{\partial \zeta_i} \right|_{t_f} Cov(\zeta_i) \left. \frac{\partial \tilde{\mathbf{X}}}{\partial \zeta_i} \right|_{t_f}^T \quad (6.15)$$

where  $\Phi(t_f, 0)$  is the state transition matrix from time 0 to  $t_f$ .

#### 6.4.1 Qualitative Sensitivity Results

Sensitivity of the constant thrust translation controller to parameter uncertainty is a function of the time of transfer, endpoints of the trajectory, and small-body parameters. Instead of trying to cover this entire parameter space, this study will look only at low altitude descent trajectories traveling from an outer spherical shell to an inner sphere with the starting position and target having the same latitude and longitude. Uncertainty in any system parameter results in a six-dimensional hyper-ellipsoid in phase space representing the final state covariance. This study is concerned only with uncertainty in final position, parameterized by the square root of the largest eigenvalue of the final position covariance matrix,

$$\sigma = \max \left[ \sqrt{\lambda_{eig}} \in \Re : [\lambda_{eig} \mathbf{I}_{3 \times 3} - Cov(\tilde{\mathbf{r}}(t_f))] \hat{\mathbf{v}} = 0 \right] \quad (6.16)$$

where  $\hat{\mathbf{v}}$  is an arbitrary unit vector.

First, sensitivity to errors in the initial state is studied. The sensitivity matrix in this case is equivalent to the state transition matrix. For descents above a spherical body, errors in initial position are amplified most when descending near the equator and least at the poles. Magnitude of the error in final position is generally on

the order of error in the initial position. Assuming the spacecraft uses an in-situ navigation scheme, uncertainty in the initial position should be a few meters. Errors in initial velocity produce the greatest uncertainty in final position for descents near the pole and the least near the equator. Miss due to velocity uncertainty can be large if initial velocity is not well known. Velocity should be known to within a few  $mm/s$  to keep  $\sigma$  on the order of a few meters. When the same descents are integrated over an ellipsoidal body, the final position uncertainty is largest at the equator above the elongated ends of the body and smallest at the equator near the body's intermediate semi-major axis for both initial position and velocity errors. The magnitude of error due to this equatorial "shape effect" dominates the difference in final position uncertainty between polar and equatorial descents.

Sensitivity to errors in rotation rate is determined using Eq. (6.12), where  $\partial f/\partial\omega$  is defined in Eq. (6.17).

$$\frac{\partial f}{\partial\omega} = \left[ 0, \quad 0, \quad 0, \quad 2\omega x + 2\dot{y}, \quad 2\omega y - 2\dot{x}, \quad 0 \right]^T \quad (6.17)$$

Generally, uncertainty in  $\omega$  is very small. For the NEAR mission, one-sigma uncertainty in  $\omega$  was  $3.03 \times 10^{-11} \text{ rad/sec}$ [21], corresponding to about a  $2 \text{ ms}$  error in rotation period. For the class of descents studied here, this uncertainty resulted in  $\sigma$  on the order of  $10 \mu m$ , which is negligible compared to the effects of other uncertainties. Uncertainty in final position was found to be largest for descents near the equator and went to zero for polar descents, which is expected since  $\omega$  has no effect on descent along the  $\hat{\mathbf{z}}$  axis. Again, when the body is elongated, the largest uncertainty in final position occurs above the long ends of the body.

Rotation rate is unique in that it is the only parameter whose sensitivity is directly dependent on initial velocity. Radial initial velocities away from the body are found

to produce smaller errors than for toward the body and initial velocities in the retrograde direction induce smaller errors than velocities in the direct direction.

Error in the thrust vector  $\tilde{\mathbf{T}}$  (Eq. (6.18)), results from error in thrust magnitude and error in thrust direction,

$$\begin{aligned} \delta\tilde{\mathbf{T}} = & \delta\lambda_T \begin{bmatrix} -T_{mag,0} \cos \phi_{T,0} \sin \lambda_{T,0} \\ T_{mag,0} \cos \phi_{T,0} \cos \lambda_{T,0} \\ 0 \end{bmatrix} \\ & + \delta\phi_T \begin{bmatrix} -T_{mag,0} \sin \phi_{T,0} \cos \lambda_{T,0} \\ -T_{mag,0} \sin \phi_{T,0} \sin \lambda_{T,0} \\ T_{mag,0} \cos \phi_{T,0} \end{bmatrix} + \delta T_{mag} \begin{bmatrix} \cos \phi_{T,0} \cos \lambda_{T,0} \\ \cos \phi_{T,0} \sin \lambda_{T,0} \\ \sin \phi_{T,0} \end{bmatrix} \end{aligned} \quad (6.18)$$

where  $\phi_T$  and  $\lambda_T$  are the latitude and longitude of the thrust direction respectively, and  $T_{mag}$  is the thrust magnitude. The zero subscript indicates nominal quantities.

$\partial f / \partial \tilde{\mathbf{T}}$  is given in Eq. (6.19).

$$\frac{\partial f}{\partial \tilde{\mathbf{T}}} = \begin{bmatrix} \mathbf{0}_{3 \times 3} \\ \mathbf{I}_{3 \times 3} \end{bmatrix} \quad (6.19)$$

Since thrust is applied in an open-loop manner, miss due to thruster error can be large if the thrust direction and magnitude are not well known. The very low level of thrust necessary to perform these maneuvers, on the order of  $10^{-2} - 10^{-5} N/kg$ , is also a challenge, particularly near very small bodies. Wolff *et al.* found in calibration simulations for an ion propulsion system that thrust magnitude can be tuned to an accuracy of 1.2% with a maximum error of 0.5 mN and thrust orientation to within 0.5 to 5 degrees[71]. With this type of calibration, errors due to thruster uncertainty are reasonable.

Error due to thruster uncertainty is the largest contributor to  $\sigma$  in almost all cases. Depending on the transfer and the calibration,  $\sigma$  due to thrust alone can be

from meters to kilometers. The error in final position due to thruster uncertainty as a function of latitude and longitude cannot be easily characterized. For a spherical body, the maximum  $\sigma$  due to thrust uncertainty can occur above the equator or the pole. Which of these is the case and the relative magnitudes of the errors for a particular situation seem to depend on the transfer time and the time to drop the specified distance without thrust. If the ratio of these times for a particular body is too high or too low, the maximum  $\sigma$  will occur at the equator. On the other hand, if this ratio is just about right, maximum  $\sigma$  is induced at the pole and minimum error is at the equator. For an ellipsoidal gravity field, the maximum error in the final position occurs for descents either over the intermediate or largest semi-major axis of the body. Generally, for longer transfer times relative to the time to drop freely, the largest  $\sigma$  for descents is found above the long ends of the body. For shorter transfer times, the largest  $\sigma$  for descents is found above the intermediate semi-major axis. The minimum error occurs at either the poles or the non-maximum equatorial axis depending on the spherical body result.

Finally, sensitivity to errors in the spacecraft's potential model as defined by a spherical harmonic expansion (Eq. (2.13)) are studied. Errors in the small-body mass estimate are found to produce the largest errors in final position above the poles and elongated ends of the body. The NEAR mission was able to determine the mass of Eros to within  $4.5 E - 2\%$  [21]. Using the same percentage error, errors due to mass uncertainty are found to be on the order of centimeters or less.

Errors in the  $C_{10}$ ,  $C_{11}$ , and  $S_{11}$  coefficients correspond to offsets of the center of mass in the  $\hat{\mathbf{x}}$ ,  $\hat{\mathbf{y}}$ , and  $\hat{\mathbf{z}}$  directions respectively. If uncertainty due to each term is studied individually, each causes maximum uncertainty in final position for descents along its respective axis. When all three are considered concurrently, uncertainty in

final position is found to be maximal for polar descents and minimal for equatorial descents. Using the one-sigma uncertainty in these coefficients found by the NEAR mission ( $4E - 6$ )[21], errors in final position for the descent scenarios tested here were on the order of millimeters.

Looking at the higher order harmonics, a general pattern emerges. For the  $C_{nm}$  coefficient,  $\sigma$  for these descents is proportional to  $P_{nm}(\sin \phi) \cos m\lambda$ . Similarly, the error due to uncertainty in the  $S_{nm}$  coefficient is proportional to  $P_{nm}(\sin \phi) \sin m\lambda$ . This is not surprising since the sensitivity equation is driven by  $\partial^2 U / (\partial \mathbf{r} \partial [C_{nm}, S_{nm}])$  and the spacecraft moves with nearly constant latitude and longitude. The one-sigma errors that arise from uncertainties in the harmonic coefficients are generally on the order of meters or less.

When all these parameters are considered simultaneously, uncertainty in the final position is likely to be largest for descents above the equator of an elongated body, either near the longest or intermediate semi-major axis. Descents with minimum uncertainty in final position may occur above the equatorial semi-major axis not corresponding to the maximum error or above the poles depending on the distance and duration of the transfer. For a nearly spherical body, it is possible that the largest values of  $\sigma$  will be found for descents above the poles. Thruster error is the dominant contributor to  $\sigma$ , followed by error in the initial state. Since maximum uncertainty in the final position can occur about anywhere depending on the transfer parameters, covariance studies using the above described method should be performed for each case of interest.

### 6.4.2 Covariance Simulations

Numerical covariance analysis, including uncertainty in all of the parameters above, has been performed for descent trajectories at a range of latitudes and longitudes above three realistic asteroid shapes. Polyhedral models of the asteroids Itokawa and Eros have been considered, as well as an ellipsoidal approximation of the asteroid Vesta. For each body, the three different sets of parameter covariances given in Table 6.1 were implemented. For all three covariance sets, it is assumed that

Covariance Set	#1	#2	#3
Position (x,y,z)	1 m	5 m	10 m
Velocity (x,y,z)	0.1 mm/s	1 mm/s	5 mm/s
$\theta_T$	0.5°	2°	5°
$\phi_T$	0.5°	2°	5°
$T_{mag}$	0.1%	0.8%	2.0%
$\omega$	$3.03 E - 11 \text{ rad/s}$	$3.03 E - 11 \text{ rad/s}$	$3.03 E - 11 \text{ rad/s}$
Mass	0.0448%	0.0448%	0.0448%
1st Order Harmonics	$4 E - 6$	$4 E - 6$	$4 E - 6$
2nd Order Harmonics	$4 E - 6$	$4 E - 6$	$4 E - 6$
3rd Order Harmonics	$5 E - 6$	$5 E - 6$	$5 E - 6$

Table 6.1: One-sigma Parameter Uncertainties for Descent Simulations

the spacecraft uses in-situ measurements (i.e. optical navigation and/or altimetry) in addition to Doppler range and range rate measurements to refine its position estimate to the given level. The spacecraft thruster (electric propulsion or low-thrust chemical) is assumed to have been calibrated in the manner discussed by Wolff *et al.*[71], though a maximum error in the thrust magnitude is not imposed here. The one-sigma values given for covariance set #1 correspond to a mission with a well-calibrated thruster and advanced navigation instruments, while the accuracy in set #3 may be obtained by a cheaper mission. The uncertainties used for  $\omega$ ,  $M_{sb}$ , and the harmonic coefficients are those found during the NEAR Mission[21]. It is as-

sumed here that other visiting spacecraft can characterize their target to this level of certainty.

### Itokawa

The first small-body studied here is asteroid Itokawa, the target of the JAXA's Hayabusa spacecraft. Itokawa is relatively small, measuring only 548 x 312 x 276  $m$ , and is very nearly a perfect ellipsoid. The rotation period of Itokawa is 12.132 hours and its bulk density is approximately  $2.5 g/cm^3$ <sup>1</sup>. For these runs, the spacecraft will descend from an outer sphere with radius 600  $m$  to an inner sphere of radius 310  $m$  in 1200 seconds. A 6098 vertex constant density polyhedron was used to model the body's potential[35].

The results of these simulations for the three covariance sets in Table 6.1 are shown in Table 6.2. The largest and smallest  $\sigma$  values and their locations are given. For all three bodies, descents were done every 9° latitude and longitude, so the locations given are accurate only to 9° resolution. The area averaged  $\sigma$  is also given.

Covariance Set	Max $\sigma(m)$ (Lat/Long(°))	Min $\sigma(m)$ (Lat/Long(°))	Avg $\sigma(m)$
#1	2.704 (0,-90)	2.630 (90,-)	2.650
#2	11.302 (0,-90)	11.015 (90,-)	11.091
#3	27.733 (0,-90)	27.004 (90,-)	27.207

Table 6.2: Results of Covariance Analysis of Descents Above Itokawa

Figure 6.3 shows  $\sigma$  as a function of longitude and latitude for descents using covariance set #3. The effect of longitude and latitude on descents using the other covariance sets are similar. Here, it is seen that the largest uncertainty in final

<sup>1</sup>These parameters and comments are based on the now dated estimates obtained from ground-based radar before the arrival of the Hayabusa spacecraft.

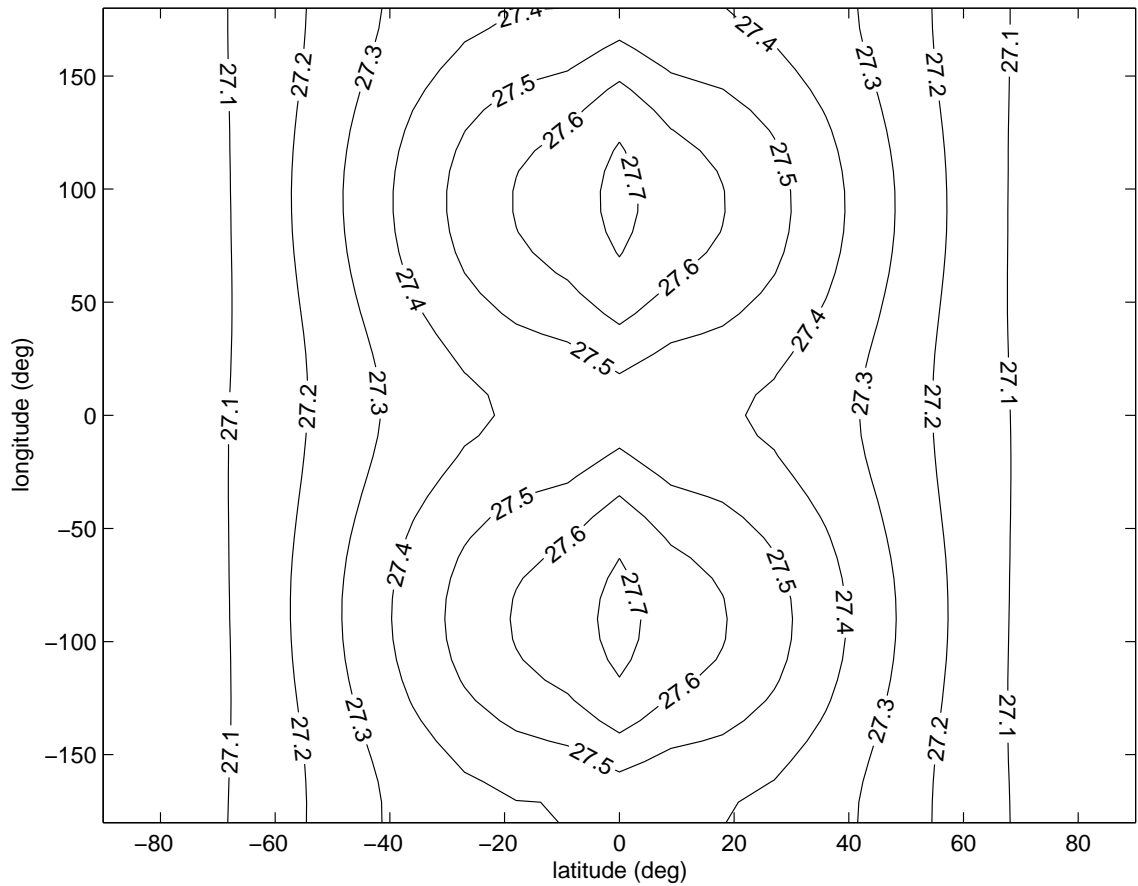


Figure 6.3:  $\sigma$  ( $m$ ) as a Function of Latitude and Longitude for Radial Descent over Asteroid Itokawa

position occurs above the body's intermediate semi-major axis at the equator. This maximum is largely attributable to thrust uncertainty. For Itokawa, the duration of this transfer is short enough relative to the distance covered that the maximum error occurs here. The secondary effect of the remaining parameter uncertainties causes  $\sigma$  to increase above the body's largest semi-major axis. Polar descents yield the minimum uncertainty in final position for this transfer. However, there is not much variation in  $\sigma$  over Itokawa for these descents; there is less than 3% difference between the maximum and minimum  $\sigma$  for all covariance sets.

Considering no feedback is used, the magnitude of errors induced by covariance

sets #1 and #2 are quite reasonable. One reason for this is that the necessary thrust magnitude for these maneuvers is so small; errors in thrust magnitude and orientation do not push the spacecraft off course very strongly. However, it may be difficult for an actual spacecraft to reliably implement these very low thrust levels. The 27 m average  $\sigma$  value from set #3 is also small, but corresponds to about 5° angular error, which may be significant.

## Eros

The asteroid Eros was recently visited by the NEAR spacecraft. The first successful descent to an asteroid was performed by this spacecraft using a series of open-loop burns to descend from orbit[24]. In these descent simulations, an 809 vertex polyhedral shape model of Eros measuring approximately 32.8 x 14.4 x 11.9 km is used[21]. The orbit period of Eros is 5.27 hours and the bulk density used here is 2.67 g/cm<sup>3</sup>. The shape of Eros, shown in Figure 6.4, is quite elongated with two large craters on either side of its midsection. The results presented here are for descents from an outer sphere of radius 16.2 km to an inner sphere of 15.7 km in 1500 seconds.

The results of these simulations are shown in Table 6.3. There is a large difference between maximum and minimum  $\sigma$ ; the maximum value is nearly 5 times the minimum. This is attributable to Eros' elongated shape and varied surface. The minimum value occurs above one of the large craters on the body's side near the  $\hat{y}$  axis and the maximum occurs at the most elongated end of the body. The polar area is also a relatively good place to descend. Figure 6.5 shows  $\sigma$  as a function of latitude and longitude for these descents using covariance set #2. Descents above most of the surface produce a  $\sigma$  of between 30 and 40 meters. Near the long ends of the body, uncertainty quickly grows large and there is some improvement near the

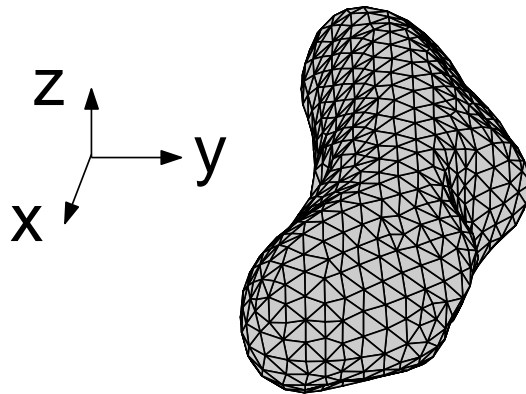


Figure 6.4: 809 Vertex Polyhedral Model of the Asteroid Eros

Covariance Set	Max $\sigma(m)$ (Lat/Long( $^{\circ}$ ))	Min $\sigma(m)$ (Lat/Long( $^{\circ}$ ))	Avg $\sigma(m)$
#1	24.816 (-9,-171)	5.280 (0,36)	10.315
#2	99.597 (-9,-171)	21.585 (0,36)	41.536
#3	249.024 (-9,-171)	53.319 (0,36)	103.716

Table 6.3: Results of Covariance Analysis of Descents above Eros

large craters. The average errors for descents to Eros seem reasonable considering the size of the body. The maximum  $\sigma$  obtained with covariance set #3 corresponds to a miss of only  $0.9^{\circ}$  and the average is only  $0.36^{\circ}$ . With improved calibration and parameter certainty, results are even better.

### Vesta Ellipsoid

Finally, covariance in the final position is studied for descents above a very large asteroid, Vesta. The true shape of Vesta is approximated by a tri-axial ellipsoid with semi-major axes of 289, 280, and 229 km. Thomas et. al. approximated the density of Vesta to be  $3.7 g/cm^3$  and its rotation rate to be 5.342 hours[72]. Here, results for

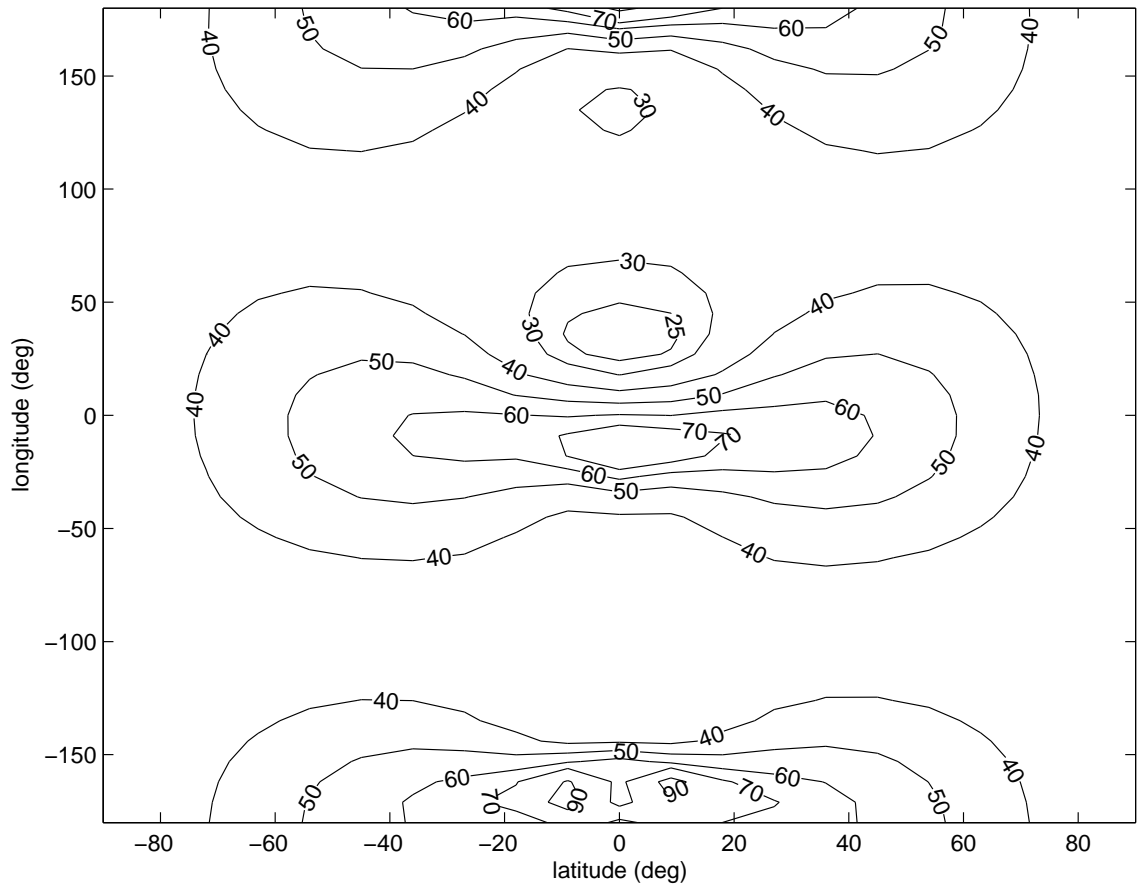


Figure 6.5:  $\sigma$  ( $m$ ) as a Function of Latitude and Longitude for Radial Descent over Asteroid Eros

an 1800 second radial descent covering 10  $km$  from a radius of 300  $km$  to 290  $km$  are presented.

The maximum, minimum, and average  $\sigma$ 's for these simulations are given in Table 6.4 and  $\sigma$  as a function of longitude and latitude for covariance set #2 is shown in Figure 6.6. Errors due to parameter uncertainty in these descents are quite large. These errors are primarily due to thruster orientation errors. Because the necessary thrust is so large, any misalignment causes a significant perturbing force, which goes unchecked because of the nearly constant gravitational attraction in the immediate vicinity of the spacecraft.

Covariance Set	Max $\sigma(m)$ (Lat/Long( $^{\circ}$ ))	Min $\sigma(m)$ (Lat/Long( $^{\circ}$ ))	Avg $\sigma(m)$
#1	2469.9 (0,180)	2104.5 (-18,-90)	2113.2
#2	9989.6 (0,180)	8444.9 (-18,-90)	8559.8
#3	24977 (0,180)	21116 (-18,-90)	21403

Table 6.4: Results of Covariance Analysis of Descents above a 289 x 280 x 220 *km* Ellipsoid

In reality, a constant thrust translation approach would probably be a poor choice for a body as large as Vesta. A large amount of fuel would be necessary to perform constant thrust maneuvers and impact velocity for a free-drop or constant thrust descent would be high. Also, initial position accuracy could probably not be refined to the levels in covariance sets #1–#3 for this large of a small-body, so the covariance in final position would be probably be even larger than found here.

## 6.5 Detailed Descent Scenario

Now a detailed look at a descent using the constant thrust and free-drop solutions is presented. The descent described here is very similar to the final phase of the NEAR mission descent[24]. The spacecraft will descend from roughly 2.25*km* altitude to touchdown in the vicinity of the Himeros depression on the asteroid Eros (modeled by the 809-vertex polyhedron). The spacecraft will begin at (2.25 *km* altitude,  $-35^{\circ}$  latitude,  $82^{\circ}$  longitude) with about 70% of orbital speed (3 *m/s* retrograde in the body-fixed frame). A constant thrust segment will then slow the spacecraft to arrival at (156 *m*,  $-30^{\circ}$ ,  $60^{\circ}$ ). The spacecraft will then drop without thrust to the surface target at (0 *m*,  $-29.345^{\circ}$ ,  $61.123^{\circ}$ ). The constant thrust maneuver is performed over 40 minutes and the free-drop segment takes 206 seconds.

Given the initial state and the target position, Eqs. (6.2) and (6.8) are used to obtain the corrected constant thrust value,  $\tilde{\mathbf{T}} = [-0.557, 4.259, -2.542]^T$  *mN/kg*,

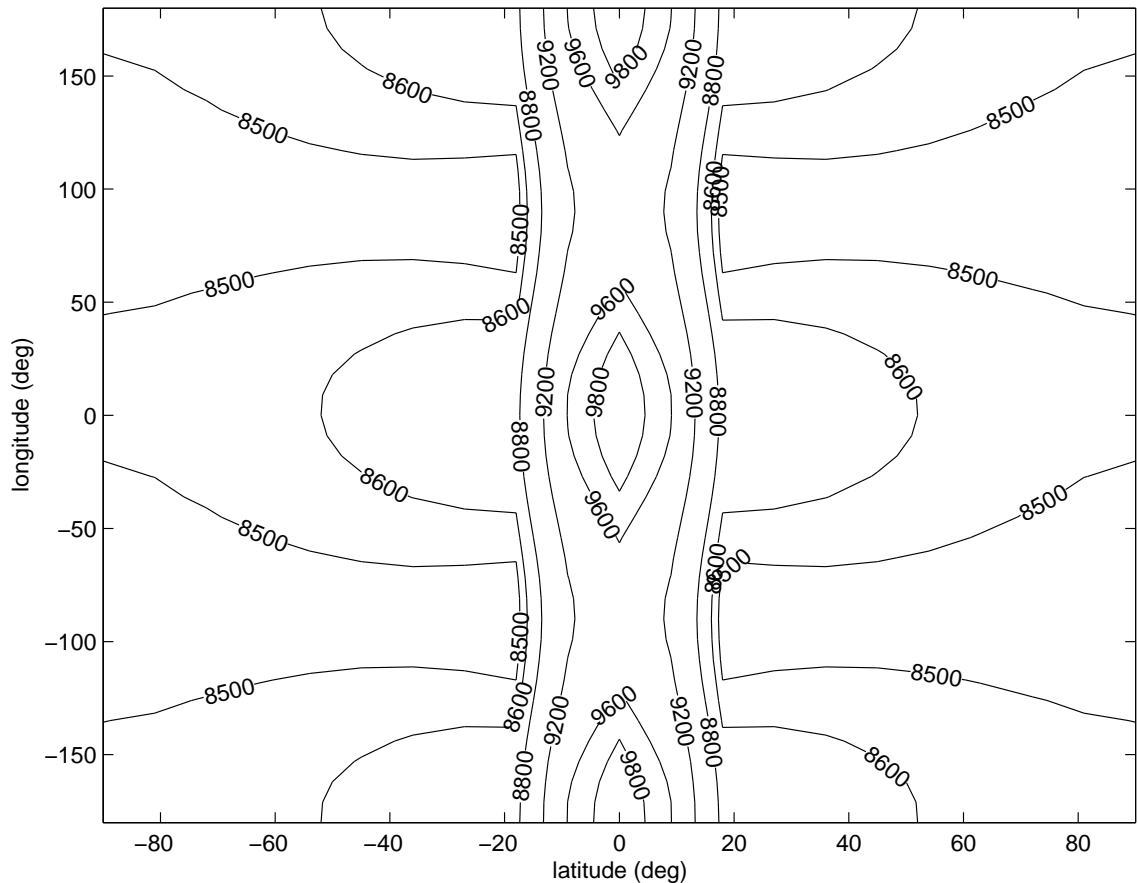


Figure 6.6:  $\sigma$  ( $m$ ) as a Function of Latitude and Longitude for Radial Descent over a  $289 \times 280 \times 220$   $km$  Ellipsoid

to complete the first segment. Eq. (6.3), corrected similarly to the thrust, gives the predicted velocity at the way point. Eq. (5.43) is then used to numerically determine the time to free-drop from the predicted state to the surface. The free-drop trajectory cannot be corrected through error estimate because the target state cannot be freely changed without thrust.

Figure 6.7 shows the planned path (way points indicated by circles) and the actual trajectory of the descent (x's show actual position at the way point time). The dashed line is the powered portion and the solid line is the free-drop trajectory. The nominal miss distance due to non-linearity of the potential at the first way point

was 11.39 *m*. The nominal miss distance at the touchdown point was 20.65 *m*. The touchdown velocity was nominally 1.165 *m/s* normal to the surface and 1.230 *m/s* tangent to the surface. When the uncertainties in covariance set #2 were included, the one-sigma ellipsoid was found to have semi-major axes of 374.90 *m*, 346.71 *m*, and 185.65 *m* at the thrust cut-off way point and 375.20 *m*, 346.79 *m*, and 190.67 *m* at the touchdown point. On the ground, these errors correspond to a few degrees longitude or latitude error, which may be acceptable. However, the one-sigma error at the way point is larger than the nominal altitude. Without measurements, the way point must be at a higher altitude, which means a larger impact velocity. Errors in thrust application account for most of the uncertainty found here. Without it, the one-sigma ellipsoid at the surface target is 69.04 x 28.88 x 9.94 *m*.

## 6.6 Sliding Dead-band Descent

In this section, a different approach to descent is discussed. The idea is to use a dead-band body-fixed hovering control (discussed in Chapters III-V) with a variable target altitude to drive the spacecraft down to the small-body surface. Since hovering with an dead-band on altitude has been shown to be bounded near the small-body surface (Section 5.2.1), this may be a good approach to descend in a stable and tightly controlled way. This section presents a numerical test of the feasibility of this idea using HoverSim. This brief analysis utilizes the IATNS body-fixed, station-keeping controller (Section 3.4.1). This controller offers an advantage in that the sensing and control directions are different. This may prevent contamination of the surface regolith to be sampled by the thruster outgassing in sample return missions. A formulation of the maximum altitude at which particles may be lifted off the surface by the thruster plume is also presented.

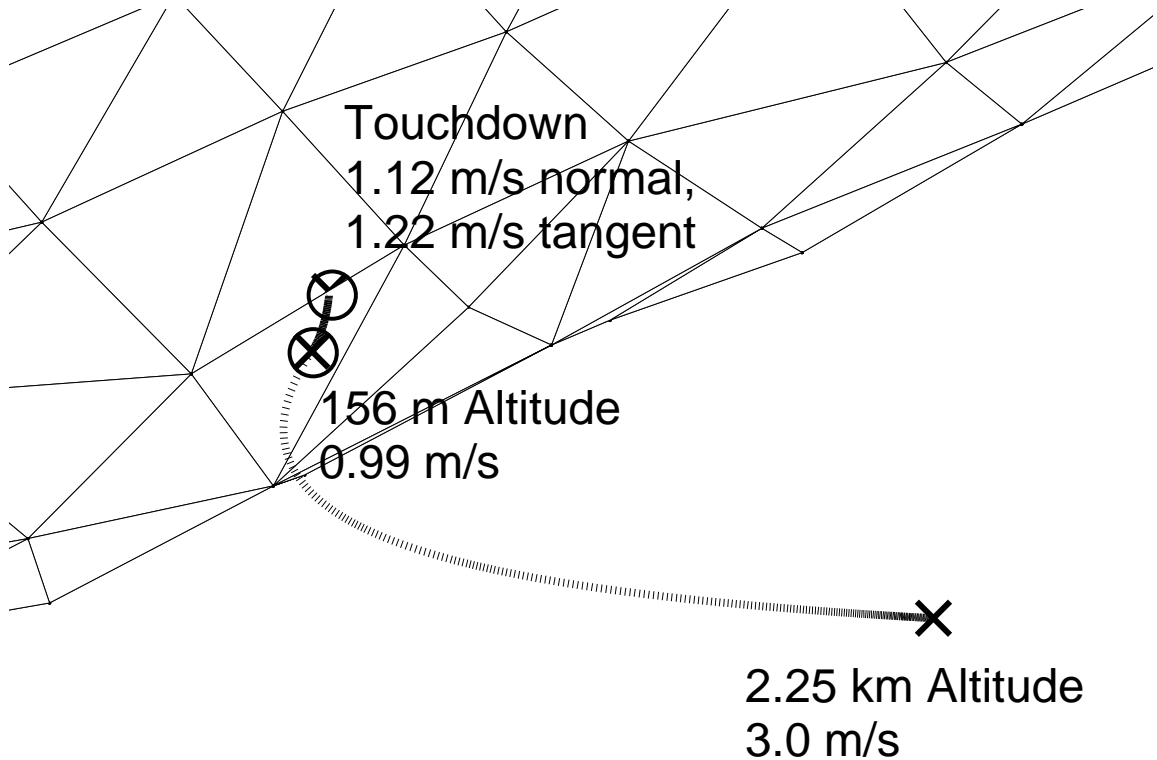


Figure 6.7: Descent to the Surface of Asteroid Eros Using Constant Thrust and Free-drop Control

The strategy for descent to the surface will be as follows. Using the IATNS thrust controller, the target altitude for the spacecraft is varied linearly in time down to the surface. During ascent, the target altitude will initially be put at some distance off the surface to give the spacecraft an initial thrust so that oscillations around the dead-band do not cause the spacecraft to reimpact the surface. Because this initial period of thrusting will cause large oscillations in distance from the desired hovering point (the altitude dead-band has no effective damping), the velocity dead-band controller discussed in Section 3.2.1 is implemented during ascent. Only the part of the velocity controller regulating negative altitude rates-of-change is used, as not to impede the initial thrusting off the surface.

It is important that the controller keep the velocity of the spacecraft as small as possible at impact to protect the spacecraft. Touchdown should occur very close to the target landing site and the spacecraft should also ascend to a point near where it began.

### 6.6.1 Derivation of Necessary Control Thrust

In the descent maneuver, deviations from the prescribed hovering point have more serious consequences than in station-keeping maneuvers. The larger the deviations from the desired altitude, the larger the maximum velocity obtained by the spacecraft is. As mentioned previously, it is important that the spacecraft impact the surface at a reasonable velocity. This impact can occur at any point in the dead-band, so it is important to keep the spacecraft's velocity low at all times. It is also important to have tight control on the spacecraft to avoid unplanned collisions with the surface when operating at very low altitudes. To maintain this tight control on the spacecraft,  $\gamma$  must be very small and overshoot beyond the dead-band boundary must be limited.

The way to limit overshoot outside the dead-band is through  $T_m$ . Over a small range of motion (as in a dead-band with small  $\gamma$ ), it is reasonable to approximate the spacecraft dynamics as one-dimensional motion in a constant gravity field. Let the spacecraft begin stationary at altitude  $h_0$  with the lower dead-band boundary at altitude  $h_0 - \gamma$ . Downward acceleration is  $\|\tilde{\mathbf{a}}_0\|$  when inside the dead-band and upward acceleration is  $T_m - \|\tilde{\mathbf{a}}_0\|$  when outside the dead-band. Motion in this one-dimensional system is periodic with the spacecraft overshooting the lower dead-band boundary by  $d$  (Eq. (6.20)) once per cycle.

$$d = \frac{\|\tilde{\mathbf{a}}_0\| \gamma}{T_m - \|\tilde{\mathbf{a}}_0\|} \quad (6.20)$$

For optimal descent controller performance, this overshoot should be kept as small

as possible by selecting a dead-band thrust magnitude  $T_m \gg \|\tilde{\mathbf{a}}_0\|$ . Overshoot can be kept small (1 – 2% of the dead-band width) by selecting a magnitude of control thrust between 50 and 100 times the nominal gravitational acceleration. This thrust should not be selected too large though, as the larger it becomes, the more trouble small errors in the thruster on/off times become.

### 6.6.2 Effect of Thrust on Surface Material

Surface materials that may be kicked up by the thruster plume are another concern for this type of descent, since thrust is used very close to the surface. Surface dust may degrade the performance of the spacecraft’s solar panels, cover the lenses of cameras, or otherwise interfere with sensitive on-board equipment. Here, a “back of the envelope” computation of the altitude at which particles could be lifted off the surface is presented. This altitude could determine when cameras are shuttered or when a free-drop descent trajectory begins.

Here, a downward thrust of magnitude  $m_{s/c} \|\tilde{\mathbf{T}}\|$ , where  $m_{s/c}$  is the mass of the spacecraft, is considered at altitude  $h$  above the small-body surface. A conical thruster plume is considered with half angle  $\psi$ . The geometry of the problem is shown in Figure 6.8.

The circular cross-section of the thrust plume at the surface,  $A_T$ , is given by Eq. (6.21).

$$A_T = \pi h^2 \sin^2 \psi \quad (6.21)$$

If a uniform density plume is considered, the pressure at the surface due to the thrust  $p$  is given in Eq. (6.22).

$$p = \frac{m_{s/c} \|\tilde{\mathbf{T}}\|}{A_T} \quad (6.22)$$

For a spherical surface particle with radius  $r_p$  and density  $\rho$  to rise off the surface,

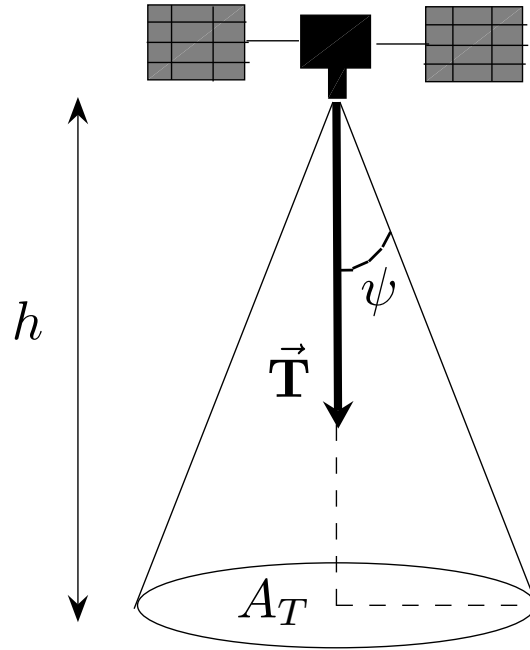


Figure 6.8: Thruster Plume Geometry

the vertical acceleration from the thruster plume pressure must be greater than or equal to the gravitational acceleration on the particle<sup>2</sup>. If a spherical small body with radius  $R_{sb}$  and density  $\rho$  is assumed, then the acceleration on the surface particle due to pressure is given in Eq. (6.23) and the acceleration due to gravity is given in Eq. (6.24).

$$a_p = \frac{3p}{4\rho r_p} \quad (6.23)$$

$$a_g = \frac{4}{3}\pi G\rho R_{sb} \quad (6.24)$$

Equating these accelerations and rearranging gives the spacecraft altitude at which particles could first lift off the ground as a function of thrust magnitude, plume

<sup>2</sup>A more detailed model could include centrifugal acceleration terms.

half-angle, and particle radius (Eq. (6.25)).

$$h = \frac{3}{4\pi} \frac{1}{\rho \sin \psi} \sqrt{\frac{m_{s/c} \|\tilde{\mathbf{T}}\|}{GR_{sb}r_p}} \quad (6.25)$$

This equation can be used to predict the maximum altitude at which dead-band thrust could cause surface dust to impact the spacecraft. This altitude is proportional to the thrust magnitude and inversely proportional to the thruster plume half-angle and the particle size.

Though the dynamics are similarly defined, hovering very close to the small-body surface differs from hovering at higher altitude because of possible interference from surface material. Under an open-loop hovering control, Eq. (6.25) can be reduced further. For hovering above a spherical small-body,

$$\|\tilde{\mathbf{T}}\| = \frac{4\pi G \rho R_{sb}^3}{3(R_{sb} + h)^2}. \quad (6.26)$$

Substituting this into Eq. (6.25) and solving a quadratic predicts the maximum altitude at which open-loop hovering can lift material off the surface in Eq. (6.27).

$$h = -\frac{R_{sb}}{2} + \sqrt{\frac{R_{sb}^2}{4} + \frac{3R_{sb}}{2 \sin \psi} \sqrt{\frac{m_{s/c}}{3\pi \rho r_p}}} \quad (6.27)$$

### 6.6.3 Results of Sliding Dead-band Descent Simulations

Numerical simulations of descent trajectories using sliding IATNS dead-band control have been conducted over an ellipsoidal shape that roughly approximates asteroid Itokawa. A 50 meter descent to the surface and ascent was simulated for a range of latitudes and longitudes. The descent was designed to take 1200 seconds. The ellipsoidal shape model used was 0.3 x 0.18 x 0.17 km with a density of 2300 kg/m<sup>3</sup>. A two meter altitude dead-band was implemented with a 0.1 m/s velocity dead-band. Control thrust was set to roughly 60 times the local gravitational acceleration.

For this particular case, the average impact velocity was found to be  $3.24 \pm 1.75 \text{ cm/s}$ , which should be acceptable for most missions. Figure 6.9 shows the lateral drift from the initial position for the complete descent/ascent cycle. These results seem to suggest that this drift is a regular and predictable phenomenon, dependent on the rotation rate and shape of the body. It can be seen that the greatest drift over the cycle occurs on the trailing edge of the body. The distance between the initial groundtrack point and the actual touchdown point, shown in Figure 6.10, exhibits similar regularity, but  $180^\circ$  out of phase with the drift distance after ascent; that is, the maximum miss distance at touchdown occurs on the body's leading edge and the minimum value occurs on the trailing edge. For both the miss at touchdown and the drift after ascent, values are at a minimum at  $90^\circ$  latitude, i.e. the poles. This is expected since no centrifugal acceleration exists at these points and the spacecraft motion is entirely vertical.

## 6.7 Discussion

In this chapter, we have used a closed-form solution to the linearized two-body equations of motion to model constant thrust translations. The necessary constant thrust to complete a translation between two arbitrary positions was formulated, as well as the locus of initial states that result in interception of a target position without thrust (free-drop solution). The constant thrust translation solution is improved by including an error estimate calculated using the linearized trajectory and the spacecraft's on-board potential model. This translation controller was designed with autonomous spacecraft operations in mind; the computation load for computing an accurate transfer thrust is reduced and the closed form solution is certain to exist. Numerical studies detailing the accuracy of this translation controller were presented

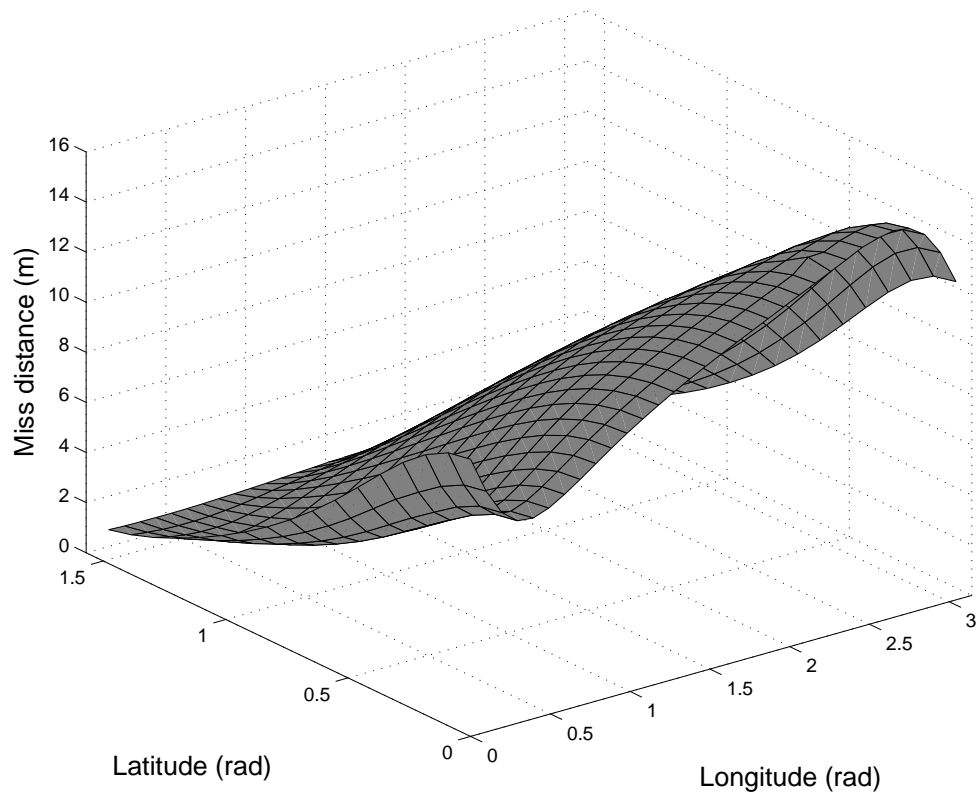


Figure 6.9: Drift for Sliding Dead-band Descent/Ascent Maneuver

and the accuracy was found to be good within a range of radial distances and angular deviations around the starting position.

This chapter also contained a covariance study that detailed the effects of uncertainty in initial state, thrust, small-body rotation, and small-body gravitational potential on descent trajectories using the proposed constant thrust control. Understanding how uncertainty effects spacecraft trajectories near small-bodies is critical since the environment is inherently very uncertain, especially upon the arrival of the spacecraft. To my knowledge, this is one of the first covariance studies for maneuvers near small-bodies formally presented in the literature (see Broschart and Scheeres[73]). We found that errors in thrust and initial state have the greatest

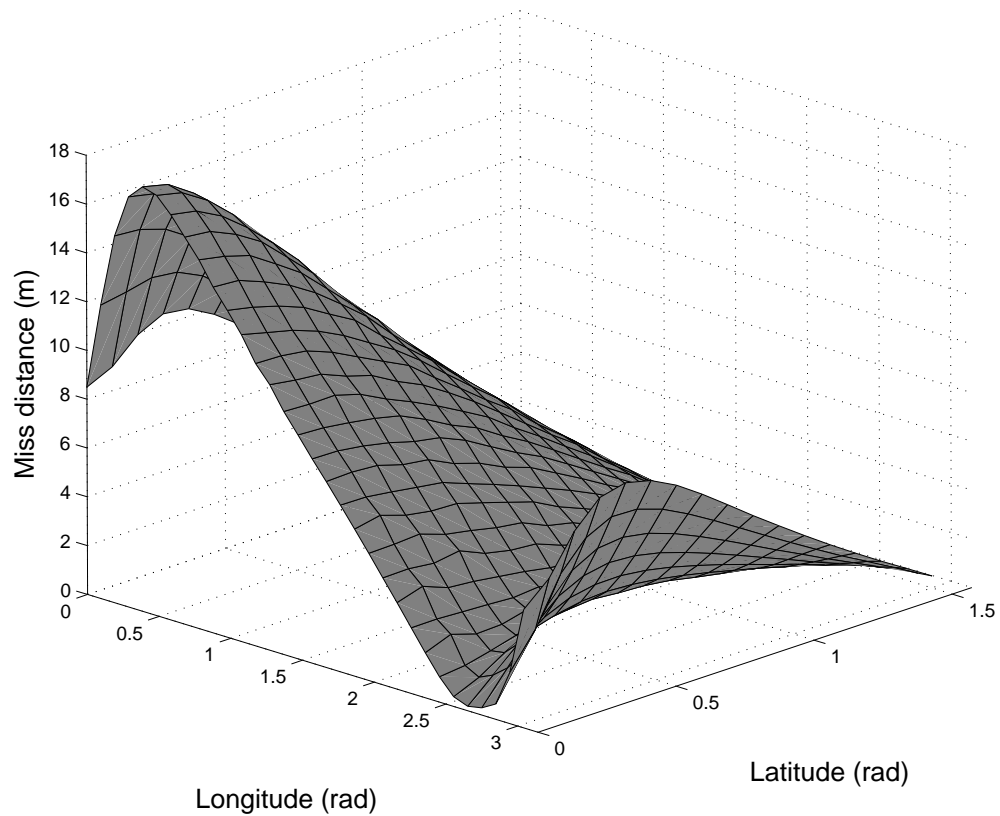


Figure 6.10: Miss Distance for Sliding Dead-band Descent

impact on error in the final position of the parameters studied for constant thrust descents. Numerical examples of descent uncertainty above realistic asteroid shapes were presented for models of asteroids Itokawa, Eros, and Vesta, as well as a detailed discussion of a descent scenario to asteroid Eros.

The final section of the chapter suggests that the hovering results of the previous chapters may extend well to descent maneuvers. Using a sliding dead-band as described seems to be a very good approach for keeping tight control of the spacecraft position and velocity during descent. The zero-velocity surface boundedness results can likely be applied to this problem as well. A good topic for future study would be determining how to bleed off the energy that accumulates during the descent such

that a tight zero-velocity boundary is maintained all the way down.

A study of the zero-velocity surface induced by the constant thrust translation controller is another topic for future consideration. Since the thrust is constant, the Jacobi constant is preserved. At the least, understanding the zero-velocity surface during a translation should give a good way to determine if the translation has sufficient energy to escape. At the best, such understanding could lead to novel control ideas.

## CHAPTER VII

### Conclusions

This thesis is the culmination of a multi-year study on spacecraft maneuvers in the complex dynamical environment in close proximity to small solar system bodies. Specifically, research on hovering, translation, and descent maneuvers has been presented here. I hope that these results will promote future understanding of dynamics in the vicinity of small-bodies and expand the dynamical options available to space mission planners for small-body exploration.

#### 7.1 Summary of the Research Results

In Chapter III, body-fixed hovering under altitude dead-band control was studied numerically using the HoverSim simulation software. In this study, we were able to compare and contrast numerical results with previously existing analytical stability criteria for hovering under the GDTS w/OL control. Our numerical results corresponded well with the stability criteria for hovering positions in the  $X - Z$  and  $Y - Z$  planes near the small-body, but unexpected large deviations in the hovering trajectory were found above the small-body's leading edge in the  $X - Y$  plane (and by extension, for all positions above the leading edge). An explanation is presented which attributes this discrepancy with the stability criteria to Coriolis forces unmod-

eled in the analytical derivation. Another controller which was designed with this effect in mind was found to delay the onset of large deviations above the leading edge. It was also found that with proper design, this effect can be eliminated completely. The analytical stability criteria from the previous work were derived from a linear stability analysis. In Chapter V, we were able to apply a boundedness condition derived from energetic constraints on the spacecraft motion to the results for the GDTS w/OL controller in Chapter III. It was found that much of the region with unexpected large deviations from the nominal hovering point is not bounded; this suggests that if the time of simulation was increased, hovering at these positions may ultimately prove to be unstable.

Chapter III also presents an analysis of hovering in the inertial frame. It is found analytically that an instability in the linear two-dimensional lateral dynamics (it is assumed that the radial direction, which is usually unstable, is controlled) exists for hovering near the small-body resonance radius. Numerical simulation validated this linear instability, though inertial hovering is found to be non-linearly stable (possibly with very large deviations from the nominal position) at all radii under the chosen controller.

Chapter IV defines the zero-velocity surface in the vicinity of a spacecraft under open-loop hovering control in time-invariant dynamical systems. This important observation leads to a method of dead-band control design that restricts motion in the minimum number of directions necessary to ensure a bounded trajectory. It is found that the region closest to the small-body usually requires control on only one direction of motion for boundedness. The question of whether or not a dead-band control based on altitude measurements can be used to bound hovering in this one-dimensional region is addressed in Chapter V. It is found that an altitude dead-band

is often sufficient to bound this type of hovering. A significant region is also identified where two directions of motion must be controlled for boundedness. In Chapter V, we find that in the two-body problem, hovering at these locations cannot be bound by a dead-band control based on optical navigation measurements. The effects of errors in the initial state and open-loop thrust on the zero-velocity surface are also defined.

In addition to the contributions mentioned above, Chapter V also investigated fuel use and control application frequency under dead-band hovering control. Simulations demonstrating the validity of the zero-velocity surface result were also presented.

In Chapter VI, a constant thrust translation controller is presented and shown to accurately intercept positions in its vicinity at the chosen time. Also, the locus of states that result in touchdown at a specified point on the small-body surface without thrust is defined. A method of assessing uncertainty in the final position resulting from parameter uncertainty in the dynamic model is also presented and applied to descending translations under the constant thrust controller. Covariance analysis is applied to a sample trajectory that incorporates the constant thrust translation control and the no thrust solution. Finally, simulations of descent using a hovering dead-band with variable target altitude are discussed. This discussion includes a simple calculation of the altitude at which dust particles can be lifted off the surface by the thruster plume.

Throughout, the analytical work presented was supported with numerical data for realistic implementations from the HoverSim and SBDT software packages. A case study of inertial and body-fixed hovering over the asteroid Itokawa was presented in Chapter III. In Chapter IV, the zero-velocity surface type is given for positions near models of the asteroids Eros and Golevka and in Chapter V boundedness under alti-

tude dead-band hovering control is demonstrated. Chapter VI applies the constant thrust translation control and covariance analysis to maneuvers near the asteroids Itokawa, Eros, and Vesta.

### 7.1.1 Summary of Hovering Strategies Discussed

Since hovering maneuvers are a focus of this work, an explicit list of the different strategies covered with their strengths and weaknesses is given here.

#### **Hovering in the Rotating Body-fixed Two-body Equations of Motion** This

approach fixes the spacecraft position relative to the small-body surface. This may be advantageous for taking high resolution measurements or in preparation for a descent maneuver. This approach applies to hovering near the small-body where only acceleration from its gravity must be considered. This dissertation studies body-fixed hovering with three different types of measurements:

- **Position measurements** If position of the spacecraft in the rotating frame can be measured, dead-band control (possibly of reduced order) can be designed (as the examples in Section 4.2) such that boundedness of the trajectory can be determined in a straightforward manner without significant approximation (see Sections 4.2.2 and 4.4.1). The disadvantage of this approach is that it requires accurate estimation of the spacecraft position at all times.
- **Altitude measurements** Section 5.2.1 demonstrates that hovering can often be bounded using only altitude measurements near the surface of a small-body. This has the advantage of requiring only one measurement instrument (good for cost saving and when other measurements are not available) and being relatively simple to implement. The disadvantages

of this approach are that fewer hovering positions can be bounded than with position measurements and the boundedness result relies strongly on surface topography, open-loop thrust magnitude, and dead-band size. Numerical results for two body-fixed dead-band hovering controllers (GDTS w/OL and IATNS) that rely on altitude measurements are presented (Sections 3.3 and 3.4.1). It is found that the orientation of the curved dead-band surface induced by this type of measurement may destabilize motion.

- **Optical navigation measurements** Hovering under a dead-band control on optical navigation measurements (assumed to give information on latitude and longitude only) is found to not bound hovering in the two-body problem (Section 5.2.2).

**Hovering in an Inertial Frame above a Rotating Small-body** This approach, studied in Section 3.4.2, fixes the spacecraft position in an inertial frame while the small-body rotates beneath it. This may be useful for characterizing the small-body shape or keeping a fixed communication or solar panel geometry. The advantage of this approach is that it is usually stable under control on one direction of motion. The disadvantage is that it only applies close to the body where forces other than the small-body gravity can be neglected.

**Hovering in the Three-body Problem** This approach can be applied to hovering near a planetary satellite or in a region around a small-body where the gravity and SRP from the Sun must be considered. Position knowledge is assumed and the necessary dead-band control to bound hovering can be computed in a straightforward manner (Section 4.2.2). The disadvantage of this approach is that it does not allow arbitrary small-body shape, rotation state,

or orbit. Hovering in the circular restricted and Hill three-body problems are discussed in Sections 4.4.2 and 4.4.3.

## 7.2 Topics for Future Study

One of the main contributions of this work was the development of the zero-velocity surface bound on hovering motion. This result has great application to station-keeping controller design. However, this bound on the motion relies on preservation of the Jacobi constant. Two issues have been identified that may destroy this bound. First, this result must be extended to time-varying systems since all real spacecraft dynamics are ultimately time-varying. It may be possible to find a result by assuming the effect of the time-varying portion of the dynamics is small or by studying the dynamics over a short period of time with the slowly-varying parameters fixed.

Second, a method of realistic implementation of the idealized dead-band controller must be developed that avoids the problems introduced by a finite measurement sampling frequency and measurement errors shown in the last section of Chapter V. Such an implementation must keep the Jacobi constant within a small range around the nominal value through repeated dead-band thrust activations. This problem may be resolved by applying a filter to the measurement values and predicting thrust on/off times in advance.

The final section of Chapter VI introduces the idea of using dead-band hovering control with a variable target altitude to descend to the small-body surface. This method keeps a tight rein on spacecraft velocity, which is desirable for soft landing maneuvers. A tight bound on the position of the spacecraft is inferred by the numerical results in this section. Using the Jacobi constant and the zero-velocity surface

bound (possibly changing with time), I suspect that a method of maintaining tight position control on the spacecraft through descent can be developed and shown to work analytically. This would be an excellent topic for future study.

Implementation of two-dimensional dead-band control using optical navigation measurements is also a topic worthy of further study. It was shown here that using optical navigation measurements of spacecraft latitude and longitude as the basis of a two-dimensional dead-band control is not an effective method of bounding the possible spacecraft motion in close proximity to the small-body, but it could be a useful approach for hovering in the three-body problem at a greater distance from the small-body. Also, the two-dimensional dead-band presented here only assumed information on the spacecraft latitude and longitude; some optical navigation techniques give range information as well. It may be possible to exploit this range information to create a dead-band controller from these measurements that bounds hovering close to the small-body.

Also, the work here on implementation of one-dimensional hovering using altimetry could be extended to allow for arbitrary small-body shapes, though I suspect a numerical approach to that problem will be necessary.

Also, the zero-velocity surface result should be used to study constant thrust translation maneuvers. Since the thrust is constant, the Jacobi constant is preserved throughout these maneuvers. Zero-velocity surface analysis could be used to determine when escape from the small-body is possible or may yield novel insight into translation control design.

Finally, the applicability of this research to small-body mapping strategies should be studied. Since these maneuvers allow a spacecraft to move around the small-body arbitrarily and linger at a fixed position relative to the surface, they could be used to

improve the temporal efficiency and coverage of current mapping techniques. With these maneuvers, coverage need not be limited in certain areas and repeated in others (though additional fuel costs will likely apply).

### **7.3 Application of this Research**

For the maneuver approaches developed here to be used on a small-body mission, some additional work and testing is required to bring the technology to flight readiness.

For implementation of all the maneuvers discussed, the measurement and estimation process must be shown to reliably determine spacecraft position, velocity, and attitude to sufficient accuracy. A detailed study of the estimation process, including all measurements, conservative uncertainties, and a detailed dynamical model, should be done to characterize the expected uncertainty in these quantities. Uncertainty in the state must be shown to be acceptable for the chosen maneuver and pointing accuracy must be shown to be sufficient for reliable thrust application.

If using altitude measurements, the reliability and accuracy of the chosen altimeter should be well characterized before flight. This requires hardware testing with the selected instrument against probable small-body surface types across a range of orientations and ranges and, if available/applicable, study of the altimeter performance during the NEAR and Hayabusa missions. Optical navigation measurements should be characterized via computer simulation as realistically as possible.

To be used on a mission, hovering with a reduced order dead-band control must be demonstrated to be fail safe. If the hovering control fails, impact with the surface or escape will usually occur; both cases would likely be catastrophic to a mission. To avoid this, the thrusting, measurement, and estimation components of this control

must be very reliable. Safe hovering requires reliable and redundant thrusters to accurately produce low levels of thrust (in order to preserve the Jacobi constant). Typical error in the applied thrust for the thrusters being used should be characterized in the lab and the effect of those errors on the spacecraft velocity and zero-velocity surface determined using the perturbation theory presented here. The effect of the expected level of uncertainty in the dynamical parameters, state, and attitude on the bounding zero-velocity surface must be carefully studied as well.

For use of constant thrust translation maneuvers in practice, it may be desirable to extend the approach so that the constant thrust solution is used to move between waypoints spaced in short intervals along the desired trajectory. This preserves accuracy and allows the applied thrust to be updated based on the latest state estimates.

Descent to the small-body surface is potentially a very dangerous maneuver since uncontrolled or unplanned impact with the surface may disable the spacecraft. If a mission includes a descent to the surface, the strategy to be used should be very carefully studied. Again, navigational accuracy and altimeter reliability should be demonstrated if using altitude as a trigger for maneuvers during the descent. However, because of the risk and critical importance of this mission phase, detailed hardware-in-the-loop simulation on the ground is justified. The final descent and touchdown phases should be tested in a ground simulation with realistic spacecraft dynamics and a realistic spacecraft model. The control logic to be applied during the mission should be used based on actual hardware measurements (assuming altitude) taken off a realistic small-body surface mock-up. Though it is outside the scope of this thesis, the actual sample collection hardware should be tested as well across a range of likely surface properties. Such a descent test should be performed for a

range of possible initial conditions.

## APPENDICES

## APPENDIX A

### Author's Bibliography

#### On Hovering:

- S. Sawai, D.J. Scheeres, and S.B. Broschart, "Control of Hovering Spacecraft using Altimetry," *Journal of Guidance, Control, and Dynamics*, Vol. 25, No. 4, pp. 786-795.
- S. Broschart and D.J. Scheeres, "Numerical Solutions to the Small-Body Hovering Problem", paper presented at the 2003 AAS/AIAA Spacecraft Mechanics Meeting, Ponce, Puerto Rico, February 9-13, 2003, AAS 03-157.
- S.B. Broschart and D.J. Scheeres, "Control of Hovering Spacecraft near Small-Bodies: Application to Asteroid 25143 Itokawa", *Journal of Guidance, Control, and Dynamics*, Vol.28, No. 2, pp. 343-354.
- S.B. Broschart and D.J. Scheeres, "Lyapunov Stability of Hovering Spacecraft in Time-Invariant Systems", paper presented at the 2005 AAS/AIAA Astrodynamics Specialists Meeting, Lake Tahoe, CA, August 2005, AAS Paper 05-381.
- S.B. Broschart and D.J. Scheeres, "Boundedness of Spacecraft Hovering Under Dead-band Control in Time-invariant Systems", paper accepted for publication in the *Journal of Guidance, Control, and Dynamics*, April 2006.

On Translation and Descent:

- S.B. Broschart and D.J. Scheeres, “Spacecraft Descent and Translation Near Small-Bodies”, paper presented at the 24th International Symposium on Space Technology and Science, Miyazaki, Japan, May 31-June 6, 2004, ISTS 2004-d-35.
- S.B. Broschart and D.J. Scheeres, “Spacecraft Descent and Translation in the Small-body Fixed Frame”, paper presented at the 2004 AIAA/AAS Astrodynamics Specialists Meeting, Providence, RI, August 2004, AIAA 2004-4865.

On Small-body Characterization:

- D.J. Scheeres, S.B. Broschart, S.J. Ostro, and L.A. Benner, “The Dynamical Environment about Asteroid 25143 Itokawa”, paper presented at the 24th International Symposium on Space Technology and Science, Miyazaki, Japan, May 31-June 6, 2004, ISTS 2004-d-36.
- D.J. Scheeres, S.B. Broschart, S.J. Ostro, and L.A. Benner, “The Dynamical Environment about Asteroid 25143 Itokawa, target of the Hayabusa Mission”, paper presented at the 2004 AIAA/AAS Astrodynamics Specialists Meeting, Providence, RI, August 2004, AIAA 2004-4864.
- S.J. Ostro, L.A.M. Benner, M.C. Nolan, C. Magri, J.D. Giorgini, D.J. Scheeres, S.B. Broschart, M. Kaasalainen, D. Vokrouhlicky, S.R. Chesley, J. Margot, R.F. Jurgens, R. Rose, D.K. Yeomans, S. Suzuki, E.M. DeJong, “Radar Observations of Asteroid 25143 Itokawa (1998 SF36)”, *Meteoritics and Planetary Science*, Vol. 39, No. 3, pp. 407-424.

- S.J. Ostro, L.A.M. Benner, C. Magri, J.D. Giorgini, R. Rose, R.F. Jurgens, D.K. Yeomans, A.A. Hine, M.C. Nolan, D.J. Scheeres, S.B. Broschart, M. Kaasalainen, and J. Margot, “Radar Observations of Itokawa in 2004 and improved shape estimation”, *Meteoritics and Planetary Science*, Vol. 40, No. 11, pp. 1563-1574.
- S.B. Broschart, “Small Body GN&C Research Report: Subroutines for faceted shape model computations: Ray intersection algorithm (SB1) and Mass property calculations (SB2)”, Internal Document JPL D-32824, Jet Propulsion Laboratory, Pasadena, CA, August 2005.
- M.W. Busch, S.J. Ostro, L.A.M. Benner, J.D. Giorgini, R.F. Jurgens, C. Magri, P. Pravec, D.J. Scheeres, and S.B. Broschart, “Radar and Optical Observations and Physical Modeling of Near-Earth Asteroid 10115 (1992 SK)”, *Icarus*, Vol. 181, No. 1, pp. 145-155.
- S.J. Ostro, J.-L. Margot, L.A.M. Benner, J.D. Giorgini, D.J. Scheeres, E.G. Fahnestock, S.B. Broschart, J. Bellerose, M.C. Nolan, C. Magri, P. Pravec, P. Scheirich, R. Rose, R.F. Jurgens, S. Suzuki, and E.M. DeJong, “Asteroid 66391 (1999 KW4): Radar Images and a Physical Model of a Near-Earth Binary System”, submitted to *Science*, August 2006.
- D.J. Scheeres, E.G. Fahnestock, S.J. Ostro, J.-L. Margot, L.A.M. Benner, S.B. Broschart, J. Bellerose, J.D. Giorgini, M.C. Nolan, C. Magri, P. Pravec, P. Scheirich, R. Rose, R.F. Jurgens, S. Suzuki, and E.M. DeJong, “Extraordinary Dynamical Configuration of Binary NEA 1999 KW4”, submitted to *Science*, August 2006.
- M. W. Busch, J. D. Giorgini, S. J. Ostro, L. A. M. Benner, R. F. Jurgens, R.

Rose, P. Pravec, D. J. Scheeres, S. B. Broschart, C. Magri, M. C. Nolan, and A. A. Hine, “Physical Modeling of Near-Earth Asteroid 29075 (1950 DA)”, to be submitted for journal publication.

On Measurement Formulations:

- S.B. Broschart, “Small Body GN&C Research Report: Geometric Formulation of Altimeter and Time-of-Flight Velocimeter Measurements”, Internal Document JPL D-32851, Jet Propulsion Laboratory, Pasadena, CA, August 2005.

## APPENDIX B

### Constant Density Gravity Computations

This appendix gives the literature results for the gravitational potential and its derivatives of an ellipsoid or polyhedral body with uniform density.

#### B.1 Potential of a Constant Density Ellipsoid

The gravitational potential of a constant density ellipsoid is defined by MacMillian[44]. The results are presented here in the notation used by Scheeres[45].

The gravitational potential of a constant density ellipsoidal small-body at a spacecraft position  $\tilde{\mathbf{r}}$  is defined in Eq. (B.1),

$$U = -\frac{1}{2}\mu_{sb} \left[ x^2 R_D (b^2 + \lambda, c^2 + \lambda, a^2 + \lambda) + y^2 R_D (c^2 + \lambda, a^2 + \lambda, b^2 + \lambda) + z^2 R_D (a^2 + \lambda, b^2 + \lambda, c^2 + \lambda) - 3R_F (a^2 + \lambda, b^2 + \lambda, c^2 + \lambda) \right] \quad (\text{B.1})$$

where (for a constant density ellipsoid)

$$\mu_{sb} = \frac{4\pi}{3} G \rho abc. \quad (\text{B.2})$$

$R_D$  (Eq. (B.3)) and  $R_F$  (Eq. (B.4)) are Carlson forms of the elliptic integrals,

$$R_F (a^2, b^2, c^2) = \frac{1}{2} \int_0^\infty \frac{du}{\sqrt{(a^2 + u)(b^2 + u)(c^2 + u)}} \quad (\text{B.3})$$

$$R_D (a^2, b^2, c^2) = \frac{3}{2} \int_0^\infty \frac{du}{(c^2 + u) \sqrt{(a^2 + u)(b^2 + u)(c^2 + u)}} \quad (\text{B.4})$$

which are solved numerically using the method of Press et al[74].  $\lambda = 0$  for positions in the ellipsoid interior and is defined implicitly by Eq. (B.5) for exterior positions.

$$\phi(x, y, z; \lambda) = \frac{x^2}{a^2 + \lambda} + \frac{y^2}{b^2 + \lambda} + \frac{z^2}{c^2 + \lambda} - 1 = 0 \quad (\text{B.5})$$

The gravitational attraction vector is defined by Eqs. (B.6) - (B.8).

$$\frac{\partial U}{\partial x} = -\mu_{sb} x R_D (b^2 + \lambda, c^2 + \lambda, a^2 + \lambda) \quad (\text{B.6})$$

$$\frac{\partial U}{\partial y} = -\mu_{sb} y R_D (c^2 + \lambda, a^2 + \lambda, b^2 + \lambda) \quad (\text{B.7})$$

$$\frac{\partial U}{\partial z} = -\mu_{sb} z R_D (a^2 + \lambda, b^2 + \lambda, c^2 + \lambda) \quad (\text{B.8})$$

If  $\tilde{\mathbf{r}}$  is inside the ellipsoid (see Section 2.1),

$$\left. \frac{\partial^2 U}{\partial x^2} \right|_{interior} = -\mu_{sb} R_D (b^2 + \lambda, c^2 + \lambda, a^2 + \lambda) \quad (\text{B.9})$$

$$\left. \frac{\partial^2 U}{\partial y^2} \right|_{interior} = -\mu_{sb} R_D (c^2 + \lambda, a^2 + \lambda, b^2 + \lambda) \quad (\text{B.10})$$

$$\left. \frac{\partial^2 U}{\partial z^2} \right|_{interior} = -\mu_{sb} R_D (a^2 + \lambda, b^2 + \lambda, c^2 + \lambda) \quad (\text{B.11})$$

and

$$\begin{aligned} \left. \frac{\partial^2 U}{\partial x \partial y} \right|_{interior} &= \left. \frac{\partial^2 U}{\partial y \partial x} \right|_{interior} = \left. \frac{\partial^2 U}{\partial x \partial z} \right|_{interior} = \\ &= \left. \frac{\partial^2 U}{\partial z \partial x} \right|_{interior} = \left. \frac{\partial^2 U}{\partial y \partial z} \right|_{interior} = \left. \frac{\partial^2 U}{\partial z \partial y} \right|_{interior} = 0. \end{aligned} \quad (\text{B.12})$$

If  $\tilde{\mathbf{r}}$  is outside the small-body,

$$\left. \frac{\partial^2 U}{\partial \tilde{\mathbf{r}}^2} \right|_{exterior} = \left. \frac{\partial^2 U}{\partial \tilde{\mathbf{r}}^2} \right|_{interior} + \frac{3\mu_{sb}}{\sqrt{(a^2 + \lambda)(b^2 + \lambda)(c^2 + \lambda)}} \frac{\tilde{\zeta} \tilde{\zeta}^T}{\tilde{\zeta}^T \tilde{\zeta}} \quad (\text{B.13})$$

where

$$\tilde{\zeta} = \left[ \frac{x}{a^2 + \lambda}, \frac{y}{b^2 + \lambda}, \frac{z}{c^2 + \lambda} \right]^T. \quad (\text{B.14})$$

For both cases, the Laplacian is defined by Eq. (B.15).

$$\nabla^2 U = \frac{\partial^2 U}{\partial x^2} + \frac{\partial^2 U}{\partial y^2} + \frac{\partial^2 U}{\partial z^2} \quad (\text{B.15})$$

## B.2 Potential of a Constant Density Polyhedron

The gravitational potential of a constant density polyhedral small-body is derived in Werner and Scheeres[42]. The potential and its derivatives are computed using the summations over the polyhedron's faces and edges given in Eqs. (B.16)-(B.19),

$$U = \frac{1}{2}G\varrho \sum_{e \in \text{edges}} \tilde{\mathbf{r}}_e^T E_e \tilde{\mathbf{r}}_e \cdot L_e - \frac{1}{2}G\varrho \sum_{i \in \text{faces}} \tilde{\mathbf{r}}_i^T F_i \tilde{\mathbf{r}}_i \cdot \omega_i \quad (\text{B.16})$$

$$\frac{\partial U^T}{\partial \tilde{\mathbf{r}}} = -G\varrho \sum_{e \in \text{edges}} E_e \tilde{\mathbf{r}}_e \cdot L_e + G\varrho \sum_{i \in \text{faces}} F_i \tilde{\mathbf{r}}_i \cdot \omega_i \quad (\text{B.17})$$

$$\frac{\partial^2 U}{\partial \tilde{\mathbf{r}}^2} = G\varrho \sum_{e \in \text{edges}} E_e \cdot L_e - G\varrho \sum_{i \in \text{faces}} F_i \cdot \omega_i \quad (\text{B.18})$$

$$\nabla^2 U = -G\varrho \sum_{i \in \text{faces}} \omega_i \quad (\text{B.19})$$

where

$$\tilde{\mathbf{r}}_e = \tilde{\mathbf{r}}_{e,1} - \tilde{\mathbf{r}} \quad (\text{B.20})$$

$$E_e = \hat{\mathbf{n}}_{i1} \hat{\mathbf{n}}_{e,i1}^T + \hat{\mathbf{n}}_{i2} \hat{\mathbf{n}}_{e,i2}^T \quad (\text{B.21})$$

$$L_e = \ln \frac{\rho_{e,1} + \rho_{e,2} + e_{1,2}}{\rho_{e,1} + \rho_{e,2} - e_{1,2}} \quad (\text{B.22})$$

$$\tilde{\mathbf{r}}_i = \tilde{\rho}_{i,1} \quad (\text{B.23})$$

$$F_i = \hat{\mathbf{n}}_i \hat{\mathbf{n}}_i^T. \quad (\text{B.24})$$

Here for edge  $e$ ,  $\tilde{\mathbf{r}}_{e,1}$  and  $\tilde{\mathbf{r}}_{e,2}$  are the positions of the two constituent vertices,  $\hat{\mathbf{n}}_{i1}$  and  $\hat{\mathbf{n}}_{i2}$  are the surface normals to the two constituent faces, and  $\hat{\mathbf{n}}_{e,i1}$  and  $\hat{\mathbf{n}}_{e,i2}$  are the outward pointing normal vectors to the edge in the plane of face  $i1$  and  $i2$  respectively. Also,

$$\rho_{e,1} = \|\tilde{\mathbf{r}}_{e,1} - \tilde{\mathbf{r}}\| \quad (\text{B.25})$$

$$\rho_{e,2} = \|\tilde{\mathbf{r}}_{e,2} - \tilde{\mathbf{r}}\| \quad (\text{B.26})$$

$$e_{1,2} = \|\tilde{\mathbf{r}}_{e,1} - \tilde{\mathbf{r}}_{e,2}\|. \quad (\text{B.27})$$

$\tilde{\rho}_{i,1}$  is defined in Eq. (2.11) and  $\omega_i$  is defined in Eq. (2.7). Note that the summations should be conducted over the polyhedron's unique edges, not all of the edges for each face.

## APPENDIX C

# Use and Outputs of the Small-body Characterization Tool

The Small-body Characterization Tool<sup>1</sup> is initialized by a set of text files that contain descriptions of the small-body shape, gravity, and orbit, basic spacecraft properties, proposed mission parameters, and desired outputs.

The software is designed as a *C++* class that can be compiled to run as a stand-alone program or as a class to be called from other *C++* programs or compatible software (such as JPL's MONTE software or Matlab). The stand-alone version of the tool also must be told which functional blocks to execute while the individual methods can be called upon when the tool is used as a class within other software.

The SBCT class has six functional blocks (public methods), that can be called on to report specifics of the dynamic environment.

**Fundamental Properties** gives basic parameters of the small body shape and gravity including gravitational parameter ( $\mu_{sb}$ ), volume, surface area, bulk density,  $J_2 (= -C_{20})$ ,  $C_{22}$ , spatial extent, ratios of the moments of inertia, and the dynamically equivalent equal volume ellipsoid (DEEVE).

---

<sup>1</sup>Requests to secure use of the SBCT should be sent to Shyam Bhaskaran (Shyam.Bhaskaran@jpl.nasa.gov).

**Two-Body Dynamics** describes the two-body problem in the rotating frame (Section 2.3.1) for the input body. Outputs from this block include the resonance radius (Eq. (2.16)), the two-body equilibria (including their location, stability, and characteristic times), and the small-body type[75].

**Solar Effects** describes the effect of the Sun on the dynamics near the small-body (using equations of motion in Sections 2.3.2 and 2.3.3) and reports values of the Hill radius (Eq. (2.22)), spacecraft mass to area ratio, normalized SRP strength[17], and three-body equilibrium locations (with and without SRP included).

**Orbital Environment** takes the proposed orbit from the input file and determines the period of the secular orbital element oscillations, the relative strength of the major perturbations (solar tide, small-body oblateness, and SRP), the offset of the terminator orbit center due to SRP, and the orbital elements for the frozen orbits at the proposed semi-major axis[14]. It also determines if it is energetically possible for the orbit to escape the vicinity of the small-body.

**Surface Properties** reports on the surface accelerations (assuming two-body dynamics), slopes, escape speeds[15], and the dynamically plausible composition of the body[76].

**Hovering Environment** describes hovering near the small-body by reporting the nominal acceleration, daily required  $\Delta V$ , and local zero-velocity surface[62] for a given hovering position.

## APPENDIX D

# Small-body Dynamics Toolbox Description

The Small-body Dynamics Toolbox<sup>1</sup> is a collection of Matlab and Simulink software tools that have been developed to aid in this research. The functions of the SBDT include small-body shape and gravity modeling tools, trajectory integration (including HoverSim which is described in Section 3.2), covariance computations, periodic orbit computations, small-body surface characterization, and output visualization.

### Small-body Shape and Gravity Modeling

The SBDT allows the use of tri-axial ellipsoidal or triangular faceted polyhedral small-body shape models (as described in Section 2.1) in its computations. A constant density gravity model corresponding to the chosen shape (as described in Appendix B) is assumed. For the given shape and gravity, the volume, center of mass, and moments of inertia are determined using the method of Mirtich[49]. For each facet of a polyhedral model, the center, normal vector, maximum extent, and surface area are computed. The edges of the polyhedron are also determined and specified by which two vertices they connect. The rotation rate of the small-body

---

<sup>1</sup>Requests to obtain portions of the SBDT should be sent to Steve Broschart (sbroscha@gmail.com) and Dan Scheeres (scheeres@umich.edu).

is determined from the specified rotation period, which allows computation of the resonance radius (Eq. (2.16)).

### **Trajectory Integration**

The SBDT uses Matlab's 'ode45' function to integrate various equations of motion. Functions exist to integrate the two-body equations of motion in the frame rotating with the small-body (Section 2.3.1), the linearized two-body equations of motion in the rotating frame (Section 2.3.1), the circular restricted three-body problem (Section 2.3.2), the elliptic restricted three-body problem, the generalized elliptic restricted three-body problem (Section 2.3.4), and one-dimensional dynamics with linearly varying gravity. Each of these integrators returns the position and velocity history of the spacecraft, corresponding times, Jacobi constant (if applicable), and dead-band crossing times and states (if applicable).

The various control types discussed in this dissertation can be applied in any of these equations of motion. These include open-loop cancellation of the nominal acceleration (also can cancel a percentage of the nominal acceleration), one, two, or three dimensional dead-band control based on position measurements (as in Eqs. (4.9)-(4.9)), dead-band control on altitude (measured along  $\hat{\mathbf{v}}_3$ ,  $\hat{\vartheta}_3$ , or a specified direction), and dead-band control on altitude rate-of-change. The formulations used for altitude and altitude rate-of-change are presented in Sections 2.4.1 and 2.4.2 respectively. Controls also exist that compute and implement constant thrust translation trajectories given a target position in the two-body problem (Section 6.3) and for sliding dead-band descent (Section 6.6).

## Covariance Computations

The SBDT can determine the evolution of the linear covariance ellipsoid around a nominal trajectory considering uncertainty in initial state, small-body rotation rate, small-body mass, first through third order spherical harmonic coefficients, thrust magnitude, and thrust direction using the technique presented in Section 6.4. It does not use measurements to update the uncertainty, but simply propagates the initial uncertainty in state along a nominal trajectory.

## Periodic Orbit Computation

The SBDT has the capability to compute periodic orbits around polyhedral small-bodies. Given an initial state guess, the tool can converge on a state that results in a periodic orbit in a conservative system using the monodromy matrix. This matrix is made invertible by reducing the dynamics onto a Poincaré surface, then reducing again using the Jacobi constant by the method of Scheeres *et al.*[16]. The stability of a periodic orbit is determined from the eigenvalues of the monodromy matrix.

Orbit families can be mapped out from an initial orbit for changing Jacobi constant or small-body gravitational parameter. Equilibrium points in the rotating two-body problem (orbits with period equal to the small-body rotation period) are also found using a Newton algorithm to converge on positions where the nominal acceleration is zero.

## Small-body Surface Characterization

The SBDT can compute the total acceleration, surface slope (angle between the surface normal and total acceleration vector), acceleration normal to the surface, acceleration tangent to the surface, the downhill vector (vector in the small-body surface that points in the acceleration direction), sufficient escape speed[15], and

necessary escape speed[15] for each facet of a polyhedral small-body model. These quantities can be used for studies of surface regolith distribution, small-body composition, and surface particle or spacecraft “hopper” dynamics.

### **Visualization Tools**

The SBDT utilizes Matlab’s excellent visualization routines to display the results of its calculations. Plotting routines for trajectory integration show the computed trajectory relative to the small-body surface, trajectory relative to the nominal position (with quadratic zero-velocity surface shown for hovering), distance from the nominal position versus time, Jacobi constant versus time, altitude versus time, sub-altimeter point latitude and longitude (on small-body surface), altitude rate-of-change versus time, range from the small-body center of mass versus time, velocity magnitude versus time, spacecraft latitude and longitude relative to the small-body center of mass, thrust magnitude versus time, and expended  $\Delta V$  versus time.

There are also scripts which evaluate the zero-velocity surface type in the two-body, circular restricted three-body, and Hill three body problems and plot the results as a function of hovering position (as in Section 4.4). The sufficient conditions for bounded hovering under an altitude dead-band can also be evaluated as a function of position and plotted (as in Section 5.2.1).

Polyhedral shape models can also be visualized with the option to color code the surface facets as a function of any of the computed surface properties (slope, acceleration, escape speed, etc.).

## APPENDIX E

### Zero-velocity Surfaces near Equilibria in Lagrangian Dynamics

The results found for equilibria in spacecraft dynamical systems of the form of Eq. (4.1) are applicable to a broader class of unconstrained, time-invariant Lagrangian systems. This more general formulation follows.

For a time-invariant rheonomic system, there exists a Lagrangian function of the form of Eq. (E.1).

$$L(\tilde{\mathbf{q}}, \dot{\tilde{\mathbf{q}}}) = T(\tilde{\mathbf{q}}, \dot{\tilde{\mathbf{q}}}) + V(\tilde{\mathbf{q}}) \quad (\text{E.1})$$

The Jacobi constant is defined as

$$J(\tilde{\mathbf{q}}, \dot{\tilde{\mathbf{q}}}) = \frac{\partial L}{\partial \dot{\tilde{\mathbf{q}}}} \dot{\tilde{\mathbf{q}}} - L = C_L, \quad (\text{E.2})$$

which has constant value for all states on a valid trajectory. The equations of motion for this system are given by the standard form of Lagrange's equations,

$$\dot{\tilde{\mathbf{q}}} = \dot{\tilde{\mathbf{q}}} \quad (\text{E.3})$$

$$\dot{\tilde{\mathbf{p}}} = \frac{d}{dt} \left( \frac{\partial L^T}{\partial \dot{\tilde{\mathbf{q}}}} \right) = \frac{\partial L^T}{\partial \tilde{\mathbf{q}}}. \quad (\text{E.4})$$

For a state to be an equilibrium,  $\dot{\tilde{\mathbf{q}}}_{eqm} = \mathbf{0}_{3 \times 1}$ . In addition,  $\partial L / \partial \tilde{\mathbf{q}}$  must equal zero. When evaluated at  $\dot{\tilde{\mathbf{q}}}_{eqm}$ , this second condition reduces to finding  $\tilde{\mathbf{q}}_{eqm}$  such that  $\partial J / \partial \tilde{\mathbf{q}}|_{(\tilde{\mathbf{q}}_{eqm}, \mathbf{0}_{3 \times 1})} = \mathbf{0}_{1 \times 3}$ .

The discussion follows from here in the same manner as in Section 4.1. If the trajectory is initialized at the equilibrium point  $(\tilde{\mathbf{q}}_{eqm}, \mathbf{0}_{3x1})$ , all possible future states must have the same value of Jacobi constant. A quadratic expansion around the equilibrium can be performed and because  $\|\dot{\tilde{\mathbf{q}}}\| > 0$ , this defines the zero-velocity surface of the system in the vicinity of the equilibrium.

## **BIBLIOGRAPHY**

## BIBLIOGRAPHY

- [1] “JPL’s Horizons System,” Website, Dec. 2003, <http://ssd.jpl.nasa.gov/horizons.html>.
- [2] Email Correspondence with S. Sawai (JAXA), Oct. 2002.
- [3] Selby, S. M., *CRC Standard Mathematical Tables*, The Chemical Rubber Company, Cleveland, OH, 21st ed., 1973.
- [4] Thomas, P. C., “Gravity, Tides, and Topography on Small Satellites and Asteroids: Application to Surface Features of the Martian Satellites,” *Icarus*, Vol. 105, 1993, pp. 326–344.
- [5] Ostro, S. J., Hudson, R. S., Nolan, M. C., Margot, J. L., Scheeres, D. J., Campbell, D. B., Magri, C., Giorgini, J. D., and Yeomans, D. K., “Radar observations of asteroid 216 Kleopatra,” *Science*, Vol. 288, 2000, pp. 836–839.
- [6] Hudson, R. S., Ostro, S. J., Jurgens, R. F., Rosema, K. D., Giorgini, J. D., Winkler, R., Rose, R., Choate, D., Cormier, R. A., Franck, C. R., Frye, R., Howard, D., Kelley, D., Littlefair, R., Slade, M. A., Benner, L. A. M., Thomas, M. L., Mitchell, D. L., Chodas, P. W., Yeomans, D. K., Scheeres, D. J., Palmer, P., Zaitsev, A., Koyama, Y., Nakamura, A., Harris, A. W., and Meshkov, M. N., “Radar Observations and Physical Modeling of Asteroid 6489 Golevka,” *Icarus*, Vol. 148, No. 1, 2000, pp. 37–51.
- [7] Scheeres, D. J., “Close Proximity and Landing Operations at Small-bodies,” presented at the AIAA/AAS Astrodynamics Conference, San Diego, CA, July 29–31, 1996. AIAA Paper 96-3580.
- [8] Scheeres, D. J., “Stability of Hovering Orbits around Small Bodies,” *Spaceflight Mechanics 1999: Advances in the Astronautical Sciences, Part II*, Vol. 102, 1999, pp. 855–875, AAS Paper 99-159.
- [9] Kubota, T., Hashimoto, T., Uo, M., Maruya, M., and Baba, K., “Maneuver Strategy for Station Keeping and Global Mapping around an Asteroid,” *Spaceflight Mechanics 2001: Advances in the Astronautical Sciences*, Vol. 108, 2001, pp. 769–779, AAS Paper 01-156.

- [10] Sawai, S., Scheeres, D. J., and Broschart, S. B., "Control of Hovering Spacecraft using Altimetry," *Journal of Guidance, Control and Dynamics*, Vol. 25, No. 4, 2002, pp. 786–795.
- [11] Miller, J. K., Weeks, C. J., and Wood, L. J., "Orbit Determination Strategy and Accuracy for a Comet Rendezvous Mission," *Journal of Guidance, Control, and Dynamics*, Vol. 13, No. 5, 1990, pp. 775–784.
- [12] Hamilton, D. P. and Burns, J. A., "Orbital Stability Zones about Asteroids," *Icarus*, Vol. 92, No. 1, 1991, pp. 118–131.
- [13] Hamilton, D. P. and Burns, J. A., "Orbital Stability Zones about Asteroids, II. The Destabilizing Effects of Eccentric Orbits and of Solar Radiation," *Icarus*, Vol. 96, No. 1, 1992, pp. 43–64.
- [14] Scheeres, D. J., "Satellite Dynamics about Asteroids," *Spaceflight Mechanics 1994: Advances in the Astronautical Sciences, Part I*, Vol. 87, 1994, pp. 275–292, AAS Paper 94-112.
- [15] Scheeres, D. J., Ostro, S. J., Hudson, R. S., DeJong, E. M., and Suzuki, S., "Dynamics of Orbits Close to Asteroid 4179 Toutatis," *Icarus*, Vol. 132, No. 1, 1998, pp. 53–79.
- [16] Scheeres, D. J., Williams, B. G., and Miller, J. K., "Evaluation of the Dynamic Environment of an Asteroid: Applications to 433 Eros," *Journal of Guidance, Control and Dynamics*, Vol. 23, No. 3, 2000, pp. 466–475.
- [17] Scheeres, D. J. and Marzari, F., "Spacecraft Dynamics in the Vicinity of a Comet," *Journal of the Astronautical Sciences*, Vol. 50, No. 1, 2002, pp. 35–52.
- [18] Lara, M. and Scheeres, D. J., "Stability Bounds for Three-dimensional Motion Close to Asteroids," *Journal of the Astronautical Sciences*, Vol. 50, No. 4, 2002, pp. 389–409.
- [19] Scheeres, D. J., "Close Proximity Operations at Small Bodies: Orbiting, Hovering, and Hopping," *Mitigation of Hazardous Comets and Asteroids*, Cambridge University Press, 2004, pp. 313–336.
- [20] Scheeres, D. J., "Satellite Dynamics about small bodies: Averaged Solar Radiation Pressure Effects," *Journal of the Astronautical Sciences*, Vol. 47, No. 1, 1999, pp. 25–46.
- [21] Miller, J. K., Konopliv, A. S., Antreasian, P. G., Bordi, J. J., Chesley, S., Helfrich, C. E., Owen, W. M., Wang, T. C., Williams, B. G., and Yeomans, D. K., "Determination of Shape, Gravity, and Rotational State of Asteroid 433 Eros," *Icarus*, Vol. 155, No. 1, 2002, pp. 3–17.

- [22] McInnes, C. R., "Astronomical Engineering Revisited: Planetary Orbit Modification Using Solar Radiation Pressure," *Astrophysics and Space Science*, Vol. 282, 2002, pp. 765–772.
- [23] Lu, E. T. and Love, S. G., "A Gravitational Tractor for Towing Asteroids," *Nature*, Vol. 438, No. 2, 2005, pp. 177–178.
- [24] Dunham, D. W., Farquhar, R. W., McAdams, J. V., Holdridge, M., Nelson, R., Whittenburg, K., Antreasian, P., Chesley, S., Helfrich, C., Owen, W. M., Williams, B., Veverka, J., and Harch, A., "Implementation of the first asteroid landing," *Icarus*, Vol. 159, No. 2, 2002, pp. 433–438.
- [25] Guelman, M. and Harel, D., "Power limited soft landing on an asteroid," *Journal of Guidance, Control and Dynamics*, Vol. 17, No. 1, 1994, pp. 15–20.
- [26] Cui, H. T. and Cui, P. Y., "Autonomous navigation and guidance for soft-landing asteroid," *Journal of Astronautics (1000-1328)*, Vol. 23, No. 5, 2002, pp. 1–4.
- [27] Kominato, T., Matsuoka, M., Uo, M., Hashimoto, T., and Kawaguchi, J., "Optical Hybrid Navigation in Hayabusa Approach, Station Keeping, & Hovering," presented at the AAS/AIAA Spaceflight Mechanics Meeting, Tampa, Florida, January 22-26, AAS Paper 06-209.
- [28] Kubota, T., Hashimoto, T., Sawai, S., Kawaguchi, J., Ninomiya, K., Uo, M., and Baba, K., "An Autonomous Navigation and Guidance System for MUSES-C Asteroid Landing," *Acta Astronautica (0094-5765)*, Vol. 52, No. 2-6, 2003, pp. 125–131.
- [29] Hashimoto, T., Kubota, T., Sawai, S., Kawaguchi, J., and Uo, M., "Final Autonomous Descent Based on Target Marker Tracking," presented at the AIAA/AAS Astrodynamics Specialists Conference, Keystone, Colorado, August 21-24, AIAA Paper 2006-6538.
- [30] Kawaguchi, J., Aida, S., and Morita, H., "Hayabusa, Detailed Guidance and Navigation Operations during Descents and Touchdowns," presented at the AIAA/AAS Astrodynamics Specialists Conference, Keystone, Colorado, August 21-24, AIAA Paper 2006-6536.
- [31] Kubota, T., Otsuki, M., Hashimoto, T., Bando, N., Yano, H., Uo, M., Shirakawa, K., and Kawaguchi, J., "Touchdown Dynamics for Sampling in Hayabusa Mission," presented at the AIAA/AAS Astrodynamics Specialists Conference, Keystone, Colorado, August 21-24, AIAA Paper 2006-6539.
- [32] Byram, S. M., Scheeres, D. J., and Combi, M. R., "Navigation Models of Comet Outgassing Jets," presented at the 2005 Astrodynamics Specialist Conference, Lake Tahoe, California, August 2005. AAS Paper 05-284.

- [33] Fahnestock, E. G., Scheeres, D. J., McClamroch, N. H., and Werner, R. A., “Simulation And Analysis Of Binary Asteroid Dynamics Using Mutual Potential And Potential Derivatives Formulation,” presented at the 2005 Astrodynamics Specialist Conference, Lake Tahoe, California, August 2005. AAS Paper 05-356.
- [34] Diniega, S., *Regolith Distribution Model for Sub-kilometer Ellipsoidal Asteroids*, Master’s thesis, International Space University, July 2004.
- [35] Ostro, S. J., Benner, L. A. M., Nolan, M. C., Magri, C., Giorgini, J. D., Scheeres, D. J., Broschart, S. B., Kaasalainen, M., Vokrouhlicky, D., Chesley, S. R., Margot, J., Jurgens, R. F., Rose, R., Yeomans, D. K., Suzuki, S., and De Jong, E. M., “Radar Observations of Asteroid 25143 Itokawa (1998 SF36),” *Meteoritics and Planetary Science*, Vol. 39, No. 3, 2004, pp. 407–424.
- [36] Ostro, S. J., Benner, L. A. M., Magri, C., Giorgini, J. D., Rose, R., Jurgens, R. F., Yeomans, D. K., Hine, A. A., Nolan, M. C., Scheeres, D. J., Broschart, S. B., Kaasalainen, M., and Margot, J., “Radar Observations of Itokawa in 2004 and improved shape estimation,” *Meteoritics and Planetary Science*, Vol. 40, No. 11, 2005, pp. 1563–1574.
- [37] Busch, M. W., Ostro, S. J., Benner, L. A. M., Giorgini, J. D., Jurgens, R. F., Magri, C., Pravec, P., Scheeres, D. J., , and Broschart, S. B., “Radar and Optical Observations and Physical Modeling of Near-Earth Asteroid 10115 (1992 SK),” *Icarus*, Vol. 181, No. 1, 2006, pp. 145–155.
- [38] Ostro, S. J., Margot, J. L., Benner, L. A. M., Giorgini, J. D., Scheeres, D. J., Fahnestock, E. G., Broschart, S. B., Bellerose, J., Nolan, M. C., Magri, C., Pravec, P., Scheirich, P., Rose, R., Jurgens, R. F., Suzuki, S., and DeJong, E. M., “Asteroid 66391 (1999 KW4): Radar Images and a Physical Model of a Near-Earth Binary System,” submitted to *Science*, August 2006.
- [39] Scheeres, D. J., Fahnestock, E. G., Ostro, S. J., Margot, J. L., Benner, L. A. M., Broschart, S. B., Bellerose, J., Giorgini, J. D., Nolan, M. C., Magri, C., Pravec, P., Scheirich, P., Rose, R., Jurgens, R. F., Suzuki, S., and DeJong, E. M., “Extraordinary Dynamical Configuration of Binary NEA 1999 KW4,” submitted to *Science*, August 2006.
- [40] Busch, M. W., Giorgini, J. D., Ostro, S. J., Benner, L. A. M., Jurgens, R. F., Rose, R., Pravec, P., Scheeres, D. J., Broschart, S. B., Magri, C., Nolan, M. C., and Hine, A. A., “Physical Modeling of Near-Earth Asteroid 29075 (1950 DA),” to be submitted for journal publication.
- [41] Broschart, S. B., “Small Body GN&C Research Report: Geometric Formulation of Altimeter and Time-of-Flight Velocimeter Measurements,” Internal Document JPL D-32851, Jet Propulsion Laboratory, Pasadena, CA, USA, Aug. 2005.

- [42] Werner, R. A. and Scheeres, D. J., “Exterior Gravitation of a Polyhedron Derived and Compared with Harmonic and Mascon Gravitation Representations of Asteroid 4769 Castalia,” *Celestial Mechanics and Dynamical Astronomy*, Vol. 65, No. 3, 1996, pp. 313–344.
- [43] Hudson, S., “Three-dimensional Reconstruction of Asteroids from Radar Observations,” *Remote Sensing Reviews*, Vol. 8, 1993, pp. 195–203.
- [44] MacMillan, W. D., *The Theory of the Potential*, McGraw-Hill, 1930.
- [45] Scheeres, D. J., “Satellite Dynamics About Tri-Axial Ellipsoids,” presented at “Advances in Non-Linear Astrodynamics”, University of Minnesota, November 8-10, 1993.
- [46] Kaula, W. M., *Theory of Satellite Geodesy*, Blaisdell Publishing Company, Waltham, Massachusetts, 1966.
- [47] Pines, S., “Uniform Representation of the Gravitational Potential and its Derivatives,” *AIAA Journal*, Vol. 11, No. 11, 1973, pp. 1508–1511.
- [48] Lundberg, J. B. and Schutz, B. E., “Recursion Formulas of Legendre Functions for Use with Nonsingular Geopotential Models,” *Journal of Guidance, Control and Dynamics*, Vol. 11, No. 1, 1988, pp. 31–38.
- [49] Mirtich, B., “Fast and Accurate Computation of Polyhedral Mass Properties,” *journal of graphics tools*, Vol. 1, No. 2, 1996, pp. 31–50.
- [50] Montenbruck, O. and Gill, E., *Satellite Orbits: Models, Methods, Applications*, Springer-Verlag, Berlin, Germany, 2nd ed., 2001.
- [51] Greenwood, D. T., *Principles of Dynamics*, Prentice-Hall, New York, 2nd ed., 1988.
- [52] Roy, A. E., *Orbital motion*, Institute of Physics Publishing, Bristol and Philadelphia, 3rd ed., 1988.
- [53] Wintner, A., *The Analytical Foundations of Celestial Mechanics*, Princeton University Press, 1947.
- [54] Broschart, S. B., “Small Body GN&C Research Report: Subroutines for faceted shape model computations: Ray intersection algorithm (SB1) and Mass property calculations (SB2),” Internal Document JPL D-32824, Jet Propulsion Laboratory, Pasadena, CA, USA, Aug. 2005.
- [55] Eisenman, A. R., Alexander, J. W., and Stanton, R. H., “CCD sensors for spacecraft optical navigation,” presented at the 17th AIAA Aerospace Sciences Meeting, New Orleans, LA, January 1979. AIAA Paper 01979-392.

- [56] Bayard, D. S. and Brugarolas, P. B., “An Estimation Algorithm for Vision-Based Exploration of Small Bodies in Space,” presented at the American Control Conference, Portland, OR, June 8-10, 2005.
- [57] Fujiwara, A., Kawaguchi, J., Yeomans, D. K., Abe, M., Mukai, T., Okada, T., Saito, J., Yano, H., Yoshikawa, M., Scheeres, D. J., Barnouin-Jha, O., Cheng, A. F., Demura, H., Gaskell, R. W., Hirata, N., Ikeda, H., Kominato, T., Miyamoto, H., Nakamura, A. M., Nakamura, R., Sasaki, S., and Uesugi, K., “The Rubble-Pile Asteroid Itokawa as Observed by Hayabusa,” *Science*, Vol. 312, No. 5778, 2006, pp. 1330 – 1334.
- [58] Broschart, S. B. and Scheeres, D. J., “Control of Hovering Spacecraft near Small-Bodies: Application to Asteroid 25143 Itokawa,” *Journal of Guidance, Control, and Dynamics*, Vol. 28, No. 2, 2005, pp. 343–354.
- [59] Kawaguchi, J., Kuninaka, H., Fujiwara, A., Uesugi, T., and Ohnishi, T., “Muses-C Launch and Early Operations Report,” 2003, AAS Paper 03-662.
- [60] Hashimoto, T., Kubota, T., Kawaguchi, J., Uo, M., Baba, K., and Yamashita, T., “Autonomous Descent and Touch-down via Optical Sensors,” *Spaceflight Mechanics 2001: Advances in the Astronautical Sciences*, Vol. 108, 2001, pp. 469–490, AAS Paper 01-134.
- [61] Kaasalainen, M., Kwiatkowski, T., Abe, M., Piironen, J., Nakamura, T., Ohba, Y., Dermawan, B., Farnham, T., Colas, F., Lowry, S., Weissman, P., Whiteley, R. J., Tholen, D. J., Larson, S. M., Yoshikawa, M., Toth, I., and Velichko, F. P., “CCD Photometry and Model of MUSES-C Target (25143) 1998 SF36,” *Astronomy and Astrophysics*, Vol. 405, 2003, pp. L29–L32.
- [62] Broschart, S. B. and Scheeres, D. J., “Lyapunov Stability of Hovering Spacecraft in Time-invariant Systems,” presented at the 2005 Astrodynamics Specialist Conference, Lake Tahoe, California, August 2005. AAS Paper 05-381. To be published in the *Journal of Guidance, Dynamics, and Control* under the name “Boundedness of Spacecraft Hovering Under Dead-Band Control in Time-Invariant Systems”.
- [63] Khalil, H. K., *Nonlinear Systems*, Prentice Hall, Upper Saddle River, NJ, 3rd ed., 2002.
- [64] Greenwood, D. T., *Principles of Dynamics*, Prentice-Hall, New York, 2nd ed., 1988.
- [65] Dupont, L., Lazard, D., Lazard, S., and Petitjean, S., “Near-optimal Parameterization of the Intersection of Quadrics,” presented at the 19th ACM Symposium on Computational Geometry, San Diego, CA, June 2003.
- [66] “Hyperboloid – From Wolfram Mathworld,” Website, Aug. 2006, <http://mathworld.wolfram.com/Hyperboloid.html>.

- [67] Cipolla, R. and Giblin, P., *Visual Motion of Curves and Surfaces*, Cambridge University Press, Cambridge, UK, 1st ed., 2000.
- [68] Abe, S., Mukai, T., Hirata, N., Barnouin-Jha, O. S., Cheng, A. F., Demura, H., Gaskell, R. W., Hashimoto, T., Hiraoka, K., Honda, T., Kubota, T., Matsuoka, M., Mizuno, T., Nakamura, R., Scheeres, D. J., , and Yoshikawa, M., “Mass and Local Topography Measurements of Itokawa by Hayabusa,” *Science*, Vol. 312, 2006, pp. 1344–1347.
- [69] Konopliv, A. S., Yoder, C. F., Standish, E. M., Yuan, D.-N., and Sjogren, W. L., “A global solution for the Mars static and seasonal gravity, Mars orientation, Phobos and Deimos masses, and Mars ephemeris,” *Icarus*, Vol. 182, No. 1, 2006, pp. 23–50.
- [70] “JPL’s Small-body Database,” Website, July 2006, <http://ssd.jpl.nasa.gov/sbdb.cgi>.
- [71] Wolff, P. J., Pinto, F., Williams, B. G., and Vaughan, R. M., “Navigation Considerations for Low-thrust Planetary Missions,” presented at the AAS/AIAA Spaceflight Mechanics Meeting, Monterey, CA, February 9-11, 1998. AAS Paper 98-201.
- [72] Thomas, P. C., Binzel, R. P., Gaffey, M. J., Storrs, A. D., Wells, E., and Zellner, B. H., “Impact Excavation on Asteroid 4 Vesta: Hubble Space Telescope Results,” *Science*, Vol. 277, 1997, pp. 1492–1495.
- [73] Broschart, S. B. and Scheeres, D. J., “Spacecraft Descent and Translation in the Small-body Fixed Frame,” presented at the 2004 AIAA/AAS Astrodynamics Specialist Conference, Providence, Rhode Island, August 2004. AIAA Paper 2004-4865.
- [74] Press, W. H., Teukolsky, S. A., Vetterling, W. T., and Flannery, B. P., *Numerical Recipes in C: The Art of Scientific Computing*, Cambridge University Press, 2nd ed., 1992.
- [75] Scheeres, D. J., “Dynamics About Uniformly Rotating Tri-Axial Ellipsoids. Applications to Asteroids,” *Icarus*, Vol. 110, No. 2, 1994, pp. 225–238.
- [76] Holsapple, K. A., “Equilibrium Configurations of Solid Cohesionless Bodies,” *Icarus*, Vol. 154, 2001, pp. 432–448.